International Committee for Future Accelerators

Sponsored by the Particles and Fields Commission of IUPAP

Beam Dynamics Newsletter

No. 65

Issue Editor:
Y. Zhang

Editor in Chief:
W. Chou

December 2014

Contents

1 Foreword

1.1 From the Beam Dynamics Panel Chair

Weiren Chou, Fermilab
Mail to: chou@fnal.gov

The International Committee for Future Accelerators (ICFA) met on October 27, 2014 at the IHEP, Beijing, China during the ICFA Seminar. Nigel Lockyer, Fermilab Director and ICFA Chair chaired the meeting.

The ICFA Seminar series is organized by the ICFA once every three years. The 2014 Seminar took place from October 27 to 30 at the IHEP. The participation is by invitation only. There is a quota for each country. About 170 people from around the world attended. The invitees included directors of major accelerator laboratories, representatives from funding agencies, scientists all over the world, as well as media reporters. All talks presented at the seminar can be found on the web: http://indico.ihep.ac.cn/confRegistrationFormDisplay.py?confId=3867. The next one is in 2017, and TRIUMF has offered to host it.

At the ICFA meeting, Atsuto Suzuki, Director General of KEK, reported on the ILC progress in Japan. MEXT, the Japanese funding agency, and its counterparts in the US formed a US-Japan Friendship Caucus, which issued a joint statement calling for the early creation of a task force to further the ILC project. MEXT has also asked Nomura Research Institute (NRI) in Japan to investigate technology spin-offs from the ILC.

During a discussion on the global planning for HEP, Yifang Wang, Director of the IHEP, described the recent ICFA Advanced Beam Dynamics Workshop *Higgs Factory 2014* in Beijing. About 100 circular e+e- accelerator experts attended. The workshop website is: http://hf2014.ihep.ac.cn/. Sergio Bertolucci, Research Director of CERN, discussed the FCC status. He noted the many technical issues that need to be resolved in addition to that of the high field superconducting magnets. A goal is to produce a CDR by 2018/9 for input to the next European Strategy document.

Steinar Stapnes, leader of the CLIC study, reported on the future plans of the linear collider school. The 2015 school will be hosted by TRIUMF, the 2016 School at KEK, and a specialized CERN School in 2017 in Europe. Budget issues for future schools are still under study.

Atsuto Suzuki presented a proposal for a new ICFA Panel on Sustainable Accelerator/Colliders. He said that energy consumption and costs are becoming significant issues for accelerators from medical/industrial accelerators to frontier accelerators for particle physics research. It was agreed to discuss this issue further at the next ICFA meeting.

The US Liaison Committee for IUPAP has submitted a proposal to the IUPAP General Assembly that an IUPAP Commission on Accelerator Science be formed. Accelerator science has become broader over the past decades, and is more than just HEP accelerators. Accelerator physicists want recognition that their field is a branch of science. In Germany, accelerator physicists have been pushing for similar recognition. Accelerator physicists in fields such as light sources, nuclear physics, ADS etc. would like recognition; so far only HEP accelerator physicists have recognition, through ICFA and its parent body IUPAP's Commission 11 (Particles and Fields). Roy Rubinstein, the

ICFA Secretary was asked by IUPAP to coordinate among all interested parties a discussion on a path forward.

Starting from January 1, 2015, Joachim Mnich, Research Director of DESY, will become the chair of ICFA for a term of three years. The ICFA members expressed their appreciation to Nigel for his leadership of the committee over the past 1.5 years.

The editor of this issue is Dr. Yuhong Zhang, a senior scientist at Jlab, USA, and the archivist of this ICFA Beam Dynamics Newsletter. The theme is the second part of "*Beam Cooling and Related Topics.*" He collected another 13 well-written articles on this theme. Together with the 12 articles in Part 1 published in No. 64, the 25 articles are a complete collection of literatures in beam cooling and give a comprehensive review of this important field in beam dynamics.

In this issue there is also a workshop report (*Superconducting Undulators*), and four workshop announcements (*Space Charge 2015, ERL 2015, Advanced Optics Control,* and *ICFA Mini-Workshop on Beam Commissioning for High Intensity Accelerators*). I want to thank Yuhong for editing two high quality and valuable newsletters for the accelerator community.

1.2 From the Editor

Yuhong Zhang
Thomas Jefferson National Accelerator Facility, Newport News, Virginia, USA
Mail to: yzhang@jlab.org

The theme section of this issue contains the second half of the articles for beam cooling and related topics. There are thirteen well written review articles covering the topics of lazer cooling, cooling of muon beams, newly proposed cooling programs, new cooling concepts and their proof-of-principle experimental demonstrations, cooling simulations and beam crystallization. I want to thank the authors of these articles for their contributions to this newsletter issue.

This issue also has one beam dynamics workshop summary and four workshop announcement.

2 THEME: Beam Cooling and Related Topics (Part II)

2.1 Laser Cooling of Ion Beams at Relativistic Energies

Michael Bussmann
Helmholtz-Zentrum Dresden Rossendorf e.V.
Bautzner Landstrasse 400, 01328 Dresden, Germany
Mail to: m.bussmann@hzdr.de

2.1.1 Introduction

Laser cooling of ion beams [1,2] can achieve unprecedented low momentum spreads and is strong enough to overcome intra-beam scattering and induce beam crystallization [3]. When compared to stochastic cooling [4] and electron cooling [5], laser cooling

promises to show better performance than the latter two in cooling highly relativistic ion beams [6]. Thus, laser cooling at future facilities such as FAIR and HIAF has come into the focus of ion accelerator research.

This work is intended to give the reader a comprehensive overview of laser cooling at relativistic energies and related experiments at the storage rings ESR [7,8,9] at GSI Darmstadt, S-LSR [10,11] at ICR Kyoto and CSRe [12] at IMP Lanzhou.

2.1.2 **Fundamentals of Laser Cooling at Storage Rings**

For laser cooling to work efficiently the atomic transition used for cooling should be saturated by the laser photons absorbed by the ions. In the interaction of these photons with the ions in a beam of velocity βc, with c being the vacuum speed of light and β the relativistic unit-less speed, it is essential to correct for relativistic effects which depend on the beam energy denoted by $\gamma=(1-\beta^2)^{-1/2}$. Laser cooling will throughout this text be considered for ion beams of near constant velocity circulating in a storage ring of circumference C. Throughout the text non-primed variables are used for the laboratory frame and primed variables for the ion beam rest frame.

2.1.2.1 ***Spatial Overlap of Ion and Laser Beam***

In a head on scattering geometry, ion beam and laser beam are fully overlapped over a straight section of length L inside the ring. With the ion beam full-width half-maximum (FWHM) diameters in transverse direction denoted by $d_{ion,x}$ and $d_{ion,y}$ assumed to be constant inside this overlap region, it is beneficial to choose a laser beam spot size $2\,w_{laser}$ smaller than both ion beam diameters, so that no laser power is wasted. Thus, only a part of the ion beam denoted by $\eta_{diam} = 4w_{laser}^2 / \left(d_{ion,x} \cdot d_{ion,y}\right)$ interacts with the laser beam.

In order to reach high photon fluxes, the laser beam is usually focused. The length of the focal region is denoted by the Rayleigh length $z_R = \pi w_{laser}^2 / \lambda_{laser}$ [13] and increases with shorter laser wavelength λ_{laser}. It is preferential to choose $z_R \geq L/2$, as the laser intensity outside the focal region is quickly reduced. This condition links the lateral and longitudinal spatial overlap. If laser power $P_{laser} = I_{laser} \cdot \pi w_{laser}^2$ is limited, it might be necessary to reduce the laser beam waist to reach the intensity required for saturation, potentially reducing the overlap length to $L_{overlap} = \min\left(L, z_R\right)$, yielding an efficiency factor of $\eta_{overlap} = L_{overlap} / C$. Note, however, that then $\eta_{diam}\eta_{overlap} \propto w_{laser}^4$.

With $L_{overlap} < C$, ions mix outside the overlap region and at each turn different ions will be in resonance with the laser photons, so that laser beam waists smaller than the ion beam diameter pose no problem and only reduce the cooling efficiency.

2.1.2.2 ***Saturating the Cooling Transition – the Laser Cooling Force***

In the simplest case a cooling transition is a transition between two electronic states defined by a central transition wavelength λ'_{trans} and a natural line width $\Gamma'_{trans} = 1/\tau'_{trans}$. For efficient cooling the life time $\tau'_{trans} = \tau_{trans}/\gamma$ of the cooling transition should be short compared to the beam revolution time $T_{rev} = \beta c / C = f_{rev}^{-1}$.

A key feature of laser cooling of relativistic ion beams is the exploitation of the relativistic Doppler shift of the laser wavelength to match the (shorter) cooling transition wavelength in the head-on geometry where the laser beam is counter-propagating to the ion beam

$$\lambda'_{trans} \equiv \lambda'_{laser} = \lambda_{laser} / \left((1+\beta)\gamma\right) \xrightarrow{\beta \to c} \lambda_{laser} / (2\gamma). \tag{1}$$

Powerful laser systems available at ultra-short EUV, XUV or X-ray wavelengths are sparse, thus by increasing ion beam energies a compact and readily available laser operating in the visible or UV wavelength range can be used for exciting cooling transitions. Equation 1 reverses to $\lambda_{laser} \xrightarrow{\beta \to c} \lambda'_{trans} / (2\gamma)$ when laser and ion beam are co-propagating, making it essentially impossible to use a co-propagating laser for laser cooling at high beam energies.

If a photon of wavelength λ'_{phot} excites an ion the ion momentum changes by the momentum of the photon absorbed

$$p'_{phot} = \hbar k'_{phot} = h / \lambda'_{phot} = (1+\beta)\gamma h / \lambda_{phot} = (1+\beta)\gamma p_{phot} \xrightarrow{\beta \to c} 2\gamma p_{phot}., \tag{2}$$

with $\hbar = h/(2\pi)$, h Planck's constant and the wave number $k'_{phot} = 2\pi / \lambda'_{phot}$, assuming counter-propagating ion and laser beam.

The ion momentum change $\Delta p'_{ion}$ in a time interval $\Delta t'$ depends on the momentum of the photon absorbed and the scattering rate $R'\left(\vec{k}'_{phot}, \vec{p}'_{ion}\right)$ for photons of wave vector $\vec{k}'_{phot}$ off an ion of momentum $\vec{p}'_{ion}$ and mass m'_{ion}. In the ion beam rest frame non-relativistic thermal motion dominates and the non-relativistically Doppler-shifted photon frequency $\omega'_{Doppler} = \omega'_{phot} - \vec{p}'_{ion} \cdot \vec{k}'_{phot} / m'_{ion}$ can cause a significant change in the probability to absorb a laser photon of frequency $\omega'_{phot} = ck'_{phot}$. The probability L' for exciting the transition strongly depends on the total detuning

$$\delta' = \omega'_{Doppler} - \omega'_{trans} = \omega'_{phot} - \omega'_{trans} - \vec{p}'_{ion} \cdot \vec{k}'_{phot} / m'_{ion} \tag{3}$$

between the Doppler-shifted laser frequency and the transition frequency $\omega'_{trans} = 2\pi c / \lambda'_{trans}$.

At a laser intensity equal to the saturation intensity $I'_{sat} = \pi hc / \left(3\lambda'^{3}_{sat} \tau'_{sat}\right)$ [2] the on-resonance saturation parameter $S'_0 = I'_{laser} / I'_{sat}$ becomes unity and efficient laser cooling possible. The scattering rate for the cooling transition then reads [1,2]

$$R' = \Gamma'_{trans} \cdot L' = \Gamma'_{trans} \cdot \frac{1}{2} \frac{S'_0 \left(\Gamma'_{trans}/2\right)^2}{\delta'^2 + \left(1+S'_0\right)\left(\Gamma'_{trans}/2\right)^2}. \tag{4}$$

The laser cooling force accordingly amounts to

$$\vec{F}'_{laser} = \vec{p}'_{phot} R' = \frac{S'_0 \left(\Gamma'_{trans}/2\right)^3}{\delta'^2 + \left(1+S'_0\right)\left(\Gamma'_{trans}/2\right)^2} \hbar \vec{k}'_{phot}, \tag{5}$$

acting solely in the direction of the photon momentum, and becomes maximum

$$\left|\vec{F}'_{laser,\max}\left(\delta'=0\right)\right| = \frac{h\Gamma'_{trans}}{2\lambda'_{phot}}\frac{S'_0}{\left(1+S'_0\right)} \xrightarrow{S'_0\to\infty} \frac{\Gamma'_{trans}}{2}\frac{h}{\lambda'_{phot}} = \frac{p'_{phot}}{2\tau'_{trans}} \tag{6}$$

at zero total detuning. Therefore, a single laser beam acting on the ions of a coasting beam in a head-on scattering geometry always decelerates the ions and stable cooling without a counteracting accelerating force is impossible. Later in the text moderate bunching of the ion beam will be introduced as a method for stable cooling.

Setting $\omega'_{phot} = \omega'_{trans} + \vec{p}'_{ion}\cdot\vec{k}'_{phot}/m'_{ion}$ maximizes the laser. For head-on scattering the laser photon frequency $f'_{phot} = \omega'_{phot}/(2\pi)$ must be red-shifted to $f'_{phot} = f'_{trans}/\left(1+p'_{ion}/\left(m'_{ion}c\right)\right)$ to decelerate these ions. The laser force decreases to half its maximum strength for $\delta' = \pm\sqrt{\left(1+S'_0\right)}\Gamma'_{trans}/2$ and one can define the momentum acceptance of the laser force for a single laser photon wavelength λ'_{phot} as

$$\Delta p'_{l,acc} = \sqrt{\left(1+S'_0\right)}\Gamma'_{trans}\lambda'_{trans}m'_{ion}/2\pi \tag{7}$$

which is usually smaller than the momentum spread of the ion beam.

2.1.2.3 *Minimum Temperature Estimates and Cooling Rates*

When discussing laser cooling of ion beams with large momentum spread it will become obvious that cooling times in laser cooling do not only depend on the atomic transition properties. A variety of heating processes [1,14] of which intra-beam scattering is the most dominant will counteract laser cooling. Minimum temperatures attainable by laser cooling are equal to or lower than the Doppler limit temperature

$$T'_{Doppler} = \frac{\hbar\Gamma'_{trans}}{2k_B} \tag{8}$$

with k_B being Boltzmann's constant. Cooling rates can be estimated by the recoil frequency $f_{recoil} = h/\left(2m'_{ion}\lambda'^2_{trans}\right)$ as $R_{cool} = f_{recoil}/2$ [2]. It should be noted that the transverse beam heating [1,14] due to spontaneous emission becomes negligible at high beam energies due to the relativistic boost of the emission cone.

2.1.2.4 *Using the Bucket Force to Counteract the Laser Force*

At relativistic beam energies moderate bunching of the ion beam is essential as the ponderomotive bucket force is needed to counteract the velocity-dependent laser force [15] in order to create a stable cooling point in momentum space [16]. Although various bucket forms are of potential interest for laser cooling [17], ultra-cold beams [18] and crystalline beams [19-21] can be attained by a simple harmonic confinement force that depends on the position s_{ion} of the ion relative to the bucket potential center

$$F_{bucket}\left(s_{ion}\right) = \frac{q_{ion}U_{bucket}}{C}\sin\left(\frac{2\pi N_{bunch}}{C}s_{ion}\right) \xrightarrow{s_{ion}\to 0} 2\pi\frac{q_{ion}U_{buncket}}{C}\frac{s_{ion}}{\Delta s_{bunch}} \tag{9}$$

for a sinusoidal bunching voltage of frequency $f_{bunch} = f_{rev} N_{bunch}$ dividing the ion beam in N_{bunch} bunches of spacing $\Delta s_{bunch} = C / N_{bunch}$ and approximately equal ion number $N_{ion,b} = I_{ion} / (q_{ion} f_{rev} N_{bunch}) = I_{ion} / (q_{ion} f_{bunch})$ for a given current I_{ion} of ions of charge $q_{ion} = Qe$. In one passage through a drift tube of length L_{Drift} ions gain a maximum energy of $q_{ion} U_{bucket}$ corresponding to a synchrotron frequency of

$$f_{syn} = \sqrt{\frac{|\eta_c| N_{bunch} q_{ion} U_{bucket}}{2\pi m_{ion} C^2}} = \sqrt{\frac{|\eta_c| N_{bunch} q_{ion} U_{bucket}}{2\pi \beta c p_{ion}}} f_{rev} = Q_{syn} f_{rev} \qquad (10)$$

where Q_{syn} is the synchrotron tune, $m_{ion} = \gamma m'_{ion}$, $p_{ion} = \gamma m'_{ion} \beta c$ and η_c the momentum compaction [1]. When storing relativistic ion beams the synchrotron frequency is usually much smaller than the revolution frequency, $Q_{syn} << 1$. The momentum acceptance of the bucket potential is then given by $\Delta p_{b,acc} \approx 2 Q_{syn} p_{ion} / (N_{bunch} \eta_c)$ for small distances s_{ion} from the bucket center where the bucket force is linear. This acceptance usually is much larger than the momentum acceptance of the laser force $\Delta p_{l,acc}$ and the single photon momentum p_{phot}. For sufficiently high numbers of bunches the maximum bunch length $l_{b,acc} = c|\eta_c| \Delta p_{b,acc} / (2\pi f_{syn} p_{ion}) \xrightarrow{\beta \to 1} C / (\pi N_{bunch})$ is smaller than the overlap length $L_{overlap}$. Moreover, the bunch length of a cold, space-charge dominated beam is usually much smaller than $l_{b,acc}$ [7,20], see also Fig. 1.

2.1.3 **Increasing the Momentum Acceptance of the Laser Force**

For a single frequency laser the momentum acceptance of the laser force is much smaller than the initial momentum spread $\Delta p_{ion,hot}$ of the ion beam. Increasing the momentum acceptance of the laser force thus becomes critical for high energy ion beams as precooling by stochastic or electron cooling cannot be employed. Several schemes for efficient laser cooling of ion beams with large momentum spread have been demonstrated - such as using a rapid adiabatic passage [23] or detuning the bucket frequency relatively to the laser frequency [24] - which locally manipulate the ion momentum. Such manipulations become more and more difficult with increasing beam energy and thus the focus has shifted to using laser systems that can deliver photons of variable wavelength.

One approach is based on scanning the frequency of a single frequency laser system [25-28]. A modern continuous-wave laser system delivers photons at a fixed wavelength λ_{cw} with a small line width $\Delta\lambda_{cw} < c / \Gamma_{trans}$.

Scanning should cover a frequency span of at least

$$\Delta f_{scan} = \frac{\beta}{2} \frac{\Delta p_{ion,hot}}{p_{ion}} \frac{c}{\lambda_{trans}} = \frac{\beta}{2} \frac{\Delta p_{ion,hot}}{p_{ion}} \frac{c}{(1+\beta)\gamma} \frac{1}{\lambda'_{trans}} . \qquad (11)$$

At high energy ion storage rings the initial relative momentum spread of the injected beam is limited by the momentum acceptance of the ring and is typically in the range of

$\Delta p_{ion,hot} / p_{ion} \approx 10^{-5} \ldots 10^{-4}$. Current state-of-the-art laser systems [29] can reach scanning ranges of $\Delta f_{scan} \lambda_{cw} / c \approx 10^{-5}$ at scan rates of $R_{scan} \cong 50\,Hz << f_{rev}$. As $R_{scan} << f_{recoil}$ cooling times are essentially limited by the scanning rate of the laser system.

Another approach lies in using a broadband laser system. First experiments using a acousto-optically modulated Argon ion laser [30] have proven the feasibility of this technique. With diode-pumped [31] disc or fiber amplifiers available bandwidth-limited laser pulses of high peak power $P_{peak} = E_{pulse} / \tau_{pulse}$ can be delivered at high repetition rates R_{rep}.

Using a pulsed laser of central wavelength $\lambda_{center} = c / f_{center}$ and spectral bandwidth

$$\Delta f_{BW} = \frac{\beta}{2} \frac{\Delta p_{ion,hot}}{p_{ion}} \frac{c}{\lambda_{trans}} = \frac{\beta}{2} \frac{\Delta p_{ion,hot}}{p_{ion}} \frac{c}{(1+\beta)\gamma} \frac{1}{\lambda'_{trans}} \tag{12}$$

one can cool all ions in the initially hot ion beam simultaneously. With the time-bandwidth product $\Delta f_{BW} \tau_{pulse} = s_{tb} \approx 0.5$ one can estimate the corresponding pulse duration

$$\tau_{pulse} = \frac{2 s_{tb} p_{ion} \lambda_{trans}}{\beta c \Delta p_{ion,hot}} = \frac{2 s_{tb} p_{ion} (1+\beta) \gamma \lambda'_{trans}}{\beta c \Delta p_{ion,hot}}. \tag{13}$$

Unlike in single-frequency laser cooling, bringing the center wavelength of a pulsed laser in resonance with the cooling transition wavelength would lead to laser heating of those ions slower than the ion beam velocity as the laser force and bucket force for laser wavelengths $\lambda < \lambda_{trans}$ point in the same direction, quickly driving the ions out of the bucket. Thus, one chooses the central frequency as

$$f_{center} = c / \lambda_{center} \equiv \frac{c}{\lambda_{trans}} - \frac{\Delta f_{BW}}{2} = \frac{c}{(1+\beta)\gamma} \frac{1}{\lambda'_{trans}} \left(1 - \frac{\beta}{4} \frac{\Delta p_{ion.hot}}{p_{ion}} \right). \tag{14}$$

It remains to calculate the laser pulse energy $P_{peak} = E_{pulse} / \tau_{pulse}$ which depends on the chosen laser beam radius from the saturation fluence $\Phi_{sat} = I_{sat} \tau_{trans}$ by

$$E_{pulse} = \pi w_{laser}^2 \Phi_{sat} \tag{15}$$

and is equivalent to demanding that the peak intensity of the laser pulse is given by $I_{peak} = P_{peak} / (\pi w_{laser}^2) = I_{sat} \Delta f_{BW} / (s_{tb} \Gamma_{trans})$.

This simply means that for all ion velocities the local spectral density at the respective Doppler-shifted transition frequency must be at least I_{sat} / Γ_{trans} and a pulsed laser then resembles a dense frequency comb of single frequency laser lines of equal intensity, each of which exerting the single-frequency laser force Eq. 5 on the respective sub-ensemble of ions in velocity space. It should be noted that this discussion only holds true if $\tau_{trans} << \tau_{pulse}$, which might be hard to fulfill for large momentum spreads.

The total cooling force then amounts to

$$F'_{laser,pulse} = \int_{\Delta f'_{BW}} \int_{\Delta p'_{ion}} \frac{\partial^2 \left|\vec{F}'_{laser}\right|}{\partial S'_0 \partial \delta'} \frac{\partial S'_0}{\partial I'_{pulse}} \frac{\partial I'_{pulse}}{\partial \omega'_{phot}} \frac{\partial \delta'}{\partial p'_{ion}} dp'_{ion} d\omega'_{phot} \tag{16}$$

where $\partial I'_{pulse} / \partial \omega'_{phot}$ defines the spectrum of the pulse. With $\Delta f_{BW} >> \Gamma_{trans}$ for ion beams with large momentum spread the center frequency and thus the position of maximum spectral intensity is widely red-shifted from the transition frequency for ions resting in the bucket center. For a Gaussian spectrum this means the spectral intensity observed by very cold ions is low and in turn the laser force is weak for these ions. Therefore efficient cooling to ultralow momentum spreads requires either the addition of a scanning single frequency laser or a constantly high spectral intensity on the red-shifted side and negligible spectral intensity on the blue-shifted side of the transition frequency. As such a box-like spectrum is hard to achieve and would alter the temporal pulse structure significantly, a combination of a scanning and a pulsed laser system [27] seems to be the more promising choice.

It has been observed in experiment [32] that close Coulomb collisions in intra-beam scattering [33] can lead to a sudden increase in the momentum spread of the ion beam. Such an increase could be efficiently counteracted with a broadband pulsed laser system as the laser cooling force would instantaneously recool the scattered ions while scanning would last at least $1/R_{scan}$.

Temporal overlap of the ion bunches with the laser pulses in the overlap region can be achieved by synchronizing the laser pulses to the bunching frequency and choosing appropriate delay and is easily achieved as bunching frequencies are typical on the order of MHz and laser pulse durations are much shorter than ion bunch durations. However, a duty cycle $\eta_{duty} = R_{rep} / f_{bunch}$ close to unity requires repetition rates on the order of MHz and thus high average power

$$P_{av} = E_{pulse} R_{rep} \leq \pi w_{laser}^2 I_{sat} \tau_{trans} N_{bunch} f_{rev}. \tag{17}$$

2.1.4 **Relativistic and Quantum Effects in Laser Cooling and Consequences**

Opposite to electron and stochastic cooling the laser cooling force increases with beam energy provided sufficient laser intensity is available [1,6]. Laser cooling of heavy ions of atomic number Z, charge state Q and mass number A at high beam energies has been discussed in detail in [6,34] and thus this text concentrates on providing useful approximations for applying laser cooling to any ion of interest.

2.1.4.1 ***Cooling Transition Properties and Laser System Design***

For heavy, highly-charged ions the accuracy ε_λ at which transition wavelengths are known [1,35-37] is often comparable or even greater than the initial momentum spread of a relativistic ion beam at injection. This poses a problem for laser cooling as the relativistically Doppler-shifted laser wavelength has to be matched to the transition wavelength and neither ion beam energy nor laser frequency can be changed relatively by more than 10^{-4}. However, promising experimental and theoretical advances [38,39] can ultimately lead to a better knowledge of transition wavelengths [40].

Table 1: Scaling of laser cooling parameters with beam energy γ_{res} as defined in the text.

Transition wavelength	*Transition life time*	*Saturation intensity*	*Maximum laser force*
$\lambda'_{trans} \propto \gamma_{res}^{-1}$	$\tau_{trans} \propto \gamma_{res}^{-1}$	$I_{sat} \propto \gamma_{res}$	$F_{laser,\max} \propto \gamma_{res}$

The maximum magnetic rigidity $B\rho$ of a storage ring defines the maximum beam energy

$$\gamma \le \gamma_{B\rho} = \sqrt{\left(B\rho Qe/\left(m'_{ion}c\right)\right)^2 + 1} \tag{18}$$

at which an ion can be stored. Roughly estimating the effective nuclear charge by the charge state $Z_{eff} \approx Q$ one finds from a simple Bohr model approach $\lambda'_{trans} \propto Q^{-2}$ and thus a scaling for the ion beam energy required to relativistically Doppler-shift a laser of fixed wavelength λ_{laser} to the cooling resonance as $\gamma_{res} \xrightarrow{\beta\to 1} \lambda_{laser}/(2\lambda'_{trans}) \propto Q^2$. Moreover, the transition life time scales as $\tau'_{trans} \propto \lambda'^2_{trans} \propto Q^{-4}$ [1,2,6], assuming the oscillator strength of the transition does not vary strongly with the transition of interest. Due to time dilatation the transition life time measured in the laboratory frame increases as $\tau_{trans} = \gamma\tau'_{trans} \overset{\gamma=\gamma_{res}}{\propto} Q^{-2}$. Note that one can obtain the scaling with γ_{res} summarized in Tab. 1 for any given quantity by dividing the result derived in [1] for the 'Opt. frame' system by the result for 'Lab frame (in)' and setting $\gamma = \gamma_{res}$.

In the ion beam rest frame the saturation intensity scales as $I'_{sat} \propto \lambda'^{-3}_{trans}\tau'^{-1}_{trans} \propto Q^{10}$ while in the laboratory frame the saturation intensity for a given transition is relativistically decreased by $I_{sat} = \gamma^{-4} I'_{sat}$. Consequently, $I_{sat} \overset{\gamma=\gamma_{res}}{\propto} Q^2$ from which it becomes clear that saturating the transition in the laboratory frame becomes more and more difficult when aiming for laser cooling of highly charged ions. Although it would be favorable to use fourth harmonic generation in a laser system to boost diode laser light from infrared wavelengths $\approx 1\,\mu m$ to the UV $\approx 200\,nm$, the drop in laser power by usually much more than a factor four and the poor transport efficiency for UV light over long distances suggest to compromise for second harmonic generation and thus for solid-state laser systems in the visible range $\approx 400\,nm \ldots 600\,nm$.

If the cooling transition can be saturated, the maximum laser force observed in the laboratory frame $F_{laser,\max} = h\Gamma_{trans}/\left(2\lambda_{laser}\right) \overset{\gamma=\gamma_{res}}{\propto} Q^2 \propto \gamma_{res}$, see Eq. 6, increases and cooling becomes stronger. One has to be careful in interpreting the laser force for high beam energies. As the photon momentum in the ion rest frame increases as $p'_{laser} \propto Q^2$, the line width decreases and the Doppler limit temperature, Eq. 8, increases roughly as $T'_{Doppler} \propto m'_{ion}\lambda'^2_{trans}\tau'^{-2}_{trans} \propto Q$, using the Bethe-Weizsäcker mass formula $Q \propto Z \approx A/\left(2 + 0{,}015A^{2/3}\right)$ [41]. This is counter-intuitive as one expects lower minimum beam temperatures for stronger cooling forces. However, for high beam energies and highly charged heavy ions the laser action resembles a random walk in momentum space with few high momentum photons being absorbed by an ion in one

beam revolution [6,42], which in [34] is realistically estimated to about 4 photons per turn and ion for Li-like U^{89+} at $\gamma \equiv 25.68$.

2.1.4.2 *Confinement and Stability of Ultra-cold Beams*

For ultra-cold beams, the space charge of the beam counteracts the confining forces and induces synchrotron tune shifts [1], the longitudinal ion density in the bunch becomes parabolic [19-21] and the bunch length independent of the ion beam momentum spread [1,20], see Fig. 1.

Strong coupling is required for beam crystallization [1] and electron cooling experiments [43] have only seen onsets of ordering at very low ion currents and thus weak coupling. Laser cooling in principle is independent of the ion current [24], provided absorption in the beam does not significantly reduce the laser intensity [2] and intra-beam scattering is overcome [44]. In a storage ring the plasma frequency $f_p^2 = Q^2 e^2 n_{beam} / \left(4\pi^2 \varepsilon_0 m_{ion}\right)$, ε_0 being the vacuum permittivity, of space-charge dominated beams of density n_{beam} is determined by the transverse confinement $f_\beta^2 = Q_\beta^2 f_{rev}^2 \approx f_p^2$ [20], Q_β being the betatron tune.

If the beam is in a crystalline state, only processes on time scales comparable to $1/f_p$ or shorter can alter the crystalline structure non-adiabatically [45] while the beam is decoupled from RF heating [1]. Consequently, intra-beam scattering heating processes happen on the same time scale and with $R_{cool} \geq f_p \approx f_\beta$ laser cooling should be able to overcome them. With $f_{syn} << f_{rev} \approx f_p / Q_\beta$ crystalline structures are dominantly one-dimensional and coupling between betatron and synchrotron motion is weak. Even with increasing bucket depths, shearing forces due to ring dispersion would destroy any three-dimensional order [42,46].

2.1.4.3 *Three-dimensional Laser Cooling*

From Eq. 5 it is evident that the laser force itself only acts along the laser beam axis and sufficient overlap $\eta_{overlap}$ requires head-on scattering geometries. As laser cooling can act faster than the plasma frequency, $R_{cool} \geq f_p$, the synchrotron motion can decouple from the betatron motion [42].

At low beam energies beam dispersion can increase this coupling [47], while at higher beam energies dedicated coupling cavities introduced into in a ring can change the ratio of betatron to synchrotron tune [48-50]. At high beam densities high Coulomb collision rates efficiently induce heat transfer from the transverse to the longitudinal degree of ion motion [51-53].

2.1.5 **Optical and Non-optical Measurements of Ion Beam Properties**

Schottky spectral analysis reveals the longitudinal dynamics of laser-cooled ion beams with high precision even at low ion currents [9,12,54] but is limited in momentum resolution [22 and Fig. 1]. At low momentum spread the Schottky power is greatly reduced [24], see Fig. 1, and optical momentum diagnostics [55,56] become important as fluorescence rates Γ_{trans} increase with higher beam density.

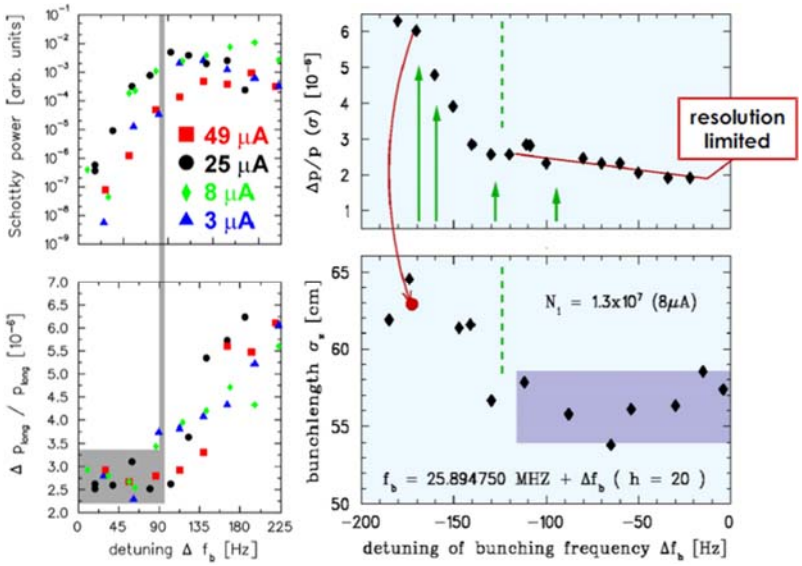

Figure 1: Left: Schottky power compared to momentum spread of a bunched, laser-cooled C^{3+} ion beam at β=0.47 as a function of detuning of the bunching frequency relative to the cooling resonance. At low detuning the Schottky power drops quickly and the measurement resolution is reached. Right: Bunch length compared to momentum spread. At low detuning the bunch length stays constant as expected for a space-charge dominated beam [59].

In conclusion, Schottky and optical momentum measurements are complimentary and optical measurements are preferential at ultra-low momentum spreads [26,40,57]. With increasing beam energy the fluorescence spectrum

$$hf_{out}(\theta) = \frac{hf'_{trans}}{\gamma\left(1-\beta\cos(\theta)\right)}, \quad \tan(\theta) = \frac{\sin(\theta')}{\gamma\left(\cos(\theta')+\beta\right)} \tag{18}$$

depends on the observation angle θ and is Lorentz-boosted in the ion beam forward direction. At mildly relativistic speeds this requires sophisticated in-vacuum mirror systems [58] or in-vacuum detectors [55] to collect a large percentage of the scattered light.

At high relativistic energies, the fluorescence peaks in a small cone $\tan(\theta) \xrightarrow{\beta\to c} \gamma^{-1}$ around the ion beam axis and can thus be measured outside the beam pipe. Then, the beam energy can be inferred from spectroscopy of the scattered light since $\gamma \xrightarrow{\beta\to c} \sqrt{f_{out}\lambda_{laser}/c}/2$ and precision spectroscopy [34] of the cooling transition is obtained 'for free', as $\lambda'_{trans} \xrightarrow{\beta\to c} \sqrt{c\lambda_{laser}/f_{out}}$.

2.1.6 **Conclusion**

Laser cooling is an exciting alternative to electron and stochastic cooling to obtain ultra-low momentum spreads for beams of heavy, highly charged ions in high energy storage rings. Optical diagnostics complement standard beam diagnostics while at the same time providing for high-precision spectroscopy of the cooling transition, which is of interest in itself as it can be a good test for quantum-electrodynamic contributions to the transition energy. The successful application of laser cooling at future storage ring

facilities such as HIAF and FAIR strongly depends on the development of powerful, compact and energy-efficient laser systems.

The author would like to thank Ulrich Schramm, Danyal Winters, Wen Weiqiang, the ESR team and all other colleagues involved for their help in studying laser cooling at PALLAS, ESR and CSRe.

2.1.7 **References**

1. U. Schramm, D. Habs, "Crystalline ion beams", Progress in Particle and Nuclear Physics 53, 583 (2004) and references therein.
2. H.J. Metcalf, P. van der Straten, "Laser Cooling and Trapping of Atoms and Ions", Springer (1999)
3. T. Schätz, U. Schramm, D. Habs, „Crystalline Ion Beams", Nature 412, 717 (2001)
4. D. Möhl, "Stochastic Cooling of Particle Beams", Springer Lecture Notes in Physics 866, Springer (2013)
5. G. I. Budker, "An effective method of damping particle oscillations in proton and antiproton storage rings", Soviet Atomic Energy 22(5), 438 (1967)
6. U. Schramm, M. Bussmann, D. Habs "From laser cooling of non-relativistic to relativistic ion beams", Nuclear Instruments and Methods in Physics Research Section A 532(1-2), 348 (2004)
7. U. Schramm, M. Bussmann, D. Habs, M. Steck, T. Kühl, K. Beller, P. Beckert, B. Franzke, F. Nolden, G. Saathoff, S. Reinhardt, S. Karpuk, "Laser Cooling of Relativistic Heavy Ion Beams" Proceedings of the 2005 Particle Accelerator Conference, PAC05, FOAD004, 401 (2005)
8. M. Bussmann, F. Kroll, M. Löser, M. Siebold, U. Schramm, C. Novotny, W. Nörtershäuser, C. Dimopoulou, F. Nolden, M. Steck, C. Kozhuharov, T. Kühl, T. Stöhlker, D. F. A. Winters, S. Tichelmann, G. Birkl, T. Beck, B. Rein, T. Walther, X. Ma, W. Wen, "Laser cooling of relativistic C3+ ions at the ESR", GSI Scientific Report 2010 - GSI Report 2011-1, 339 (2011)
9. D. Winters, C. Clark, C. Dimopoulou, T. Giacomini, C. Kozhuharov, T. Kühl, Y. Litvinov, M. Lochmann, W. Nörtershäuser, F. Nolden, R. Sanchez, S. Sanjari, M. Steck, T. Stöhlker, J. Ullmann, T. Beck, G. Birkl, B. Rein, S. Tichelmann, T. Walther, X. Ma, W. Wen, J. Yang, D. Zhang, U. Schramm, M. Seltmann, M. Siebold, M. Bussmann, "Laser cooling of stored relativistic C3+ ions at the ESR" GSI Scientific Report 2012 - GSI Report 2013-1, 313 (2013)
10. A. Noda, "Ion beam cooling at S-LSR project", Nuclear Instruments and Methods in Physics Research Section A: Accelerators, Spectrometers, Detectors and Associated Equipment 532(1–2), 150 (2004)
11. A. Noda, M. Nakao, H. Souda, H. Tongu, M. Grieser, Z.Q. He, K. Jimbo, H. Okamoto, K. Osaki, Y. Yuri, "Latest Results of Experimental Approach to Ultra-cold Beam at S-LSR", Proceedings of the Workshop on Beam Cooling and Related Topics, COOL2013, THAM1HA02, 157 (2013)
12. W. Q. Wen, X. Ma, D. Zhang, M. Bussmann, X. Zhu, D. Winters, L. Meng, H. Liu, D. Zhao, Z. Wang, J. Li, R. Mao, T. Zhao, J. Wu, G. Li, X. Yang, Y. Liu, J. Yang, Y. Yuan, J. Xia, H. Xu "Preparations for laser cooling of relativistic heavy-ion beams at the CSRe", Physica Scripta 2013(T156), 014090 (2013)
13. N. Hodgson, H. Weber, "Laser Resonators and Beam Propagation", Springer Series in Optical Sciences, Vol. 108 (2003)
14. J. Javanainen, M. Kaivola, U. Nielsen, O. Poulsen, E. Riis, „Laser cooling of a fast ion beam", Journal of the Optical Society of America B 2(11), 1768 (1985)
15. J.S. Hangst, S. Nielsen, O. Poulsen, P. Shi, J. P. Schiffer, "Laser Cooling of a Bunched Beam in a Synchrotron Storage Ring", Physical Review Letters 74, 4432, (1995)

16. D. Habs, R. Grimm, “Crystalline Ion Beams”, Annual Review of Nuclear and Particle Science 45, 391 (1995)
17. U. Eisenbarth, B. Eike, M. Grieser, R. Grimm, I. Lauer, P. Lenisa, V. Luger, M. Mudrich, T. Schätz, U. Schramm, D. Schwalm, M. Weidemüller, „Laser cooling of fast stored ions in barrier buckets“, Nuclear Instruments and Methods in Physics Research Section A: Accelerators, Spectrometers, Detectors and Associated Equipment 441(1–2), 209 (2000)
18. H.-J. Miesner, M. Grieser, R. Grimm, I. Lauer, V. Luger, P. Merz, A. Peters, U. Schramm, D. Schwalm, M. Stößel, „Transverse laser cooling of a radio-frequency bunched ion beam in the storage ring TSR”, Nuclear Instruments and Methods in Physics Research Section A: Accelerators, Spectrometers, Detectors and Associated Equipment 383(2–3) 634 (1996)
19. U. Schramm, T. Schätz, D. Habs, „Bunched Crystalline Ion Beams“, Physical Review Letters 87, 184801 (2001)
20. U. Schramm , T. Schätz , M. Bussmann , D. Habs, „Spatial Compression of Bunched Crystalline Ion Beams“, Physica Scripta 2003(T104), 189 (2003)
21. M. Bussmann, U. Schramm, T. Schätz, D. Habs, „Structural changes in bunched crystalline ion beams“, Journal of Physics A: Mathematical and General Volume 36(22), 6119 (2003)
22. M. Bussmann, U. Schramm, D. Habs, M. Steck, T. Kühl, K. Beckert, P. Beller, B. Franzke, W. Nörtershäuser, C. Geppert, C. Novotny, J. Kluge, F. Nolden, T. Stöhlker, C. Kozhuharov, S. Reinhardt, G. Saathoff, S. Karpuk, „The Dynamics of Bunched Laser-Cooled Ion Beams at Relativistic Energies”, Journal of Physics: Conference Series 88, 012043 (2007)
23. B. Wanner, R. Grimm, A. Gruber, D. Habs, H.-J. Miesner, J. S. Nielsen, and D. Schwalm, „Rapid adiabatic passage in laser cooling of fast stored ion beams”, Physical Review A(58), 2242 (1998)
24. M. Bussmann, D. Habs, U. Schramm, K. Beckert, P. Beller, B. Franzke, C. Kozhuharov, T. Kühl, W. Nörtershäuser, F. Nolden, M. Steck, S. Karpuk, C. Geppert, C. Novotny, G. Saathoff, S. Reinhardt, “Schottky Noise Signal and Momentum Spread for Laser-Cooled Bunched Ion Beams at Relativistic Energies”, Proceedings of the Workshop on Beam Cooling and Related Topics, COOL07, FRM1C0, 226 (2007)
25. J. S. Hangst, M. Kristensen, J. S. Nielsen, O. Poulsen, J. P. Schiffer, P. Shi, “Laser cooling of a stored ion beam to 1 mK”, Physical Review Letters 67, 1238 (1991)
26. T. Schätz, U. Schramm, M. Bussmann, D. Habs, „Crystallisation of ion beams in the rf quadrupole storage ring PALLAS“, Applied Physics B 76(2), 183 (2003)
27. M. Bussmann, U. Schramm, W. Nörtershäuser, C. Novotny, C. Geppert, T. Walther, G. Birkl, D. F. A. Winters, T. Kühl, C. Kozhuharov, M. Steck, F. Nolden, C. Dimopoulou, T. Stöhlker, “All-Optical Ion Beam Cooling and Online Diagnostics at Relativistic Energies”, Proceedings of Workhop on Beam Cooling and Related topics, COOL09, 22 (2009)
28. W. Wen, D. Winters, T. Beck, B. Rein, T. Walther, S. Tichelmann, G. Birkl, R. Sanchez-Alarcon, J. Ullmann, M. Lochmann, W. Nörtershäuser, C. Clark, C. Kozhuharov, T. Kühl, S. Sanjari, Y. Litvinov, T. Giacomini, M. Steck, C. Dimopoulou, F. Nolden, T. Stöhlker, J. Yang, D. Zhang, X. Ma, M. Seltmann, M. Siebold, U. Schramm, M. Bussmann, “Laser cooling of stored relativistic ion beams with large momentum spreads using a laser system with a wide scanning range”, Journal of Physics: Conference Series 488(12), 122005 (2014)
29. T. Beck, B. Rein, T. Walther, “An all-solid-state Argon ion laser replacement”, Proceedings CLEO 2013, JTh2A, 66 (2013)
30. S. N. Atutov, R. Calabrese, R. Grimm, V. Guidi, I. Lauer, P. Lenisa, V. Luger, E. Mariotti, L. Moi, A. Peters, U. Schramm, M. Stößel, ““White-light” Laser Cooling of a Fast Stored Ion Beam”, Physical Review Letters 80, 2129 (1998)

31. M. Siebold, F. Roeser, M. Loeser, D. Albach, U. Schramm, „PEnELOPE: a high peak-power diode-pumped laser system for laser-plasma experiments", Proc. SPIE 8780, High-Power, High-Energy, and High-Intensity Laser Technology; and Research Using Extreme Light: Entering New Frontiers with Petawatt-Class Lasers, 878005 (2013)
32. W. Petrich, M. Grieser, R. Grimm, A. Gruber, D. Habs, H.-J. Miesner, D. Schwalm, B. Wanner, H. Wernøe, A. Wolf, R. Grieser, G. Huber, R. Klein, T. Kühl, R. Neumann, S. Schröder, „Laser cooling of stored high-velocity ions by means of the spontaneous force", Physical Review A 48, 2127 (1993)
33. M. Seurer, P.-G. Reinhard, C. Toepffer, „On emittance growth of strongly coupled heavy ion beams", Nuclear Instruments and Methods in Physics Research Section A: Accelerators, Spectrometers, Detectors and Associated Equipment 351(2–3), 286 (1994)
34. H. Backe, "Precision spectroscopy at heavy ion ring accelerator SIS300", Hyperfine Interactions 171(1-3), 93 (2007)
35. W. R. Johnson, S. A. Blundell, J. Sapirstein, „Many-body perturbation-theory calculations of energy levels along the lithium isoelectronic sequence", Physical Review A 37, 2764 (1988)
36. V. A. Yerokhin, A. N. Artemyev, V. M. Shabaev, M. M. Sysak, O. M. Zherebtsov, G. Soff, "Evaluation of the two-photon exchange graphs for the 2p1/2−2s transition in Li-like ions" Physical Review A 64, 032109 (2001)
37. Bengt Edlén, "Comparison of Theoretical and Experimental Level Values of the n = 2 Complex in Ions Isoelectronic with Li, Be, O and F", Physica Scripta 28(1), 51 (1983)
38. H. Beyer, H.-J. Kluge, V. Shevelko, "X-Ray Radiation of Highly Charged Ions", Springer Series on Atomic, Optical, and Plasma Physics, Vol. 19 (1997)
39. P. Schwerdtfeger, Relativistic Electronic Structure Theory, Part 2. Applications, Elsevier Science, ISBN 978-0444512994 (2004)
40. U. Schramm, M. Bussmann, D. Habs, T. Kühl, P. Beller, B. Franzke, F. Nolden, M. Steck, G. Saathoff, S. Reinhardt, S. Karpuk "Laser-Spectroscopy of the 2s2S-2p2P transitions of relativistic Li-like carbon ions at the ESR", Proceedings of the 6th International Conference on Nuclear Physics at Storage Rings, STORI-2005, 324 (2005)
41. J.W. Rohlf, "Modern Physics from α to Z0", John Wiley & Sons, ISBN 978-0471572701 (1994)
42. U. Schramm, T. Schätz, M. Bussmann, D. Habs, "Cooling and heating of crystalline ion beams", Journal of Physics B 36(3), 561 (2003)
43. See discussion by I. Meshkov, A. Smirnov and A. Noda in this ICFA Beam Dynamics Newsletter
44. U. Eisenbarth, M. Mudrich,, B. Eike, M. Grieser, R. Grimm, V. Luger, T. Schätz, U. Schramm, D. Schwalm, M. Weidemüller, „Anomalous behaviour of laser cooled fast ion beams", Hyperfine Interactions 127(1-4), 223 (2000)
45. D. Dubin, T.M. O'Neil "Trapped nonneutral plasmas, liquids, and crystals (the thermal equilibrium states)", Reviews of Modern Physics 71(1), 87. (1991)
46. J. Wei, H. Okamoto, A. M. Sessler, "Necessary Conditions for Attaining a Crystalline Beam", Physical Revíew Letters 80, 2606 (1998)
47. I. Lauer, U. Eisenbarth, M. Grieser, R. Grimm, P. Lenisa, V. Luger, T. Schätz, U. Schramm, D. Schwalm, M. Weidemüller, "Transverse Laser Cooling of a Fast Stored Ion Beam through Dispersive Coupling", Physical Review Letters 81, 2052 (1998)
48. H. Okamoto, "Transverse laser cooling induced through dispersion at an rf cavity", Physical Review E 50, 4982 (1994)
49. A. Noda, M. Ikegami, T. Shirai, "Approach to ordered structure of the beam at S-LSR", New Journal of Physics 8, 288 (2006)
50. A. Noda, M. Nakao, H. Okamoto, K. Osaki, Y. Yuri, H. Souda, H. Tongu, K. Jimbo, M. Grieser, Z. He, A. Smirnov, "Ultralow Emittance Beam Production based on Doppler

Laser Cooling and Coupling Resonance", Proceedings of the 5th International Particle Accelerator Conference, IPAC2014, MOZA01, 28

51. H.-J. Miesner, R. Grimm, M. Grieser, D. Habs, D. Schwalm, B. Wanner, A. Wolf, "Efficient, Indirect Transverse Laser Cooling of a Fast Stored Ion Beam", Physical Review Letters 77, 623 (1996)
52. M. Tanabe, T. Ishikawa, M. Nakao, H. Souda, M. Ikegami, T. Shirai, H. Tongu, A. Noda, "Longitudinal and Transverse Coupling of the Beam Temperature Caused by the Laser Cooling of $^{24}Mg^{+}$", Applied Physics Express 1(2), 028001 (2008)
53. U. Schramm, M. Bussmann, D. Habs, T. Kühl, P. Beller, B. Franzke, F. Nolden, M. Steck, G. Saathoff, S. Reinhardt, S. Karpuk, "Combined Laser and Electron Cooling of Bunched C3+ Ion Beams at the Storage Ring ESR" AIP Conference Proceedings 821(1) of the International Workshop on Beam Cooling and Related Topics, COOL05, 501 (2006)
54. D. Winters, C. Clark, C. Dimopoulou, T. Giacomini, C. Kozhuharov, Y. A. Litvinov, F. Nolden, R. Sanchez, M. S. Sanjari, M. Steck, J. Ullmann, M. Bussmann, U. Schramm, M. Seltmann, M. Siebold, T. Beck, G. Birkl, B. Rein, S. Tichelmann, T. Walther, T. Kühl, M. Lochmann, X. Ma, W. Wen, J. Yang, D. Zhang, W Nörtershäuser, T. Stöhlker, "Laser Cooling of Relativistic C3+ Ion Beams with Large Initial Momentum Spread", Proceedings of the Workshop on Beam Cooling and Related Topics, COOL2013, THAM1HA04, 166 (2013)
55. W. Q. Wen, M. Lochmann, X. Ma, M. Bussmann, D. F. A. Winters, W. Nörtershäuser, B. Botermann, C. Geppert, N. Frömmgen, M. Hammen, V. Hannen, R. Jöhren, T. Kühl, Y. Litvinov, R. Sánchez, T. Stöhlker, J. Vollbrecht, C. Weinheimer, C. Dimopoulou, F. Nolden, M. Steck, "Optical measurement of the longitudinal ion distribution of bunched ion beams in the ESR", Nuclear Instruments and Methods in Physics Research Section A : Accelerators, Spectrometers, Detectors and Associated Equipment 711, 90 (2013)
56. A. Noda, M. Ikegami, T. Ishikawa, M. Nakao, T. Shirai, H. Souda, M. Tanabe, H. Tongu, I. Meshkov, A.V. Smirnov, M. Grieser, K. Noda, "Present Status and Recent Activity on Laser Cooling at S-LSR", Proceedings of the Workshop on Beam Cooling and Related Topics, COOL07, FRM1I01, 221 (2007)
57. U. Schramm, M. Bussmann, D. Habs, M. Steck, T. Kühl, K. Beckert, P. Beller, B. Franzke, F. Nolden, G. Saathoff, S. Reinhardt, S. Karpuk (2005), "Laser Cooling and Spectroscopy of Relativistic C3+ Beams at the ESR", Hyperfine Interactions 162(1), 181 (2005)
58. V. Hannen, D. Anielski, C. Geppert, R. Jöhren, T. Kühl, M. Lochmann, R. López-Coto, W. Nörtershäuser, H.-W. Ortjohann, R. Sánchez, J. Vollbrecht, C. Weinheimer, D. F. A. Winters, „Detection system for forward emitted photons at the Experimental Storage Ring at GSI", Journal of Instrumentation 8, P09018 (2013)
59. M. Bussmann, "Laser-Cooled Ion Beams and Strongly Coupled Plasmas for Precision Experiments", Dissertation Ludwig-Maximilians University Munich (2007)

2.2 Bunched Beam Electron Cooling for Low Energy RHIC Operation

Alexei V. Fedotov for the LEReC team
Brookhaven National Laboratory, Upton, NY 11973
Mail to: fedotov@bnl.gov

2.2.1 Introduction

Mapping the quantum chromodynamics (QCD) phase diagram is one of the fundamental goals of heavy-ion collision experiments. The QCD critical point is a distinct feature of the phase diagram, the existence of which is predicted by various QCD models. The first phase beam energy scan (BES-I) physics program was successfully conducted at the Relativistic Heavy Ion Collider (RHIC) in Brookhaven National Laboratory (BNL) during 2010-14. During BES-I physics runs data sets were collected for Au+Au centre-of-mass collisions at 7.7, 11.5, 14.6, 19.6 and 39 GeV. Driven by physics and BES-I results, future physics program called BES Phase-II (BES-II) is proposed for Au+Au centre-of-mass energies below 20 GeV (γ=10.7). However, required event statistics for this physics program is much higher than previously achieved and relies on significant luminosity improvement in RHIC at energies below γ=10.7 with the help of an electron cooling upgrade.

Applying electron cooling directly in RHIC can increase the average integrated luminosity significantly [1-2]. An electron cooling technique requires electron beam co-propagating with the same velocity as the ion beam in a localized portion of circular accelerator called the cooling section. An electron beam up to a 5 MeV kinetic energy is required to cover the full energy range of interest.

Although maximum required electron energy is not very high, an attractive option is to use electron bunches produced with the RF accelerator. Such a scheme of cooling with bunched electron beam is also a natural approach for high-energy electron cooling where RF acceleration is required. The Low Energy RHIC electron Cooler (LEReC) based on the SRF linac is presently under design at BNL (where the term “low energy” refers to the low energy of ion beam compared to much higher designed energies of RHIC operation).

2.2.2 Cooling Considerations

The energies of electron beam needed for low-energy RHIC are sufficiently high which allows us to consider cooling using bunched electron beam. One of the challenges for bunched beam cooling is providing beam transport of electron bunches without significant degradation of beam emittance and energy spread. This becomes of a special concern for lowest energies of proposed LEReC operation. In addition, the baseline choice of a 704 MHz SRF linac results in a very short electron bunch. To avoid significant energy spread increase due to the longitudinal space charge of electron beam itself, bunches need to be stretched to an acceptable bunch length. At the same time the bunch length should not be too long to allow for energy spread correction due to the RF curvature. To satisfy such requirements a very careful RF manipulation and design of electron beam transport is required. The use of long ion bunches [3-4] with new 9 MHz RHIC RF system allows us to place several electrons bunches (bunch-train) on a single

ion bunch. This relaxes requirement on the charge of an individual electron bunch which should allow us to achieve good beam quality needed for cooling.

Since non-magnetized cooling significantly simplifies electron beam transport and reduces the cost of the cooler, it was chosen as our baseline approach. Due to a relatively low beam current required for LEReC, an approach with zero magnetic field on the cathode and thus no magnetic field in the cooling section is feasible. In the cooling section, short solenoids will be placed every 2 m to correct the angular spread accumulated due to the electron beam space-charge self field.

The use of undulators for recombination suppression in the cooling section is compatible with approach chosen. However, the use of undulators would require significant engineering additions to the cooling section while, in our case, the expected benefit for luminosity with recombination suppression seems rather modest. Thus, the recombination suppression with undulators is presently not included in the LEReC baseline.

2.2.3 **Electron Accelerator**

The LEReC electron accelerator consists of a superconducting RF (SRF) 704 MHz photoemission electron gun (or photoemission DC gun with a booster cavity as a back-up) and a 704 MHz five-cell SRF cavity providing electron beam acceleration up to 5 MeV kinetic energy (the existing five-cell cavity can accelerate electrons to much higher energy thus providing even higher energy cooling but it is not required for the present project). A normal conducting cavity operating at 2.1 GHz (third harmonic of the SRF frequency) follows the SRF linac. It is used for energy spread correction.

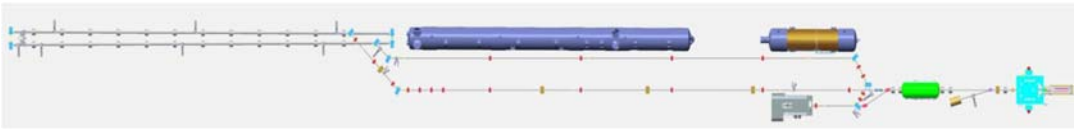

Figure 1: Layout of LEReC in IP2 region of RHIC (from right to left: gun shown with light blue color followed by the SRF 5-cell cavity (green), electron beam transport line, two cooling sections with solenoids, return beam line and beam dump).

The LEReC accelerator will operate in two modes:

1. Gun mode: kinetic energies from 1.6 MeV to 2 MeV will be provided just by the gun. There will be no energy recovery in this mode.
2. ERL mode ("energy-upgrade"), not shown in Fig. 1: starting with a 2 MeV final kinetic energy, LEReC will work as an Energy Recovery Linac (ERL) with a factor of 2.4 difference between the beam momentum after the gun and the final electron beam momentum.

The 704 MHz SRF gun is being commissioned at the R&D ERL facility [5]. This half-cell gun [6] was designed to operate at an accelerating voltage up to 2 MV with a beam current ten times larger than planned for LEReC operation. This provides a very good safety margin. The electron beam is generated in the gun by illuminating a K2CsSb photocathode with green (532 nm) light from a laser.

Three types of high QE photocathodes are used nowadays in SRF and DC guns: GaAs(Cs), Cs2Te, and K2CsSb [7-9]. For LEReC parameters, cesium potassium antimonide is preferred option at present.

For LEReC, the gun will produce bunch trains with individual electron bunches of about 50 ps full length at ~9 MHz bunch train repetition frequency. The bunch train repetition rate will be the same as the repetition rate of ion bunches in RHIC. An optical system will allow creating dedicated bunch patterns for different RHIC energies and ion bunch lengths. Each bunch train will be followed by a long gap (about 100 ns) corresponding to the gap between ion bunches, as illustrated in Figure 2. Recent information on commissioning of this gun can be found in [10, 11].

The five-cell BNL1 SRF five-cell cavity [12] is currently installed in the R&D ERL blockhouse. It is commissioned to operate in CW mode with an accelerating voltage up to 12 MV. This is much higher than the maximum voltage required for LEReC. No modifications of this system are required for use in LEReC.

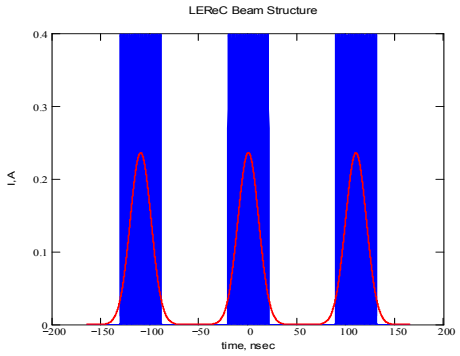

Figure 2: Thirty electron bunches with 1.4 ns spacing in a bunch train (blue) placed on a single ion bunch (red). Example for long ion bunches with future 9 MHz RHIC RF system at γ=4.1.

2.2.4 **Electron Beam Parameters**

The requirement on the transverse angles of electron beam in the cooling section is given by the angular spread of the ion beam. For example, for the rms normalized emittance of 2.5 mm-mrad at γ=4.1, and 30 m beta function in the cooling section, the ion beam rms angular spread in the lab frame is 0.14 mrad. The ion beam will have rms longitudinal momentum spread in the range of σ_p=4-5×10^{-4}. This sets requirement on the rms momentum spread of electron beam of < 5×10^{-4}. Basic parameters of needed electron beam are shown in Table

To keep the transverse angles of electron beam at an acceptable level (< 0.15 mrad) an integral of residual transverse magnetic field in the space used for cooling should be kept below 1 Gauss·cm (at γ=4). Shielding of residual magnetic field to such a level will be provided by several concentric cylindrical layers of high permeability alloy. Some cooling section space is taken up by very short (10 cm) weak (200 G) correction solenoids (to control angular spread due to the space charge), steering dipoles and beam position monitors to keep the electron and ion beam in close relative alignment.

Table 1: LEReC electron beam parameters are shown only for low and upper bound of energies

Beam		
Lorentz factor	4.1	10.7
RHIC RF frequency	9.10 MHz	9.34 MHz
Electron beam kinetic energy	1.58 MeV	4.96 MeV
Total charge per bunch train, nC	3 (30 bunches)	5.4 (18 bunches)
$\Delta p/p$, rms momentum spread	$5 \cdot 10^{-4}$	$5 \cdot 10^{-4}$
Normalized rms emittance	2.5 mm·mrad	2.5 mm·mrad
Transverse rms beam size	4.3 mm	2.6 mm
Full bunch duration	50-100 ps	50-100 ps
Average electron beam current	27 mA	50 mA
Beam power	43 kW	90 kW (with energy recovery)

Since the electron beam does not have any magnetization, space used by the correction solenoids will be lost from the cooling process. Longitudinal field of 1 G produces rotational angles of 75 μrad at γ=4. Presently, design of these solenoids, placed every 2 m, is being optimized to maximize the space between them which satisfies requirement on $B_z < 1$ G.

The charge per bunch needed depends on the energy at which cooling is applied and optimization scenario to get maximum luminosity gain for this energy. The details on expected cooling performance and luminosity projections could be found in Refs. [13,14]. For example, for γ=4.1 with new 9 MHz RHIC RF system, the use of a bunch train allows us to split the total charge of 3 nC required for cooling, into 30 bunches with 100 pC per bunch. Although electron bunch occupies a small portion of the ion bunch, all ions could be cooled as a result of the synchrotron oscillations. To provide effective cooling of ions with different amplitudes a slow motion of the electron bunch through the ion bunch ("painting") is possible. With the present scenario of many electron bunches spread through the ion bunch such a painting maybe not necessary.

2.2.5 **Bunched Beam Electron Cooling**

Providing electron beams with energies above few MeV is easier with RF acceleration of electron beam, thus using bunched electron beam for cooling (resulting electron beam characteristics and application to cooling are somewhat different from conventional low-energy DC electron beams).

Significant efforts were devoted in the past to explore various aspects of such bunched electron beam cooling in simulations as part of R&D for high-energy electron cooling in RHIC [15-17], including such techniques as "painting" with a short electron beam and control of ion beam distribution under cooling which is essential if cooling is provided in a collider [18]. As well as accurate luminosity predictions with ions beam distributions evolving under combined effects of the intra-beam scattering and electron cooling. However, experimental studies of such cooling are still lacking. Establishing this technique experimentally would be extremely useful for future high-energy applications.

2.2.6 **Challenges**

Successful operation of LEReC cooler requires stable and reliable CW operation of the gun with electron beam current up to 50 mA. A long lifetime of the photocathode

with a charge per bunch up to 100 pC at low energy of 1.6-2 MeV and up to 300 pC at highest energy is also required. Demonstration of some of the unique and challenging features is being planned with the existing 704 and 112 MHz SRF guns at BNL, which are presently under commissioning. For a photoemission electron DC gun such beam currents were already demonstrated at Cornell [19].

The achievement of very low transverse angular spread for the electron beam is challenging and is being addressed by a proper beam transport and engineering design. The attainment of required low energy spread in the electron beam relies on stretching of electron bunches and on RF manipulations, including the use of a third harmonic RF cavity for the energy spread correction. The repeatability of low energy electron transport is challenging due to remnant fields in the optics and hardware. At the same time, quality of the beam should be preserved through the entire beam transport since the same electron beam will be used twice for cooling in both RHIC rings. In addition, electron beam with small emittance and energy spread should be provided for several energies of planned operation.

Besides many technical issues and attempts to apply high-energy cooling techniques for relatively low energies of LEReC, this will be the first electron cooler to cool beams under collisions. This puts special requirements on the control of the ion beam profile under cooling. Careful optimizations between electron cooling and ion beam lifetime will determine how close one can actually get to the projected luminosity improvement [14].

Since electron beam will be fully non-magnetized and there will be no magnetic field in parts of the cooling sections used for cooling it will be also a first demonstration of the fully non-magnetized cooling.

2.2.7 **Acknowledgements**

We would like to thank many people at the Collider-Accelerator Department of BNL who are actively working on the LEReC project.

2.2.8 **References**

1. A. Fedotov, I. Ben-Zvi, X. Chang, D. Kayran, T. Satogata, Proc. of COOL'07 workshop (Bad Kreuznach, Germany, 2007), p. 243.
2. A. Fedotov, I. Ben-Zvi, X. Chang, D. Kayran, V. Litvinenko, E. Pozdeyev and T. Satogata, BNL Collider-Accelerator Department Tech Note: C-A/AP/307 (2008).
3. A. Fedotov and M. Blaskiewicz, BNL C-AD Tech Note: C-A/AP/449 (2012).
4. V. Litvinenko, BNL C-AD Tech Note: C-A/AP/476 (2012).
5. I. Ben-Zvi, et al., "The status of the BNL R&D ERL," *ICFA Beam Dynamics Newsletter* No. 58 (April 2010), p. 151.
6. W. Xu, et al., "BNL SRF gun commissioning," *Proc. SRF2013* (Paris, France, 2013), MOP027.
7. D. H. Dowell, "Cathode R&D for future light sources," *Nucl. Instr. and Meth. in Phys. Res. A* **622** (2010), p. 685.
8. A. Arnold and J. Teichert, "Overview on superconducting photoinjectors," *Phys. Rev. ST Accel. Beams* **14** (2011) 024801.
9. S. Belomestnykh, "Survey of SRF guns," *Proc. SRF2011* (Chicago, IL, 2011), p. 23.
10. W. Xu, "The commissioning program of the 704 MHz SRF gun," The International Workshop on Accelerator Science and Technology for Electron-Ion Collider EIC14, JLab, TUCF1132 (2014).

11. D. Kayran et al., Proc. of IPAC14 (Dresden, Germany, 2014), MOPRI064, p. 748.
12. B. Sheehy, et al., "BNL 703 MHz superconducting RF cavity testing," *Proc. PAC2011* (New York, NY, USA, 2011), p. 913.
13. A. Fedotov, Proc. of IPAC12 (New Orleans, Louisiana, 2012), WEPPR016, p. 2973.
14. A. Fedotov, BNL Collider-Accelerator Tech Note: C-A/AP/481 (2013).
15. I. Ben-Zvi, "Status of the R&D towards electron cooling of RHIC", Proc. of PAC07 (Albuquerque, New Mexico, 2007), p. 1938.
16. A. Fedotov, "Progress of high-energy electron cooling for RHIC", Proc. of COOL07 (Bad Kreuznach, Germany, 2007), MOM2103, p. 11.
17. A. Fedotov et al., "High-energy electron cooling based on realistic six dimensional distribution of electrons", Proc. of PAC07 (Albuquerque, New Mexico, 2007), p. 3699.
18. A. Fedotov, I. Ben-Zvi, D. Bruhwiler, V. Litvinenko, A. Sidorin, "High-energy electron cooling in a collider", New Journal of Physics 8 (2006), p. 283.
19. B. Dunham, et al., "Record high-average current from a high-brightness photoinjector," *Appl. Phys. Lett.* **102**, 034105 (2013).

2.3 Electron Cooling System in the High Intensity Heavy Ion Accelerator Facility HIAF

L.J. Mao, J.W. Xia, J.C. Yang, G.Q. Xiao, H.S. Xu, H.W. Zhao, X.H. Zhou, X.W. Ma, J. Li, J. Shi, W.P. Chai, G.D. Shen, D.Y. Yin, L.N. Sheng, X.M. Ma, T.L. Yan
Institute of Modern Physics, Chinese Academy of Sciences, 730000, Lanzhou, China
Mail to: maolijun@impcas.ac.cn

2.3.1 Introduction

A new accelerator complex HIAF is under design and will be constructed at IMP Lanzhou to provide intense primary and radioactive ion beams for nuclear and atomic physics research [1]. The schematic layout of HIAF complex is shown in Fig. 1 [2]. Highly charged heavy ion beams provided by a superconducting electron cyclotron resonance ion source (SECR), or H^{2+} beam provided by an intense proton ion source (LIPS), can be injected into a linear accelerator (iLinac). The iLinac will be used as the injector of the booster ring (BRing), which is designed to accelerate the H^{2+} up to the energy of 70 MeV/u or Z/A=1/7 ions to the energy of 25 MeV/u. Ion beams should be cooled, accumulated and accelerated to the required intensity and energy in the BRing, and then fast extracted and transferred either to the compression ring (CRing), or to the target to produce radioactive secondary beams. It is also planned to equip the BRing with a slow beam extraction system for a wide range of applied research in biology and material science. As the key part of the HIAF complex, the CRing allows further accumulation of the ion beams by a combination of electron cooling and Barrier Bucket method. A dedicated bunch compression system will serve in the CRing in order to prepare very short beam pulse for high energy density physical experiments.

To obtain the required phase space density and beam quality for experiments, powerful magnetized electron cooling devices should be used in the BRing and CRing, respectively. By a combination of transverse phase space painting injection and fast electron cooling, the ions can be accumulated up to the intensity limited by space charge effect at the injection energy in the BRing. The maximum electron energy of the BRing cooler is 60 keV, which is performed to cover the injection energy in the range of 25-70 MeV/u. The electron cooling system in the CRing is mainly used to provide

high phase space density and high quality beams for the high energy density physical research area. The maximum electron energy of the CRing cooler is 800 keV, which allows cooling down ions up to the energy of 1.4 GeV/u.

Electron cooling, proceeding by the energy loss of heavy ions on free electrons, is well known to provide high quality beam in circular accelerators [3]. It is a fast process for shrinking the size, the divergence and the momentum spread of stored ion beams. Therefore it is attractive for beam accumulation in combination with multiturn injection. On the other hand it is also applied to the stored ion beam for the compensation of the heating effects. The both electron coolers are designed as a magnetized DC electron cooling system. The basic idea is to use high magnetic field along the orbit of the electron beam from the gun to the collector to transfer the electrons [4]. In the magnetized electron beam, the transverse electron motion is frozen and as a result, the ions interact with a cool Larmor circle. Because the effective temperature of the Larmor circle is much less than the free electrons, the electron cooling rate is much faster than non-magnetized electron cooling system.

In this paper, only modes of HIAF operation with highly charged heavy ion beams are discussed. The conceptual design of the electron cooling system for the HIAF complex is presented. The ion beam cooling process is calculated by numerical simulation and the main parameters of both coolers are selected by the simulation result. The ions $^{238}U^{34+}$ at the energy of 25 MeV/u in the BRing and 1.0 GeV/u at the CRing are taken for reference in the simulation work, because they have the minimum design ratio Z/A=1/7 of HIAF.

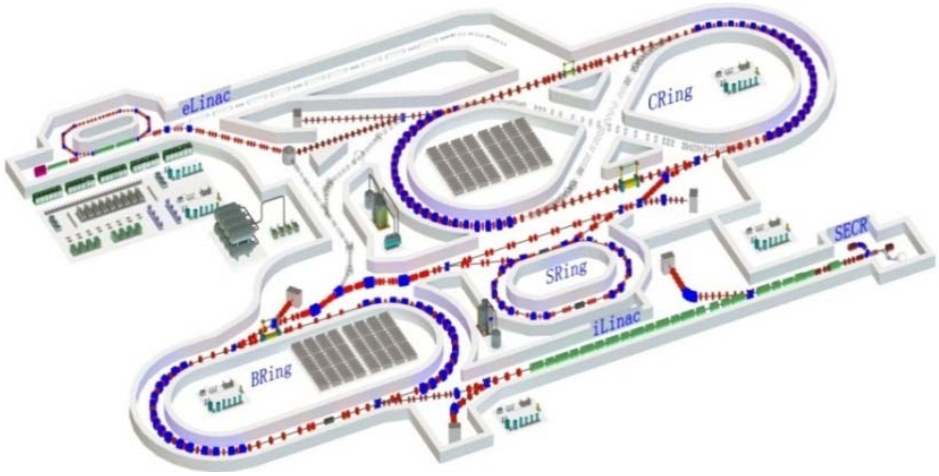

Figure 1: Layout of the HIAF accelerator complex

2.3.2 **Optical Lattice of HIAF Synchrotrons**

The main optical parameters of the HIAF synchrotrons are summarized in Table 1.

Table 1: Main parameters of the BRing and CRing

	BRing	***CRing***
Circumference	402 m	804 m
Maximum magnetic rigidity	34.0 Tm	43.0 Tm
Horizontal/vertical acceptance	250/100 π mm mrad	120/30 π mm mrad
Momentum acceptance	$\pm 5\times10^{-3}$	$\pm 5\times10^{-4}$
Horizontal/vertical tune	6.15/6.30	8.62/8.63
Horizontal/vertical beta function in cooler	10/10 m	20/20 m
Transition energy γtr	6.6	4.6

The proposed racetrack style lattice of BRing consists of four FODO arcs and two 20 m long free-dispersion straight sections. One straight section will mainly be occupied by the electron cooling system. The beta function in the cooling section is 10 m in both horizontal and vertical planes. The maximum magnetic rigidity of 34 Tm can be realized at a dipole field of 2.25 T using superconducting magnet [5]. The BRing offers a transverse acceptance of 250π•mm•mrad horizontally and 100π mm mrad vertically. The momentum acceptance is $\pm 5\times10^{-3}$. The large emittance acceptance allows injection of beam with phase space painting method. The tunes of 6.16 horizontally and 6.30 vertically are optimized for the space charge effect limitation. The BRing is always operated below the transition energy γtr to avoid beam loss during transition energy crossing.

The lattice structure of the CRing adopted the similar design of the BRing. The electron cooling system locates in a straight section where the dispersion function is zero and the beta function is 20 m in both planes. Considering a future upgrade, the space inside the CRing is reserved exclusively for a set of figure-8 shape electron and ion collider.

2.3.3 **Electron Cooling System at BRing**

It is planned to equip the BRing with a magnetized electron cooling system, which is necessary for accumulating the required intensity of the ions by multiply repeated injection pulses. In order to cover the entire energy range of the injector iLinac, the electron cooling system with a maximum energy of 60 keV is designed. The main parameters of the cooler are listed in Table 2.

Table 2: Main parameters of the BRing electron cooler

Maximum electron energy	60.0 keV
Effective length of cooling section	9.0 m
Electron beam current	0.1 – 3.0 A
Cathode radius	15.0 mm
Magnetic field in cooling section	0.05 – 0.2 T
Magnetic field homogeneity	<5×10-5
Magnetic field in gun/collector section	0.25 T
Transverse electron beam temperature	<0.1 eV
Longitudinal electron beam temperature	<0.5 meV
Vacuum condition	$\sim1\times10^{-11}$ mbar

The empirical Parkhomchuk cooling force formula is used to calculate the cooling force in this article [6]. The expression is in a reasonable agreement with available results of the electron cooling force measurements in many devices.

$$\vec{F}(\vec{V}) = -4n_e m_e c^4 r_e^2 Z^2 \frac{\vec{V}}{\left(V^2 + v_{eff}^2\right)^{3/2}} \ln\left(\frac{\rho_{\max} + \rho_{\min} + \rho_L}{\rho_{\min} + \rho_L}\right) \quad (1)$$

Here n_e is the density of electron beam, m_e is the mass of the electron, r_e is the electron classical radius, V is the ion velocity, v_{eff} is the effective velocity of the center of the electron Larmor orbit, the impact parameters ρ_{max}, ρ_{min} and ρ_L are determined by several conditions. All parameters are written in the Particle Reference Frame (PRF) system.

The shrinking of each particle emittance ε and momentum deviation δp are expressed by [7]:

$$\frac{d}{dt}\varepsilon = -2\lambda\varepsilon \quad (2)$$

$$\frac{d}{dt}(\delta p) = -\lambda(\delta p) \quad (3)$$

Here λ is the cooling rate in the Laboratory Reference Frame (LRF):

$$\lambda_{\text{e-cooling}} = 4n_e c^4 r_e r_i \eta \frac{1}{\gamma^2} \frac{Z^2}{A} \frac{1}{\left(V^2 + v_{eff}^2\right)^{3/2}} \ln\left(\frac{\rho_{\max} + \rho_{\min} + \rho_L}{\rho_{\min} + \rho_L}\right) \quad (4)$$

Intrabeam scattering (IBS) effect, which involves multiple small angle Coulomb scattering of charged particles within beams, is a major limitation for high density ion accelerators [8]. This phenomenon leads to the growth in beam emittances and momentum spread, which places limitation on the ability to achieve ultra small beam emittances even by the electron cooling method. The detailed theory of IBS is described in a number of publications [9]. The simplest model of the IBS effect gives the heating rate (LRF) of IBS diffusion as:

$$\lambda_{\text{IBS}} = n_{ion} \frac{\sqrt{\pi}}{4} \frac{c r_{ion}^2 L_C}{\beta^3 \gamma^3 \left\langle \sqrt{\beta_\perp} \right\rangle C_{ring}} \frac{1}{\varepsilon^{3/2} (\delta p)^2} \quad (5)$$

Here n_{ion} is the number of ions in the ring, rion is the classical ion radius, L_C=20 is the Coulomb logarithm, $\beta_\perp$ is the betratron amplitudes, C_{ring} is the ring's circumference. One can see that the IBS heating rate could be very large for small emittances and momentum spread.

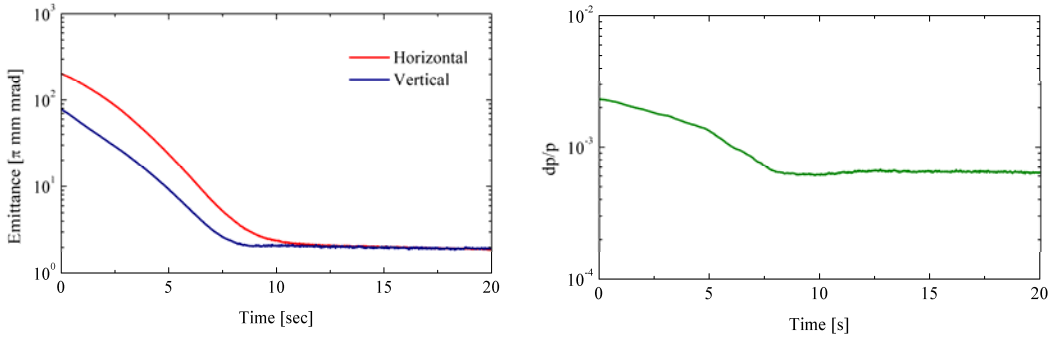

Figure 2: emittance and momentum spread versus time at cooling of 25 MeV/u $^{238}U^{34+}$ ion beam in BRing.

The dependence of the cooling time on cooler's parameters has been demonstrated by simulations with the TRUBS codes [10]. An example of such simulations is show in Fig.2 for the reference ion. As the phase space occupied by the beam shrinks due to

cooling, the IBS heating rate increases, and finally equilibrium values of emittance and momentum spread are reached. In effect, the high density ion beam with such small equilibrium values cannot be stored because of the space charge limitations. The expected horizontal emittance (total) is 20π mm mrad. The characteristic cooling time is defined as required time to achieve the expected emittance.

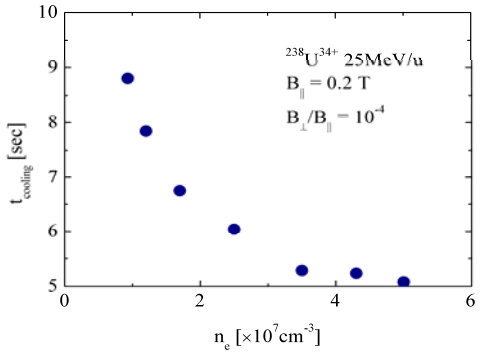

Figure 3: Cooling time as function of the electron beam density.

In principle the cooling rate is essentially proportional to the product of electron density. But the space charge effects lead to dependence of the mean electron velocity and electron velocity spread on co-ordinates inside the electron beam. These additional longitudinal and transverse velocity components in the electron beam can heat ions and reduce the cooling effect. The influence of the electron beam density on the cooling time is shown in Fig.3. For small electron densities the cooling rate increases with electron density, but for higher electron density the cooling rate increases very weakly.

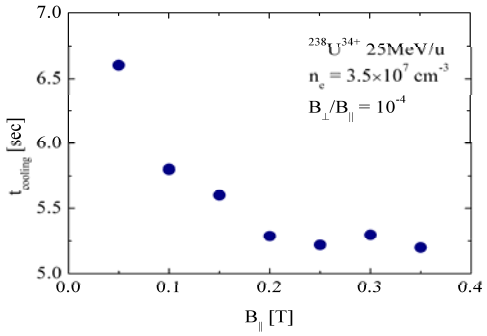

Figure 4: Cooling time as function of the longitudinal magnetic field in the cooling section

The cooling times as functions of the longitudinal magnetic field strength in the cooling section are show in Fig.4. The cooling time decreases strongly for magnetic fields increase and remains nearly constant above 0.2 T. according to the cooling force formula, the magnetic field is major influence in the Larmor radius, thereby affect the Coulomb logarithm. The Larmor radius contribution to the Coulomb logarithm will be much smaller for higher magnetic field. Taking into account the orbit distortion caused by magnetic field in the cooler, the maximum longitudinal magnetic field in the cooling section is designed as 0.2 T.

Finally, the cooling time were calculated for different magnetic field straightness, as shown in Fig.5. The effective velocity veff is determined by the electrical field from

space charge effect of the electron beam and the transverse component magnetic field at the cooling section. The cooling time decreases fast for magnetic field straightness decrease and remains nearly constant below10^{-4}. In this case the effect of the magnetic field straightness is negligible. For preliminary design magnetic field straightness better than 10^{-4} is necessary in the cooling section.

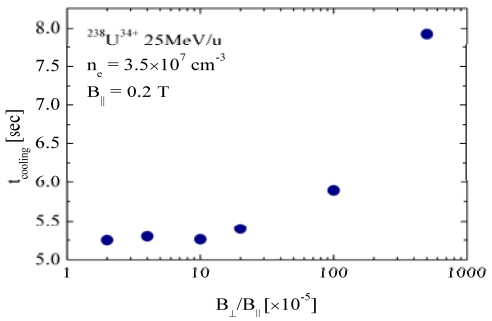

Figure 5: Cooling time as function of the magnetic field straightness in the cooling section

2.3.4 **Electron Cooling System at CRing**

The proposed electron cooling system at the CRing is operated to cool down the ions at the energy up to 1.4 GeV/u, which means the maximum energy of the electron beam is about 800 keV. It will be able to completely suppress the IBS and other heating effects to provide highest phase space density beams and optimum beam quality for physical experiments. The main parameters of the CRing cooler are listed in Table 3. The beam equilibrium in our simulations is achieved by the balance of electron cooling and IBS heating. Fig.6 shows the calculated results for reference ions $^{238}U^{34+}$ at the energy of 1.0GeV/u.

Table 3: Main parameters of the CRing electron cooler

Maximum electron energy	800.0 keV
Effective length of cooling section	15.0 m
Electron beam current	0.1 – 2.0 A
Cathode radius	10.0 mm
Magnetic field in cooling section	0.05 – 0.2 T
Magnetic field homogeneity	$<5\times10^{-5}$
Magnetic field in gun/collector section	0.5 T
Transverse electron beam temperature	<0.1 eV
Longitudinal electron beam temperature	<0.5 meV
Vacuum condition	$\sim1\times10^{-11}$ mbar

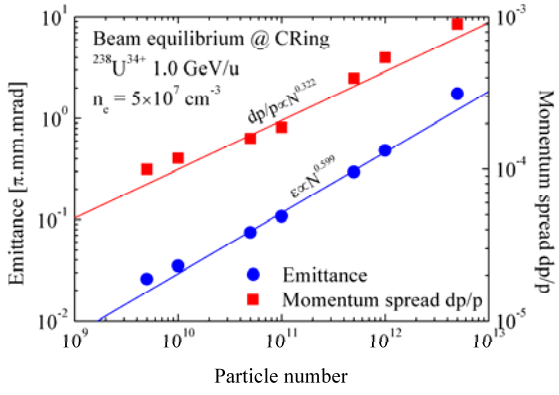

Figure 6: The equilibrium momentum spread and emittance of a cooled beam as a function of the number of stored particles.

2.3.5 **Electron Ion Recombination**

The electron-ion recombination can significantly affect the beam losses of ions which are prepared with high beam quality by electron cooling in storage rings. Generally the recombination between electrons and ions largely proceeds through the capture of a single electron on an ion under emission of a photon, which is called radiative recombination (RR) [11]:

$$A^{q+} + e^{-} \rightarrow A^{(q-1)+} + h\nu \tag{6}$$

The down charged ions will be lost because out of the momentum acceptance. The definition of the RR time during electron cooling can be written as follow:

$$\tau = \frac{\gamma^2}{n_e \eta_c \alpha_{RR}} \tag{7}$$

Here n_e is the electron density in the laboratory reference frame, η_c the ratio of the cooling section length to the ring circumference, γ the relativistic factor. The recombination rate coefficient α_{RR} is calculated by:

$$\alpha_{RR} = 3.02\times10^{-13} q^2 \sqrt{\frac{\mathrm{eV}}{kT_\perp}}\left[\ln\left(\frac{11.32q}{\sqrt{kT_\perp/\mathrm{eV}}}\right) + 0.14\left(\frac{kT_\perp}{q^2\mathrm{eV}}\right)^{1/3}\right]\frac{\mathrm{cm}^3}{\mathrm{s}} \tag{8}$$

It is clear that the recombination rate coefficient is determined by the electron beam density and the transverse electron temperature, as shown in Fig.7. A reduction of the electron density will increase the cooling time by the same factor as the recombination time. The only way to reduce the recombination rate is to increase the effective transverse electron temperature. It has been demonstrated that excitation of transverse electron motion is an efficient way of reducing recombination rate in electron coolers, but do not strongly affect the cooling time in the regime of magnetized electron cooling system.

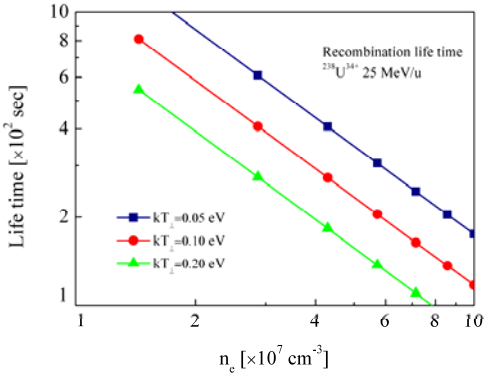

Figure 7: Recombination life time of $^{238}U^{34+}$ at 25 MeV/u as a function of the electron beam current and the transverse electron temperature of the cooler at Bring

2.3.6 **Conclusions**

The use of electron cooling method is a key feature of the HIAF accelerator complex. Its operation requires new coolers, which are being developed with the aid of numerical simulation and experimental investigations with existing coolers in HIRFL-CSR project at IMP.

A classical magnetized electron cooling system with the maximum electron energy of 60 keV will be equipped in the BRing. In combination with phase space painting injection, the required number of ions could be stored at the injection energy.

A similar magnetized electron cooling system with the maximum electron energy of 800 keV is supposed to be used in the CRing, in order to provide high density charged ions for internal and external experiments.

Numerical simulation of beam cooling process in the HIAF is ongoing. The preliminary design parameters were presented based on the calculation results. A series of experimental investigations will be done at the HIRFL-CSR facility in next few years.

2.3.7 **Acknowledgments**

The authors would like to thank the HIAF colleagues for discussions. The study is jointly supported by the Hundred Person Project of the Chinese Academy of Sciences.

2.3.8 **References**

1. Yang J C, Xia J W, Xiao G Q, et al. High Intensity Heavy Ion Accelerator Facility (HIAF) in China. Nuclear Instruments and Methods in Physics Research Section B: Beam Interactions with Materials and Atoms, 2013, 317: 263-265.
2. Yang J C, Xia J W, Xiao G Q, et al. Conceptual Design Report of the HIAF Project. (internal report)
3. Poth H. Electron cooling: theory, experiment, application. Physics reports, 1990, 196(3): 135-297.
4. Dietrich J, Kamerdzhiev V, Bryzgunov M, et al. Status of the 2 MeV Electron Cooler for COSY Juelich. PAC11, New York, 2011.
5. Yao Q G, Ma L Z, He Y, et al. Optimization Of Magnetic Field For Cr Dipole Magnet J. Chinese Physics C, 2008,32 (Suppl. 1):19-21.

6. Parkhomchuk V V. New insights in the theory of electron cooling. Nuclear Instruments and Methods in Physics Research Section A: Accelerators, Spectrometers, Detectors and Associated Equipment, 2000, 441(1): 9-17.
7. Katayama T. Simulation of the electron cooling effect. Private communication.
8. Bjorken J D, Mtingwa S K. Intrabeam scattering. Particle Accelerators, 1983, 13(3-4): 115-43.
9. Meshkov I, Sidorin A, Smirnov A, et al. Physics guide of BETACOOL code Version 1.1[R]. BNL Note CA/AP/262, 2006.
10. Parkhomchuk V V. The electron cooling simulation code TRUBS. Private communication.
11. Wolf A, Gwinner G, Linkemann J, et al. Recombination in electron coolers. Nuclear Instruments and Methods in Physics Research Section A: Accelerators, Spectrometers, Detectors and Associated Equipment, 2000, 441(1): 183-190.

2.4 MEIC Electron Cooling Program

Yaroslav Derbenev and Yuhong Zhang
Thomas Jefferson National Accelerator Facility, Newport News, Virginia, USA
Mail to: yzhang@jlab.org

2.4.1 Introduction

Cooling of proton and ion beams is essential for achieving high luminosities (up to above 10^{34} $cm^{-2}s^{-1}$) for MEIC, a *M*edium energy *E*lectron-*I*on *C*ollider envisioned at JLab [1] for advanced nuclear science research. In the present conceptual design, we utilize the conventional election cooling method and adopted a multi-staged cooling scheme for reduction of and maintaining low beam emittances [2,3,4]. Two electron cooling facilities are required to support the scheme: one is a low energy (up to 2 MeV) DC cooler installed in the MEIC ion pre-booster (with the proton kinetic energy up to 3 GeV); the other is a high electron energy (up to 55 MeV) cooler in the collider ring (with the proton kinetic energy from 25 to 100 GeV). The high energy cooler, which is based on the ERL technology and a circulator ring, utilizes a bunched electron beam to cool bunched proton or ion beams. To complete the MEIC cooling concept and a technical design of the ERL cooler as well as to develop supporting technologies, an R&D program has been initiated at Jefferson Lab and significant progresses have been made since then. In this report, we present a brief description of the cooler design and a summary of the progress in this cooling R&D.

2.4.2 The MEIC Proposal

MEIC, designed as a traditional ring-ring collider, aims to cover a medium range of center-of-mass (CM) energy up to 70 GeV. It will collide 3 to 12 GeV electrons with 25 to 100 GeV protons or up to 40 GeV/u light to heavy ions at multiple (up to 3) interaction points (IP). The design is optimized to reach high luminosities (above 10^{33} $cm^{-2}s^{-1}$/u per IP) over a broad CM energy range with a peak luminosity above 10^{34} $cm^{-2}s^{-1}$/u per IP. It maintains capability for future upgrade for reaching higher CM energy and higher luminosity. Figure 1 shows a schematic layout of MEIC.

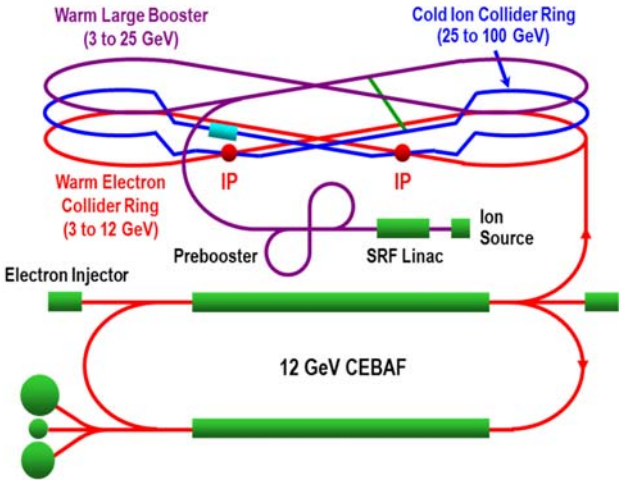

Figure 1: A schematic drawing of MEIC.

The MEIC takes advantage of several unique machine design features for delivering high performances. Among others, it utilizes a high repetition rate CW electron beam from the CEBAF and matched ion beams from a new ion facility. This enables MEIC to adopt a luminosity concept [5] which is based on high bunch repetition rate CW crab crossing colliding beams and has been successfully proved in several lepton-lepton colliders for achieving ultra high luminosity. A multi-phased cooling scheme provides strong cooling of ion beams not only at their formation stage but also during collisions.

2.4.3 Multi-Stage Cooling Scheme

Figure 2 illustrates the schematic layout of the MEIC ion complex. The ions from polarized or un-polarized sources are accelerated step-by-step to the colliding energies in the following major machine components [1]: a 285 MeV pulsed SRF linac, a 3 GeV pre-booster synchrotron, a 25 GeV large booster synchrotron, and finally a collider ring of 25 to 100 GeV.

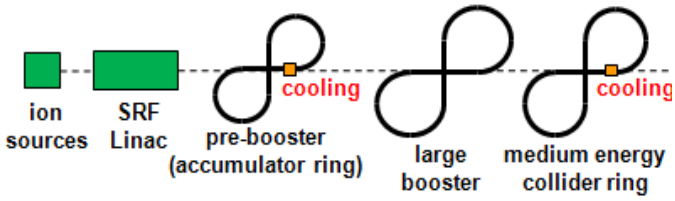

Figure 2: A schematic drawing of MEIC ion complex.

Conventional electron cooling is chosen for the MEIC design. We believe such technology would most likely meet the MEIC requirement, and carry the least technical uncertainty in the project time frame. Further, in order to achieve an adequate cooling efficiency, a multi-staged cooling scheme [1,4] has been adopted:

- *Stage 1*: A DC electron cooling (up to 100 keV electron energy) in the pre-booster for assisting accumulation of positive ions after injected from the linac;
- *Stage 2a*: ***Pre-cooling*** at the top energies of the ion pre-booster utilizing a 2 MeV DC electron cooler for the initial stage of ion emittance reduction;

- *Stage 2b*: If *necessary*, another round of ***pre-cooling*** will be performed at the injection energy (25 GeV) of the collider ring utilizing an ERL cooler;
- *Stage 3*: A ***final cooling*** in the collider ring and at the collision energies (up to 100 GeV) for achieving the designed low 6D emittance and short bunch length;
- *Stage 4*: ***Continuous electron cooling*** during collisions for suppressing IBS induced beam degradation.

Pre-cooling at energies far below the ion collision energies is clearly advantageous. Since the electron cooling time is roughly proportional to both square of the relativistic factor γ of protons or ions and the beam six-dimensional emittance, pre-cooling would provide a superior efficiency over the enire cooling process, both from being at a lower energy (thus small γ) for that stage of cooling itself, as well as due to a significant reduction of the starting beam emittance at the final cooling stage, thus dramatically reducing the total cooling time to meet the design requirement. Cooling during collision is critical for preserving the MEIC's luminosities since the intra-beam scattering (IBS) induced emittance growth time is very short (less than a minute for the design case) [1].

Recently, this cooling scheme of MEIC has been optimized by beginning the pre-cooling phase at the pre-booster (at its top energy) for gaining a significant improvement of the cooling efficiency [6]. As a result, the pre-cooling at the injection energy of the collider ring (namely, stage 2a) may not be required. This change of the design achieves a reduction of technical uncertainty since more cooling burdens are shifted to the well-developed technology -- low energy DC cooling. Table 1 below shows the main parameters and design cooling times [1,3,4]. In fact, the emittance of the ion beam after pre-cooling in the pre-booster is limited by the acceptable space charge tune-shift (~0.2) in the large booster whose circumference is five times larger than that of the pre-booster, instead of the cooler capability.

Table 1: Electron cooling of proton beam in MEIC

Ion ring		Pre-booster	Collider
Energy (p/e)	GeV/MeV	3/2	100/55
Cooling length	M	5	60
Bunch frequency	MHz	~ 1	748.5
Energy spread	10^{-4}	10 / 3	5 / 3
Ion bunch length	Cm	Coasted	1
Electron bunch length	Cm	DC	3
Proton emittance (x/y)	μm	1.6	0.35/0.07
Cooling time	Cin	~5	~ 0.4

2.4.4 Cooling Simulations

Ideally a start-to-end simulation should be carried out for the entire process of MEIC ion beam formation and electron cooling, nevertheless, presently there is no such a simulation code capable of taking such a task. Therefore we simulated various physics processes independently using BETACOOL [7]. By "connecting" them together, namely, extracting the beam parameters at the end of the previous stage cooling simulation and feeding them as the initial parameters to the next stage cooling simulation, we gained a basic picture of the MEIC electron cooling. Figure 3 shows the results of a typical simulation run [8].

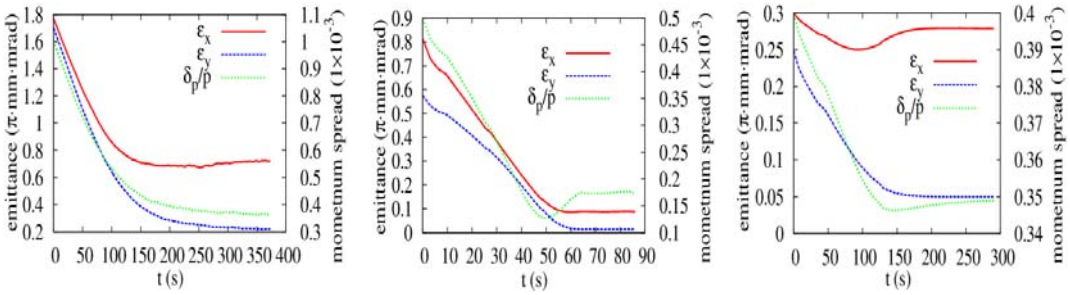

Figure 3: Electron cooling in the MEIC pre-booster (left), in the collider ring at the injection energy (middle) and at the collision energy 60 GeV (right)

2.4.4.1 *DC Cooling in the Pre-booster*

In the pre-booster, the initial normalized emittance of the proton beam is assumed to be 1.75 mm-mrad in both transverse directions, which is limited by the space charge tune-shift at the beam accumulation phase. Figure 3 (left) shows the evolution of the normalized emittance and the momentum spread of a proton beam during the cooling process with the IBS effect included. After about 250 s, the emittance reaches an equilibrium value at which the electron cooling and IBS effect are balanced. However, to avoid an over-cooling such that the space-charge tune-shift becomes too large at the injection energy in the large booster, the DC cooling must be terminated at about 120 s, the emittances are correspondingly are 0.81 and 0.58 mm-mrad in horizontal and vertical directions respectively.

2.4.4.2 *Bunched Cooling in the Collider Ring*

The proton beam is accelerated from 3 GeV to 25 GeV in the large booster, then transferred to the collider ring for further energy boost to 100 GeV. The beam will be first de-bunched and then re-bunched to ~3750 short bunches with a 748.5 MHz repetition rate. The cooling in the collider ring includes the following two steps.

The first step (stage 2b as discussed above) is to use a bunched electron beam to cool coasting proton beam at the injection energy (25 GeV). We assume the initial normalized emittances of the proton beam are 0.81 and 0.58 mm-mrad in horizontal and vertical directions respectively, and the initial momentum spread is 5×10^{-4}. The evolution of the normalized emittance and momentum spread during the cooling process is shown in Figure 3 (middle). As it can be seen, the cooling is very efficient. Within 40 second, the proton beam emittances are already as low as 0.30 and 0.25 mm-mrad, very close to the MEIC nominal design parameters [1].

The second step (stage 3 and 4 discussed above) is to use a bunched electron beam to cool the re-bunched proton beam before and during the collision. We assume the initial transverse emittances are 0.30 and 0.25 mm-mrad and the momentum spread is 4×10^{-4}. The initial proton bunch length is slightly longer than 1 cm and it will reduce to 1 cm at equilibrium. The evolution of the emittances and momentum spread during the cooling process at a 60 GeV design point (the IBS effect is also included) is shown in Figure 3 (right). After carefully adjusting the transverse coupling and the dispersion function in the cooler for helping to redistribute the IBS effect and the cooling effect in different directions, the normalized emittances can be slightly reduced to 0.28 and 0.05 mm-mrad and further be *maintained* at these values. It takes only 200 seconds to reach the equilibrium.

The above three-stage simulations show that the MEIC cooling design should in principle work and the nominal design parameters (transverse emittances and energy spread) can be reached and further maintained. We are present working to refine the simulation model and algorithm by including other beam physics effects to improve the validity and accuracy of the simulation [9,10]. For example, the particle-particle base simulations using VORPOL code were performed for gaining accurate information on the damping kernels in the MEIC high energy cooling [10].

2.4.5 **ERL Circulator Cooler**

The first two stages (1 and 2a) of beam cooling in MEIC take place in the pre-booster utilizing the DC cooling technology; the cooler parameters are well within the present state-of-art. In fact, a 2 MeV DC cooler has been constructed and successfully commissioned recently for the COSY facility [11,12]. A DC cooler similar to that should meet the need in the MEIC pre-booster.

The other stages (2b, 3 and 4) of cooling are in the MEIC collider ring at energy from 25 GeV to 100 GeV. Since the cooling electron energy is up to 55 MeV, it rules out any electrostatic apparatus which are used in all low energy coolers for acceleration of electrons. Thus, the MEIC high energy cooler must rely on the RF/SRF linac technology. Further, by the conceptual design, this cooler must deliver an electron beam with a 2 nC bunch charge at a 748.5 MHz repetition rate, resulting in an unprecedented 1.5 A averaged current from an SRF linac. Such a beam could not be provided presently or in the MEIC project time frame without utilizing additional advanced technologies and schemes.

Figure 4 (left) illustrates a design concept of a high energy electron cooler based on three advanced technologies: a magnetized photo-cathode gun/injector, an SRF linac with energy recovery (ERL) and a circulator cooler ring. These technologies are adopted for the purpose of overcoming the two most critical technical challenges, namely, delivering and disposing an ultra high beam power (up to 81 MW) and achieving a long lifetime (>a week or 168 hours uninterrupted operation) of the photo-cathode gun. As a matter of the fact, both ERL and circulator ring ideas were considered separately in the previous high energy electron cooler proposals for luminosity upgrades of HERA [13] and RHIC [14,15].

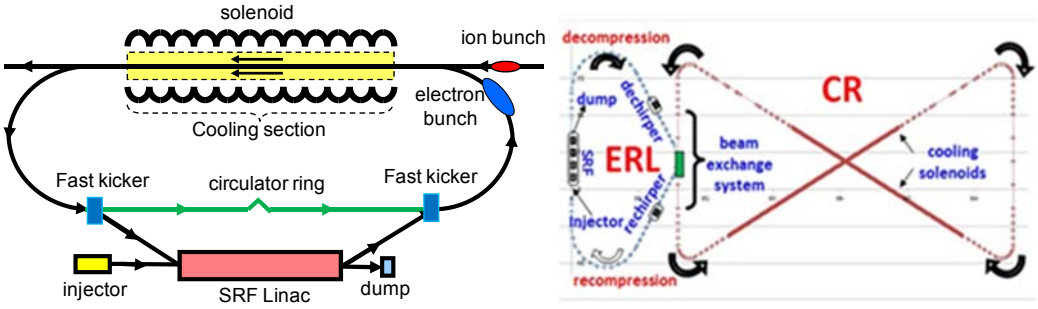

Figure 4: (Left) A schematic drawing of an ERL-circulator ring based electron cooling facility; (right) The layout of a technical design of the MEIC ERL cooler located in the vertex of the figure-8 shaped ion collider ring

The working principle of this ERL-circulator ring based electron cooler is as follows. A high intensity electron bunch from a magnetized photo-cathode gun is accelerated in the SRF linac to the required energy and sent to the circulator cooler ring for cooling ion bunches. The photo-cathode gun ensures a high quality (small emittance and energy spread) of the beam. The electron bunch circulates a large number (ideally up to 100) turns inside the circulator cooler ring while continuously cooling ion bunches in an optically matched section with a solenoid, thus leading to a reduction of the averaged current from the photo-cathode gun and ERL by a factor equal to the number of circulations. The bunch then returns to the SRF linac for energy recovery and finally is sent to a dump while the recovered energy is used to accelerate a new bunch from the photo-injector.

Figure 5 (right) shows a lattice design of the ERL-circulator cooler [16]. It also illustrates an optimization of the location of this cooler - placing at the crossing point of the figure-8 shaped ion collider ring - so two cooling sections could be arranged. Therefore, the cooling rate can be doubled by taking advantage of this unique ring geometry. The MEIC ion booster and collider rings are designed in a figure-8 shape for delivering superior high polarization for polarized proton and light ions.

The ERL ring of this electron cooler includes a pair of de-chirper and re-chirper SRF cavities as shown in Figure 5 (right) for a longitudinal matching of the electron beam [16]. The electron bunches must be very short in the SRF linac in order to maintain a low energy spread required for cooling and for a good energy recovery; however, they must be modestly long (a few cm in RMS size) for wrapping around the relatively long ion bunches in order to achieve a satisfactory cooling efficiency.

Table 2 below shows a typical design parameter set of MEIC ERL cooler [1] assuming the number of circulations is 30.

Table 2: The MEIC ERL-circulator cooler parameters

Min/max energy of electron beam	MeV	5.5/55
Electrons/bunch	10^{10}	1.25
bunch revolutions in CR		~30
Current in CR/ERL	A	1.5/0.05
Bunch repetition in CR/ERL	MHz	750/25
CR circumference	m	~150
Cooling section length	m	30×2
RMS Bunch length	cm	1-3
Energy spread	10^{-4}	1-3
Solenoid field in cooling section	T	2
Beam radius in solenoid	mm	~1
Beta-function	m	0.5
Thermal cyclotron radius	μm	2
Beam radius at cathode	mm	3
Solenoid field at cathode	T	0.2
Longitudinal inter/intra beam heating	μs	200

2.4.6 **Beam Dynamics in the Circulator Ring**

Success of the ERL-circulator cooler design concept is measured by how many circulations of the electron bunches allowed in the cooler ring while delivering a satisfactory cooling efficiency plus whether good energy recovery can be achieved after these circulations. It is expected that the cooler performance is largely limited by

various collective beam effects in the circulator ring. Beam dynamics simulation studies have been initiated to study these effects. We tracked an electron bunch with the MEIC cooling beam parameters turn-by-turn in the circulator cooler ring using Elegant [17]. This code is flexible such that the multi beam effects can be included individually in simulations.

The first collective beam effect investigated is coherent synchrotron radiation (CSR). The study [18,19] has shown that, in the MEIC parameter regime, the beam quality could be seriously affected by the CSR, causing a noticeable deterioration as the number of circulations increases. In worst cases, the undesired micro-bunching instabilities could be quickly excited. The study has further shown that severity of the CSR induced beam degradation strongly depends on the bunch length as anticipated. Figure 5 shows increase of the beam energy spread as a function of circulations for 1 and 3 cm RMS bunch lengths respectively while the bunch charge is a constant. The study has also shown a correlation of the emittance aspect ratio to preservation of the energy spread, suggesting that a flat beam can hold itself much longer than a round beam, thus supporting a long standing assertion that a magnetized electron beam with a round-to-flat conversion would improve the beam circulation in the cooler ring [20]. It is clear that schemes for mitigating the CSR effect should be explored. More studies including additional effect such as longitudinal space charge, are in progress.

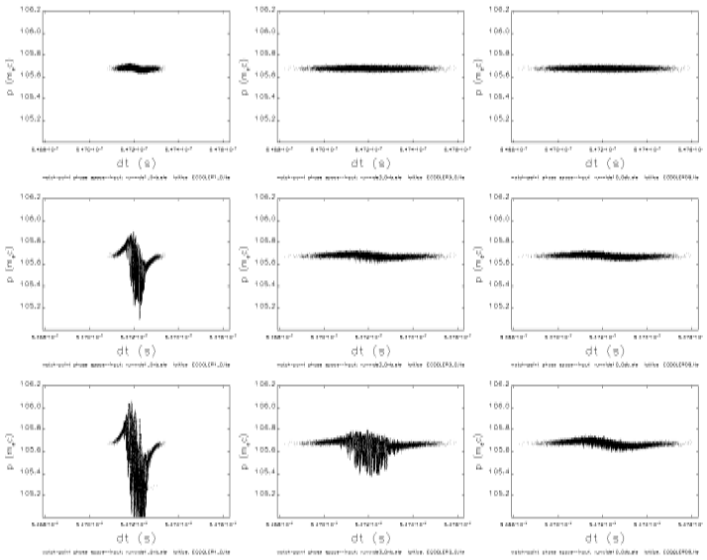

Figure 5: The longitudinal phase space of an electron bunch after 1, 10 and 20 circulations in the MEIC circulator cooler ring. The first two columns are for a 1 and 3 cm RMS bunch length. The last column is also for a 3 cm RMS bunch length, however, with an emittance aspect ratio of 10. A micro-bunching instability was excited before 20 circulations in the first two columns.

2.4.7 **Technology R&D**

Operation of an ERL-circulator electron cooler depends on a number of accelerator technologies, among them, a high brightness electron source and an ultra fast kicker are the two most challenging ones.

According to the operation scheme of the ERL circulator cooler, an electron bunch is first kicked into a circulator ring, and later kicked out from it after a pre-determined

number of circulations. The repetition rate of this kicker is on the order of 7.5 to 75 MHz if the number of circulations is 10 to 100. To avoid affecting the neighboring electron bunches, the rise and full time of this kicker must be shorter than the bunch spacing (1.25 ns). These specifications, high repetition rate and fast rise/full time combined together, represent orders of magnitude beyond the state-of-art. To provide a technical solution, we have been exploring concepts of RF harmonic based and beam-beam based faster kicker.

In principle, an RF kicker [21] acts like an RF separator used in CEBAF for diverting one linac beam alternately to three experimental halls. In this case, an RF signal with a special wave form is required to drive a physical kicker that kicks only every n-th bunches in a bunch train. Such an RF wave form can be constructed straightforwardly by superposition of a set of harmonic wave forms of different frequencies. It needs to be amplified by a digital apparatus for gaining a required power. An electronic system that can achieve a high gain at each of all the individual frequencies is under development and a proto-type will be tested soon [22].

An innovative idea recently under investigation utilizes a non-relativistic sheet beam for providing transverse kicking to an electron bunch [3], as illustrated in Figure 6. This idea of a beam-beam kicker was first proposed by V. Shiltsev [23] for two round Gaussian beams. A proof-of-principle experiment is under consideration for being carried out at the ASTA facility at Fermilab [24]

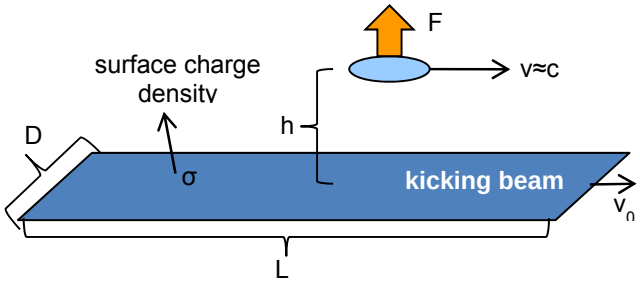

Figure 6: A schematic drawing of beam-beam fast kicker

2.4.8 **Proof-of-Principle Experiments**

Two machine study experiments for proof of the MEIC cooling concept are actively explored presently.

The first proposed experiment is a demonstration of cooling of ion beams by a bunched electron beam. We propose this experiment to be carried out at an existing DC cooler at a collaborating institution, utilizing the existing facilities including an ion storage ring. A DC cooler is equipped with a thermionic gun and an electrostatic accelerating device. We propose replacing the thermionic gun by a laser driven photo-cathode gun for this experiment. By controlling the driver laser (its repetition rate and pulse time structure), a bunched electron beam can be drawn from the cathode.

Alternately, by pulsing the grid voltage, a thermionic gun can also generate a bunched electron beam [25]. This method has an advantage of low invasiveness to an existing facility; however, it usually can not make the bunch as short as that in the MEIC design, nor deliver a very high repetition rate. A plan [26] has been developed at the Institute of Modern Physics, China, in collaboration with Jefferson Lab and Budker

Institute of Nuclear Physics, Russian Federation, a test stand of the new power source is under construction [26].

The second proposed experiment is focused on a proof of the concept of an ERL-circulator cooler and studies of the beam dynamics in the circulator ring [27]. The driver ERL of JLab FEL has been selected as a test facility for this study. It will also be used as a test bed for technology development. The goals of the first phase study include

- Demonstrate longitudinal phase matching and fast exchange of high repetition rate bunches between the ERL and the circulator ring;
- Develop and test technologies such as high current ERLs and faster kickers;
- Study the collective effects in the circulator ring, and determine the maximum number of circulations;

The FEL at JLab is an ERL based light source presently delivering the highest average power laser in the infrared (IR) region. It also generated an ultra violet (UV) laser. The facility consists of a 350 kV photo-cathode DC gun, a 9 MeV boosting injector, a 130 MeV three-module SRF linac, and two recirculators for IR and UV beams respectively. It can provide a high quality electron beam with an energy range and bunch repetition rates [28] similar to the MEIC cooler design. This allows maximum reuse of the existing hardware, thus reducing the capital costs of this experiment.

The layout of the cooler test facility is shown in Figure 7. The presence of the parallel IR and UV beam lines provides an opportunity for a most straight-forward implementation of a compact circulator ring by adding two 180° bends. The photo-cathode DC injector, SRF linac and ERL beam line will have no change while providing the electron bunches to the circulator ring. One fast kicker and two septum magnets will be installed in the UV beam line and are responsible for the bunch switching in and out of the circulator ring.

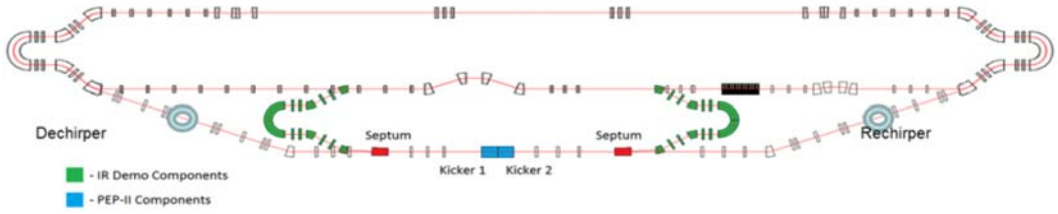

Figure 7: Layout of an ERL-circulator cooler test facility based on JLab FEL Driver ERL.

2.4.9 **Conclusions**

Electron cooling of proton and ion beam has a great impact on the Jefferson Lab MEIC proposal for reaching high luminosities. The adopted multi-stage cooling scheme provides a promising path to reach this luminosity goal. The required low energy DC cooler is well within the present state-of-art, however, there are significant technology challenges to realize cooling at high electron energy utilizing an ERL-circulator ring based cooler. Jefferson Lab has initiated an R&D program to address these technology challenges and to this days good progress has been achieved.

We are also exploring a technology staging approach for electron cooling to achieve a reduction of accelerator R&D requirement. One idea under evaluation is utilizing a reduced cooling electron beam current from the high energy cooler without a circulator

ring. It has been demonstrated in simulations [8] that such a "weak" version of electron cooling, despite providing much less cooling capability, still enables MEIC to reach luminosities above 10^{33} 1/cm^2/s, which is required by the physics program.

We understand that a bunched beam stochastic cooling, recently successfully desmonstrated and operated at BNL for the RHIC heavy ion program [29], can also be utilized as a supplementary cooling technique for the MEIC heavy ion collisions [30]

2.4.10 **Acknowledgements**

The work summarized in this review is completed by the Jefferson Lab MEIC accelerator design and R&D team. We would like to thank David Douglas, Andrew Hutton, Andrew Kimber, Rui Li, John Musson, Edward Nissen (now at CERN), Chris Tennant and He Zhang for their valuable contributions to this study.

We also want to thank George Bell and Ilay Pogorelov of Tech-X, Inc. for collaborations on MEIC cooling simulations; Lijun Mao and Hongwei Zhao of Institute of Modern Physics, China and Vladimir Reva of Budker Institute of Nuclear Research, Russian Federation, for collaborations on proposal of experimental demonstration of cooling by a bunched electron beam.

We would further like to thank the following colleagues for fruitful discussions: Rongli Geng, Geoffrey Krafft, Fanglei Lin, Vasiliy Morozov, Fulvia Pilat, Mathew Poelker, Robert Rimmer, Riad Suleiman, Haipeng Wang and Shaoheng Wang of Jefferson Lab; Valeri Lebedev, Sergei Nagaitsev, Phillip Piot and Vladimir Shiltsev of Fermilab; Alex Chao of SLAC; Alexei Fedotov of BNL; Takeshi Katayama of Nihon Univ., Japan; Igor Meshkov, Anatoly Sidorin and Alexander Smirnov of Joint Institute of Nuclear Research at Dubna, Russian Federation.

The work was supported by Jefferson Science Associates, LLC under U.S. DOE Contract No. DE-AC05-06OR23177.

2.4.11 **References**

1. "Science Requirements and Conceptual Design for a Polarized Medium Energy Electron-Ion Collider at Jefferson Lab MEIC", edited by Y. Zhang and J. Bisognano (2012) (arXiv:1209.0757)
2. Ya. Derbenev, J. Musson and Y. Zhang, "Electron Cooling for a High Luminosity Electron-Ion Collider", proceedings of COOL'07 Workshop, Bad Kreuznach, Germany (2007), THAP12.
3. Ya. Derbenev, Y. Zhang, "Electron Cooling for Electron-Ion Collider at JLab", proceedings COOL'09 Workshop, Lanzhou, China (2009)
4. Y. Zhang, Ya. Derbenev, D. Douglas, A. Hutton, A. Kimber, R. Li, E. Nissen, C. Tennant and H. Zhang, "Advance in MEIC Cooling Studies", proceedings of COOL'13 Workshop, Murren, Switzerland, (2013)
5. Ya. Derbenev, G. Krafft, B. Yunn and Y. Zhang, "Achieving High Luminosity in an Electron-Ion Collider", proccedings of HB2010 Workshop, Morschach, Switzerland (2010)
6. Y. Zhang, presentation at MEIC Accelerator Design and R&D meeting (2012)
7. A. Sidorin and A. Smirnov, in this issue of ICFA Beam Dynamics Newsletter
8. H. Zhang and Y. Zhang, "Simulation Study for MEIC Electron Cooling", proceedings of EIC14 Workshop, Newport News, Virginia, USA (2014)
9. H. Zhang, Jeffereson Lab LDRD proposal, 2014
10. G. Bell, I. Pogorelov, B. Schwartz, H. Zhang and Y. Zhang, "Single Pass Electron

Cooling Simulations for MEIC", proceedings of NA-PAC 2013, Pasadena, CA, USA (2013)
11. "COSY Electron Cooling Conceptual Design Report", BINP, Novosibirsk 2009
12. J. Dietrich, in this issue of the ICFA Beam Dynamics Newsletter
13. Yu. Martirosyan, V. Ayvazyan, K. Balewski, R. Brinkmann, P. Wesolowski, Y. Derbenev, "Conceptual Design of Recirculator Ring for Electron Cooling at PETRA-P", proceedings of EPAC2000, Vienna, Austria (2000)
14. I. Ben-Zvi, *et al.,* "Electron Cooling for RHIC", proceedings of PAC05 (2005)
15. "ZDR Electron Cooling for RHIC", version dated March 9, 2005
16. D. Douglas and C. Tennant, JLab Technote 12-026 (2010)
17. M. Borland, Proc. of ICAP2000 (2000)
18. D. Douglas and C. Tennant, "Coherent Synchrotron Radiation Induced Beam Degradation in the MEIC Circulator Cooling Ring", JLab Technote 12-027 (2012)
19. E. Nissen, Y. Zhang, R. Li, D. Douglas and C. Tennant, "Microbunching Effects Induced by CSR in the MEIC Circulator Cooler Ring", proceedings of EIC14 Workshop, Newport New, Virginia, USA (2014)
20. Ya. Derbenev, NIM A 532 (2004) P307
21. E.W. Nissen, A. Hutton, A.J. Kimber, "A Harmonic Kicker Scheme for the Circulator Cooler Ring in the Medium Energy Electron-ion Collider", proceedings of IPAC2013, Shanghai, China (2013)
22. E. Nissen and A. Kimber, Jefferson Lab LDRD 2013
23. V.Shiltsev, NIM. A374 (1996) 137
24. E. Harms, J. Leibfritz, S. Nagaitsev, P. Piot, J. Ruan, V. Shiltsev, G. Stancari, A. Valishev, in this issue of ICFA Beam Dynamics Newsletter
25. H. Zhao, *private communications*
26. L. Mao and V. Reva, *private communications*
27. Ya. Derbenev, D. Douglas, A. Hutton, G. Krafft, E. Nissen, Y. Zhang, "A Test Facility for MEIC ERL Circulator Ring Based Electron Cooler Design", proceedings of HB2012, Beijing, China (2012)
28. For example, C. Tennant, "Progress at the Jefferson Laboratory FEL", proceedings of PAC09, Vancourer, BC, Canada p3125 (2009)
29. J. M. Brennan, M. Blaskiewicz, K. Mernick, in this issue of ICFA Beam Dynamics Newsletter
30. T. Katayama, in this issue of ICFA Beam Dynamics Newsletter

2.5 Muon Cooling

2.5.1 Introduction

P. Snopok
Illinois Institute of Technology, Chicago, IL and Fermilab, Batavia, Illinois, USA
Mail to: psnopok@iit.edu

The two key applications of muon cooling are neutrino factories and muon colliders. Muons for these applications are produced as a tertiary beam: protons are directed onto a target to yield a beam of pions. Those pions are then captured in a high-field solenoid and allowed to drift and decay into muons. The resulting muon beam occupies a very large phase space. Tightly focused ("cooled") muon beams are desired for neutrino factories and muon colliders. Given that muons have a relatively short life span (2.2 μs in the rest frame), ionization cooling [1] is deemed to be the only technique fast enough to cool beams well within the muon lifetime.

Various aspects of muon ionization cooling have been addressed over the last two decades, first by the Neutrino Factory and Muon Collider Collaboration (NFMCC) [2] and later by the Muon Accelerator Program (MAP) [3] concentrating on the conceptual design and feasibility studies of muon-based accelerators. These muon-based facilities have the potential to discover and explore new exciting fundamental physics, but require the development of demanding technologies and innovative concepts.

Cooling muons could dramatically improve performance and cost effectiveness of the downstream accelerating complex. Neutrino factories require significant transverse cooling and benefit from full six-dimensional cooling, while muon colliders require a six order of magnitude reduction in muon beam phase space. Various scenarios were recently put forward by the Muon Accelerator Staging Study (MASS) [4], and for each of those there are corresponding cooling channel options involving vacuum RF or high-pressure gas-filled RF reaching the desired design parameters. The current status of these studies is presented in the subsequent sections, starting with the initial cooling channel that cools to some intermediate emittances, but at the same time it is capable of cooling both signs of muons simultaneously. The other two channels—the vacuum RF rectilinear cooling channel (VCC) and the high-pressure gas-filled RF helical cooling channel (HCC)—can reach the ultimate six-dimensional cooling emittance goals, but require a charge separation section, the concept for which has also been studied and published [5].

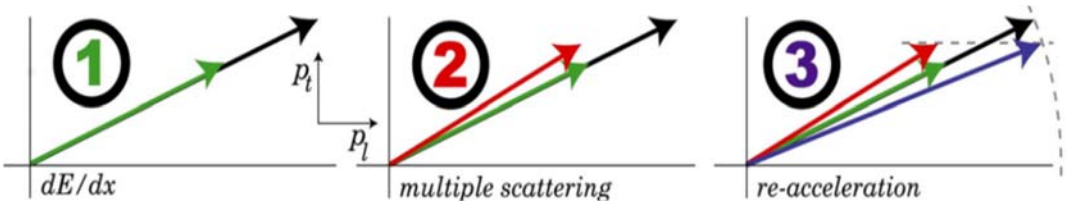

Figure 1: Ionization cooling principle. Green arrow: momentum reduction in the absorber, red arrow: reduction of the cooling effect due to multiple scattering, purple arrow: longitudinal momentum restored in a set of RF cavities.

Transverse muon cooling is achieved by letting a beam of muons pass through an energy absorbing mediumer in which all the components of each particle's momentum are reduced (Fig. 1, left). The longitudinal momentum is then restored in a set of RF cavities (Fig. 1, right). If the absorber material and optics parameters are chosen carefully, the net effect is the transverse emittance reduction. Unfortunately, multiple scattering in material effectively reduces the amount of cooling (Fig. 3, central) according to the following formula [6]:

$$\frac{d\epsilon_N}{ds} \approx -\frac{1}{\beta^2}\left\langle\frac{dE_\mu}{ds}\right\rangle\frac{\epsilon_N}{E_\mu} + \frac{\beta_\perp (0.014GeV)^2}{2\beta^3 E_\mu m_\mu X_0}, \qquad (1)$$

where $d\epsilon_N / ds$ is the rate of normalized emittance change inside the absorber; βc, E_μ, and m_μ are the muon velocity, energy and mass; $\beta_\perp$ is the lattice betatron function at the absorber; and X_0 is the radiation length of the absorber material. The last term in Eq. (1) can be minimized by reducing $\beta_\perp$ (by placing the absorber at a minimum of the betatron function), and by choosing a low-Z material to maximiz X_0.

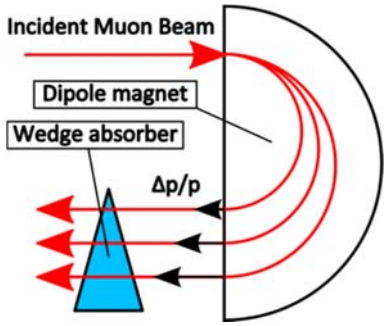

Figure 2: Emittance exchange principle.

Six-dimensional cooling reducing both the transverse and longitudinal sizes of the beam would result in the best quality beam. In order to reduce the longitudinal emittance, the so-called "emittance exchange" technique is commonly used, where a dispersive beam is passed through a discrete or continuous absorber in such a way that the high-energy particles traverse more material than the low-energy particles (see Fig. 2). The net result is a reduction of the longitudinal emittance at the cost of simultaneously increasing the transverse emittance. By controlling the amount of emittance exchange the six-dimensional emittance can be reduced. It has been shown that six-dimensional cooling down to the transverse normalized emittance of 0.3 mm and the longitudinal normalized emittance of 1.5 mm is possible, and is consistent with various technical limitations. The simulations were carried out taking into account collective effects [7].

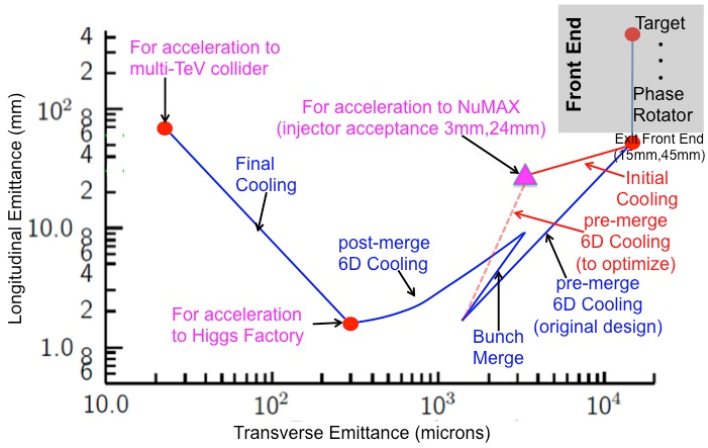

Figure 3: Emittance evolution for different applications.

Figure 3 shows the evolution of the two normalized emittances for different applications. For example, the new red line introduced recently by MASS corresponds to the ultimate Neutrino Factory dubbed NuMAX [8]. The cooling process starts in the top-right corner of the diagram where beam emerges from the muon front end at 15 mm in transverse normalized emittance, and 45 mm in longitudinal. Multiple bunches selected by the front end are cooled in the pre-merge channel, followed by the bunch merge section combining all bunches into one. The resulting single bunch is then cooled further in the post-merge cooling channel, until the design emittances of 0.3 mm in transverse and 1.5 mm in the longitudinal direction are achieved. A multi-TeV collider

will require a final cooling section in addition to the ultimate six-dimensional cooling. Final cooling is not covered in the subsequent sections.

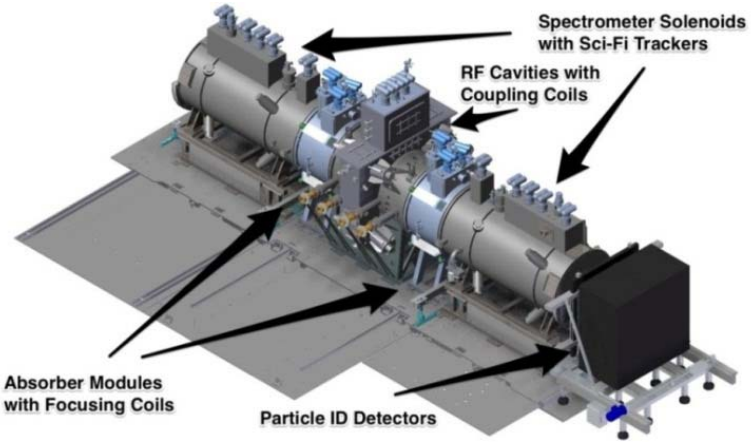

Figure 4: MICE Step V configuration to demonstrate sustainable muon ionization cooling.

Ionization cooling has never been demonstrated for muons. The international Muon Ionization Cooling Experiment (MICE) [9] will demonstrate sustainable cooling by reducing the emittance of a muon beam by ≈10% and measuring it with a precision of 0.1%. MICE is implemented in steps. Step IV is currently in an advanced stage of construction, and is being prepared for taking data in 2015. This will be the first six-dimensional emittance reduction demonstration without reacceleration. Step IV will test beam propagation in the magnetic system and allow precise measurement of ionization cooling-related properties of absorbers (liquid hydrogen, LiH, and possibly more). Step V (shown in Fig. 4) will include a second absorber module with focusing coils and four RF cavities to demonstrate sustainable cooling. Step V corresponds to one half of a lattice cell of the Neutrino Factory Feasibility Study II cooling channel [10]. The data provided by MICE will allow relevant simulation software packages to be validated and updated with new experimental results on *dE/dx* and multiple scattering.

Studies of muon cooling channels and the corresponding experimental program produce a number of results of general interest, such as RF operation in strong magnetic field [11], general magnet requirements for future muon sources, material properties of the typical absorbers used for cooling (liquid hydrogen, LiH).

2.5.1.1 *References*

1. G.I. Budker, in: Proceedings of 15th International Conference on High Energy Physics, Kiev, 1970. A.N. Skrinsky, Intersecting storage rings at Novosibirsk, in: Proceedings of Morges Seminar, 1971. See also http://www.hep.princeton.edu/mumu/physics/.
2. The Neutrino Factory and Muon Collider Collaboration (NFMCC): http://www.cap.bnl.gov/mumu/.
3. Muon Accelerator Program (MAP): http://map.fnal.gov/.
4. J-P. Delahaye *et al.* (eds.), Enabling Intensity and Energy Frontier Science with a Muon Accelerator Facility in the U.S.: A White Paper Submitted to the 2013 U.S. Community Summer Study of the Division of Particles and Fields of the American Physical Society, arXiv:1308.0494v2. See also http://map.fnal.gov/mass.
5. C. Yoshikawa *et al.* A Charge Separation Study to Enable the Design of a Complete Muon Cooling Channel, Proceedings of PAC2013, Pasadena, CA USA, 2013,

THPH019.
6. D. Neuffer, Principles and Applications of Muon Cooling, Part. Acc. Vol. 14, 75 (1983).
7. D. Stratakis, J. S. Berg, R. B. Palmer, and H. Witte, Complete 6-dimensional muon cooling scheme for a Muon Collider, Proceedings of IPAC2014, Dresden, Germany, TUPME020 (2014).
8. J-P. Delahaye *et al.* A Staged Muon Accelerator Facility for Neutrino and Collider Physics, Proceedings of IPAC2014, Dresden, Germany, 2014, WEZA02.
9. MICE collaboration: http://mice.iit.edu/. See also: P. Snopok, E. Overton, The Status of the Construction of MICE Step IV, Proceedings of IPAC2014, Dresden, Germany, 2014, TUPME011. D. M. Kaplan, P. Snopok, A. J. Dobbs, Progress Towards Completion of the MICE Demonstration of Muon Ionization Cooling, Proceedings of IPAC2014, Dresden, Germany, 2014, THPRI030.
10. S. Ozaki, R. Palmer, M. Zisman, and J. Gallardo, (eds.), Feasibility Study-II of a Muon-Based Neutrino Source, BNL-52623 (2001). See also: http://www.cap.bnl.gov/mumu/studyii/FS2-report.html.
11. See http://mice.iit.edu/mta/.

2.5.2 Helical FOFO Snake for Initial 6D Cooling of Muons

Y. Alexahin, Fermilab, USA
Mail to: alexahin@fnal.gov

2.5.2.1 *Introduction*

The major difficulty with ionization cooling of muons is anti-damping of longitudinal oscillations due to decrease of ionization losses with momentum in the most suitable for cooling range 2–300 MeV/*c*. A number of schemes were proposed to resolve this difficulty and provide 6D cooling by forcing muons with higher momentum to take a longer path in the absorber so that they lose more energy. This can be realized by creating dispersion in particle positions at wedge absorbers (without significant overall path lengthening) or by creating sufficiently large path lengthening with momentum and using a homogeneous absorber.

The early versions of the so-called FOFO snake [1] used a third possibility: locally large path lengthening in slab absorbers due to a large slope of the dispersion function there. This allowed the FOFO snake to cool muons of both signs simultaneously.

Here we present a later analysis which showed that the "helical" (HFOFO) snake can actually incorporate wedge absorbers in such a way that simultaneous cooling of μ^- and μ^+ is still possible. This allowed for smaller "snake" amplitude and improved transmission.

2.5.2.2 *Basic Principles*

The helical FOFO snake is based on the following principles: alternating solenoid focusing, periodic rotating dipole field and resonant dispersion generation [1].

The focusing magnetic field is created by a sequence of solenoids with alternating polarity and gaps between them (the name FOFO reflects the fact that solenoid focusing does not depend on polarity since it is quadratic in magnetic field). Emittances of the

two transverse normal modes[1] are swapped with each change of polarity so that both modes are cooled.

The transverse magnetic field component necessary for dispersion generation can be created by periodical inclination of solenoids. The idea of the helical FOFO snake is to make a rotating dipole field by inclining solenoids in rotating planes $x\cdot\cos(\phi_k)+y\cdot\sin(\phi_k) = 0$, $\phi_k = \pi(1–2/N_s)(k + 1)$, $k = 1, 2,\ldots, N_s$, N_s being a necessarily even number of solenoids/period.

If $N_s=2(2j+1)$ then μ^- in solenoid $k = k_1$ see exactly the same forces as μ^+ in solenoid $k = k_1 + N_s/2$ since these solenoids have the same inclination but opposite polarity. In the result μ^- and μ^+ orbits have exactly the same form with longitudinal shift by half period ($N_s/2$ solenoids) but are not mirror-symmetric as one might expect.

Large dispersion can be generated if the transverse tune $Q_\perp$ is close to a resonant value. To obtain a positive momentum compaction favorable for longitudinal cooling it must be above the resonant value $Q_\perp > n + Q_s$, Q_s being the longitudinal mode tune. Despite closeness to a resonance the momentum acceptance of such channel can be sufficiently large owing to higher order chromatic effects.

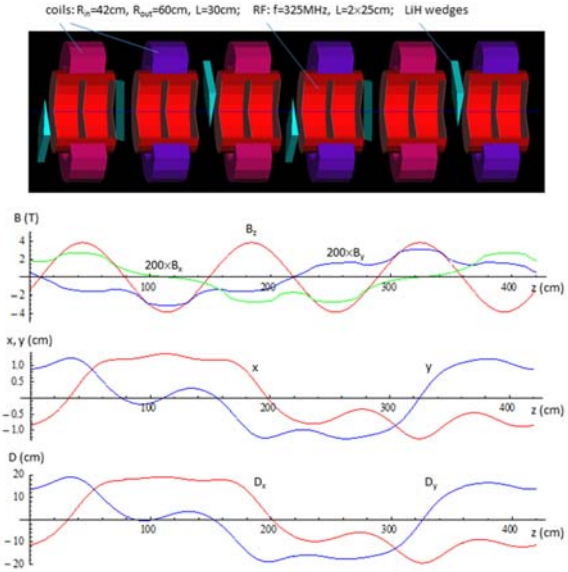

Figure 1: Layout of one period of the HFOFO lattice (top), magnetic field for muon momentum 230 MeV/c (second from top), μ+ equilibrium orbit and dispersion (bottom).

2.5.2.3 *Lattice Description*

Here we present a version of the helical FOFO snake filled with high-pressure gaseous hydrogen (GH_2) that allows for higher RF gradient and also works as an absorber. Following the HCC design [2] we assume its density to be equal to 20% that of liquid hydrogen and take for peak RF gradient $E_{max} = 25$ MV/m at $f_{RF} = 325$ MHz. It is assumed that GH_2 will provide sufficient cooling of the cavities windows so that they can be quite thin (0.12 mm of Be in the beginning of the channel).

[1] In an axisymmetric field they are cyclotron (Larmor) and drift modes (see e.g. Ref [1])

One period of the channel is schematically shown in Figure 1 (top). Its length is $L_{\text{period}} = 4.2$ m.

There are $N_s = 6$ solenoids per period inclined by angle 2.5 mrad in planes rotated by angles $\phi_k = 4\pi/3, 0, 2\pi/3, 4\pi/3, 0, 2\pi/3$; $\phi = 0$ corresponds to pitching in the vertical plane.

The relatively small radius of RF cavities at $f_{RF} = 325$ MHz made it possible—in contrast to the earlier versions of the FOFO snake [1]—to place the cavities inside the solenoids and to free up space for LiH wedge absorbers (wedge angle 0.17 rad in the beginning of the channel) between the solenoids at minima of the betatron functions. To ensure equal longitudinal cooling for μ^- and μ^+ the wedges with numbers $k = k_1$ and $k = k_1 + N_s/2$, k_1=1,2,3 are grouped in pairs of the same orientation. This orientation was then optimized to achieve maximum longitudinal cooling.

2.5.2.4 *Properties of Periodic Channel*

The lower two plots in Figure 1 show μ^+ equilibrium orbit and dispersion found for momentum 230 MeV/*c*. The normal mode tunes and normalized equilibrium emittances are given in Table 1.

Table 1: The normal mode tunes and normalized equilibrium emittances.

Parameter	*Mode I*	*Mode II*	*Mode III*
Tune	1.2271 + 0.0100 i	1.2375 + 0.0036 i	0.1886 + 0.0049 i
Emittance (mm)	2.28	6.13	1.93

The tunes were computed from eigenvalues of a one-period transfer matrix; their imaginary part describes oscillation damping due to the regular part of ionization losses. Without stochastic effects the emittances would have been damped as

$$\frac{d}{dz}\ln\varepsilon_j = -2\times\frac{2\pi}{L_{period}}\,\mathrm{Im}\,Q_j \qquad (1)$$

There is a large difference between the cooling rates and equilibrium emittances of the transverse normal modes (I and II) due to the axial symmetry breaking by the dipole field component. They can be equalized with the help of a quadrupole field of constant polarity (but not necessarily of constant gradient). Such field works for both μ^- and μ^+ despite breaking the translational symmetry between the two beams. However, then a strong β-beat is excited slightly increasing the 4D emittance.

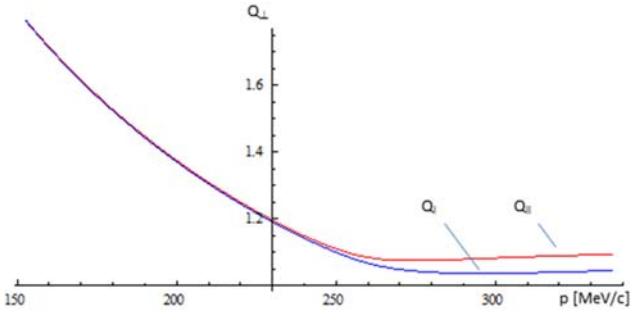

Figure 2: Betatron tunes vs muon momentum.

To estimate the momentum acceptance we can assume the longitudinal motion to be slow and calculate betatron tunes for a constant momentum *p* (Figure 2). Surprisingly, the transverse tunes are "repelled" from the integer resonance making what we may call static acceptance very large (it actually significantly exceeds the shown range). However, there is a limitation due to change in the sign of the slippage factor [1], which can be called the dynamic acceptance since it is important only in the presence of RF field. For the considered parameters it limits the available momentum range from above by value of ~333MeV/*c*.

2.5.2.5 *Initial 6D Cooling Simulations*

The HFOFO snake can be used for cooling μ^- and μ^+ beams formed in the front end [3]. The average momentum of the beam core from the front end is rather high, ~250MeV/*c,* so in order to pull it farther from the upper limit and reduce losses the design momentum was lowered along the channel to ~200MeV/*c*. This was achieved by lowering current in solenoids and adjusting RF phase and LiH absorber wedge angle while keeping the solenoid geometry and RF gradient constant. The total length of the channel with in and out matching sections is 131 m.

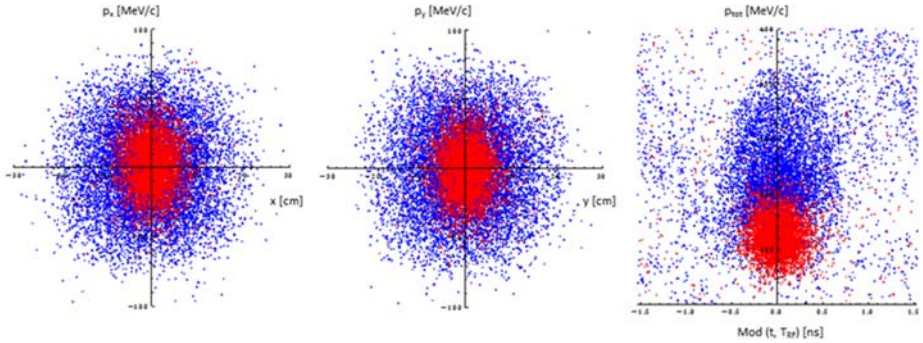

Figure 3: Initial (blue) and final (red) μ^+ beam phase space distribution. All bunches were projected onto the same RF bucket in the right plot.

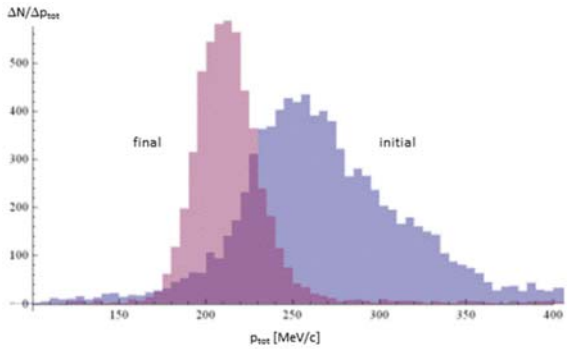

Figure 4: Initial (blue) and final (pink) μ^+ beam distribution in total mechanical momentum.

Figures 3 and 4 present distributions of the initial μ^+ beam and the cooled beam in the exit solenoid (with the same 2 T magnetic field as in the front end solenoid) obtained by tracking with G4beamline [4]. No cuts were applied. Distributions in μ^- beam look similar.

Computation of beam emittance presents a challenging problem due to long non-Gaussian tails in distribution. To obtain unambiguous results we use multi-dimensional Gaussian fit [5] which automatically suppresses halo contribution. Computed in this way normalized emittances and beam core intensities are shown in Fig. 5 for the case when no quadrupole field was added leaving equilibrium emittances unequalized. The initial 6D emittances 5.6 cm^3 and 6.2 cm^3 of μ^- and μ^+ respectively were reduced to 0.051 cm^3 for both beams.

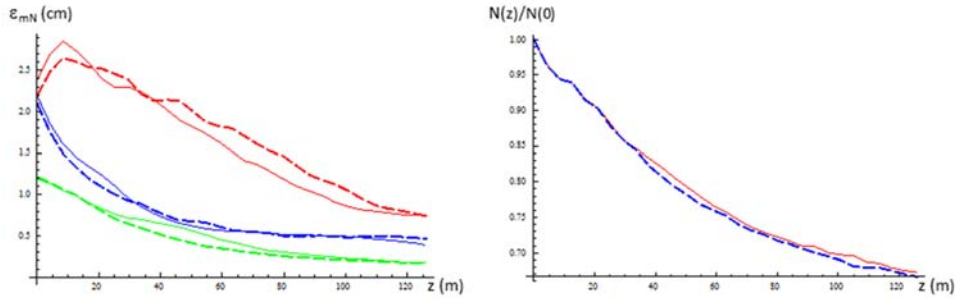

Figure 5: Normal mode emittances (left) and beam core intensity (right) for μ^+ (solid lines) and μ^- (dashed lines) along the HFOFO channel.

2.5.2.6 *Outlook*

In the present HFOFO snake design the solenoid inclination was chosen as the source of the transverse dipole field. It would be more practical however to use separate independently powered coils for this purpose.

The 6D emittance can be further reduced by a factor of ~5 by scaling down the length of all elements and increasing the solenoid current to keep the transverse tunes intact.

A more significant emittance reduction can be achieved with higher betatron phase advance per focusing unit (solenoid plus adjacent gap) than $\varphi = 74°$ in the present design. This will reduce the β-function at the minima reached between solenoids for $\varphi < 180°$ and at the solenoid centers for $\varphi > 180°$. To fully benefit from such reduction

the absorbers should be localized at the β-function minima making it necessary to use vacuum RF or – after merge when there is only one bunch per beam – pulsed radial lines.

2.5.2.7 *References*

1. Y. Alexahin, Helical FOFO snake for 6D ionization cooling of muons, AIP Conf. Proc. 1222 (2010) 313-318.
2. A. Burov, Y. Derbenev, S. Nagaitsev, Phys.Rev E66, 016503 (2002).
3. K. Yonehara, Design and Study of Helical Cooling Channel, this issue.
4. D. Neuffer, C.Yoshikawa, Use of 325 MHz RF in the Front End, MAP-doc-4355, FNAL 3013.
5. T. Roberts, http://g4beamline.muonsinc.com.
6. Y. Alexahin, Computing Eigen-Emittances from Tracking Data, MAP-doc-4358, FNAL 2013.

2.5.3 Six-Dimensional Ionization Cooling for Muon Accelerators with Vacuum RF Technology

Diktys Stratakis, Brookhaven National Laboratory, Upton, NY 11973, USA
Mail to: diktys@bnl.gov

2.5.3.1 *Introduction*

Over the years e^+e^- and $\mu^-\mu^+$ colliders have been proposed as possible candidates for a multi-TeV lepton collider. However, a relativistic particle undergoing centripetal acceleration radiates at a rate proportional to the fourth power of the Lorentz factor [1]. This poses a challenge for multi-TeV e^+e^- colliders, which cannot be circular but must have a linear geometry and, with practical acceleration schemes, be tens of km long. Furthermore, beam-beam effects at the collision point induce the electrons and positrons to radiate, which broadens the colliding beam energy distributions. On the other hand, the relative immunity of muons to synchrotron radiation due to their large rest mass (m_μ=105.7 MeV/c^2) suggests that they might be used in place of electrons in accelerators for high-energy physics experiments.

A key technical challenge in the development of a Muon Collider is that the phase space of the beam that comes from pion decay greatly exceeds the acceptance of downstream accelerator systems and therefore, a cooling channel is required. Given the short lifetime of a muon particle, ionization cooling is the only practical method that can be realized [2, 3].

Ionization cooling is achieved by reducing the beam momentum through ionization energy loss in discrete absorbers and replenishing the momentum loss only in the longitudinal direction through vacuum RF cavities. This mechanism can effectively reduce the transverse phase space of beam in the same way as radiation damping does to an electron beam. However this mechanism does not effectively cool the longitudinal momentum spread because the energy-loss rate is not sensitive to beam momentum except for very low-energy muons. To obtain longitudinal cooling, dispersion must be introduced to spatially separate muons of different longitudinal momenta, and wedged absorbers are used to reduce the momentum spread. Such a longitudinal cooling scheme is called “emittance exchange” [4] because the longitudinal cooling is achieved at the expense of transverse heating or a reduced transverse cooling rate.

Typical 6D cooling requirements for a Muon Collider [5] demand a reduction of the 6-Dimensional emittance by almost six orders of magnitude. This cooling is achieved in a series of cooling cells. Each cell consists of solenoids for focusing, weak dipoles to generate bending and dispersion, wedge-shaped absorbers where cooling takes place and vacuum RF cavities to replenish the energy lost in the absorbers. Examples of those different channels will now be discussed in more detail.

2.5.3.2 *Alternative 6D Cooling Lattices with Vacuum RF*

Three different geometries, using the same basic concept, have been proposed. In each case, the solenoids are slightly tilted to generate upward dipole fields. In the first as shown in Fig. 1(a), the lattice is bent into a circle, with the curvature corresponding to that generated by the dipole components [6]. The ring consists of a series of identical cells with two or four solenoids in each cell with opposite polarity to provide transverse focusing. The coils (yellow) are not evenly spaced; those on either side of the absorber are closer together in order to increase the focusing at the wedge absorber (magenta) and thus minimizing the beta function at that location. The relative amount of cooling can be adjusted by changing the opening angle and transverse location of the wedge. A series of RF cavities (dark red) are used to restore the momentum along the longitudinal axis. The dispersion necessary for emittance exchange is provided from the bend field generated by tilting the axes of the solenoids above and below the orbital midplane. Simulations have shown that suitable sequence of such rings, with multiple stages using different cell lengths, fields, and RF, can provide an impressive two orders of magnitude reduction of the normalized phase-space volume with a transmission above 50% [7,8]. However, injection into or extraction from such rings would be very challenging.

In the second case, represented in Fig. 1(b), the cooling cells are set on a gently upward or downward helix (as in the New York Guggenheim Museum and commonly referred to by that name). Simulations [9, 10] have shown that their performance is almost exactly the same as that of rings of the same approximate bending radii. This case would appear to be practical for the early stages of 6D cooling, but would be increasingly difficult as the radii get smaller in the later stages. An added complication is that stray fields from one pitch can influence those before and after, and must be shielded or allowed for.

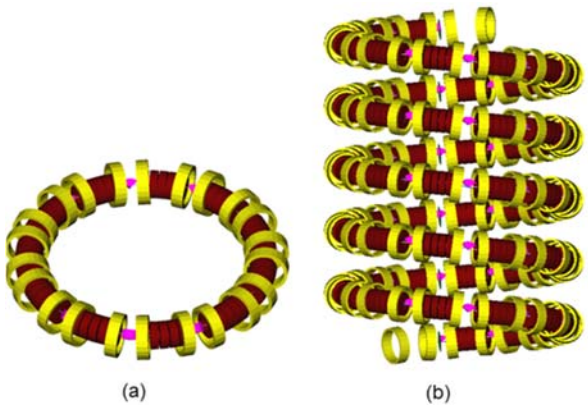

Figure 1: (a) Schematic layout of an idealized cooling ring; (b) 5 turn slice of a helix.

In the third case [11], as represented in Fig. 2, essentially the same cells from a ring or Guggenheim, including their coil tilts and resulting upward dipole fields, are laid out in straight (rectilinear) geometry. The solenoid focusing is so strong, compared with the dipole deflections that the closed orbits are merely displaced latterly, but continue down the now straight lattice. Most importantly, the performance [12] is essentially the same as with rings or a helix, but with greatly simplifying engineering. Therefore, this will be considered our baseline cooling lattice and will be analyzed in more detail in the next section.

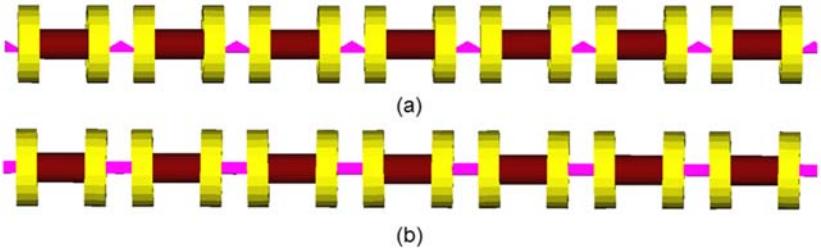

Figure 2: Conceptual design of a rectilinear channel: (a) top view; (b) side view. The large yellow cylinders are solenoids, the small red cylinders are the active volume of the RF cavities, and the magenta wedges are absorbers.

2.5.3.3 *Rectilinear Cooling Channel for a Muon Collider*

2.5.3.3.1 Lattice Design

A complete scheme for cooling a muon beam sufficiently for use in a Muon Collider has been previously described [13]. This scheme uses separate 6D ionization cooling channels for the two signs of the particle charge. In each, a channel first reduces the emittance of a train of muon bunches until they can be injected into a bunch-merging system. The single muon bunches, one of each sign, are then sent through a second 6D cooling channel where the transverse emittance is reduced as much as possible and the longitudinal emittance is cooled to a value below that needed for the collider. The beam can then be recombined and sent though a final cooling channel using high-field solenoids that cools the transverse emittance to the required value of the collider while allowing the longitudinal emittance to grow. This paper will review the design and

performance of a 6D rectilinear cooling channel for a single muon bunch after it exits the bunch merger system.

In order to improve cooling efficiency, our 6D cooling channel is tapered according to the procedure described in previous studies [10]. In this scheme, parameters such as cell length, focusing strength progressively change from stage to stage based on the emittance reduction rate and transmission. At the first stage of the channel the focusing will be relatively weak to avoid excessive angular divergence that can arise from the large transverse emittance of the initial muon beam. However, the weak focusing implies that the beta function and thus the equilibrium emittance are also relatively large, so the transverse cooling weakens as the limit is approached. To avoid this, this stage is terminated and we couple into the next stage that has a lower beta. This is achieved by simultaneously scaling down the cell dimensions and raising the strength of the on-axis solenoidal field. As a result this will produce a piecewise constant multi-stage channel where each stage will be a fixed-parameter straight channel consisting of a series of identical cells similar to the one shown in Fig. 2. As we will demonstrate later, eight tapered stages are enough to cool towards the baseline requirements of a Muon Collider. The required lattice parameters are summarized in more detail in Table 1.

Figure 3(a) shows the side view of one cell at an early stage of the channel (Stage 1). This stage consists of a sequence of 20 identical 2.75 m cells, each containing four 0.25 m-long 325 MHz pillbox cavities, and a wedge-shaped liquid hydrogen (LH) absorber, with an 120 deg. opening angle. Moreover, each cell contains two solenoid coils of opposite polarity, yielding an approximate sinusoidal variation of the magnetic field in the channel with a peak on axis value of 2.6 T and providing transverse focusing with a peak beta value of ~40 cm. The tilt of solenoids is adjusted to provide a mean bending field in order to provide adequate emittance exchange. Notice from Fig. 3(c) that the lattice transmits in a wide momentum band, namely from 148 to 235 MeV/*c,* with a central momentum of 195 MeV/*c.* Figure 3(d) displays the beta as a function of position along the cell at central momentum. One can see from Fig. 3 that the absorber is positioned at a position where the transverse beta becomes minimum. Since the lattice equilibrium emittance is proportional to the beta function, placing the absorber on that location would enhance (at least in theory) the cooling rate compared to any other location in the cell.

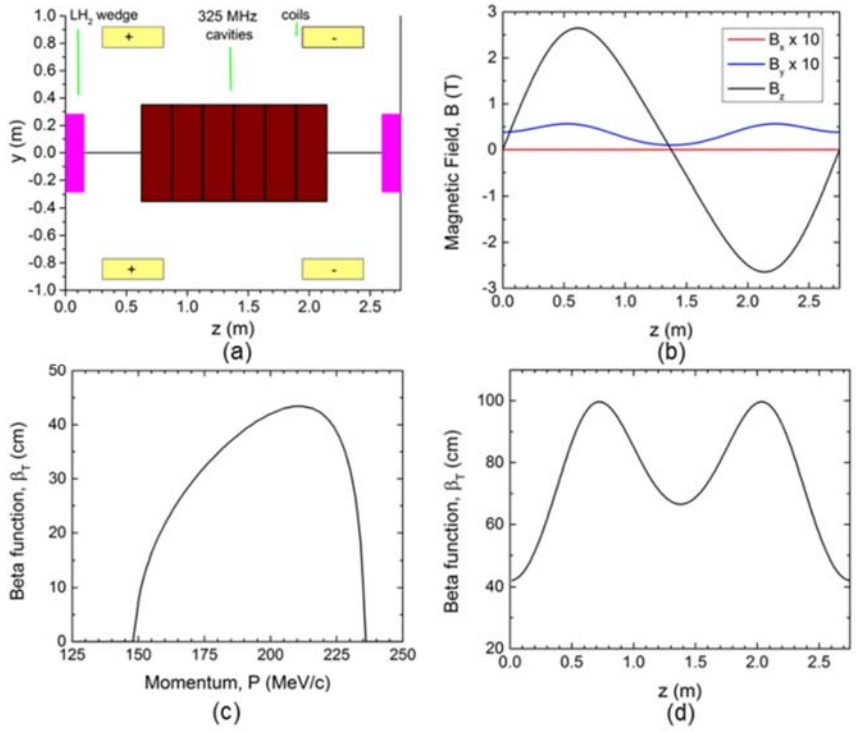

Figure 3: (a) Side view of one cell of Stage 1; (b) magnetic field on axis along the cell; (c) beta function at the absorber center vs. momentum, and (d) beta function vs position at 200 MeV/c.

Figure 4(a) shows a cell for a later stage (Stage 6) that is appropriate to cool to < 0.6 mm normalized rms transverse emittances. To achieve this, we design a lattice cell with a considerably smaller betatron function, β_T and thus equilibrium emittance. Therefore, we place the coils closer to the axis and reduce the lattice period, L, to 0.806 m ($\beta_T \propto L$). Moreover, we scale up the magnetic field to increase the muon focusing at the absorber. Stage 6 consists of 77 identical cells, each containing four 12 cm-long 650 MHz pillbox cavities and wedge-shaped lithium hydride (LIH) absorbers to produce the energy loss. Figure 4(b) displays the on-axis horizontal, vertical and longitudinal (axial) fields along the cell. The peak magnitude is 10.8 T on-axis and 14.1 T in the coil. Figure 4(c) shows that the lattice transmits particles in the momentum band 160-227 MeV/c with a central momentum near 195 MeV/c. Figure 4(d) illustrates the beta function at the reference (central) momentum as a function of the axial position in the cell.

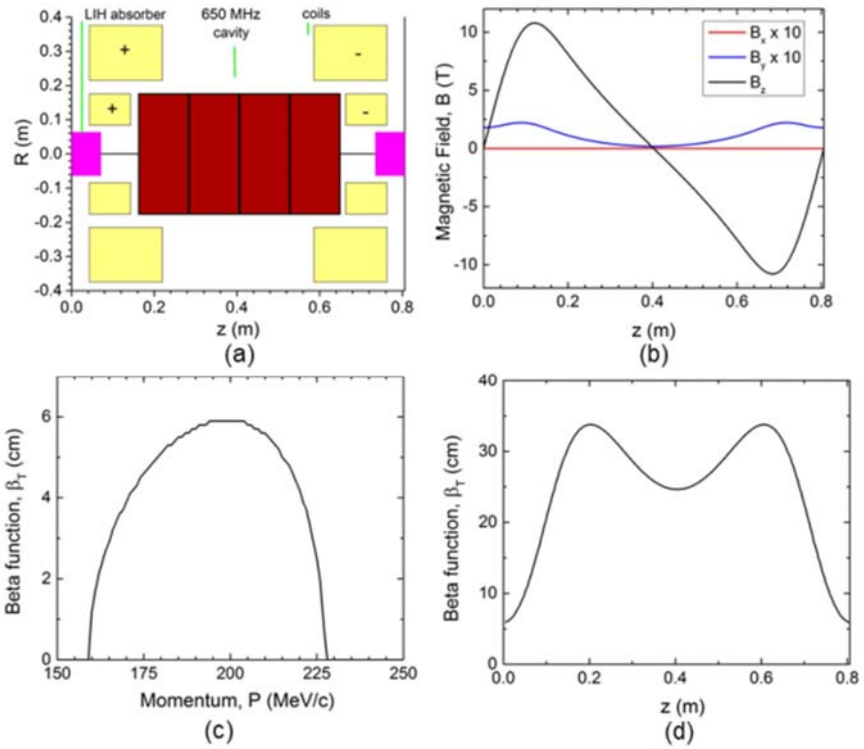

Figure 4: (a) Side view of one cell of Stage 6; (b) magnetic field on axis along the cell; (c) beta function at the absorber center vs. momentum, and (d) beta function vs position at the reference momentum.

Table 1: Main lattice parameters of a 6D cooling lattice with vacuum RF cavities for a Muon Collider. The first four stages use LH and the last four use LiH absorber.

Stage	*Cell Length [m]*	*Cell No.*	*Total Length [m]*	*Pipe Radius [cm]*	*RF Freq. [MHz]*	*RF Vol. [MV/m]*	*RF No.*	*Coil Tilt [deg.]*	*Wedge Angle [deg.]*
1	2.750	20	55.00	28.0	325	19.0	6	0.90	120
2	2.000	32	64.00	24.0	325	19.5	5	1.30	117
3	1.500	54	81.00	18.0	325	21.0	4	1.10	113
4	1.270	50	63.50	14.0	325	22.5	3	1.10	124
5	0.806	91	73.35	9.0	650	27.0	4	0.66	61
6	0.806	77	62.06	7.2	650	28.5	4	0.70	90
7	0.806	50	40.30	4.9	650	26.0	4	0.80	90
8	0.806	61	49.16	4.5	650	28.0	4	0.80	120

2.5.3.3.2 Tracking Studies

The performance of the cooling channel was simulated using the ICOOL code [14]. The code includes all relevant physical processes (e.g. energy loss, straggling, multiple scattering) and includes muon decay. We tracked 100,000 particles and included decay of muons. The transverse and longitudinal emittances and the transmission are shown as function of distance in Fig. 5. It is worth noting that after a distance of 490 m (8 Stages) the 6D emittance has fallen by a factor of 1000 with a transmission of 40%. In addition, at the end of the channel the transverse emittance decreased by a factor of ~18,

while the longitudinal emittance shrank by a factor of ~6. By carefully examining the results in Fig. 5 the following points are noteworthy. First, earlier simulations [15] revealed severe particle loss and emittance growth due to space-charge if the longitudinal emittance approaches the limit of 1.5 mm. Thus, to assure satisfactory cooling with minimum losses we choose to cool longitudinally only down to 1.5 mm. Second, the simulated results show good agreement with theoretical predictions [16] obtained by using partition functions and solving the fundamental cooling equations (black squares). The theory is published in more detail in Ref. 16. Finally, a transverse emittance $\varepsilon_T \leq 300$ μm is the baseline requirement for a Muon Collider after the final 6D cooling sequence. We can conclude from the results in Fig. 5 that 8 stages are enough to fulfill this requirement since the simulation produced a final transverse emittance of 280 μm.

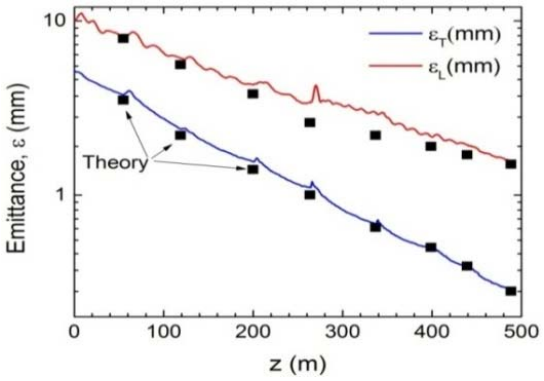

Figure 5: Evolution of the normalized rms emittances as function of distance. The black squares correspond to theoretical predictions based on Ref. 16.

2.5.3.3.3 Technology Challenges

2.5.3.3.3.1 Cavities in Magnetic Fields

Experimental [17] and numerical [18] studies have indicated that the vacuum RF gradient may be limited by the magnetic field, and it is uncertain whether the gradients specified for the cooling sections can be achieved. Results from recent experiments [19] using a cavity filled with high-pressure hydrogen gas, showed no degradation in the maximum gradient within a 3 T field [19]. Therefore, one promising solution is a hybrid approach that uses relatively low pressure gas (34 atm at room temperature) to avoid cavity breakdown, along with discrete LIH absorbers to provide the majority of energy loss. Recent simulations [20] revealed that a hybrid rectilinear channel with gas filled cavities maintains a transmission and cooling performance comparable to the conventional vacuum RF based channel. This result, in combination with the experimental studies that demonstrated that a high-pressure gas-filled cavity can operate in a multi-tesla field without degradation, suggests that the hybrid concept can be a promising cooling approach for muon based applications.

2.5.3.3.3.2 Magnet Requirements

Another challenge on any practical magnetic configuration is that the operating current in a superconducting magnet must be smaller than the critical current corresponding to the peak field in the coil. Figure 6 shows the current densities vs. the maximum local fields in the coils used. For these estimates we have used published [21]

'engineering' current densities, multiplied by factors to allow for the required support structure, the need for stabilizing copper, and the filling factor for a real conductor. The red line illustrates the current density of the coil at the peak field location for each cooling stage. Note from Fig. 6 that there is a relatively rapid increase of the magnet operating current with stage number. This is a direct consequence of the low β_T lattice design that is needed to cool towards micron scale emittances. Our findings indicate that even with inclusion of reasonable safety factors, the needed fields are consistent with the critical limits of existing conductor technology. However, the last four stages are barely within the limits of Nb_3Sn and therefore it is critically important to the development of a Muon Collider that a well thought-out test program to be continued. Most challenging is the last stage where the solenoids are expected to deliver 15 T in a bore of 4.5 cm. A detailed feasibility study for this last stage can be found in Ref. 22. The analysis highlighted that for stable operation a 1.9 K operating temperature is preferred.

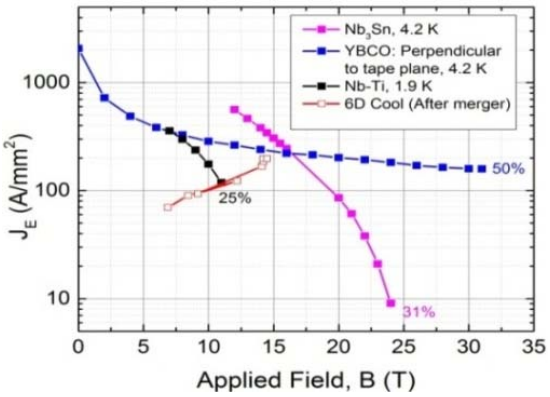

Figure 6: Engineering current densities vs applied magnetic fields for different conductors from published data [21]. The red dots indicate the required fields of a 6D cooling channel to achieve the micron-scale emittances needed for a Muon Collider.

2.5.3.4 ***Summary***

For a Muon Collider the 6-Dimensional muon beam phase space volume must be reduced by several orders of magnitude in order to be able to further accelerate it. Ionization cooling is the only feasible option for cooling the beam within the short muon lifetime (τ_0=2.2 μs). We described a fast cooling technique that simultaneously reduces all six phase-space dimensions of a charged particle beam. We showed that such cooling can be achieved in a channel that consists of periodically inclined solenoids of alternating polarity, dense absorbers placed inside the solenoids and RF cavities between them. We showed that relatively modest magnetic fields ($B \leq 15$ T, peak on axis) and a small number of different frequencies, namely 325 and 650 MHz, are enough to cool towards a micron scale emittance, which is the baseline cooling requirement of a Muon Collider. Results from numerical simulations show that an ionization cooling channel based on vacuum RF technology can result to a notable reduction of the 6D emittance by 6 orders of magnitude. Finally, our findings indicate that even with inclusion of reasonable safety factors, the needed fields are consistent with the critical limits of existing conductor technology. However, the last four stages

are barely within the limits of Nb_3Sn and therefore it is critically important to the development of a Muon Collider that a well thought-out test program to be continued.

2.5.3.5 *Acknowledgements*

The authors are grateful to V. I. Balbekov, Y. Bao, J. S. Berg, F. Borgnolutti, D. Bowring, D. Grote, D. Li, T. Luo, D. Neuffer, R. B. Palmer, S. Prestemon, R. Ryne, H. K. Sayed, P. Snopok, and H. Witte for many useful discussions. This work is supported by the U.S. Department of Energy, Contract no. DE-AC02-98CH10886.

2.5.3.6 *References*

1. J. D. Jackson, *Classical Electrodynamics*, 3rd Edition. (Wiley, New York 1999).
2. Yu M. Ad and V. I. Balbekov, Sov. Atomic Energy **31**, 731 (1971).
3. A. N. Skrinsky and V. V. Prkhomchuk, Sov. J. Part. Nucl. **12**, 223 (1981).
4. D. Neuffer, Part Accel. **14**, 75 (1983).
5. R. B. Palmer. J. S. Berg, R. C. Fernow et al, Proceedings of the 2007 Particle Accelerator Conference, Albuquerque, NM, p. 1222 (2007).
6. V. Balbekov, Proceedings of the 2003 Particle Accelerator Conference, Portland, OR, p. 2017 (2003).
7. R. B. Palmer, V. Balbekov, J. S. Berg et al., Phys. Rev. ST Accel. Beams **8**, 061003 (2005).
8. R. C. Fernow, and R. B. Palmer, Proc. of PAC 2011, New York, NY, USA, p. 106 (2011).
9. P. Snopok and G. Hanson, IJMPA 24, p. 987 (2009).
10. D. Stratakis, R. C. Fernow, J. S. Berg, and R. B. Palmer, Phys. Rev. ST Accel. Beams **16**, 091001 (2013).
11. V. Balbekov, MAP Document No. 4365 (2013).
12. D. Stratakis, J. S. Berg, R. B. Palmer, and V. I. Balbekov, Proc. of PAC2013, Pasadena, CA, USA p. 1328 (2013).
13. D. Stratakis et al. Proceedings of 2014 International Particle Accelerator Conference, Dresden, Germany, TPME021 (2014).
14. R. C. Fernow, Proceedings of the 2005 Particle Accelerator Conference, Knoxville, TN, p. 2651 (2005).
15. D. Stratakis, R. C. Fernow, and R. B. Palmer, Proceedings of the 2013 IPAC Conference, Shanghai, China, TUPFI087 (2013).
16. D. Stratakis and D. Neuffer, Proceedings of 2014 International Particle Accelerator Conference, Dresden, Germany, TUPME021 (2014).
17. A. Moretti, Z. Qian, J. Norem, Y. Torun, D. Li, M. Zisman, *Phys. Rev. ST. Accel. Beams* **8,** 072001 (2005).
18. R. B. Palmer, R. C. Fernow, J. C. Gallardo, D. Stratakis, and D. Li, *Phys. Rev. ST. Accel.Beams* **12,** 031002 (2009).
19. M. Chung, M. G. Collura, G. Flanagan et al., Phys. Rev. Lett. **111**, 184802 (2013).
20. D. Stratakis and D. Neuffer, Proceedings of 2014 International Particle Accelerator Conference, Dresden, Germany, TUPME024 (2014)
21. URL: http://fs.magnet.fsu.edu/~lee/plot/plot.htm
22. H. Witte, D. Stratakis, J. S. Berg, F. Borgnolutti, Proceedings of 2014 International Particle Accelerator Conference, Dresden, Germany, WEPRI103 (2014).

2.5.4 Design and Study of Helical Cooling Channel

K. Yonehara, Fermilab, Batavia, Illinois, USA
Mail to: yonehara@fnal.gov

2.5.4.1 *Overview of Helical Cooling Channel*

A homogeneous ionization absorber filled helical cooling channel (HCC) has been proposed [1]. The primary magnetic components in the HCC are the solenoid and counteracting helical dipole to define the reference trajectory and the helical dipole gradient that controls the dispersion and provides transverse stability. Figure 1 shows the reference orbit (red line) and beam envelope (blue line ensemble) of off-reference particles in a channel comprised of HCC magnetic field components. The envelope shows the coupled transverse and longitudinal oscillations around the reference orbit. An implementation of a helical dipole magnet is the "Siberian Snake" that has been used to manipulate the spin of polarized particles.

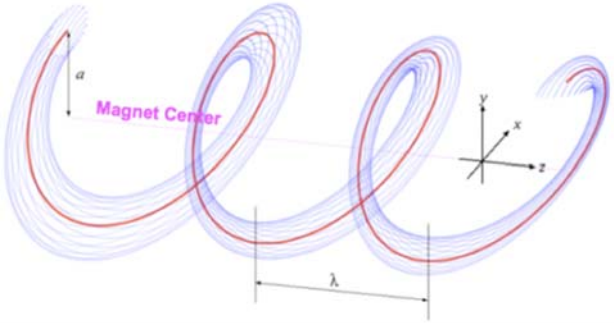

Figure 1: Typical beam path in a HCC.

High Pressure hydrogen gas filled RF (HPRF) cavities are another key element in the HCC. RF cavities are placed continuously along with the helical beam path in the HCC magnet. High-pressure hydrogen in the cavity acts as a homogeneous ionization absorber. Gaseous hydrogen is the best ionization absorber because of its long radiation length and large energy loss rate, together resulting in a low equilibrium emittance. The high-pressure gas serves a second purpose in reducing the probability of electric breakdown in the RF cavity and allowing higher operating E fields in strong magnetic fields. In the case of a vacuum RF cavity, the probability of breakdown is amplified by the external magnetic field [2]. One of breakdown mechanisms shows that the intensity of dark current beam is enhanced by focusing of the external magnetic field [3]. On the other hand, the dark current in the gas-filled RF cavity is insensitive to the external magnetic field since the dark current beam is diffused immediately via the Coulomb interaction with the gas (Paschen's law). The breakdown suppression model has been experimentally verified and no RF degradation due to the external magnetic field has been observed (see Figure 2) [4].

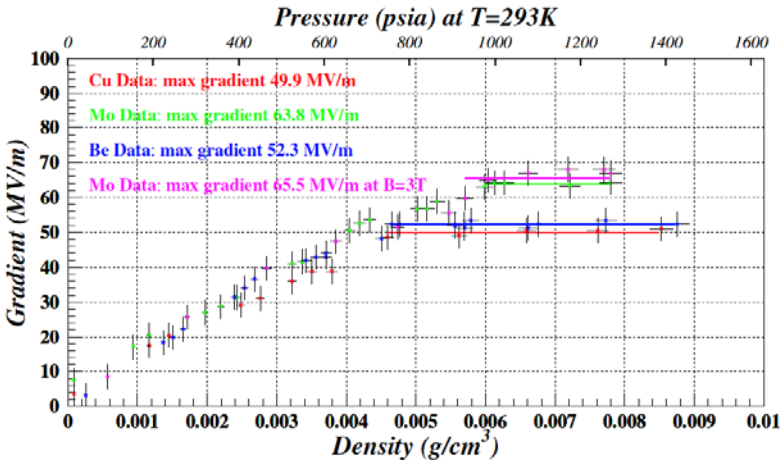

Figure 2: Maximum surface gradient in the HPRF test cell as a function of hydrogen gas density with various electrode materials. The maximum gradient is determined by Paschen's law at low gas pressure region while it is saturated in high pressure region. The observed gradient is ≥ 50 MV/m that is well above the requirement in the cooling channel. The plateau is strongly dependent on the electrode material although the mechanism is not yet understood.

Since the HCC does not adhere to conventional beam optics, we'll note its special properties:

- **Large momentum acceptance:** The optics of the HCC is continuous. Therefore, there is no betatron tune resonance; the momentum acceptance is determined by either the dynamic aperture or the admittance. This is an especially important in designing the initial cooling stage.
- **Cost effective compact channel:** Since all ionization cooling processes, including with the RF acceleration and the emittance exchange, take place simultaneously in the HPRF cavity, the HCC can be the shortest design for a 6D ionization cooling channel. Note that a shorter channel simultaneously reduces costs and muon decay losses, resulting in increased performance per unit cost.
- **Required novel beam element:** The HCC involves several novel technologies. One of the most challenging issues is to incorporate the HCC cavity system into the compact helical magnet and geometry constraints limit its cooling performance. Understanding the limits and addressing them make up a major scope of effort in designing the HCC and evaluating its performance via simulations.

First, the concept of the HCC will be discussed. Then, the present progress of design and study of the HCC based on the above concerns will be shown.

2.5.4.2 *Basic Beam Dynamics in HCC*

2.5.4.2.1 Design Reference Orbit and Dispersion

The reference particle is acted upon by two counteracting Lorentz forces in the radial direction,

$$\dot{p}_r = \frac{p_\phi^2}{m_\mu r} = \frac{e}{m_\mu}\left(p_\phi B_z - p_z b\right), \tag{1}$$

where B_z and b are the z and helical dipole components of the magnetic field, respectively. κ is defined as the helical pitch, $\kappa = p_\phi/p_z$. Noting that the reference particle has no radial motion, the reference momentum is $p = \sqrt{p_\phi^2 + p_z^2}$ and eq. (1) can be transformed into,

$$p(a) = \frac{\sqrt{1+\kappa^2}}{k}\left(B - \frac{1+\kappa^2}{\kappa}b\right), \tag{2}$$

where a is the radius of reference orbit. κ is also given from the geometric condition, $\kappa = 2\pi a/\lambda = ka$ where λ is the helical period. A helical conductor produces the solenoid component as well as the dipole one. Thus, B_z represents two components, $B - \kappa b$ where B is provided from a pure solenoid magnet and κb is generated by the helical conductor. The dispersion factor, $(da/a)/(dp/p)$, can be derived upon differentiation of eq. (2) with respect to a,

$$\widehat{D}^{-1} = \frac{\kappa^2 + (1-\kappa^2)q}{1+\kappa^2} + g, \tag{3}$$

$$g = -\frac{(1+\kappa^2)^{3/2}}{pk^2}\frac{\partial b}{\partial a}, \tag{4}$$

where $\partial b/\partial a = b'$ is the helical field gradient and g is a field index. q represents a coupling strength between horizontal and vertical motions in the helical coordinate system. The explicit form for q will be given in later section.

2.5.4.2.2 Transverse Motion and Transverse Beta Function

The transverse beam motion in the HCC is extracted in the linear approximation [1]. The betatron tune and related equations are given,

$$Q_\pm^2 = R \pm \sqrt{R^2 - G}, \tag{5}$$

$$R = \frac{1}{2}\left(1 + \frac{q^2}{1+\kappa^2}\right), \tag{6}$$

$$G = \left(\frac{2q+\kappa^2}{1+\kappa^2} - \widehat{D}^{-1}\right)\widehat{D}^{-1}, \tag{7}$$

where $Q_\pm$ are two eigenvalues in the helical coordinate system. The general solution of particle motion is the sum of these eigenmodes. The beam stability condition, $0 < G < R^2$ is derived from eq. (5). The transverse beta functions are,

$$\beta_\pm = \frac{1}{kQ_\pm} = \frac{\lambda}{2\pi Q_\pm}. \tag{8}$$

2.5.4.2.3 Longitudinal Motion and Longitudinal Beta Function

The admittance of HCC is,

$$(I_s)_{adm} = \frac{2}{\pi\omega}\sqrt{\frac{\gamma'_{max}}{\eta\omega}}, \tag{9}$$

where ω is the RF resonant frequency and γ'_{max} is the maximum energy deviation of the beam in the HCC. η is the momentum slip factor,

$$\eta = \frac{d}{d\gamma}\frac{\sqrt{1+\kappa^2}}{\beta} = \frac{\sqrt{1+\kappa^2}}{\gamma\beta^3}\left(\frac{\kappa^2}{1+\kappa^2}\widehat{D} - \frac{1}{\gamma^2}\right). \quad (10)$$

It is worth noting that η is positive in this cooling scheme. Thus, the phase slip in the HCC is above transition. The longitudinal beta function is,

$$\beta_L = \frac{1}{\omega Q_L} = \sqrt{\frac{m_\mu c}{\eta\omega e V'}}\frac{1+sin\,(\phi_s)}{1-sin\,(\phi_s)}, \quad (11)$$

where V' is the peak RF gradient and ϕ_s is the synchrotron phase.

2.5.4.2.4 Emittance Evolution

Emittance evolution in the ionization cooling channel is,

$$\varepsilon_{T(L)}(z) = (\varepsilon_{T(L),0} - \varepsilon_{T(L),eq})e^{-\Lambda_{T(L)}z} + \varepsilon_{T(L),eq}, \quad (12)$$

where $\Lambda_{T(L)}$, $\varepsilon_{T(L),0}$, and $\varepsilon_{T(L),eq}$ are the cooling decrements and the normalized initial and equilibrium emittances in transverse (longitudinal) phase space, respectively. The HCC theory predicts the cooling decrement [1],

$$\frac{\Lambda_+ + \Lambda_-}{\Lambda_0} = 2 - \frac{\kappa^2}{1+\kappa^2}\widehat{D}, \quad (13)$$

$$\frac{\Lambda_+ - \Lambda_-}{\Lambda_0} = \frac{1}{\sqrt{R^2 - G}}\left(q^2 - 1 + \kappa^2\left(R\widehat{D} - 1\right)\right)\frac{1}{1+\kappa^2}, \quad (14)$$

$$\Lambda_+ + \Lambda_- + \Lambda_L = 2\Lambda_0\left(\beta^2 + \frac{1-(\beta/\gamma)^2}{\log}\right) \equiv \Lambda, \quad (15)$$

$$\Lambda_0 = \frac{F}{\gamma\beta^2 m_\mu}, \quad (16)$$

where Λ_+ and Λ_- are the cooling decrements in the two transverse eigenmodes in the helical coordinate system. F is the drag force due to the ionization energy loss process; for a muon beam, $F = -dE/dz = K(Z/A)/\beta^2\log$, where Z and A are the atomic number and atomic mass of absorber and $K = 0.307075$ MeV/g cm^2. log is the Coulomb logarithm of ionization energy loss for fast particles,

$$\log \equiv \ln\left(\frac{2p^2}{h\nu m_\mu}\right) - \beta^2, \quad (17)$$

where $h\nu$ is the effective ionization potential. The HCC theory also predicts $\varepsilon_{T,eq}$ and $\varepsilon_{L,eq}$,

$$\varepsilon_{L,eq} = \frac{\Lambda}{4\Lambda_L}\frac{m_e}{m_\mu}\gamma\beta^2\left(\eta\beta_L\frac{\gamma^2+1}{2\log} + \frac{(Z+1)}{\gamma^2\beta^6}\frac{\widehat{D}^2}{\beta_L\eta k^2}\frac{\kappa^2}{1+\kappa^2}\right), \quad (18)$$

$$\varepsilon_{T,eq} = \varepsilon_{+,eq} + \varepsilon_{-,eq}, \quad (19)$$

$$\varepsilon_{\pm,eq} = \frac{\Gamma_\pm\beta_\pm}{4}\frac{m_e}{m_\mu\beta}\frac{\Lambda/\Lambda_\pm}{(1+\kappa^2)^{5/2}}, \quad (20)$$

$$\Gamma_{\pm} = \frac{(Z+1)(\alpha_{\pm}^2 + (1+\kappa^2)^3 Q_{\pm}^2) + \kappa^2(\alpha_{\pm} - (1+\kappa^2)^{3/2})^2(\gamma^2+1)/2\log}{\alpha_{\pm}^2 + (1+\kappa^2)\widehat{D}^{-1}}, \quad (21)$$

$$\alpha_{\pm} = \frac{1+\kappa^2}{q-1}(Q_{\pm}^2 - \widehat{D}^{-1}). \quad (22)$$

The second term in the rhs of eq. (18) shows the effect of the multiple scattering process in the longitudinal phase space, and it is smaller than the first one. Therefore, eqs. (18) and (20) show that the equilibrium emittance is linearly dependent upon the beta function. $\Gamma_{\pm}$ also has the mixing term that is the effect of the energy straggling process in the transverse phase space shown as the first term in the rhs of eq. (21), which is smaller than the second one.

q can be determined by eq. (14) with the special condition $\Lambda_+ = \Lambda_-$,

$$q \to q(\widehat{D}) = \sqrt{\frac{1+\kappa^2 - 1/2\kappa^2\widehat{D}}{1+1/2\kappa^2\widehat{D}/(1+\kappa^2)}}. \quad (23)$$

In this case, Λ_T is equivalent to Λ_+ and Λ_-.

2.5.4.2.5 HCC Field Component

Once the dispersion is determined all HCC field components on the reference orbit are fixed,

$$B_z = pk\frac{1+q(\widehat{D})}{e\sqrt{1+\kappa^2}}, \quad (24)$$

$$b = \kappa B_z \frac{1-1/(1+q(\widehat{D}))}{1+\kappa^2}, \quad (25)$$

$$g = \widehat{D}^{-1} - \frac{\kappa^2 + (1-\kappa^2)q(\widehat{D})}{1+\kappa^2}, \quad (26)$$

$$\frac{\partial b}{\partial a} = b' = \frac{-egpk^2}{(1+\kappa^2)^{3/2}}. \quad (27)$$

2.5.4.3 ***Simulation Study of HCC***

2.5.4.3.1 Equal Cooling Decrements

The HCC theory was verified via a comparison with numerical simulation [5] using G4Beamline [6]. The initial design for the HCC utilized equal cooling decrements. This condition is realized with $\Lambda_+ = \Lambda_- = \Lambda_L = \Lambda/3$. The dispersion is given from eqs. (13)~(16).

$$\widehat{D} = \frac{2(1+\kappa^2)}{\kappa^2}\left(1 - \frac{2}{3}\left(\beta^2 + \frac{1-(\beta/\gamma)^2}{\log}\right)\right). \quad (28)$$

Figure 3 shows the first end-to-end cooling simulation with equal cooling decrements, which starts at the front-end channel. The design momentum is 209 MeV/c and $\kappa = 1$, hence the dispersion function is 1.88. There are 10 RF cavities per λ and each RF cavity has a 60 μm thick Be RF window. The window is shared by the adjacent

cavity. The hydrogen gas pressure is 160 atm at room temperature. The peak RF gradient is 20 MV/m. Therefore, the synchrotron phase is 155 degrees.

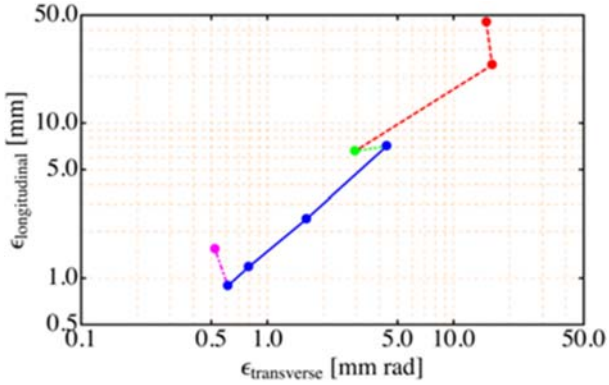

Figure 7: The blue line is the simulated emittance evolution of the HCC in G4Beamline run on NERSC [8]. The red line is the emittance evolution in the gas-filled helical FOFO 6D cooling channel [9]. The green and magenta lines are the emittance evolution in the matching-in and -out channels, respectively [10].

In order to design a large momentum acceptance at the beginning of the HCC, a long helical period channel with a low frequency RF are used to have a large dynamics aperture. The helical period becomes shorter and the RF frequency becomes higher as the beam is cooled in the HCC. One complete 6D cooling channel consists of four HCC sections in this design. Table 1 shows the parameter in each HCC section.

Table 1: Field parameters and beam emittances in the first end-to-end cooling simulation. *Tr.* is the transmission efficiency.

	λ	L	N	B_z	b	b'	$\varepsilon_{T,eq}$	$\varepsilon_{L,eq}$	$Tr.$
unit	m	m	MHz	T	T	T/m	mm rad	mm	
1	1.0	50	325	4.41	1.32	-0.32	3.44	6.82	0.94
2	0.8	70.4	325	5.52	1.65	-0.50	1.62	2.41	0.90
3	0.5	120	650	8.83	2.63	-1.28	0.79	1.18	0.81
4	0.4	77.2	975	11.04	3.29	-2.01	0.61	0.89	0.85
		317.6							0.58

The achieved equilibrium transverse and longitudinal emittances are 0.61 and 0.89 mm, respectively, while the predictions are 0.75 and 0.88 mm, respectively. It indicates that the equilibrium emittance in numerical simulation reaches to the theoretical limit. Stronger magnetic field is required to go lower equilibrium emittance. On the other hand, the total channel length is 320 m and the transmission efficiency is 58% while the predicted channel length from the analytic formula is 150 m. The dominant source of such a poor cooling efficiency is the phase space mismatching during transition between HCC sections. It is crucial to improve the transmission efficiency to reduce the beam loading effect in the RF cavity in the cooling channel. We demonstrated that the transmission efficiency is significantly improved by using a matching section between HCC sections [7]. The present design goal is a 250 m or shorter channel with the transmission efficiency 80% or higher.

2.5.4.3.2 Re-optimization of HCC

Since the prediction is quite accurate we use the analytic formula to optimize the beam optics [11]. It is crucial to generate strong focusing, b' to realize equal cooling decrements. However, it is an engineering challenge to make enough space to incorporate RF cavities into the magnet while keeping strong b' [12,13]. An alternate cooling scenario should be considered to mitigate the engineering issue. Figure 4 shows the predicted equilibrium transverse and longitudinal emittances as functions of B_z and b'. Indeed, these magnetic components are as a function of the dispersion factor. Larger $\widehat{D}$ (i.e. lower b') makes larger $\varepsilon_{T,eq}$ and smaller $\varepsilon_{L,eq}$ and vice versa. Besides, the overall 6D emittance, $\varepsilon_{6D,eq} \sim \varepsilon_{T,eq}^2 \varepsilon_{L,eq}$ is only determined by B_z. This suggests that smaller beam can be achieved with stronger B_z even if b' is small.

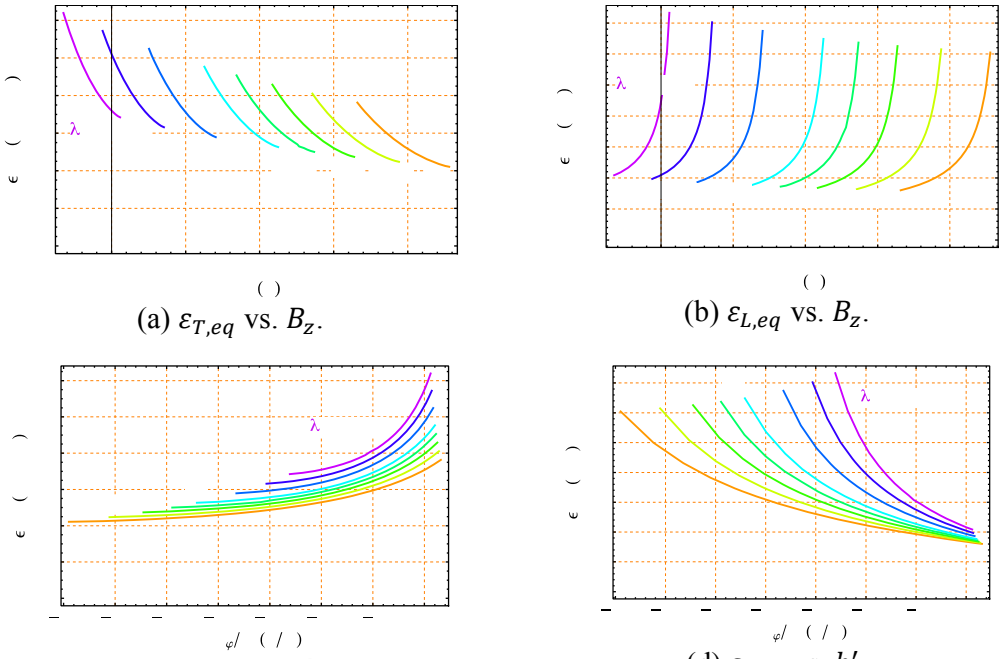

(a) $\varepsilon_{T,eq}$ vs. B_z. (b) $\varepsilon_{L,eq}$ vs. B_z.

(c) $\varepsilon_{T,eq}$ vs. b'. (d) $\varepsilon_{L,eq}$ vs. b'.

Figure 8: Estimated equilibrium emittance as functions of B_z and b' for various λ.

Figure 5 shows the proposed new emittance evolution in the HCC based on the above consideration. Because the momentum spread for the initial beam is very wide the initial HCC should start the same optics as the original one. Once the beam becomes small it is sent to the new HCC section. Since it has larger dispersion factor than the original one the longitudinal emittance of the beam is cooled dominantly. Besides, lower b' permits to generate higher B_z in the present HCC magnet technology. Therefore, it makes smaller ε_{6D} than the original one. The analytic formula predicts that the equilibrium transverse and longitudinal emittances in the HCC are 0.6 and 0.5 mm, respectively. The matching-out channel makes the reverse emittance exchange; the longitudinal emittance is exchanged to the transverse one. Therefore, the final emittances at the end of the matching out can be reached to 0.35 and 1.5 mm in transverse and longitudinal planes, respectively.

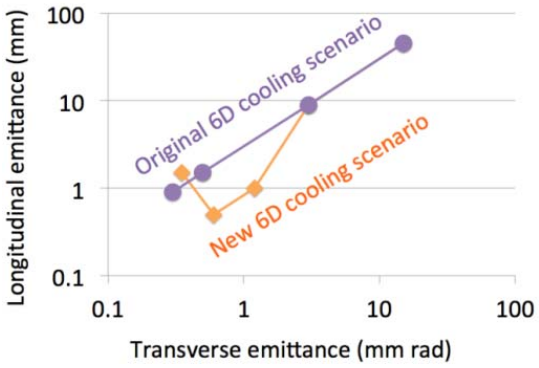

Figure 9: Proposed new emittance evolution.

2.5.4.4 *Machine Development*

One of the critical engineering issues is how to incorporate the HCC cavity system into the compact helical magnet without losing its cooling performance. Figure 6 is a conceptual drawing of an integrated HCC segment including the helical RF system and helical magnet system. A dielectric material is inserted into the HPRF cavity to make a compact cavity size. The helical magnetic field is generated using a helical solenoid coil. R&D of each beam line element will be discussed in the following section.

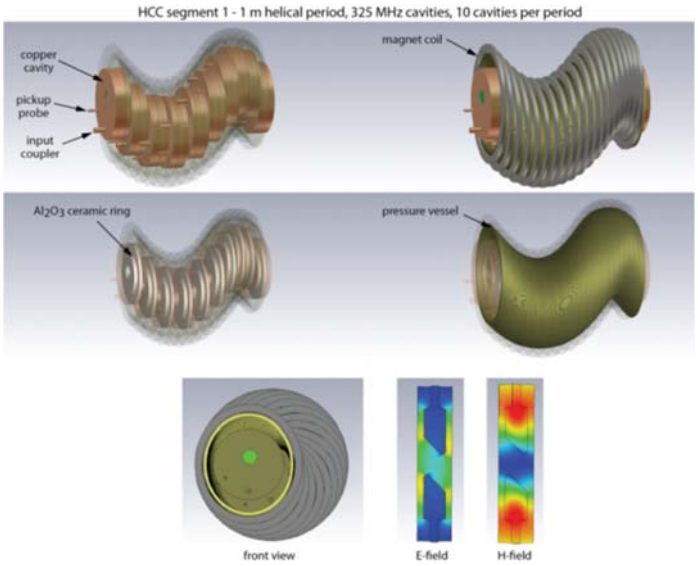

Figure 10: Conceptual design of the HCC.

2.5.4.4.1 Study of High-Pressure Gas-filled RF Cavity

When an intense beam traverses a dense gas filled RF cavity a large number of ion pairs are produced via the ionization process. Consequently, the stored RF energy is consumed by the ion pairs, which is called the plasma loading effect. A beam test has been done at the Mucool Test Area (MTA) at Fermilab in 2012. Figure 7 shows the observed plasma loading per single ion pair per one RF cycle [14]. Figure 7 verifies the simple gas-plasma model that ionization electrons are immediately thermalized by the neutral gas within one RF cycle. The plasma loading effect is lower at lower X_0 which

is the ratio between the peak RF gradient and gas pressure. However, the RF loading is still too large to be applicable for an ionization cooling channel.

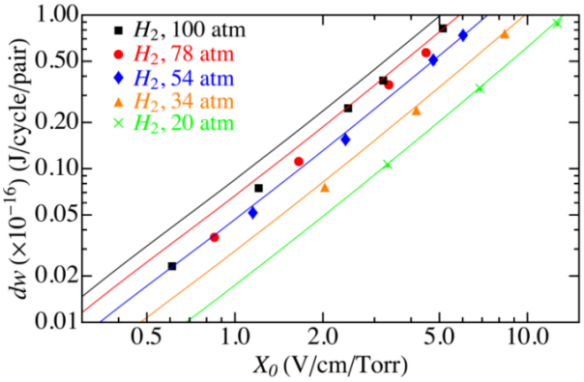

Figure 11: Observed plasma loading by single ion pair per one RF cycle. Point with various marks is the observed value. Solid line is the prediction.

A small amount of dry air, which contains oxygen, was doped in the cavity. Oxygen acts as an electronegative gas to capture ionization electrons in a very short time. Figure 8 shows the plasma loading with various concentrations of dry air. The plasma loading is 50 times lower than that in pure hydrogen.

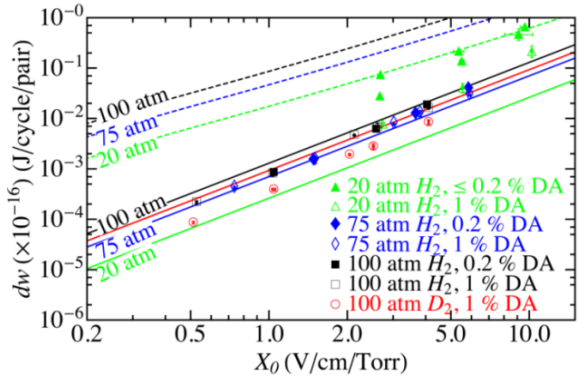

Figure 12: Observed plasma loading per single ion pair per one RF cycle with various concentrations of dry air. Points with various markers are the observed values. Solid lines are the predictions.

Figure 9 shows the estimated RF power consumption and RF voltage drop with the muon collider beam in a 650 MHz RF cavity. The voltage drops to 90% of the initial voltage after 20 bunches pass through the cavity. The plasma loading effect is two or three times lower than the beam loading [15]. Consequently, the beam loading effect is more severe issue than the plasma loading effect.

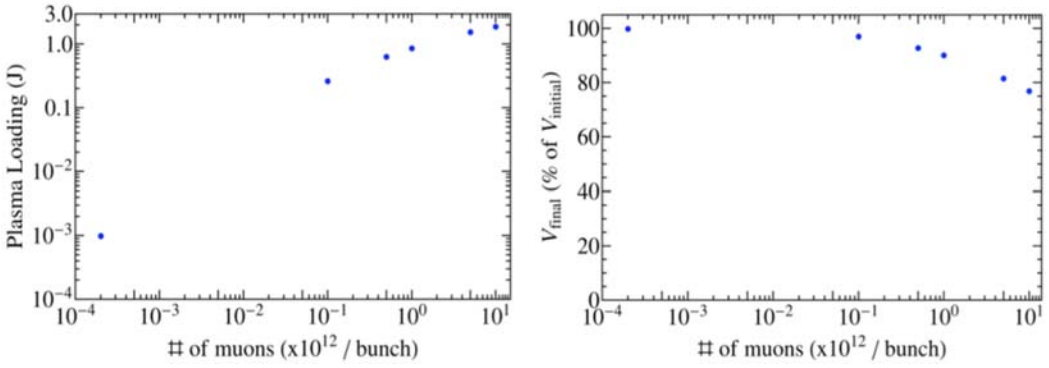

(a) RF power consumption **(b) RF voltage drop**

Figure 13: Estimated plasma loading effect in 650 MHz RF cavity with various beam intensities. The expected muon collider beam will be 10^{12} per bunch and 21 bunches.

Currently, a gas-plasma simulation is being developed to study the influence on intense muon beam. The original concern was collective effects, i.e. the wake field caused by the incident muon beam accelerating ionization electrons; hence they are not thermalized in a short time. Since the collision frequency is on the order of 10^{13}~10^{14} s^{-1} ionization electrons are thermalized even with the wake field [17]. Indeed, the wake field induces an attractive (repulsive) force on the ionization electrons and collects (repels) them into (from) the beam volume. As a result, the ionization electrons neutralize the beam charge. The residual azimuthal magnetic field focuses the incident muon beam. Figure 10 shows the plasma *Z* pinch in the incident muon beam at ideal beam condition in numerical simulation. Further study of the plasma lens effect is required [15].

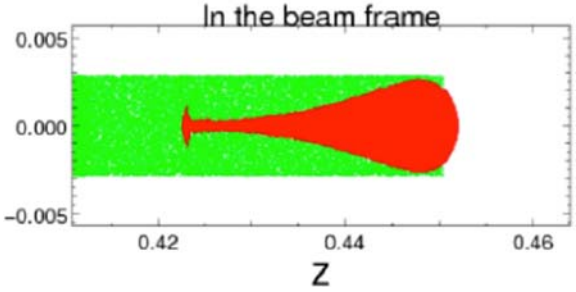

Figure 14: Simulating of beam dynamics in the gas-filled RF cavity. Red points are the incident beam and green ones are the ionization electrons. The front of the beam generates ion pairs and the back end is focused by the plasma lens effect.

2.5.4.4.2 Status of Dielectric Loaded Gas-filled RF Cavity Test

The concept of the dielectric loaded RF cavity has been proposed for a long time. However, the surface breakdown on a dielectric material was concerned in past since the secondary emission efficiency of a dielectric material is typically high. In case of the gas-filled RF cavity, the surface breakdown process can be terminated by the gas. The concept has been experimentally verified [16]. A new demonstration test is planed at the MTA to study how the gas avoids the charge-up process on the surface of dielectric material.

2.5.4.4.3 Design Helical Magnet

Initially, a helical dipole magnet was considered. However, we noticed that the beam occupies only a quarter of the magnetic field in the helical dipole conductor. A helical solenoid coil has been proposed to generate the required helical field in the beam area. Figure 11 shows a schematic drawing of the helical solenoid magnet. The helical solenoid coils are aligned along the helical beam path.

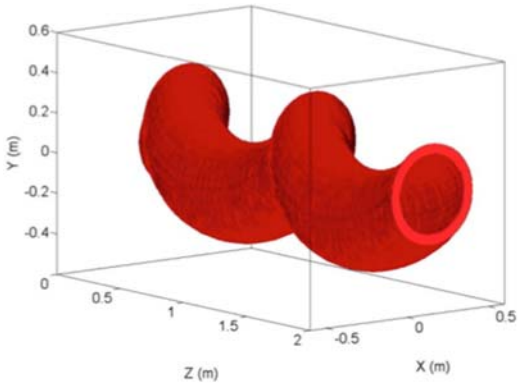

Figure 15: Schematic drawing of the helical solenoid magnet.

The helical dipole component and helical field gradient are generated by the stray field of adjacent coils. Therefore, b and b' are dependent on the geometry of the coil [12]. Figure 12 shows the geometry constraints of b and b', i.e. an inner coil diameter (*ID*), a radial thickness (*dR*), and the center of the coil (a). Several helical solenoid coils were made and the concept was experimentally verified. Specific helical field component can be enhanced by using an elliptic shape coil. Or, a titled coil is another option to generate the proper helical field [13].

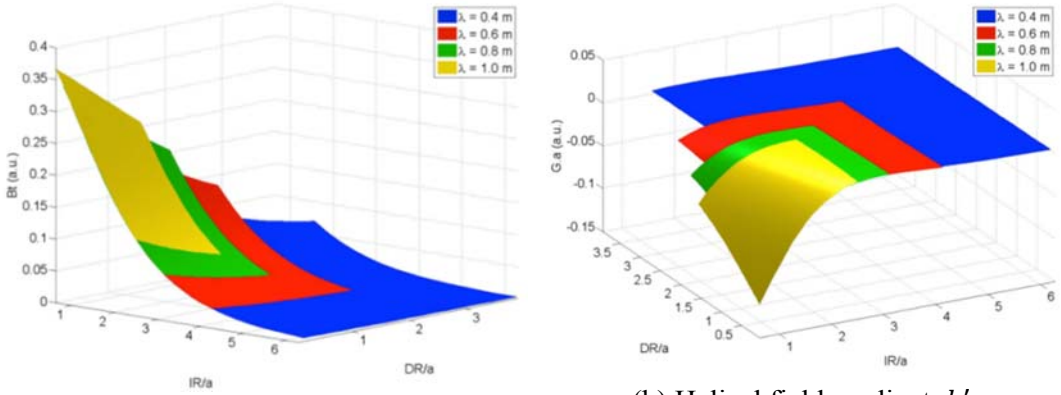

(a) Helical dipole component, b. (b) Helical field gradient, b'.

Figure 16: b and b' as a function of inner radius (*ID*) and coil radial thickness (*dR*) of the helical solenoid coil normalized by the radius of the reference orbit (a). A surface plot shows that the helical field component is independent of λ.

2.5.4.5 ***References***

1. S. Derbenev, R.P. Johnson, Phys. Rev. ST Accel. Beams 8, 041002 (2005).

2. A. Moretti et al., Phys. Rev. ST Accel. Beams 8, 072001 (2005).
3. R. Palmer et al., Phys. Rev. ST Accel. Beams 12, 031002 (2009).
4. P. Hanlet et al., EPAC'06, UK, June 2006, TUPCH147 (2006).
5. K. Yonehara et al., PAC'05, USA, June 2005, TPPP052 (2005).
6. T.J. Roberts, http://www.muonsinternal.com/muons3/G4beamline
7. C. Yoshikawa et al., "Complete Muon Cooling Channel Design and Simulations", IPAC'13, Shanghai, China, June 2013, TUPFI060 (2013).
8. National Energy Research Scientific Computing Center, https://www.nersc.gov/
9. Y. Alexahin, "Gas-Filled Helical FOFO Snake for Initial 6D Ionization Cooling of Muons", MAP-doc-4377-v1 (2014).
10. C. Yoshikawa et al., "Design and Simulation of a Matching System into the Helical Cooling Channel", IPAC'14, Dresden, Germany, June 2014, TUPME017 (2014).
11. K. Yonehara, "Development of six-dimensional Helical Muon Beam Cooling Channel for Muon Colliders", IPAC'14, Dresden, Germany, June 2014, TUPME014 (2014), "Study Cooling Performance in a Helical Cooling Channel for Muon Colliders", IPAC'14, Dresden, Germany, June 2014, TUPME015 (2014).
12. M. L. Lopes et al., "Magnetic Design Constraints of Helical Solenoids", IPAC'14, Dresden, Germany, June 2014, WEPRI100 (2014).
13. S. A. Kahn et al., "Elliptical Muon Helical Cooling Channel Coils to Incorporate RF Cavities", IPAC'14, Dresden, Germany, June 2014,TUPRO116 (2014).
14. M. Chung et al., Phys. Rev. Lett. 111, 184802 (2013).
15. M. Chung et al., "Effects of Beam Loading and Higher-Order Modes in RF Cavities for Muon Ionization Cooling", IPAC'14, Dresden, Germany, June 2014, THPRI065 (2014).
16. L. Nash et al., "High Power Tests of Alumina in High Pressure RF Cavities for Muon Ionization Cooling Channel", IPAC'13, Shanghai, China, June 2014, THPRI065 (2014).
23. K. Yu et al., "Modeling and Simulation of Beam-induced Plasma in Muon Cooling Devices", IPAC'14, Dresden, Germany, June 2014, MOPME043 (2014).

2.6 Novel Ideas in Electron Cooling

V.V. Parkhomchuk and V.B. Reva, BINP, Novosibirsk, Russia
Mail to: V.V.Parkhomchuk@inp.nsk.su

2.6.1 Introduction

The history of the development of electron cooling began at the Institute of Nuclear Physics (Novosibirsk) just after the first successful experiments with electron-electron and electron-positron colliding beams. Radiation cooling plays a decisive role in the achievement of high luminosity in electron and electron-positron colliders. Cooling based on ionization losses in matter was suggested but interaction with the target nuclei did not allow the application of this method because it makes the beam lifetime too short.

The idea of electron cooling, proposed by G.I. Budker in 1965 [1], was based on using a pure beam of electrons (without nuclei). The electrons would travel with the same average velocity as the proton beam. Of course, the electron beam density is much smaller then the electron density in condensed matter, but the electrons are travelling together with the proton beam and the Coulomb interaction between two beams became very the effective. An investigation of the problem of electron cooling was begun in

1967 with theoretical studies [2] and the development of an electron beam facility [3]. The goal of the investigation was verification of the electron cooling concept. The high value magnet field along the electrons trajectory was used for suppression of a drift motion induced by space charge of the electron beam. After cooling the ions temperature tends to temperature of electron beam. The electron beam emitted from the cathode has a temperature close to the cathode temperature $T_к$ – about 1000 K° ~0.1 eV. After acceleration in the electrostatic field the spread of longitudinal velocity becomes very small in compare with the energy spread in the laboratory system. This simple effect (practically 0 longitudinal electron beam temperature) was experimentally discovered at study longitudinal cooling force versus relative velocity ion electron beam. The electron rotates many times along Larmour cycle during collision with ion in the strong magnet field. As results the effective electron beam temperature becomes very small and ions beam can cool to temperature of about 1K. This effect was named "magnetized" cooling. Already in the first experiments at NAP-M it was experimentally demonstrated that the increase in the electron beam transverse temperature caused a weak decrease of the cooling rate but noticeably reduced recombination between protons and electrons. For the project of incorporating electron cooling in the RHIC collider, this effect turned out be rather important. The special experiments have been carried out to verify the effect of reducing recombination by high electron temperature for the highly charged ions at GSI in the ESR storage ring. In the RHIC collider, the lifetime of ion beams should be of many hours with rather fast cooling. For suppression of recombination, it was suggested using a "transversely hot" electron beam in a strong magnetic field. The temperature of transverse motion of an electron beam should be increased up to 100 eV but the cooling time should not be substantially longer.

2.6.2 **Ideas that was Realized at Coolers**

1. An electron gun was put into a solenoid producing the longitudinal guiding magnetic field, which accompanies the beam until it reaches the collector [4]. As initially and up to now the discussion continues about alternative systems of magnetic optic with using quadruples or wigglers magnets. But all operated coolers have solenoid field at cooling section. The strong magnet field suppresses transverse motion of electrons.
2. The effect of magnetization of the transverse motion of the electrons helps to reach the Kelvin range of the ion beam temperature [5,6]. The nice feature of solenoid field is the free motion of the electrons along magnet lines. It helps to have the fast cooling by absorbing the kinetic energy of the moving ions. The kinematic suppression of longitudinal motion of electrons after acceleration gives temperature close to 0 at the cooling section. The transverse motion induced by the space charge of electron beam should be suppressed by the high longitudinal field:

$$V_{\perp} = c\frac{2\pi n_e e x}{B}.$$

The cooling section with strong magnet field up to 4 kG was designed for testing cooling force of the magnetized electrons [7]. The proton or H^- ion with energy 1MeV was sent to precise spectrometers for measurement of loss energy after single pass of the electron beam through cooling section. After this results the BINP team

tries using the maximal magnetized electron beam for made the electron cooling rate as high as possible.

3. The maximum friction force is proportional to the quality of the magnetic field. The waviness of the magnetic field should have minimal value. The deviation of the magnetic force from line leads to the effective temperature of the electron gas in co-moving reference system. The straightness of the magnet line can be measured with a probe like compass [7]. This measurement can be done in air before vacuum assembling (see Fig. 1, left) or probe located in vacuum (see Fig. 1, right). After measuring the magnet lines can be corrected.

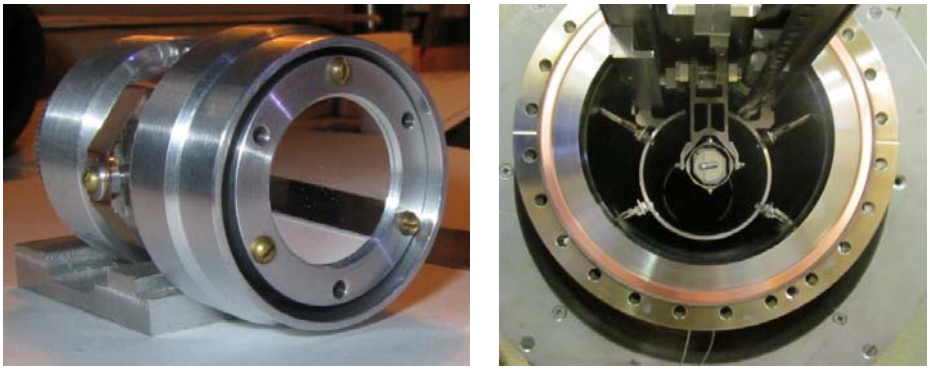

Figure 1: Probe like compass for measuring of straightness of the magnetic force line. The left picture is design for air using; the right picture is design for vacuum using.

4. The extra cooled ion beam can be source of the problem induced by a coherent instability. In order to decide this problem the electron gun with variable profile [8] can be used. The cooling rate decreased with amplitude the betatron oscillation as cubic power amplitude. It means that the central ions with amplitude 10 times less cooled down at 1000 time faster then ions with edge amplitude. Decreasing the central electron beam density increases the life time of ion beam because the very dense core isn't formed. The high density electrons for the high amplitude of ions compensated the kinematic decreasing cooling rate and return these ions at the core of ion beam. Moreover the small density in the centre of the electron beam decreases the recombination capture of ions.
5. The bend of an electron beam inside toroids traditionally made with transverse magnet field. The centrifugal drift is compensated by the drift induced by the bend field. But the electrons reflected from collector moves to the opposite direction to the prime beam and have two times high drift shift. Thus, they moved to the vacuum chamber and produce outgassing from surface of the vacuum chamber. The idea used electric field was tested Tim Ellison at first time. The first coolers that used the electrostatic bending were CSRm and CSRe [9]. The electrons flow bombarded vacuum chamber was decreased at 100-1000 times and the vacuum in the cooling section became very good. The electrostatic bending was used at LEIR cooler also [10]. The LEIR operates with high charge ions beam of lead and the good vacuum condition is very important.
6. The operation of the electron cooler with energy 4.3 MeV and 0.1-0.5 A DC current in Fermilab's Recycler storage ring [11] shows the possibility to use small

longitudinal magnetic field in the cooling section (~100 G). Also the non-magnetized optics of the electron beam was used for the transportation of the electron beam to the cooling section. The cooling rate for this ring need to be not too high and optic system was optimized for single energy at the storage ring with permanent magnets. It was very effective and economical reasonable solution but not for fast cooled systems with high electron beam density.

7. The wide range of the energy for operation stimulates design of COSY 2 MeV cooler with continuous magnetic field along accelerator tube. So, the power source needs in all sections with coils (33 sections, 300 Wt per section). The high-voltage terminal with electron gun, collector and magnetic system requires about 10-15 kWt also. This problem was decided with using multiply transformer connected in series (see Fig. 2). The core of this cascade transformer was made from amorphous iron, the AC frequency is 25 kHz. The design looks like accelerated tube with interleaved rings made with ceramic and stainless steel.

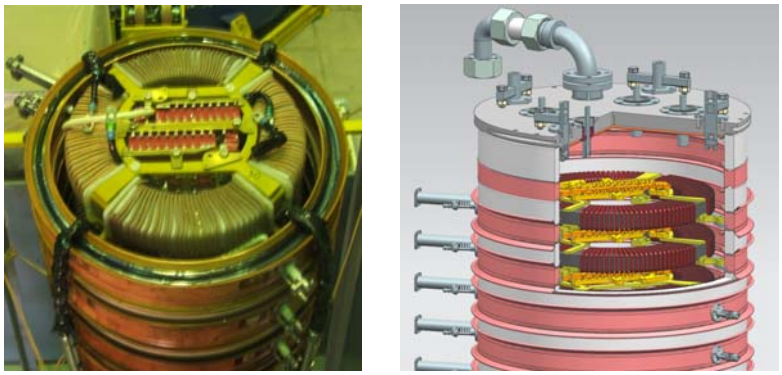

Figure 2: Cascade transformer for transfer energy along accelerator column.

8. The effective cooling and beam passing demands to minimize the electron angles and envelope oscillation of the beam. For this purpose the special electron gun with 4-sectors control electrode was designed and manufactured. The design of the gun is shown in Figure 3. The modulation signal may be supplied to each sector of the control electrode. So, the position of one quadrant sector of the electron beam can be measured by BPM system. Comparing the positions of each sectors from BPM to BPM or the sector positions in the single BPM between the different values of the corrector coils it is possible to analyze the optics of the electron beam in the transport channel. This method allows measuring both the centre and shape of the electron beam. The typical scheme of experiments consists of the excitation of motion by a magnetic element, the phase incursion of the Larmour rotation changing magnetic field in the cooling section and the registration of the beam position by BPM. Figure 4 shows moving of the centre orbit at the different value of the short dipole corrector. Initially the radius rotation of the electron beam was 1.5 mm and after correction became 0.1 mm, that correspond changing energy of transverse rotation (at beam system) at magnet field 1.5 kG from 4 keV to 17 eV.

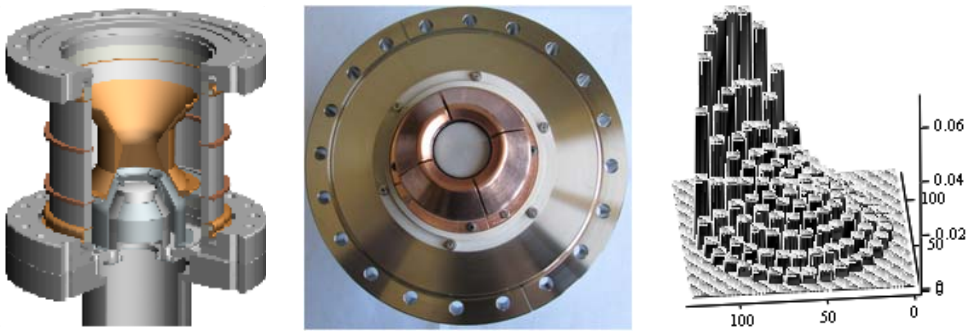

Figure 3: Design of the electron gun is left, the design of the control electrode is center, the profile of the electron current with voltage applied to one sector is right.

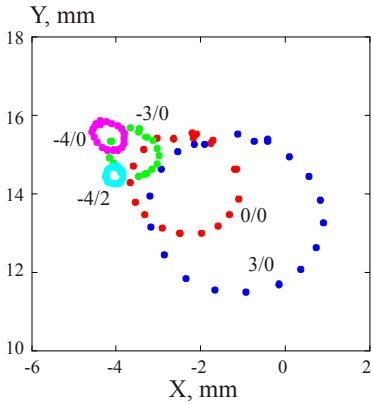

Figure 4: Larmour oscillation of the electron beam at the different currents in the dipole correctors. The numbers near curves are currents in the horizontal and vertical correctors. The electron energy is 1 MeV. The electron angle without correction is 40 mrad. The magnetic field in BPM region is 950 G.

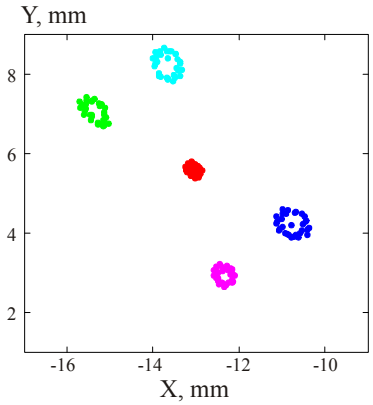

Figure 5: Measuring variation positions of 4 edges beams and central beam (when all 4 sectors have the same RF voltage) with variation magnet at cooling section. Clear see quadruple motion of edges beams. The electron energy is 150 keV.

Figure 5 show variation of position Y, X for 4 different fractions of electron beam and symmetrical modulation (all 4 sectors have the same RF voltage) show stable position center of electron beam. It indicated existing not only dipole

(synchronic) rotation of electrons but existing and quadruple Larmour rotation with amplitude increasing to edge of the electron beam.

The influence of the space charge of secondary ions accumulated inside of the electron beam was clear measured as changing slow spiral drift motion of the electron beam along cooler.

2.6.3 **Ideas for Future Coolers**

1. The idea about amplification of the cooling force with using instability at electron beam was discussed from 1980 [12]. Development of this idea at BNL [13] looks as a high energy FEL. In first stage the ion and electron beams move together. The ion produces the initial fluctuation in the electron beam. Further this fluctuation is amplified by FEL structure. In finish the electron and ion beams are overlapped again. The space-charge fluctuation of the electron beam kicks the ion. In case of the proper phase and amplitude the strong cooling effect can be observed. This idea looks very promising but the test bench for demonstration of coherent electron cooling looks very expensive.

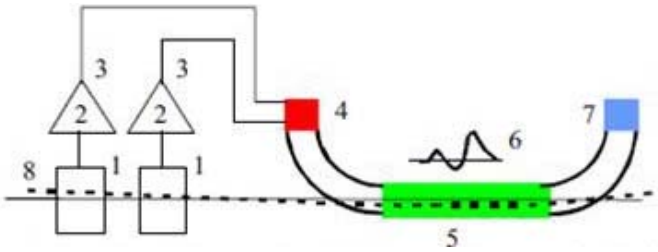

Figure 6: Stochastic cooling with using electron cooler as kickers.

2. The first step to the direction of the full scale coherent cooler can be normal cooler that can produce required plasma fluctuation at the electron gun [14]. The signal from the pick-up or pick-up's array applied to the amplifier system. The signal from the amplifier applied to the control system of the electron gun, which produces the fluctuation of the electron current of required form. After that the electron beam is accelerated and the space charge fluctuation finds itself in the cooling section. Here the fluctuation moving together with an ion impacts on it by the electrical field of the space charge (see Fig. 6).

   The effective kicker device should satisfy a list of requirements. The rate of cooling depends on the system bandwidth. The bandwidth is limited by its highest frequency. Aside from technological issues, there is a factor of the typical aperture of the kicker. The problems appear when the kicker aperture became comparable to the wavelength at high frequencies or the particle with $\beta<1$ doesn't have time for the kicker flight during the impulse. A most of the problems are easy solved in high-energy accelerators but for low and medium energy range the new decision may be useful. The physics size of the electron kicker is small. The size may be easy changed in proportion to the size of the ion beam thus the kicker parameters will be optimal. The size of the electron kicker doesn't depend from the aperture of the vacuum pipe. It is not necessary a plunging device.

   From the physics point of view the electron cooler device as kicker enables to obtain up to 30 GHz ranges of frequencies. One of limitation factors is the size of

the electron beam. The wave with wave-length about transverse size of the beam is difficult for inducing by the usual RF methods and may have strong dispersion and damping.

The electron kicker is effective for the velocity matching of kick impulse and ion. Adjusting the energy of the electron beam the phase velocity of the space-charge wave may be equalized to the ion velocities with high accuracy. This result may be obtained at large variation of the ion velocities $0< \beta <1$.

The space charge of the electron beam enables to obtain the 3D distribution of the electric field at the same time. So, if the control structure of the electron gun can modulate the electron gun axial-asymmetrical then all 3D kick types (vertical, horizontal and momentum) are available in one single device.

Such experiment may be made with COSY cooler. At this system motion of the ions at beam measured normal pick-up and the special electronic system prepare pulses for kicking at X, Y and s direction. This signals gain with using normal (for stochastic cooling) high-band amplifiers and then send in the electron gun for produce 3D fluctuation fields that will moved synchronous with ions sample at cooler. For COSY system as prototype of HESR cooler results can be very interesting. And the spending on this experiments look not too high. After successfully testing for low energy cooler this technology can be used for RF recuperators for made the electron cooling system for very high energy storage ring (for example RHIC).

3. The storage ring with longitudinal magnet field for generation high energy intensive electron beam looks suitable for using [15]. But the very strong focusing and very high tune of this type storage ring needs new ideas at magnet optic for the compensation overlapping transverse resonances.
4. The presently considering projects of the high-energy electron coolers ($\gamma>>1$) for the Relativistic Heavy Ion Collider (RHIC) [16], Facility for Antiproton and Ion Research (FAIR) [17] and Polarized Medium Energy Electron-Ion Collider at Jefferson Lab (MEIC) [18] resumes the discussion about the next steps in the progress of electron cooling technique. The electron cooler for high energy can be designed as a recycler system with low frequency RF. At this systems single pass electron open perspective obtain extremely low emitance of electron beam.
5. The carbon therapy system with using electron cooling still dream of BINP's team [19]. Few experiment with cooling carbon beam demonstrated high quality of cooled carbon beam of energy 400 MeV/u. Nice results of treatment (CSRm, IMP) with using carbon beam stimulated BINP continue efforts at development system with using cooling system. The electron cooling technology applied to the heavy ion medical accelerator will open a world of high performance yet with considerably lower cost. Novel extraction techniques, a new approach to a high intensity beam and a new scanning method of low emittance beam is possible. It also enables high energy economic beam lines less power consumption. The electron cooler opens perspective to use the injection system more simple and the reliable. The ion beam for positron emission can be accumulated after conversion of the primary beam from buster on target.
6. The cascade transformer looks optimal up to 2 MeV energy for powering solenoids along acceleration tube. It is clear that for 8 MeV cooler this solution looks impossible. BINP's and COSY's team developments pneumatic electrical generator with using pressed gases SF6 and individual generator for each section [20].

The prototype of this generator was made and tested with high voltage sections. But life time of these generators was not satisfied requirement and we turn to cascade transformer for this project. From the point of design, using turbine generators is still interesting by combination of the many advantages. Using turbine we can produce energy at any place inside high voltage system. The exhaust gas, with low temperature after turbine, will use for the magnet cooling. Such decision [21] was successfully used at Novosibirsk, AMS for many years.

2.6.4 References

1. G.I Budker, "Efficient method for damping of particle oscillations in proton and antiproron storage ring" Atomnaya Energiya, 22, p.346-348, 1967
2. Ya. S. Derbenev, A.N. Skrinsky, "The effect of an accompanying magnetic field on electron cooling" Particle Accelerators, 8, №4, pp 235-243 (1978)
3. V.I. Kudelainen, I.N. Meshkov, V.V. Parkhomchuk et al., Journal of Technical Physics 46, 1976, v.8 p.1678-1686
4. G.I. Budker, N.S. Dikansky, V.I. Kudelainen et al., "First experiments on electron cooling", IEEE Trans. Nucl. Sci. 22, 2003-7,1975.
5. Ya.S. Derbenev, A.N. Skrinsky et al., "Magnetization effects in electron cooling", Fizika Plasmy 4,492-500(1978).
6. V.V Parkhomchuk, A.N. Skrinsky, "Electron cooling: physics and prospective applications", Rep. Prog. Phys. 54 (1991), p.919-947
7. L.N. Arapov, N.S. Dikansky, V.I. Kokoulin et al., "Precise solenoid for electron cooling", 13 International conference on accelerator for high energy particles 1986, p.341-343.
8. A.Bublei, A.Goncharov, A.Ivanov, et al. "The electron gun with variable beam profile for optimization of electron cooling" Proceeding of EPAC 2002, Paris, France, p.1357 - 1358.
9. V.Bocharov, A.Bubley, Yu. Boimelstein, et al. "Electron Cooler Commissioning". Nuclear Instruments and Methods in Physics Research, A 532 (2004) p.144-149.
10. A. Bubley, V. Parkhomchuk, V. Reva et al. "Commissioning of the LEIR electron cooler with Pb^{+54} ions". Proceedings of XX Russian Accelerator Conference (RuPAC2006) Novosibirsk, Russia, September 10 - 14, 2006, WEBO01.PDF.
11. S.Nagaitsev, A. Bolshakov, D.Broemmelsiek et al. "Antiproton cooling in the Fermilab Recycler Ring " Proceedings of COOL 05, FNAL, USA, September 18-23, 2005, AIP Conf. Proc 821, March 2006, p.39-47.
12. Y.S. Derbenev, "Amplification the electron cooling by instability inside electron beam", Proceedings of the 7th National Accelerator Conference, V. 1, p. 269, (Dubna, Oct. 1980),
13. V.Litvenenko, G.Wang, G.Bell et al." Advances in coherent electron cooling" Proceeding of IPAC-2014, Dresden, Germany, p.91-94.
14. A.V. Ivanov, V. V. Parkhomchuk, V. B. Reva "Electron Beams as Stochastic 3D Kickers" Proceedings conference COOL 2007 Bad Kreuznach, Germany, September 10-14, p. 141.
15. I.N.Meshkov et al. "The development of modified betatron" Physics of Elementary Particles and Atomic Nuclei, 2005, v.36, n.5, p. 1071-1133.
16. "Electron cooling for RHIC" BNL C-A/AP/47 April 2001 http://www.bnl.gov/cad/ecooling/docs/PDF/AP_notes/ap_note_47.pdf
17. "FAIR Conceptual Design Report" (CDR), GSI 2004, https://www-alt.gsi.de/documents/DOC-2004-Mar-201.html.
18. "Science Requirements and Conceptual Design for a Polarized Medium Energy Electron-Ion Collider at Jefferson Lab", http://casa.jlab.org/meic/meic.shtml, 2012

19. E.B.Levichev, V.V.Parkhomchuk, S.A.Rastigeev "Carbon ion accelerator facility for cancer therapy" Proceedings of XX Russian Accelerator Conference (RuPAC2006) Novosibirsk, Russia, September 10 - 14, 2006, p. 363-365.
20. V.V. Parkhomchuk, M.I. Bryzgunov, A.P. Denisov et al "Conceptual Project Relativistic Electron Cooler for FAIR/HESR" Proceedings of IPAC 2014 Dresden, Germany, June 15-20 2014, p. 774-776.
21. J.Dietruch, M.I.Bryzgunov, A.D.Goncharov et al." Prototype of the high voltage sectionfor the 2 MeV electron cooler at COSY-Juelich. Proceeding of EPAC-2008, Genoa, Italy, p.3467-3469.

2.7 The Coherent Electron Cooling Experiment at RHIC

Igor Pinayev and Vladimir N. Litvinenko, BNL, Upton, New York, USA
Mail to: pinayev@bnl.gov

2.7.1 Goal and Scope

The goal of our experiment is to demonstrate longitudinal (energy spread) cooling in the coherent electron cooling (CeC) mode before the expected CD-2 for the eRHIC. The scope of our experiment is to reduce the energy spread of a single bunch of 40 GeV/u Au ions in RHIC. We expect to carry out the CeC experiment during RHIC Run 16, with the early commissioning of the accelerator during Run 15.

In addition to using the e-beam for the CeC demonstration experiment, it will be employed for studying novel aspects of beam-beam effects in eRHIC by colliding the electron- and hadron-beams as well as for some aspects of micro-bunched electron cooling. These tests will be undertaken after we have completed the CeC experiment.

2.7.2 Location

The experiment will be located at the IP2 interaction point of the RHIC tunnel (formerly the Brahms IP): some equipment for the experiment will be located in a portion of Service Bldgs. 1002A and 1002B.

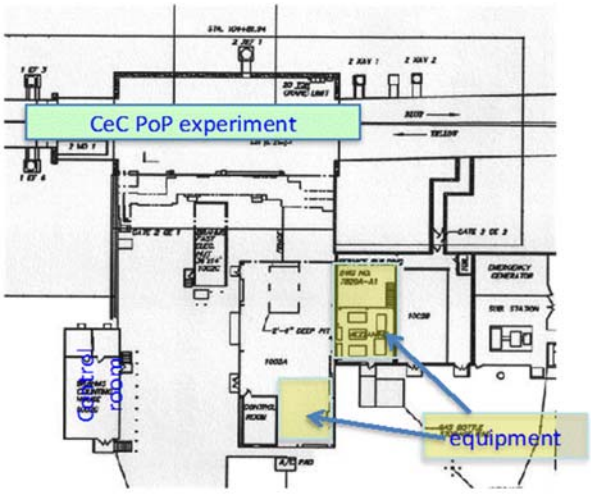

Figure 1: Approximate location of the CeC PoP experiment at IP2

Most likely, local control will be conducted from a former Brahms Counting house, i.e., a trailer located at IP2.

2.7.3 Schematic of the CeC

Fig. 2 is a schematic of a coherent-electron-cooler comprised of a modulator, a FEL-amplifier, and a kicker. The figure also depicts some aspects of coherent electron cooling. In the CeC, the electron- and hadron- beams co-propagate with the same velocity, *v*, in vacuum along a straight line in the modulator and the kicker:

$$\gamma_o = E_e / m_e c^2 = E_h / m_h c^2 = 1/\sqrt{1 - \mathrm{v}^2/\mathrm{c}^2} >> 1 \qquad (1)$$

Since the electrons are about 2,000-times lighter than a nucleon, their energy is much lower than that of the nucleon. For cooling *Au* ions with energy of 40 GeV/u, we will use electrons with energy of 22 MeV. Furthermore, since the rigidity of the ion beam is amplified by *A/Z* =197/79 ~ 2.5 fold, the effect of the magnetic elements designed to transport the electron beam have a minuscule effect on the ion beam. In our case, the magnetic elements (dipoles, trims, and quadruples) affect the trajectory of electron beam 4,578 times stronger than that of the Au-ion beam. This feature of the RHIC allows us to use common elements in the IP2, and to optimize the lattice of the electron-beam's transport channel without affecting the ion beam.

The CeC works as follows: In the modulator, each positively charged hadron (with charge *Z,* and atomic number *A*) induces a density modulation in electron beam that is amplified in the high-gain FEL; in the kicker, the hadrons interact with the electric field of the electron beam that they originated, and receive energy kicks toward their central energy. The process reduces the hadrons' energy spread, i.e., it cools the hadron beam.

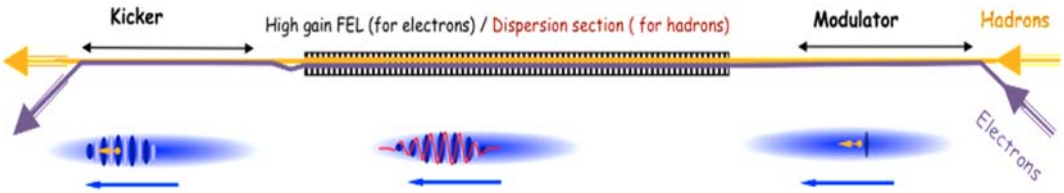

Figure 2: Schematic of the CeC – economic option (see [1] for more details)

In practice, the scheme will look like that sketched in Fig. 3 showing that we used most of the available space between the two DX magnets at IP2.

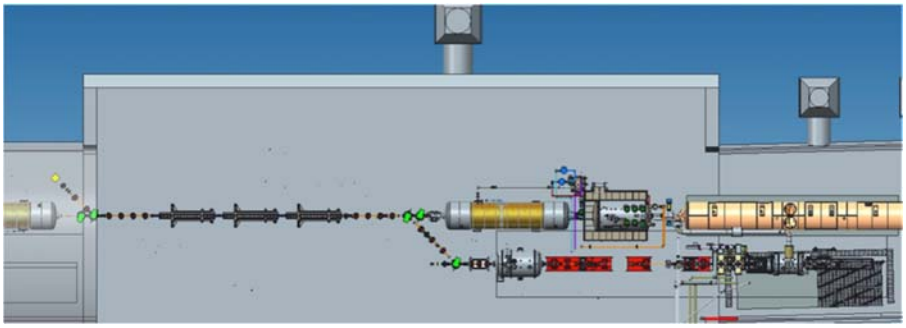

Figure 3: Schematic of the CeC experiment at IP2.

The 100-500 picoseconds long 2 MeV electron beam, generated in the superconducting RF 112 MHz gun, passes the two 300 kV 500 MHz bunching cavities, where the electrons acquire an energy chirp. After compressing in the drift section to a ~15 psec bunch, the electrons are accelerated to 21.95 MeV in 5-cell 704 MHz SRF cavity, and then pass through an achromatic dogleg to join the Yellow-ring's Au-ion beam. After passing through the CeC section, another dipole separates the electrons from the ion beam and directs them into the beam dump.

Table 1 lists the main parameters of electron- and hadron-beams that we plan to use for the experiment.

Table 1: Main beam parameters for the CeC experiment

Parameter	
Species in RHIC	Au ions, 40 GeV/u
Number of particles per bunch	10^9
Electron energy	21.95 MeV
e-bunch charge	0.5-5 nC
Repetition rate	78.3 kHz
Average *e*-beam current	0.04-0.39 mA
Electron beam power	up to 8.6 kW

Table 2: contains requirements for e-beam quality and main FEL parameters.

Table 2: Parameters of the electron beam and FEL

e-beam	
RMS Energy Spread	$\leq 1\times10^{-3}$
Normalized Emittance	≤ 5 μm·rad
Peak Current	60-100 A
FEL	
Wiggler Length	3×2.5 m
Wiggler Period	0.04 m
Wiggler Strength, a_w	0.5
FEL Wavelength	13 μm

2.7.4 **Electron Accelerator**

Fig. 4 shows details of 22 MeV electron linear accelerator. Electrons are generated at the CsKSb photocathode, which is inserted into the 112 MHz quarter-wave SRF cavity from the back of the cryomodule. We are using six focusing solenoids to focus the low- energy electron beam in the beamline between the gun and the 20-MeV linac. The first solenoid is mounted on the gun. The other five solenoids, identical in the design to that used in the R&D ERL, are placed between bunching cavities and accelerator.

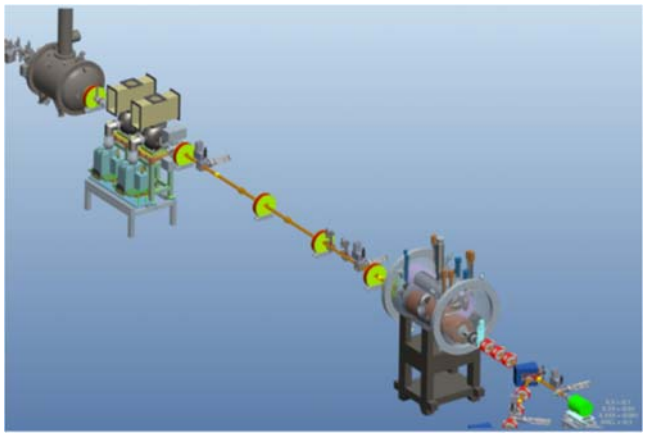

Figure 4: 3D rendering of the 21.95 MeV accelerator.

The 112 MHz SRF gun was built by Niowave Co., while the cathode stalk and transport system was manufactured by Stony Brook University. The fundamental power coupler (FPC) for this cavity was designed and manufactured at BNL. The RF transmitter for the gun was made by Tomco Technology, and the circulator was produced by Ferrite Microwave.

The 4°K helium will be provided by a heat exchanger from the CeC PoP's cryosystem.

Two 500-MHz room temperature cavities (Fig. 5) will provide the energy chirp to the electron beam. Each cavity develops up to 300-kV RF voltage to provide the necessary chirp. The chirp creates a velocity difference, with electrons at the head of the bunch having lower ones that those at the tail.

The 500 MHz cavities are fed by a transmitter (made by Thomson Broadcast Co) via an AFT microwave's circulator and a power splitter. Both 500 MHz cavities are water-cooled.

Figure 5: The 112 MHz photo-injector with 500 MHz bunching cavities inside the RHIC tunnel. The cathode stalk will be insertable from the back of the cryomodule. The cathode is illuminated by a green light from a laser (not shown in the figure). The cavity has a quarter-wave structure, with coaxial fundamental power coupler that also serves as a fine tuner.

The BNL3 704 MHz 5-cell SRF structure was produced by AES and successfully passed VTF test at 20 MV/m. It will be incorporated into a cryostat, which is under

production at Niowave, Inc. The 2°K helium will be provided from CeC PoP's cryosystem.

All necessary clocks and frequencies (78 kHz revolution clock, 112 MHz, 500 MHz, 704 MHz) will be generated locally from the 100 MHz reference frequency brought from IP4.

2.7.5 **Electron Beam Transport**

The rest of the optics assures matching of the electron beam through the dogleg and into the FEL wiggler. As mentioned in the introduction, quadrupoles located at the common trajectory of the ion- and electron-beams would focus the electrons while the effect on heavy ions is negligible.

The only common elements whose effect on the ion beam requires compensation are the dipoles where the electron- and ion-beams are merged and separated. Two dipoles, identical to the merging and separating ones, but with opposite directions of the magnetic field, are located on the ion-beam trajectory; they null the effect on the ion beam. All the focusing of the ion beam is provided by RHIC's super-conducting quadrupoles located outside the CeC section. The β-functions of the ion beam are identical in the x- and y- directions, and are symmetric with respect to the wiggler's center where the β-functions have minimum of β*=5.5.

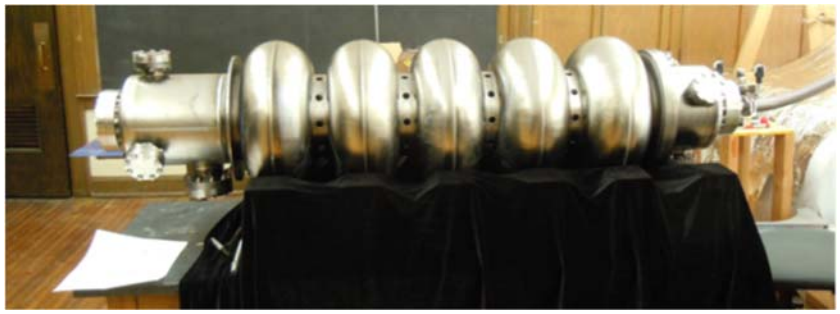

Figure 6: 5-cell 704 MHz BNL3 SRF cavity (without the cryostat).

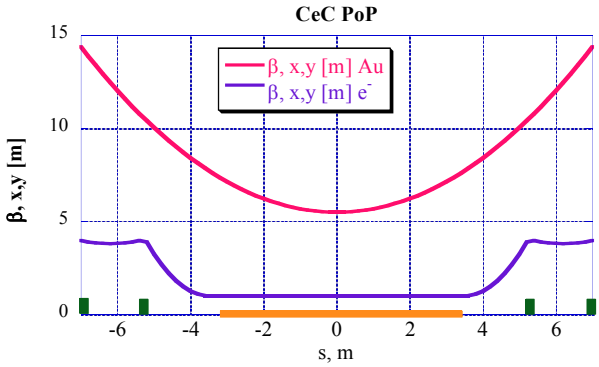

Figure 7: Desirable β-functions for the ion- and electron-beams in the IP2 for the CeC experiment.

In contrast with steadiness of the size of the ion beam the electron beam has to be matched to β=0.7 m the helical wiggler, as well as having optimal overlap with the ion beam in the kicker and the modulator sections.

Two dipoles form a dogleg bringing the e-beam to co-propagate with the Yellow beam. The dipoles are 45-degree chevron magnets with a gap sufficient to accommodate a 2" ID pipe (e.g. a gap ~ 5.6 cm). All five dipoles will be fed in series by a single power supply, and water-cooled. Each dipole has individual 1% trim-coil.

We are using 16 quadrupoles to focus the 22 MeV electron beam. The design of the quadrupoles is identical to that of R&D ERL at BNL. A quadrupole provides gradient up to 0.3 kGs/cm, and its magnetic length is about 15.7 cm. The field quality requirement is that 12-pole integral ratio is below 1.6×10^{-4} at a radius of 2 cm.

The low-energy electron beam will be steered by three dual-plane corrector magnets. The maximal deflection angle is ±3 mrad (± 200 G cm). The 20-MeV electron beam will be steered via corrector coils in the quadrupoles.

Figures 8 and 9 show the preliminary optics functions of the e-beam. Fig. 8 shows beam optics of the beamline from the end of the 5-cell accelerator to the entrance of the wiggler. Three quadrupoles are used to match the e-beam into the first dogleg. Three dogleg quads assure its achromaticity as well as the proper beam size at the entrance of the modulator section (β ~ 4.5 m). Four quads maintain the size of the e-beam through the modulator section, and then match it to the entrance of the helical wiggler.

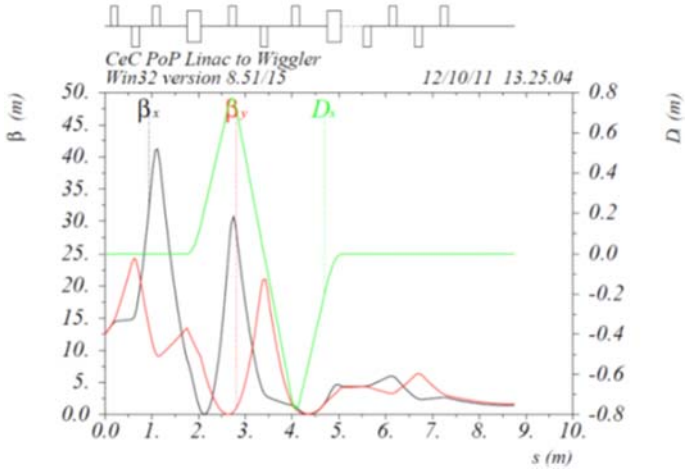

Figure 8: 22 MeV *e*-beam optics from the exit of accelerator to the entrance of the helical wiggler.

After the wiggler, the e-beam is matched by four quadrupoles in the kicker section. As Fig. 9 shows, the following dipole with two quadrupoles serves as a beam spreader by blowing up the e-beam's size tenfold. The electron beam's size is blown out for being absorbed in the dump.

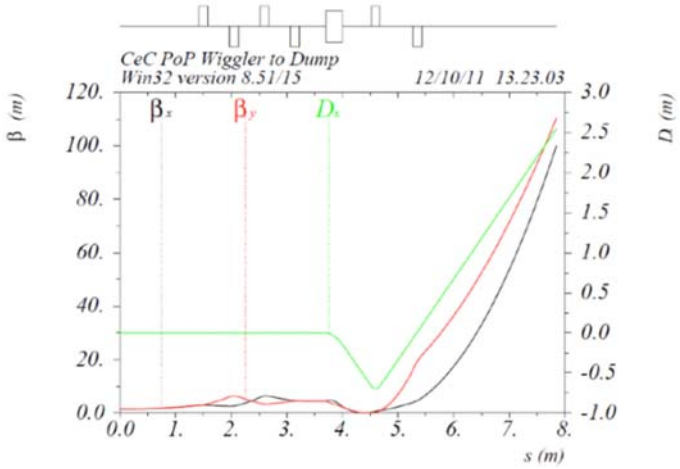

Figure 9: 22 MeV e-beam optics from the exit of the wiggler to the beam dump.

2.7.6 **Helical Wiggler**

BINP (Novosibirsk, Russia) has designed and manufactures a prototype of the helical wiggler. Presently it is manufacturing three wigglers with the following specifications:

Type	Helical
Period	4 cm
Length	2.50 m
Type	permanent magnets
Gap	3.2 cm
A_w value for 3.2 cm gap	~ 0.5 (peak field 0.14 T)
Phase errors	< ±1 degrees
First integral	$< 25\times10^{-6}$ T m
Second integral	$< 7\times10^{-6}$ T m^2

Helical geometry assures equal focusing in both transverse directions, and gives a matched β=0.7 m. We used the matched beam to simulate the amplification process in the wiggler. The wiggler has an adjustable gap and can be reused for a full-size CeC cooler in RHIC/eRHIC operations.

At the end of the wiggler, we will install a simple electromagnetic-compensated phase shifter to adjust the length of the e-beam's path for about 20 microns. Focusing of this device is negligible even for the electron beam. These phase shifters will be used for the verification of the microbunched electron cooling proposed by D.F. Ratner [4].

Figure 10: Helical wiggler at the magnetic-measurements stand.

2.7.7 **Vacuum System**

Parts of the vacuum system close to the SRF cavities require being a particulate-free system. The rest of the transport beam-line should have a 10^{-9} Torr vacuum. The vacuum system of the CeC PoP beam-line should have two automatic valves at the ends of the doglegs to shut them off from RHIC vacuum should there be a in the case of vacuum accident.

The size of the pipes of the transport lines should be the same as have the pipe-size equal to that in the gun-to-linac (i.e., 2" ID). The only exception here is a 4" pipe at the entrance to the beam's dump.

The opening of the helical wiggler has a square aperture of 32 mm, which is shown in Fig. 11. It will be installed with a 45-degree tilt to maximize the vertical aperture available for injecting the hadron beam in RHIC.

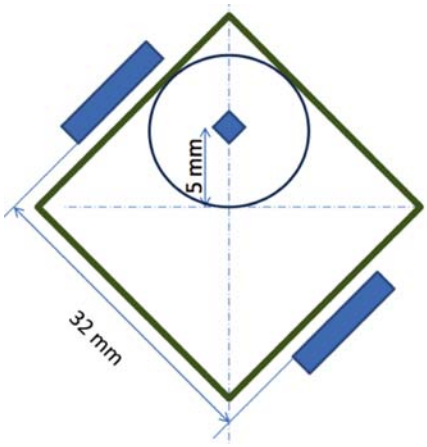

Figure 11: Profile of the vacuum chamber in the helical wiggler. The blue rectangles represent poles of the helical wiggler.

2.7.8 **Beam Diagnostics**

We plan using following diagnostics:

1. Two in-flange Bergoz integrating-current-transformers (ICT) with beam-charge monitors
2. Fluorescent screens for monitoring the beam's profile and position.
3. A low-energy-emittance measurements system utilizing a pepper-pot set-up.
4. A high-energy-emittance measurement system via a quadrupole scan.
5. Beam position monitors.
6. A RHIC wall-current monitor monitoring the ion beam profile.
7. A spectrum analyzer monitoring the evolution of the ion bunch's spectrum.
8. The Infrared Radiation Diagnostics for FEL tuning at 13-micron.
9. Beam-loss monitors to observe ion losses in the wiggler.

The position of the ion beam will be monitored with existing RHIC pick-up electrodes (strip-lines). The electron beam position will be monitored with button-type BPMs.

The flag's resolution is 50 microns, viz., sufficient to measure the beam's emittance. The flag will be placed on the extension of the beam-line after the first dipole. In such a configuration the dispersion is zero and does not affect the measurement of emittance. The flag in the dogleg will be used for measuring energy spread, and also for measuring the length of the bunch when the acceleration is off the crest. This flag can be used for measurement of the sliced emittance. For this purpose, we will feed the solenoids with opposing currents; such solution allows keeping the focusing the same while rotating the beam in the XY plane.

Coarse synchronization between the ion- and the electron-bunches will be assured by observation signals from the RHIC and electron pick-ups by an oscilloscope.

The beams' velocities equalization (and the fine tuning of the synchronization) will be attained by observing the spontaneous radiation from the wiggler. The ions would induce density modulation in electron beam increasing its spontaneous radiation in wigglers. Maximizing of the power of spontaneous radiation would indicate the synchronization for the beams velocities.

2.7.9 **Demonstration of Cooling**

We plan to detect the cooling effect by observing the modification of the longitudinal profile of the ion bunch. We expect to observe a growth of the short peak (in the case of cooling or a dip – in the case of heating) with sub-nsec duration on the top of the 5-nsec profile of the ion bunch (Fig. 12). We can detect the early phase of the cooling (or heating) of the central part by observing the ion-bunch's spectrum in the 1-3 GHz range. The ion-beam-induced signal should come from the wall current's monitor with nominal bandwidth from DC to 6 GHz.

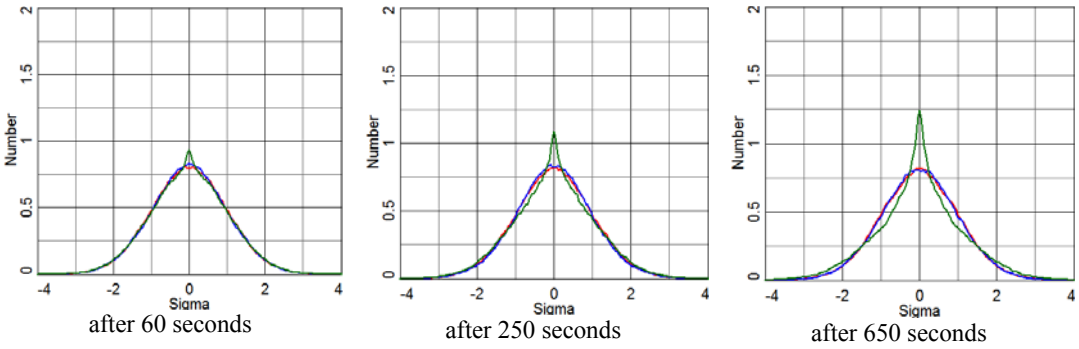

Figure 12: Evolution of the ion beam's profile modeled with betacool by A. Fedotov. Blue curve indicates the initial ion bunch profile, red one indicates Gaussian fit, and green line shows the longitudinal profile after the indicated cooling period.

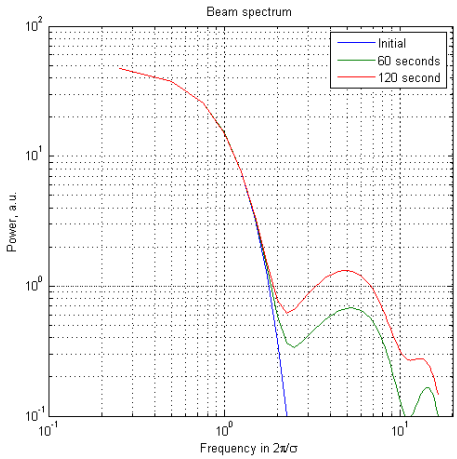

Figure 13: The evolution of the spectral content of the longitudinal beam's profile.

As was mentioned earlier, we will monitor the beam's profile with a fast digital oscilloscope using the signal from wall's current monitor. As shown in the Figure 12, the simulations predict that in few minutes the cooling (or heating) should be clearly seeing in the oscilloscope trace. To expedite the tuning process, we will monitor not only the shape of the signal, but its spectral content. Fig. 13 shows the expected evolution of bunch profile spectrum.

After 60 seconds of cooling, the high-frequency content (corresponding to the cooled part of the beam) will grow to about -40 dB for the normal (low frequency) bunch spectrum.

Fig. 14 shows the measured spectral content of the circulating beam in RHIC. The beam's signal of 50 dB above the noise floor guaranty that this method would allow us the cooling/heating process in few seconds.

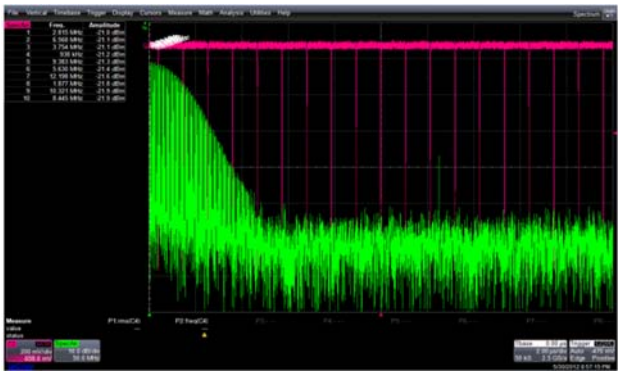

Figure 14: Spectral content (green) of the ion beam's longitudinal profile (magenta). The horizontal scale is 50 MHz/div (total span 500 MHz), and the vertical scale is 10 dB/div.

Finally, tuning the phase shifter after the FEL would allow us (a) to choose the cooling phase; (b) to optimize the cooling. When local cooling is established, we plan to demonstrate cooling of the entire ion bunch.

2.7.10 **Conclusion**

We plan to commission the 500 MHz bunching cavities and 112 MHz gun this year. We plan to install install the linac, the helical undulators, the high power beam dump, and the balance of equipment during the RHIC shutdown in 2014 and commission the electron part of the equipment during Run 15.

2.7.11 **Acknowledgements**

We acknowledge CeC PoP team F.Z. Altinbas, S. Belomestnykh, I. Ben-Zvi, D. Beavis, K.A. Brown, C. Brutus, A.J. Curcio, L. DeSanto, A. Elizarov, C.M. Folz, D.M. Gassner, H. Hahn, Y. Hao, C. Ho, Y. Huang, R. Hulsart, M.Ilardo, J. Jamilkowski, Y. Jing, F.X. Karl, D. Kayran, R. Kellermann, R. Lambiase, N.D. Laloudakis, G. Mahler, M.Mapes, W. Meng, R. Michnoff, T.A. Miller, M. Minty, P. Orfin, A. Pendzick, F. Randazzo, T. Rao, J. Reich, T. Roser, J. Sandberg, T. Seda, B. Sheehy, J. Skaritka, L.A. Smart, K. Smith, L. Snydstrup, A. Steszyn, R. Than, C. Theisen, R.J. Todd, J. Tuozzolo, E. Wang. G. Wang, D. Weiss, M. Willinski, T. Xin, W. Xu, A. Zaltsman (BNL, Upton, New York, USA), M.A. Kholopov, P. Vobly (BINP, Novosibirsk, Russia), G.I. Bell, J.R. Cary, K. Paul, I.V. Pogorelov, B.T. Schwartz, A. Sobol (Tech-X Inc., Boulder, Colorado, USA), S.D. Webb (RadiaSoft, Boulder, Colorado, USA), C. Boulware, T. Grimm, R. Jecks, N. Miller (Niowave, Lansing, Michigan, USA), P. McIntosh, A. Wheelhouse, (STFC, Daresbury Lab, Daresbury, Warrington, UK)

Work is supported by DoE NP grant KB-02-01-05-2 and BNL's PD and LDRD programs.

2.7.12 **References**

1. V. N. Litvinenko, Ya. S. Derbenev, Coherent Electron Cooling, Physical Review Letters 102, 114801 (2009), http://link.aps.org/abstract/PRL/v102/e114801.

2. V.N. Litvinenko, et al., Proof-of-Principle Experiment for FEL-based Coherent Electron Cooling, Proceedings of 2011 Particle Accelerator Conference, New York, NY, USA, pp. 2064-2066, http://www.c-ad.bnl.gov/pac2011/proceedings/papers/thobn3.pdf
3. V.N. Litvinenko, et al., Coherent Electron Cooling Demonstration Experiment, Proc. of Second International Particle Accelerator Conference, San Sebastian, Spain, p. 3442, http://accelconf.web.cern.ch/AccelConf/IPAC2011/papers/thps009.pdf
4. D. Ratner, Microbunched electron cooling for high0energy hadron beams, Physical Review Letters 111, 084802 (2013).

2.7.13 Appendix: Details of the Ions Interaction with Electrons in CeC

In detail, within the modulator each individual ion attracts the surrounding electrons and generates an imprint of density modulation (Fig. A1). In about a quarter of the plasma period, each ion becomes surrounded by a cloud of electrons with a total charge equal in value to its own, but opposite in sign, i.e., it is shielded. In the co-moving frame, the longitudinal-velocity spread is significantly smaller than that in the transverse direction. Consequently, the Debye radius in the transverse direction greatly exceeds that in the longitudinal direction, and the electron cloud assumes a very flat pancake-like shape.

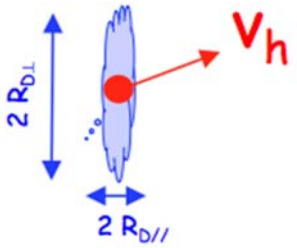

Figure A1: In the modulator, each ion generates an individual imprint on the density of the electrons, taking the form of an ellipsoid with the typical dimensions of the corresponding Debye radii.

These individual density-modulations are self-amplified when electron beam passes through a high-gain FEL into a wave-packet in the electrons' density (Fig. A2).

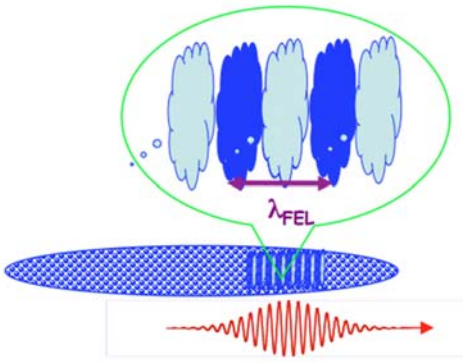

Figure A2: In the FEL, the modulation of the e-beam's density is amplified into a wave-packet, i.e., into a series of "pancakes" with increased- and reduced-density of electrons.

This periodic density-modulation generates a periodic longitudinal electric-field. When a hadron recombines with the electron beam, it is exposed to this self-induced electric field. We selected the delay between the self-induced wave-packet and an ion such that an ion with designed energy (E_0) arrives at the kicker on the top of the electron-density peak (Fig. A3), where electric field is zero. Hence, the ion does not experience any change in its energy.

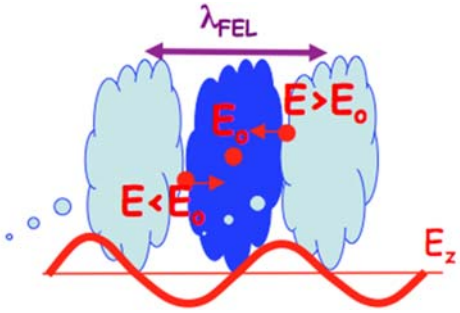

Figure A3: In the kicker, the hadron interacts with its self-induced electric field. Depending on the sign of its energy deviation from the design value, E_0, the hadron either is accelerated or decelerated.

Because ion's velocity depends on its energy, a time-of-flight for an ion also depends on its energy. Thus, a hadron with higher energy than the designed value reaches the kicker ahead of the negatively charged (high-density) peak, and is dragged back (decelerated) by its self-induced electric field. Similarly, a hadron with lower energy than designed energy enters the kicker behind the negatively charge (high density) peak, and is pulled forward (accelerated) by the self-induced electric field. The outcome of this process is a reduction in the energy spread of the hadrons, and the consequent longitudinal cooling of the hadron beam.

2.8 Coherent Electron Cooling Driven by the Microbunching Instability

Daniel Ratner
SLAC National Accelerator Laboratory, Menlo Park, California USA
Mail to: dratner@slac.stanford.edu

Cooling high energy, bunched, hadron beams is a persistent challenge for modern collider projects. Methods discussed elsewhere in this issue, such as traditional electron cooling, have proved successful on low energy beams, but scale poorly to the TeV scale [1,2]. Stochastic cooling, in which an RF 'pickup' measures particle properties and a subsequent kicker stage adjusts the particles accordingly, is effective for low intensity beams [3], but the bandwidth is too small to cool the high peak currents of bunched beams [4]. To improve cooling rates, 'optical stochastic cooling' replaces the RF with a higher bandwidth optical system [5]. An alternative approach is Coherent electron Cooling (CeC), which uses an electron beam as both the pick-up and kicker [6,7]. Various high bandwidth amplifiers exist for electrons, but the Free Electron Laser (FEL) has received the most attention in the context of CeC [8-10].

A UV FEL is an attractive amplifier because the short wavelength allows for a large bandwidth. However, the slippage in the FEL produces periodic density spikes of which only one contributes to cooling; i.e. the slippage decreases the bandwidth. Ideally, the amplifier would create just the single spike needed to cool each hadron. An alternative amplifier is the Microbunching Instability (MBI), driven by longitudinal space charge (see e.g. [11, 12]). Initially studied because of concerns over degradation of X-ray FELs, MBI is a potentially useful amplifier [13,14]. (We note that a similar scheme with a dispersive section was first introduced by Litvinenko to accelerate the plasma oscillation in CeC prior to the amplification stage [8].) Using MBI as an amplifier for CeC appeals for two reasons: the large bandwidth indicates fast cooling and the relatively simple implementation consists only of drifts and dispersive regions. The rest of this chapter describes the basic properties of an MBI driven CeC scheme [15,16].

A schematic of a one-dimensional model for MBI-driven CeC is given in Fig. 1. In the first section, the Coulomb field of the target particle, e.g. an ion, modulates the electron energies. Electrons and ions take separate paths in the second section, where dispersion converts the electron energy modulation into a density spike at the ion's former location in the electron beam. When the ion and electron beams are brought together again, an ion with lower than average energy falls behind the spike it created, and the collective electron field provides an energy boost; conversely, an ion with above average energy slips ahead of its spike, and the collective electron field pulls the ion backwards. The net effect is to push all ions towards the average energy, i.e. cooling. Note that, other than swapping the FEL for MBI as the amplifier, this is identical to the CeC scheme of [9].

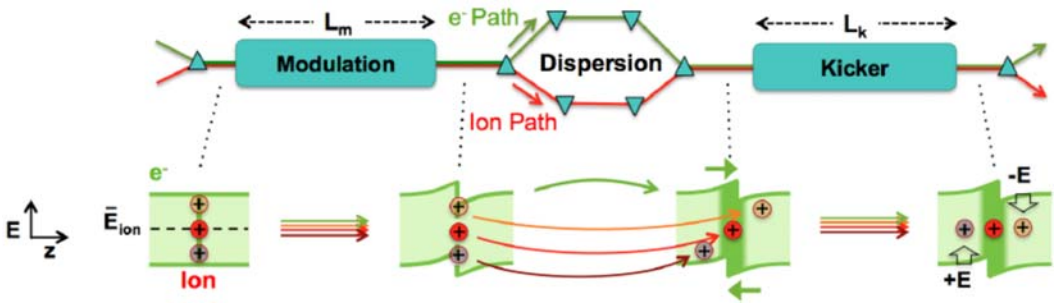

Figure 1: Schematic of the cooling mechanism. In the first stage, an ion modulates the energy of the local electrons. In the dispersive region, ions and electrons move longitudinally due to energy differences, creating an electron density spike at the overlap. In the kicker stage, an ion with nominal energy $E = \bar{E}_{ion}$ (red) returns to the center of the spike and does not change energy. A low energy ion with $E < \bar{E}_{ion}$ (purple) falls behind its original position, and receives a positive energy kick from the electron spike. A high energy ion with $E > \bar{E}_{ion}$ (orange) slips ahead of its electron spike and receives a negative energy kick. The result is that all ions are pushed towards the average ion energy. Figure taken from [15].

To model the cooling effect from MBI, we start by calculating the interaction between the ion and electrons. The specifics of the electron-ion interaction depends on the behavior of the particles throughout the modulation and kicker sections. If we assume the modulation and kicker sections are short compared to the electron β-function (L_m; $L_k \ll \beta$), then the particles are approximately frozen transversely during the interaction and can be treated as point particles. We will call this the 'ring' regime for reasons that will become clear later. In the opposite regime (L_m; $L_k \gg \beta$) the electrons

randomize during the interaction and can be treated as discs with a radius of the electron beam [17]. We will call this the 'disc' regime. We can also consider a 'hybrid' regime, where the particles are frozen during the modulation, but randomize before the kicker. The second two cases were described in [15]; here we begin with the 'ring' regime.

Following the derivation in [15], we start by calculating the energy modulation to an electron from an ion of charge q. We assume the same relativistic Lorentz factor $\gamma \gg 1$ for both beams (average electron energy $E_e = \gamma m_e c^2$ and average ion energy $E_{ion} = \gamma m_I c^2$). The particle has initial longitudinal position z and relative energy $p = (E-E_e)/E_e$ and for simplicity we assume the ion sits at the center of the bunch ($r = 0$; $z = 0$). The energy change to the electron is derived from the longitudinal component of the Coulomb field integrated over the length, L_m, of the modulator,

$$M(r,z) = \frac{-cqL_m}{I_A}\frac{z}{[r^2+\gamma^2 z^2]^{3/2}} \tag{1}$$

with Alfven current $I_A = 4\pi\varepsilon_0 m_e c^3/e$. Here we can already identify the feature that produces the density spike for cooling: if we consider only the region with $\gamma z \ll r$, we find that the interaction is approximately $M \sim C_1 z/r^3$, with strength parameter $C_1 \equiv -cqL_m/I_A$. The linear chirp (a linear energy correlation in z) implies that, for a given value of R_{56}, we can find a radius at which the electrons are all compressed to $z = 0$. (This is directly analogous to a bunch compressor, where a linear chirp and a dispersive region combine to increase the peak beam current.) After passing through a dispersive region of strength R_{56}, the final electron position is

$$z_f = z\left(1 + C_1 R_{56}\frac{1}{[r^2+\gamma^2 z^2]^{3/2}}\right) + R_{56}p \tag{2}$$

We can now see clearly that a high density ring forms at radius $r_{spike} = |C_1 R_{56}|^{1/3}$, for which the term in parentheses goes to zero for $z \ll r/\gamma$. Fig. 2 shows the behavior of electrons visually.

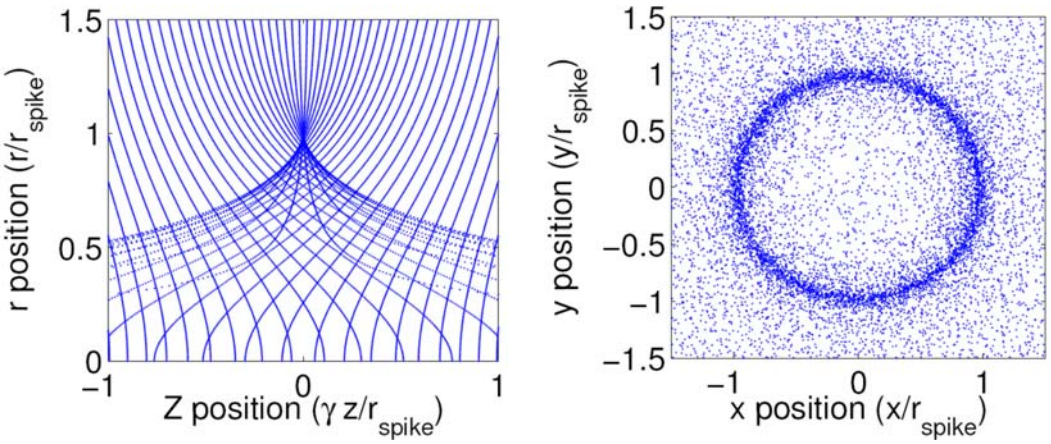

Figure 2: Graphical depiction of the mechanism for ring formation when $L_m \ll \beta$. At left, starting from an initial grid, lines show final positions, z_f. Only near $r \sim r_{spike}$ are electrons from different initial z locations all compressed to $z_f = 0$ with the same value of R_{56}. At light, starting from an initially random uniform distribution, final particle positions are plotted for the region $\gamma z_f \ll r_{spike}$. While the central region ($r < r_{spike}$) actually has a small dip in density, the high density at $r \sim r_{spike}$ is sufficient to create an overall density spike at $z_f = 0$.

Next we calculate the ion energy shift resulting from the ring spike. We assume a uniform and uncorrelated initial electron distribution and a cylindrical beam with current I, radius a, and rms energy spread σ_p. Switching to dimensionless variables $\rho \equiv r/r_{spike}$, $\varsigma = \gamma z/r_{spike}$, and $\varepsilon = \gamma|R_{56}|p/r_{spike}$, we rewrite Eq. 3 as

$$\bar{\varsigma}(\varsigma,\varepsilon) \equiv \varsigma\left(1 - \frac{s}{[\rho^2+\varsigma^2]^{3/2}}\right) + s\varepsilon \tag{3}$$

with $s \equiv \mathrm{sgn}(R_{56})$. Assuming the same interaction (Eq. 1) over a kicker of length L_k, we integrate over the final electron distribution to find the corresponding energy shift to an ion at longitudinal position $z_I = r_{spike}\varsigma_I/\gamma$,

$$W_I^{(ring)}(z_I) = \frac{2\pi|R_{56}C_1|^{1/3}C_2}{\gamma}\int d\varepsilon \frac{e^{-\varepsilon^2/2\sigma_\varepsilon{}^2}}{\sqrt{2\pi}\sigma_\varepsilon}\int \rho d\rho d\varsigma \frac{\varsigma_I - \varsigma\left[1 - s(\rho^2+\varsigma^2)^{-3/2}\right] - s\varepsilon}{\left[\rho^2 + \left(\varsigma_I - \varsigma\left[1 - s(\rho^2+\varsigma^2)^{-3/2}\right] - s\varepsilon\right)^2\right]^{3/2}} \tag{4}$$

with kicker strength parameter $C_2 \equiv qIL_k/4\pi\varepsilon_0 c\pi a^2$ and $\sigma_\varepsilon = \gamma|R_{56}|\sigma_p/r_{spike}$. Note that we have assumed the particles keep the same radial positions in the modulator and kicker, requiring a 2π betatron phase advance. We can compare this result to the 'disc' case considered in [15], where the particles are assumed to randomize in both the modulator and kicker and the fields can be treated as originating from uniform discs,

$$W_I^{(disc)}(z_I) = \frac{|R_{56}A_1|A_2}{\gamma}\int_{-\infty}^{+\infty} d\varepsilon \frac{e^{-\varepsilon^2/2\sigma_\varepsilon{}^2}}{\sqrt{2\pi}\sigma_\varepsilon}\int_{-\infty}^{+\infty} d\varsigma\left(t(\varsigma,\varepsilon) - \frac{\varsigma_I - \varsigma\left[1 - s/|\varsigma| + s(\alpha^2+\varsigma^2)^{-1/2}\right] - s\varepsilon}{\sqrt{\alpha^2 + \left(\varsigma_I - \varsigma\left[1 - s/|\varsigma| + s(\alpha^2+\varsigma^2)^{-1/2}\right] - s\varepsilon\right)^2}}\right) \tag{5}$$

with $t(\varsigma,\varepsilon)$ defined as the sign of the second term in parentheses, redefined dimensionless ion position $\varsigma_I = \gamma z_I/|R_{56}A_1|$, electron beam size $\alpha \equiv a/|R_{56}A_1|$, electron energy spread $\sigma_\varepsilon \equiv \gamma\sigma_p/|A_1|$, and new strength parameters for the modulation, $A_1 = -2cqL_m/a^2I_A$, and kicker, $A_2 \equiv -qIL_k/2\varepsilon_0 c\pi a^2$. Finally, we write down the hybrid case, with point-point interaction in the modulator, but a disc interaction in the kicker; this corresponds to the second case considered in [15], where the particles randomize transversely between the modulation and kicker stages:

$$W_I^{(hybird)}(z_I) = \frac{2\pi|R_{56}B_1|B_2}{\gamma}\int d\varepsilon \frac{e^{-\varepsilon^2/2\sigma_\varepsilon{}^2}}{\sqrt{2\pi}\sigma_\varepsilon}\int \rho d\rho d\varsigma\left(t(\varsigma,\varepsilon) - \frac{\varsigma_I - \varsigma\left[1 - s(\rho^2+\varsigma^2)^{-3/2}\right] - s\varepsilon}{\sqrt{\alpha^2 + \left(\varsigma_I - \varsigma\left[1 - s(\rho^2+\varsigma^2)^{-3/2}\right] - s\varepsilon\right)^2}}\right) \tag{6}$$

with $B_1 = -cqL_m/I_A$, $B_2 = -IqL_k/2c\varepsilon_0(\pi a^2)^2$ and back to the original definition $\varsigma_I \equiv \gamma z_I/r_{spike}$ and $\sigma_\varepsilon = \gamma|R_{56}|\sigma_p/r_{spike}$. Cooling rates are similar for all three cases, so the choice of regimes is larger driven by the parameters of the accelerator and thus the choice of L_m, L_k and β. However, in some regimes the behavior of the three regimes is different, notably the higher bandwidth limit for the 'ring' case, discussed below.

It is interesting to note that cooling is possible with either negative or positive sign of R_{56}. Whereas positive R_{56} produces a spike at the location of the ion, negative R_{56} results in a density hole. The resulting energy shift to the ion has the opposite sign (ions in front of the hole now gain energy), so the ion dispersion must also flip sign. From the pre-factor it is apparent the order of magnitude of cooling is the same, but the different form factor in the integral changes the detailed response. Examples of positive and negative R_{56} for the ring case are given in Fig. 3.

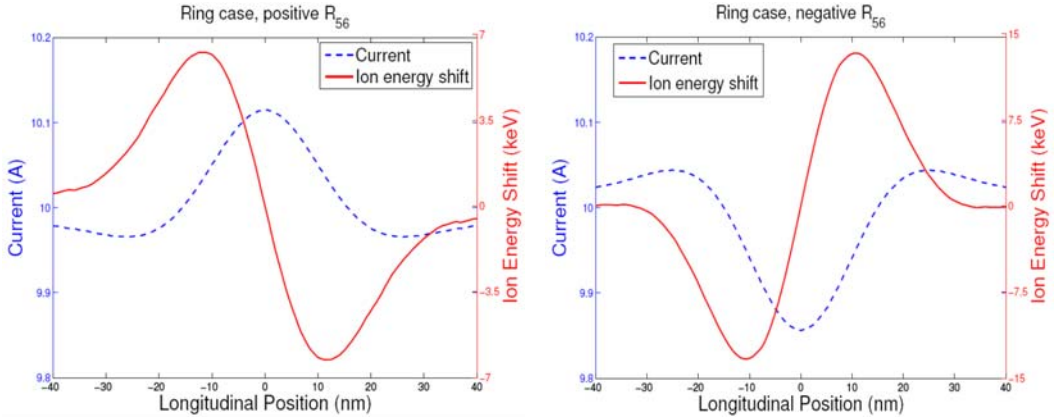

Figure 3: Example average cooling decrement for the 'ring' case with positive dispersion (left) producing a density spike, and negative dispersion (right) creating a density hole. In both plots the dashed blue line gives the electron current, while the red line shows the corresponding shift to the ions.

In all stochastic cooling and CeC methods, there is a fundamental competition between heating and cooling which determines both the cooling rate and the final equilibrium parameters. For CeC, an ion experiences cooling because of the electron beam's response to the presence of that ion. However, surrounding ions in the beam, as well as the shot noise of the electron beam itself, also produce responses by the electron beam; the result of this cross-talk between particles is a stochastic heating effect. If the particles are all randomly distributed, and mix completely turn-by-turn, then the total amplitude of the cross-talk scales as $(N_p N_t)^{1/2}$, where N_t is the number of turns through the cooling section, and N_p is the number of particles within the duration of the cooling response, τ. For the cooling term, which increases linearly with N_t, to dominate the heating term, we then require $N_t > N_p$. This requirement is the time domain analog to the need for large amplifier bandwidth; the shorter the interaction length, or equivalently the larger the bandwidth, the higher the theoretical cooling rate.

We note that in the case studied in [15], the cooling time is determined not by the bandwidth, but by the cooling decrement per turn, δ; with a large energy spread, $\sigma^{Ion}{}_p$, we may find that $\sigma^{Ion}{}_p / \delta > N_p$, in which case it is the cooling decrement, not bandwidth, that limits cooling. However, even in this case, the bandwidth can be important; it is necessary to avoid saturation of the amplifier on a single turn [9,18]. Because the heating response is larger than the cooling response by a factor of $\sqrt{N_p}$, the total gain per turn for a single ion must be a factor of $\sqrt{N_p}$ below the saturation level. As a result, the cooling decrement, δ, is smaller by the same factor as compared to the infinite bandwidth limit.

Given the importance of amplifier bandwidth to cooling, it is interesting to consider the ultimate limits to the MBI bandwidth. First, we note that we are interested in the bandwidth of the cooling response, not just the bandwidth of the MBI gain. For the disc case ($L \gg \beta$), we can approximate cooling duration, τ, by the convolution of the field of an infinitely thin sheet with the electron beam current. The cooling response for a thin sheet has duration of order $L_{res} \sim a/\gamma$, while the current spike, for large energy spreads, has duration of order $L_{spike} \sim R_{56}\sigma_p$. Typically, the MBI bandwidth is limited by the slice energy spread (see e.g. chapter 4.2 of [19]). For the case of Table 1 in [15], $L_{spike} \gg L_{res}$, and reducing the slice energy spread would increase the cooling bandwidth. However,

the cooling response has a fundamental limit of $\tau \geq L_{res}$ regardless of spike duration; any further reduction in L_{spike} has no effect on the bandwidth. It is interesting to note that the limit is different for the ring case (Eq.4), where the response has duration of order $L_{res} \sim r_{spike}/\gamma$ independent of the beam size, a. By choosing parameters so that $r_{spike} \ll a$, it is in principle possible to increase the bandwidth and reduce cooling times. The difference between the ring and disc cases is illustrated in Fig. 4.

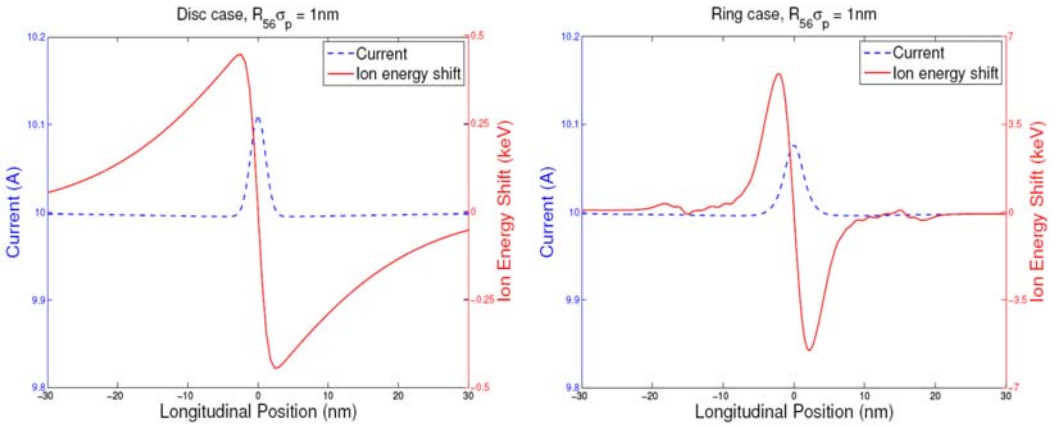

Figure 4: Examples of cooling decrements for $R_{56}\sigma_p$ = 1 nm for the disc case (left) and the ring case (right). In Fig. 3 cooling response duration was determined by the duration of the current spike. In the disc case here, with small energy spread, we see even though the spike has very short duration $L_{spike} \sim$ 1 nm, the cooling duration is still limited by the beam size, $L_{res} \sim a/\gamma$ = 20 nm. In the ring case (right), the cooling response duration is $L_{res} \sim r_{spike}/\gamma$ = 2 nm, allowing for higher bandwidth cooling.

MBI-induced CeC faces a number of technical challenges, including the need for long, high brightness beams and small slice energy spread. Sample parameters for an LHC case are given in [15], but a wide range of parameter space can be considered. The theoretical models presented above all assume a single modulation and dispersion section, but multi-stage schemes are also possible; the extra stages increase the total gain, loosening constraints on dispersion, current, beam size, etc. In addition, using multiple stages allows for the total system to be isochronous (R_{56} = 0), which reduces timing mismatch between the electron and ion beams due to energy jitter.

At present, MBI looks promising as an amplifier for CeC. The potential for very large bandwidths makes MBI appropriate for cooling high density beams, and the implementation is relatively simple. A variety of parameter sets are possible and optimization should be tailored to specific applications. Studies to date have been relatively limited in scope, with detailed 3D tracking simulations remaining to be completed. A proof of principle test is planned as part of Brookhaven National Lab's CeC studies; these efforts are described elsewhere in this issue.

Research is supported by the U.S. Department of Energy under Contract No. DE-AC02-76SF00515.

References

1. G. Budker, At. Energ. 22, 346 (1967).
2. S. Nagaitsev et al., Phys. Rev. Lett. 96, 044801 (2006).
3. S. V. de Meer, Rev. Mod. Phys. 57, 689 (1985).

4. F. Caspers and D. Mohl, in 17th Int. Conf. on High Energy Accelerators (Dubna, Russia, 1998) p. 397.
5. A. Mikhailichenko and M. Zolotorev, Phys. Rev. Lett. 71, 4146 (1993).
6. Y. S. Derbenev, in Proceedings of AIP 253 (AIP, College Park, MD, 1992) pp. 103-110.
7. Y. Derbenev, in Proceedings of COOL (Bad Kreuznach, Germany, 2007).
8. V. Litvinenko, in Proceedings of the 2007 FEL Conference (Novosibirsk, Russia, 2007).
9. V. Litvinenko and Y. Derbenev, Phys. Rev. Lett. 102, 114801 (2009).
10. I. Pinayev et al., in Proceedings of IPAC2012 (New Orleans, USA, 2012) p. MOPPD016.
11. E. L. Saldin, E. A. Schneidmiller, and M. V. Yurkov, Nucl. Instrum. Meth. A 483, 516 (2002).
12. R. Akre et al., Phys. Rev. ST Accel. Beams 11, 030703 (2008).
13. E. A. Schneidmiller and M. V. Yurkov, Phys. Rev. ST Accel. Beams 13, 110701 (2010).
14. A. Marinelli, E. Hemsing, M. Dunning, D. Xiang, S. Weathersby, F. O'Shea, I. Gadjev, C. Hast, and J. Rosenzweig, Phys. Rev. Lett. 110, 264802 (2013).
15. D. Ratner, Phys. Rev. Lett. 111, 084802 (2013).
16. Portions of this summary are taken from reference [15].
17. A. Marinelli and J. Rosenzweig, Phys. Rev. ST Accel. Beams 13, 110703 (2010).
18. G. Stupakov and M. Zolotorev, Phys. Rev. Lett. 110, 269503 (2013).
19. Z. Huang, J. Wu, and T. Shaftan, ICFA Beam Dynamics Newsletter 38 (2005).

2.9 Optical Stochastic Cooling

V. Lebedev, Fermilab, Batavia, IL60510, USA
Mail to: val@fnal.gov

Abstract :

Intrabeam scattering and other diffusion mechanisms result in a growth of beam emittances and luminosity degradation in hadron colliders. In particular, at the end of Tevatron Run II when optimal collider operation was achieved only about 40% of antiprotons were burned in collisions to the store end and the rest were discarded. Taking into account a limited rate of antiproton production further growth of the integral luminosity was not possible without beam cooling. Similar problems limit the integral luminosity in the RHIC operating with protons. For both cases beam cooling is the only effective remedy to increase the luminosity integral. Unfortunately, neither electron nor stochastic cooling can be effective at the beam energy and the bunch density required for modern hadron colliders. Even in the case of LHC where synchrotron radiation damping is already helpful for beam cooling its cooling rates are still insufficient to support an optimal operation of the collider. In this paper we consider principles and main limitations for the optical stochastic cooling (OSC) representing a promising technology capable to achieve required cooling rates. The OSC is based on the same principles as the normal microwave stochastic cooling but uses much smaller wave length resulting in a possibility of dense beam cooling.

2.9.1 Introduction

The stochastic cooling was suggested by Simon Van der Meer [1]. It was critically important technology for success of the first proton-antiproton collider [2]. Since then it has been successfully used in a number of machines for particle cooling and accumulation. There is considerable literature on the subject. Here we would like to point out two references [3,4] reviewing its theory and development for the Tevatron Run II, as well as practical aspects of stochastic cooling usage. These papers also present extended bibliography on the subject.

Although the usage of stochastic cooling has been indispensable for antiproton accumulation and precooling its efficiency is limited for bunched beam cooling at high energy. The bunched beam cooling has been demonstrated for heavy ions in RHIC [5] where the number of particles in the bunch is comparatively small. However it cannot be used for cooling of dense bunched beams in proton-(anti)proton colliders due to much larger number of particles per bunch and, consequently, much higher beam brightness. In the case of optimal cooling the maximum damping rate can be estimated as:

$$\frac{1}{\tau} \approx \frac{2W\sigma_s}{NC} , \qquad (0)$$

where W is the bandwidth of the system, N is the number of particles in the bunch, σ_s is the rms bunch length, and C is the machine circumference. Assuming a system with one octave band and upper boundary of 8 GHz one obtains τ=12000 hour for the LHC proton beam (σ_s=9 cm, C=26.66 km). Effective cooling requires damping rates being at least 3 orders of magnitude higher.

The OSC suggested in Ref. [6] was aimed to address this deficiency. Instead of microwave frequencies it operates at the optical frequencies and, consequently, it can have a bandwidth of ~10^{14} Hz; thus, suggesting a way to achieve the required damping rates. The basic principles of the OSC are similar to the normal (microwave) stochastic cooling. The key difference is the use of optical frequencies, which allows one an increase of system bandwidth by almost 4 orders of magnitude.

Although the OSC was proposed 20 years ago it was not tested in experiment yet. There were suggestions of its experimental implementation in Tevatron [7,8] and RHIC [9] but it was too risky to implement it on the operating collider and the work did not proceed beyond initial proposal. The first attempt to make a test of the OSC with small energy electrons was done in the BATES [10] but it did not get enough support. Presently, Fermilab is constructing a new ring [11,12] devoted to test of the integrable optics and the OSC.

In this paper we consider the theory of stochastic cooling and its implications to the beam and light optics.

2.9.2 Principle of OSC Operation

The wavelength of e.-m. radiation used in the OSC is orders of magnitude smaller than the transverse size of vacuum chamber. In this case usual pickups and kickers employed in the microwave stochastic cooling cannot be used; instead, undulators were suggested [6] to be used for both a pickup and a kicker. In other words, in the OSC a particle emits e.-m. radiation in the first (pickup) undulator. Then, the radiation

amplified in an optical amplifier (OA) makes a longitudinal kick to the particle in the second (kicker) undulator as shown in Figure 1. Further we will call these undulators as the pickup and the kicker. Note that efficiency of transverse kicks is much smaller and therefore the OSC is based on the longitudinal kicks only. Cooling in other planes is based on the plane-to-plane coupling of particle motion. A magnetic chicane is used to make space for the OA and to bring the particle and its amplified radiation together in the kicker undulator.

In further consideration we assume that the path lengths of particle and radiation are adjusted so that the relative longitudinal momentum change of a particle is equal to:

$$\frac{\delta p}{p} = \kappa \sin(k s) \ . \tag{0}$$

Here $k=2\pi/\lambda$ is the radiation wave number, and s is the particle displacement on the way from the pickup to the kicker relative to the reference particle which obtains zero kick. In the linear approximation one can write:

$$s = M_{51} x + M_{52} \theta_x + M_{56} (\Delta p / p) \ , \tag{0}$$

where M_{5n} are the elements of 6×6 transfer matrix from pickup to kicker, x, θ_x and $\Delta p/p$ are the particle coordinate, angle and relative momentum deviation in the pickup center, respectively. In such arrangement the horizontal cooling is achieved by coupling between horizontal and longitudinal motion in the chicane. The vertical cooling is supported by x-y coupling in the rest of the ring.

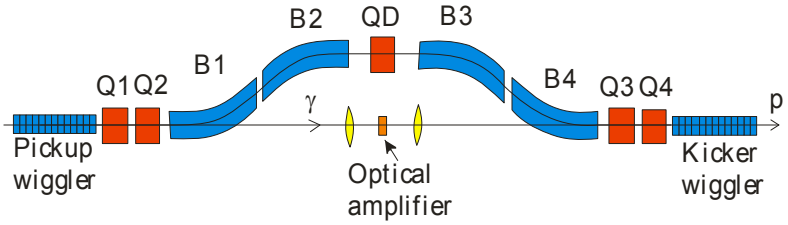

Figure 1: Layout of the cooling system.

2.9.3 Transfer Matrix for Coupled Longitudinal and Horizontal Motions

We assume that a particle motion in the cooling chicane is only coupled between longitudinal and horizontal planes. Consequently, the vertical motion is uncoupled and can be safely omitted from the below analysis. The motion symplecticity binds up the transfer matrix elements so that for 4×4 matrix only 10 of its 16 elements are independent. In the absence of longitudinal kicks between points 1 and 2 (see Figure 2) the matrix between them can be expressed through the Twiss parameters of the points and the M_{56} element, so that:

$$\mathbf{M} = \begin{bmatrix} M_{11} & M_{12} & 0 & M_{16} \\ M_{21} & M_{22} & 0 & M_{26} \\ M_{51} & M_{52} & 1 & M_{56} \\ 0 & 0 & 0 & 1 \end{bmatrix}, \quad \mathbf{x} = \begin{bmatrix} x \\ \theta_x \\ s \\ \Delta p / p \end{bmatrix}. \tag{0}$$

Here the matrix elements of horizontal motion are well-known:

$$M_{11}=\sqrt{\frac{\beta_2}{\beta_1}}\left(\cos\mu+\alpha_1\sin\mu\right),\qquad M_{12}=\sqrt{\beta_1\beta_2}\sin\mu,$$
$$M_{21}=\frac{\alpha_1-\alpha_2}{\sqrt{\beta_1\beta_2}}\cos\mu-\frac{1+\alpha_1\alpha_2}{\sqrt{\beta_1\beta_2}}\sin\mu\ ,\quad M_{22}=\sqrt{\frac{\beta_1}{\beta_2}}\left(\cos\mu-\alpha_2\sin\mu\right), \tag{0}$$

and the matrix elements describing *x*-*s* coupling are bound up by motion symplecticity,

$$\mathbf{M}^T\mathbf{U}\mathbf{M}=\mathbf{U}\ , \tag{0}$$

resulting:

$$M_{16}=D_2-M_{11}D_1-M_{12}D_1',\qquad M_{26}=D_2'-M_{21}D_1-M_{22}D_1',$$
$$M_{51}=M_{21}M_{16}-M_{11}M_{26},\qquad M_{52}=M_{22}M_{16}-M_{12}M_{26}, \tag{0}$$

where $\beta_{1,2}$ and $\alpha_{1,2}$ are the beta-functions and their negative half derivatives at the points 1 and 2, $D_{1,2}$ and $D'_{1,2}$ are the dispersions and their derivatives, respectively, μ is the betatron phase advance between points 1 and 2, and

$$\mathbf{U}=\begin{bmatrix}0&1&0&0\\-1&0&0&0\\0&0&0&1\\0&0&-1&0\end{bmatrix} \tag{0}$$

is the unit symplectic matrix. The matrix elements are enumerated similar to a 6x6 matrix but the elements related to the vertical motion (decoupled from other two degrees of freedom) are omitted. Note that the symplecticity condition implies that the *s* coordinate used in Eq. (0) and (0) represents particle displacement in the bunch frame but not the orbit lengthening often used in the definition of the transfer matrix, so that $\Delta L=\tilde{M}_{56}\Delta p/p$. For an ultra-relativistic bunch these two definitions are bound up as following:

$$M_{56}=\frac{1}{\gamma^2}-\tilde{M}_{56}\ . \tag{0}$$

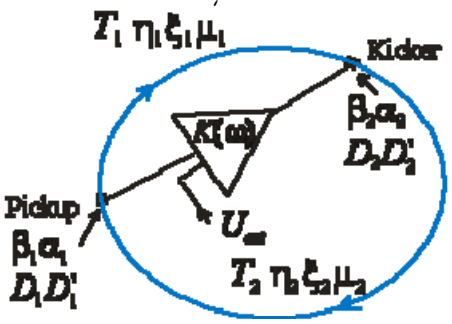

Figure 2: OSC schematic.

Similar to the ring slip-factor, $\eta=1/\gamma^2-\alpha$, we introduce the partial pickup-to-kicker slip-factor, η_{12}, which describes the longitudinal displacement for a particle with momentum deviation $\Delta p/p$ in the absence of betatron oscillations:

$$\eta_{12}=\frac{M_{51}D_1+M_{52}D_1'+M_{56}}{2\pi R}\ . \tag{0}$$

Here α is the ring momentum compaction, and R is the average ring radius ($C=2\pi R$). To simplify further formulas we also introduce the pickup-to-kicker slip-parameter $S_{12}=2\pi R\eta_{12}$. Substituting the matrix elements from Eq. (0) one obtains:

$$S_{12}\equiv 2\pi R\eta_{12}=M_{56}-D_1D_2\left(\frac{1+\alpha_1\alpha_2}{\sqrt{\beta_1\beta_2}}\sin\mu_1+\frac{\alpha_2-\alpha_1}{\sqrt{\beta_1\beta_2}}\cos\mu_1\right)-D_1D_2'\sqrt{\frac{\beta_2}{\beta_1}}\left(\cos\mu_1+\alpha_1\sin\mu_1\right) \quad (0)$$
$$+D_1'D_2\sqrt{\frac{\beta_1}{\beta_2}}\left(\cos\mu_1-\alpha_2\sin\mu_1\right)-D_1'D_2'\sqrt{\beta_1\beta_2}\sin\mu_1\,,$$

where indices 1 and 2 mark the Twiss parameters at the pickup and kicker locations, correspondingly, and μ_1 is the pickup-to-kicker betatron phase advance.

2.9.4 **Ratio of Damping Rates**

The longitudinal kick to a particle due to its interaction with own amplified radiation in the kicker is determined by Eq.(2). Leaving only linear term in the expansion of sin(*ks*) and expressing *s* through the particle positions in the pickup (see. Eq.(0)) one obtains:

$$\frac{\delta p}{p}=\kappa k\left(M_{1_{51}}x_1+M_{1_{52}}\theta_{x_1}+M_{1_{56}}\frac{\Delta p}{p}\right)\,, \quad (0)$$

or in the matrix form:

$$\boldsymbol{\delta}\mathbf{x}_2=\mathbf{M}_c\mathbf{x}_1\,,\quad \mathbf{M}_c=k\kappa\begin{bmatrix}0&0&0&0\\0&0&0&0\\0&0&0&0\\M_{1_{51}}&M_{1_{52}}&0&M_{1_{56}}\end{bmatrix}. \quad (0)$$

Here $\mathbf{x}_1$ is the vector of particle coordinates in the pickup, and we additionally denote the matrix elements of the pick-up to kicker transfer matrix by index 1. Taking this into account one can write down a kicker-to-kicker one turn map:

$$\left(\mathbf{x}_2\right)_{n+1}=\mathbf{M}_1\mathbf{M}_2\left(\mathbf{x}_2\right)_n+\left(\boldsymbol{\delta}\mathbf{x}_2\right)_n=\left(\mathbf{M}_0+\mathbf{M}_c\mathbf{M}_2\right)\left(\mathbf{x}_2\right)_n\,, \quad (0)$$

where n enumerates turns, $\mathbf{M}_2$ is the kicker-to-pickup transfer matrix, $\mathbf{M}_0=\mathbf{M}_1\mathbf{M}_2$ is the entire ring transfer matrix, $(\mathbf{x_2})_n$ is related to the particle coordinates at n-th turn at the point immediately downstream of the kicker, and we took into account $(\mathbf{x_1})_n=\mathbf{M}_2\,(\mathbf{x_2})_n$.

The perturbation theory developed in Ref. [13] (see also [4] for details) for the case of symplectic unperturbed motion yields that the tune shifts are:

$$\delta Q_k=\frac{1}{4\pi}\mathbf{v}_k{}^{+}\mathbf{U}\;\mathbf{M}_c\;\mathbf{U}\,\mathbf{M}_1{}^{T}\mathbf{U}\,\mathbf{v}_k\,, \quad (0)$$

where $\mathbf{v}_k$ are two of four eigen-vectors of unperturbed motion chosen out of each complex conjugate pair and normalized so that $\mathbf{v}_k{}^{+}\mathbf{U}\,\mathbf{v}_k=-2i$ (k=1,2). Performing matrix multiplication and taking into account that the symplecticity binds up M_{51}, M_{52} and M_{16}, M_{26} one finally obtains:

$$\delta Q_k=\frac{k\kappa}{4\pi}\mathbf{v}_k{}^{+}\begin{bmatrix}0&0&0&0\\0&0&0&0\\M_{1_{26}}&-M_{1_{16}}&0&M_{1_{56}}\\0&0&0&0\end{bmatrix}\mathbf{v}_k\,. \quad (0)$$

In the case of small synchrotron tune, $\nu_s << 1$, one can neglect the effect of RF cavities on components of the eigen-vector related to the horizontal betatron motion. Then, the eigen-vector is equal to:

$$\mathbf{v}_1 = \begin{bmatrix} \sqrt{\beta_2} \\ -(i+\alpha_2)/\sqrt{\beta_2} \\ -\left(iD_2(1-i\alpha_2)+D_2'\beta_2\right)/\sqrt{\beta_2} \\ 0 \end{bmatrix} , \qquad (0)$$

Substituting Eq. (0) to Eq. (0) and using Eq. (0) one obtains the damping rate (amplitude, per turn) of the betatron motion:

$$\lambda_1 \equiv \lambda_x = -2\pi \,\mathrm{Im}\,\delta Q_1 = -\frac{k\kappa}{2}\left(D_2 M_{1_{2,6}} - D_2' M_{1_{1,6}}\right) = -\frac{k\kappa}{2}\left(M_{1_{56}} - S_{12}\right) \qquad (0)$$

The condition $\nu_s << 1$ also allows one to neglect the betatron motion on the synchrotron motion. Consequently, for the second eigen-vector (related to the synchrotron motion) one obtains:

$$\mathbf{v}_2 = \begin{bmatrix} -iD_2/\sqrt{\beta_s} \\ -iD_2'/\sqrt{\beta_s} \\ \sqrt{\beta_s} \\ -i/\sqrt{\beta_s} \end{bmatrix} , \qquad (0)$$

where $\beta_s = R\eta/\nu_s$ is the β-function of the longitudinal motion introduced so that $s_{\max} = \beta_s (\Delta p/p)_{\max}$. That yields the damping rate (amplitude, per turn) of the synchrotron motion:

$$\lambda_2 \equiv \lambda_s = -2\pi \,\mathrm{Im}\,\delta Q_2 = -\frac{k\kappa S_{12}}{2} \ . \qquad (0)$$

Summing Eqs. (0) and (0) one obtains the sum of the damping rates:

$$\lambda_1 + \lambda_2 = -\frac{k\kappa}{2} M_{1_{56}} \ . \qquad (0)$$

Although $M_{1_{56}}$ and, consequently, the sum of damping rates depend only on focusing inside the chicane, the ratio of damping rates depends on the dispersion at the chicane beginning, *i.e.* on the ring dispersion. Eqs. (0) and (0) yield the ratio of damping rates,

$$\frac{\lambda_x}{\lambda_s} = \frac{M_{1_{56}}}{S_{12}} - 1 \ . \qquad (0)$$

2.9.5 **The Cooling Range**

The cooling force is linear for small amplitude oscillations only. Combining Eqs. (0) and (0), and performing simple transformations one obtains:

$$\frac{\delta p}{p} = \kappa \sin\left(a_x \sin(\psi_x) + a_p \sin(\psi_p)\right) , \qquad (0)$$

where a_x, a_p, ψ_x and ψ_p are the dimensionless amplitudes (expressed in the phase advance of laser wave) and phases of pickup-to-kicker path lengthening due to betatron and synchrotron motions, respectively. The dimensionless amplitude due to synchrotron motion directly follows from Eq. (0):

$$a_p = k\left(M_{1_{51}} D_1 + M_{1_{52}} D_1' + M_{1_{56}}\right)\left(\frac{\Delta p}{p}\right)_m , \qquad (0)$$

where $(\Delta p/p)_m$ is the amplitude of momentum oscillations. To find the dimensionless amplitude due to betatron motion we express particle coordinates through its Courant-Snyder invariant[2], $\tilde{\varepsilon}$, and phase, ψ:

$$x_1 = \sqrt{\tilde{\varepsilon}\beta_1}\cos\psi\ , \qquad \theta_{x_1} = -\sqrt{\tilde{\varepsilon}/\beta_1}\left(\sin\psi + \alpha_1\cos\psi\right). \tag{0}$$

Substituting these expressions to the equitation describing the longitudinal displacement due to betatron motion, $M_{1_{51}}x_1 + M_{1_{52}}\theta_{x_1}$, and performing simple transformations one obtains the dimensionless amplitude due to betatron motion:

$$a_x = k\sqrt{\tilde{\varepsilon}\left(\beta_1 {M_{1_{51}}}^2 - 2\alpha_1 M_{1_{51}}M_{1_{52}} + \left(1+\alpha_1^2\right){M_{1_{52}}}^2/\beta_1\right)}\ . \tag{0}$$

Averaging momentum kicks over betatron and synchrotron oscillations one obtains the fudge factors for the transverse and longitudinal damping rates:

$$\begin{bmatrix}\lambda_1(a_x,a_p)/\lambda_1\\ \lambda_2(a_x,a_p)/\lambda_2\end{bmatrix} \equiv \begin{bmatrix}F_1(a_x,a_p)\\ F_2(a_x,a_p)\end{bmatrix} = \begin{bmatrix}2/(a_x\cos\psi_c)\\ 2/a_p\end{bmatrix} \int\!\!\int \sin\left(a_x\sin\left(\psi_x+\psi_c\right)+a_p\sin\psi_p\right)\begin{bmatrix}\sin\psi_x\\ \sin\psi_p\end{bmatrix}\frac{d\psi_x}{2\pi}\frac{d\psi_p}{2\pi}, \tag{0}$$

where ψ_c is the phase shift of the transverse cooling force. Computation of the integrals yields:

$$\begin{bmatrix}F_1(a_x,a_p)\\ F_2(a_x,a_p)\end{bmatrix} = 2\begin{bmatrix}J_0(a_p)J_1(a_x)/a_x\\ J_0(a_x)J_1(a_p)/a_p\end{bmatrix}, \tag{0}$$

where J_0(x) and J_1(x) are the Bessel functions. One can see that the damping rates oscillate with growth of amplitudes. For a given degree of freedom the damping rate changes the sign at its own amplitude equal to $\mu_{11}\approx 3.832$ and at the amplitude of $\mu_{01}\approx 2.405$ for other degree of freedom. Taking into account that the both cooling rates have to be positive for all amplitudes one obtains the stability condition, $a_{x,p}\le\mu_{01}\approx 2.405$. That yields the stability boundaries for the emittance and the momentum spread:

$$\varepsilon_{\max} = \frac{{\mu_{01}}^2}{k^2\left(\beta_p {M_{1_{51}}}^2 - 2\alpha_p M_{1_{51}}M_{1_{52}} + \gamma_p {M_{1_{52}}}^2\right)}\ , \tag{0}$$

$$\left(\frac{\Delta p}{p}\right)_{\max} = \frac{\mu_{01}}{kS_{12}}\ .$$

(0)

For further analysis we introduce the relative cooling ranges as ratios of cooling area boundaries $(\Delta p/p)_{\max}$ and ε_{max} to the rms values of momentum spread, σ_p, and horizontal emittance, ε. That yields:

$$n_{\sigma s} = (\Delta p/p)_{max}/\sigma_p\ , \quad n_{\sigma x} = \sqrt{\varepsilon_{\max}/\varepsilon}\ . \tag{0}$$

As one can see the transverse cooling range does not depend on the dispersion in the pickup undulator but depends on the beta-function in there. Beam cooling in a collider requires $n_{\sigma x}, n_{\sigma s} \ge 4$.

[2] The Courant-Snyder invariant is defined as following: $\tilde{\varepsilon} = x^2/\beta + 2\alpha x\theta + \left(1+\alpha^2\right)\theta^2/\beta$.

2.9.6 **Beam Optics and its Limitations**

The analysis of possible optics arrangements in the cooling area yields that the layout presented in Figure 1 is not only the most straightforward but also represents a reliable and effective choice. The cooling chicane consists of four dipoles with parallel edges, which in the absence of other focusing elements does not produce focusing in the horizontal plane resulting in that $M_{1_{56}} = S_{12}$. As one can see from Eq. (0) transverse cooling requires $M_{1_{56}}$ and S_{12} being different. It is achieved by placing a defocusing quad in the chicane center.

To make a simple estimate showing interdependency of cooling parameters we leave only leading terms in the thin lens approximation assuming also that the bends have zero length and do not produce horizontal focusing. That yields:

$$M_{1_{56}} \approx 2\Delta s\,, \quad S_{12} \approx 2\Delta s - \Phi D^* h\,, \quad \lambda_x / \lambda_s \approx \Phi D^* h / \left(2\Delta s - \Phi D^* h\right). \tag{0}$$

Here Δs and h are the path lengthening and the trajectory offset in the chicane, respectively, $\Phi=1/F$ is the defocusing strength of the quad located in the chicane center, and D^* is the dispersion in there. Similarly, using Eq. (0) one obtains estimates for the cooling ranges:

$$n_{\sigma s} \approx \frac{\mu_{01}}{\left(2\Delta s - \Phi D^* h\right) k\sigma_p}\,, \qquad n_{\sigma x} \approx \frac{\mu_{01}}{2kh\Phi\sqrt{\varepsilon\beta^*}}\,, \tag{0}$$

where β^* is the beta-function in the chicane center. Above we assumed that the optics is symmetric relative to the chicane center, *i.e.* $dD/ds=0$ and $d\beta/ds=0$ in the chicane center. Such choice minimizes the maximal dispersion and beta-function in the cooling area.

Table 1: Tentative beam optics parameters for the Fermilab OSC test and the LHC

	Fermilab OSC test	OSC for the LHC
Rms momentum spread, σ_p	$1.2\cdot10^{-4}$	10^{-4}
Rms emittance, ε, nm	4.4	0.5
Delay in the cooling chicane, Δs, mm	2	2
Cooling range, $n_{\sigma x}$, $n_{\sigma s}$	3	4
Required wave length, μm	1.8	2.1
Dispersion invariant in the chicane center, A^*, m	1.3	0.35

As one can see from Eq. (0) the parameter $\Phi D^* h$ determines the ratio of cooling rates. Assuming equal damping rates one obtains, $\Delta s=\Phi D^* h$, and, consequently, the cooling ranges are:

$$n_{\sigma s} \approx \frac{\mu_{01}}{k\sigma_p \Delta s}\,, \qquad n_{\sigma x} \approx \frac{\mu_{01}}{2k\Delta s}\sqrt{\frac{D^{*2}}{\varepsilon\beta^*}} \equiv \frac{\mu_{01}}{2k\Delta s}\sqrt{\frac{A^*}{\varepsilon}}\,, \tag{0}$$

where $A^*=D^{*2}/\beta^*$ is the dispersion invariant[3] in the chicane center. Its value is conserved in a straight line where bending magnets are absent. As one can see from the above equations the cooling dynamics is determined by a handful of parameters: the initial rms momentum spread and emittance (σ_p,ε), the wave number of optical amplifier (k), the dispersion invariant (A^*) and the path length delay (Δs). The value of Δs is determined

[3] The dispersion invariant is defined as follows: $A_x = D_x^2\left(1+\alpha_x^2\right)/\beta_x + 2\alpha_x D_x' D_x + \beta_x D_x'^2$. The derivatives of beta-functions and dispersion are equal to zero in the chicane center. That yields: $A^* = D_x^2/\beta_x$.

by signal delay in optical amplifier and normally should be in the range of few mm. In this evaluation we will assume Δs=2 mm – the value expected for the OSC test in Fermilab [12]. Table 1 presents tentative beam optics parameters for the Fermilab OSC test and the LHC operating at 4 TeV. Note that while parameters presented for the Fermilab OSC test are close to the actual proposal (as will be seen later), the LHC parameters are not supported by detailed consideration and therefore can be considered only as a numerical example. Note also that one can significantly affect the optics parameters by changing the ratio of cooling rates. In particular, an increase of horizontal damping can allow a reduction of the optical amplifier wavelength, but at the same time it makes more difficult to handle an increase of beta-function in the cooling area required to keep sufficiently large value for the horizontal cooling range.

Large value of the dispersion invariant required for the OSC leads to a collider type optics, *i.e.* optics with small value of the beta-function in the chicane center so that the large value of the invariant could be achieved with manageable value of dispersion. Figure 3 presents beta-functions and dispersion in the cooling area for the Fermilab OSC test. Figure 4 shows corresponding dispersion invariant. The equilibrium horizontal emittance is mainly excited by synchrotron radiation which contribution to the diffusion is proportional to the average value of dispersion invariant in dipoles. In order to minimize the equilibrium horizontal emittance, the strength of quadrupoles in the chicane vicinity was adjusted to reduce the dispersion invariant as fast as possible outside of cooling area As one can see the value of the invariant is significantly larger than the value presented in Table 1. It allowed significant increase of cooling ranges. It has been required for an improvement of beam lifetime which is mainly determined by particle scattering on atoms of residual gas. The choice of optics supports: $n_{\sigma x}$=9.2, $n_{\sigma s}$=5.6, λ_x/λ_s=2.5. Figure 5 presents dependences for $M_{1_{56}}$ and S_{12} on the beam travel from pickup to kicker. One can see that S_{12} has large variations of its value on the beam travel through the chicane. These variations are excited by large dispersion in the chicane. In the absence of focusing S_{12} and $M_{1_{56}}$ would be equal at the chicane end. Non-zero focusing makes them different. Large S_{12} variations make resulting S_{12} being quite sensitive to optics errors. There is even higher sensitivity of sample lengthening to optics errors in the case of betatron motion. Figure 6 presents sample lengthening due to betatron motion. One can see that the final lengthening is about 300 times smaller than its peak value located between chicane dipoles.

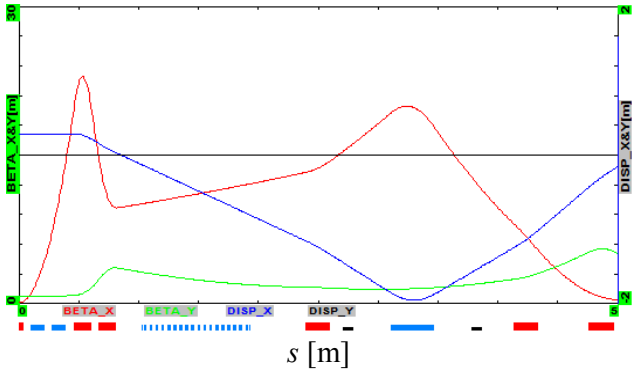

Figure 3: Beta-functions (β_x – red, β_y – green) and dispersion (dark blue) for half of cooling area of the Fermilab OSC test. Chicane center is located at $s = 0$; red squares at the bottom mark positions of quadrupoles, the blue squares – dipoles and undulator.

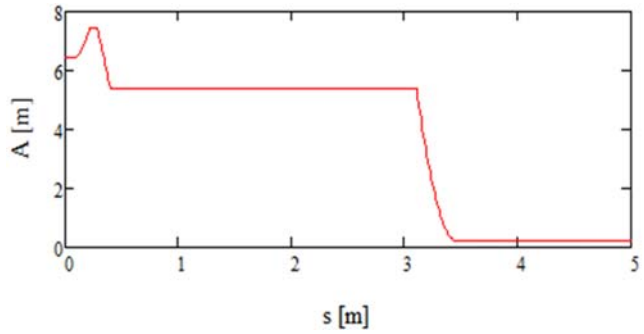

Figure 4: The dispersion invariant, A_x, for half of cooling area of the Fermilab OSC test.

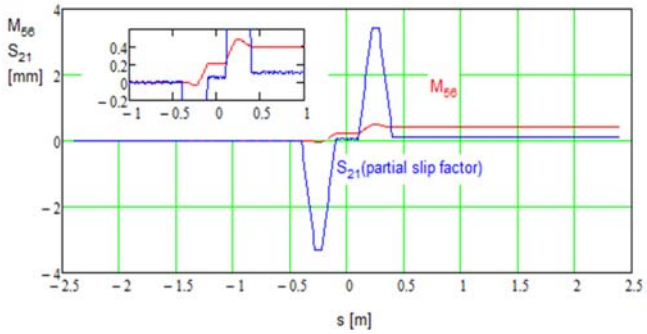

Figure 5: Dependence of M_{56} and S_{12} in the cooling area of the Fermilab OSC test; $s = 0$ corresponds to the chicane center.

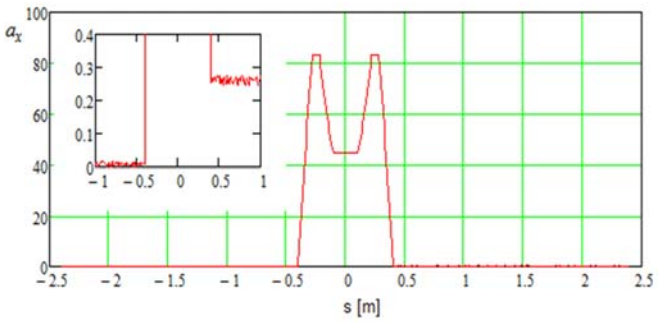

Figure 6: Dimensionless rms sample lengthening due to betatron motion, a_p, in the cooling area of the Fermilab OSC test; $s = 0$ corresponds to the chicane center.

Another important limitation on the beam optics is associated with the higher order contributions to the sample lengthening coming from the betatron and synchrotron motions. The major contribution comes from particle angle, $\theta(s)$, which introduces the relative delay $\Delta s/s$ equal to $\theta(s)^2/2$. To obtain the particle angle on the way from the pickup to the kicker we differentiate its horizontal position, $x(s) = \sqrt{\varepsilon\beta(s)}\cos\left(\mu(s)-\mu_0\right)$, over s. An integration of square of the obtained angle yields the orbit lengthening:

$$\Delta s_2 = \frac{1}{2}\int_{-L_c/2}^{L_c/2}\left(\sqrt{\frac{\varepsilon}{\beta(s)}}\left(\sin\left(\mu(s)-\mu_0\right)+\alpha(s)\cos\left(\mu(s)-\mu_0\right)\right)\right)^2 ds = \frac{\varepsilon}{2}\int_{-\mu_c/2}^{\mu_c/2}\left(\sin\left(\mu-\mu_0\right)+\alpha(\mu)\cos\left(\mu-\mu_0\right)\right)^2 d\mu\,. \quad (0)$$

Here μ_0 is the initial betatron phase, μ is the betatron phase advance along the particle trajectory, L_c is the total path length from pickup to kicker, and we took into account that $d\mu=ds/\beta$. Assuming that the optics in the cooling area is symmetric relative to the chicane center one can reduce Eq. (0) to the following form:

$$\Delta s_2 = \frac{\varepsilon}{2}\left(I_1 - I_2\cos(2\mu_0)\right),\quad I_1 = \int_0^{\mu_c/2}\left(1+\alpha^2(\mu)\right)d\mu\,,\quad I_2 = \int_0^{\mu_c/2}\left(\left(1-\alpha^2(\mu)\right)\cos(2\mu)-2\alpha(\mu)\sin(2\mu)\right)d\mu\,, \quad (0)$$

where μ_0 is now referenced to the particle betatron phase in the chicane center (it was referenced to $s = -L_c/2$ in Eq. (0)). The maximum lengthening is achieved for $\mu_0=\pi/2$ and is equal to: $\Delta s = \varepsilon\left(I_1 + I_2\right)/2$.

Numeric averaging of cooling force with the second order lengthening taken into account shows that to avoid shrinking of cooling boundary the second order contribution at the cooling boundary has to be less or about half of the first order contribution (see Eq.(0)). That yields the requirement on an acceptable value of the second order contribution computed at the boundary of cooling range (defined by Eq. (0)): $k\Delta s_2 \le 1.5$.

Figure 7 presents integrals I_1 and I_2 as functions of path length for the Fermilab OSC test. One can see that the values of integrals are significantly larger for the horizontal plane. It is related to the small beta-function in the chicane center which yields large particle angles in the area between focusing doublets, $\theta = \sqrt{\varepsilon/\beta^*}$. In this case the total lengthening can be estimated by simple formula: $\Delta s \approx L_q\varepsilon/2\beta^*$, where L_q is the distance between quadrupole doublets. For the Fermilab OSC test the non-linear path lengthening due to vertical betatron motion is 0.017 μm at 1σ and does not

represent a problem. However its value for the horizontal plane of 0.25 μm at 1σ destroys cooling for betatron amplitudes above 1.5σ and therefore has to be compensated.

The compensation is achieved by placing a sextupole in between dipoles of each chicane leg. It decreases the sample lengthening by more than an order of magnitude so that the contribution for the horizontal plane is smaller than for the vertical one. The sextupoles are located at the betatron phase advance close to 180 deg. It significantly decreases the driving terms of sextupole related resonances. However the compensation is not perfect and an additional suppression by ring sextupoles is required. They also have to compensate undesired chromaticity introduced by the chicane sextupoles.

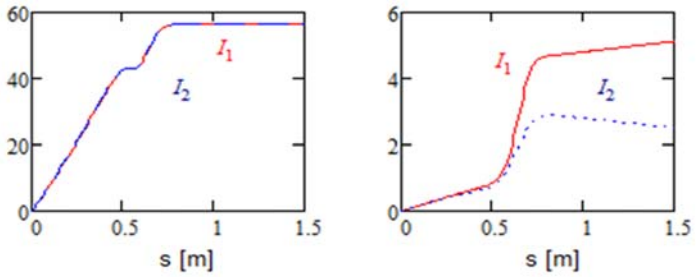

Figure 7: Integrals I_1 (red) and I_2 (blue) of Eq. (0) in the cooling area of the Fermilab OSC test; horizontal plane – left, vertical plane – right.

2.9.7 **Damping Rates**

To compute the OSC damping rates we need to find a longitudinal kick which a particle receives in the kicker undulator from its own radiation radiated in the pickup undulator and then amplified and focused to the kicker undulator. We split this problem into the following steps: finding electric field of the radiation on the focusing lens surface, computing the electric field in the kicker undulator by integration of the field distribution on the lens, and, finally, finding the longitudinal kick in the kicker undulator. We assume that the distances from the pickup center to the lens and from the lens to the kicker center are equal and are much larger than the pickup and kicker lengths; so large that the depth of field would not result in a deterioration of the interaction. Applicability of such requirement will be discussed later. We also assume that the pickup and kicker undulators are flat, have the same length and the same number of periods.

The e.-m. radiation coming out from the pick-up undulator is determined by the Liénard-Wiechert formula [14]:

$$\mathbf{E}(\mathbf{r},t)=\frac{e}{c^2}\frac{(\mathbf{R}-\boldsymbol{\beta}R)(\mathbf{a}\cdot\mathbf{R})-\mathbf{a}\left(R-(\boldsymbol{\beta}\cdot\mathbf{R})\right)}{\left(R-(\boldsymbol{\beta}\cdot\mathbf{R})\right)^3},\quad \mathbf{a}=\frac{d\mathbf{v}}{dt},\quad \mathbf{R}=\mathbf{r}-\mathbf{r}'\ . \tag{0}$$

Here e is the particle charge, $\boldsymbol{\beta}=\mathbf{v}/c$ is the dimensionless particle velocity, $\mathbf{R}$ is the vector from point of the radiation, $\mathbf{r}'$, to the point of observation, $\mathbf{r}$, and all values are taken at the retarded time $t'= t - R/c$. Let the coordinates of a particle moving in a flat undulator to depend on time as following:

$$\mathrm{v}_x = c\theta_e \sin\tau', \qquad \mathrm{v}_y = 0, \qquad \mathrm{v}_z = c\left(1 - \frac{1}{2\gamma^2} - \frac{\theta_e^{\,2}}{2}\sin^2\tau'\right), \qquad \tau' = \omega_u t' + \psi \qquad (0)$$

where ω_u is the frequency of particle motion in the undulator, and θ_e is the amplitude of particle angle oscillations. Substituting velocities of Eq. (0) to Eq. (0) and simplifying the obtained equation one obtains the horizontal component of electric field in the far zone:

$$E_x(r,t) = 4e\omega_u\gamma^4\theta_e \cos\tau' \frac{1+\gamma^2\left(\theta^2\left(1-2\cos^2\phi\right) - 2\theta\theta_e \sin\tau'\cos\phi - \theta_e^{\,2}\sin^2\tau'\right)}{cR\left(1+\gamma^2\left(\theta^2 + 2\theta\theta_e\sin\tau'\cos\phi + \theta_e^{\,2}\sin^2\tau'\right)\right)^3}, \qquad (0)$$

where θ and ϕ are the angles in the polar coordinate frame for the vector **R**, and we took into account that $a_x = c\theta_e\omega_u$. The vertical and longitudinal components of the electric field are averaged out at the focus and therefore can be safely omitted from further consideration.

Only the first harmonic of the radiation interacts resonantly with the particle in the kicker undulator. Therefore we keep only the first harmonic of radiation in further calculations:

$$E_\omega(r) = \frac{\omega(\theta)}{\pi}\int_0^{2\pi/\omega(\theta)} E_x(r,t)\,\mathrm{e}^{-i\omega t}\,dt, \qquad \omega(\theta) = 2\gamma^2\omega_u \Big/ \left(1+\gamma^2\left(\theta^2 + \theta_e^{\,2}/2\right)\right). \qquad (0)$$

Omitting higher harmonics is also justified by the fact that their radiation is usually absorbed in the lens(es) focusing radiation from the pickup to the kicker and is not amplified by optical amplifier (if present).

To find the electric field in the kicker undulator, where the radiation is focused, we use the Kirchhoff formula:

$$E(r'') = \frac{1}{2\pi i c}\int_S \frac{\omega(\theta)E_\omega(r)}{|r''-r|}\mathrm{e}^{i\omega(\theta)|r''-r|/c}\,ds \ . \qquad (0)$$

Here r'' is the coordinate in the observation point in the kicker undulator, the integration is performed over the lens surface S, and the electric field there is described by Eqs. (0) and (0). The focal length of the lens is equal to $R/2$. It results in that an increase of delay time related to path lengthening, $2(R\theta^2/2)$, is compensated in the lens. It makes all waves arriving to the focus point having the same phase, and, consequently, the exponent in Eq. (0) accounting for these delays is reduced to a complex constant which will be omitted in further calculations. Note that although the frequency of radiation coming out from radiation point depends on θ this dependence disappears in the kicker undulator (in the image plane) due to interference of the waves coming from different directions.

The above equations can be significantly simplified in the case of small undulator parameter, $K = \gamma\theta_e << 1$. Then Eq. (0) can be simplified yielding the wave amplitude on the lens surface:

$$E_x = \frac{4e\gamma^4\omega_u\theta_e}{cR}\frac{1+(\gamma\theta)^2\left(1-2\cos\phi\right)}{\left(1+(\gamma\theta)^2\right)^3}, \qquad (0)$$

The dependence of frequency on θ_e can be neglected and an integration in Eq. (0) results in the amplitude of electric field in the kicker undulator:

$$E_x = \frac{4e\gamma^4\omega_u^{\,2}\theta_e}{3c^2} f_L(\gamma\theta_\mathrm{m}), \quad f_L(x) = 1 - \frac{1}{\left(1+x^2\right)^3} \ . \qquad (0)$$

Here θ_m is the angle subtending the lens from the pickup undulator and we assume a round lens. Averaging the energy transfer (dE/dt=eE$_x$v$_x$) over oscillations in the kicker undulator we finally obtain the amplitude of the energy change in the kicker undulator in the absence of optical amplification:

$$\Delta \mathrm{E} = \frac{2e^4 B_0^{\,2}\gamma^2}{3m^2c^4} L_u \, f_L\left(\gamma\theta_{\mathrm{m}}\right) \quad . \tag{0}$$

Here B_0 is the peak magnetic field in the undulator, L_u is its total length, and m is the particle mass. We also took into account that $\theta_e = eB_0/\left(mc\gamma\omega_u\right)$.

Note that in the absence of optical amplification and $\gamma\theta_{\max} >> 1$ the amplitude of energy loss is equal to the total energy loss in both undulators: $\Delta \mathrm{E}_{tot} = 2e^4 B_0^{\,2}\gamma^2 L_u / \left(3m^2c^4\right)$. The interference of radiation of two undulators results in the energy loss being modulated with the path length difference on the travel from pickup to kicker: $\Delta \mathrm{E}(\Delta s) = -\Delta \mathrm{E}_{tot}\left(1+\cos(k\Delta s)\right)$. For longitudinal motion we can rewrite it as:

$$\Delta \mathrm{E}(\Delta p) = -\Delta \mathrm{E}_{tot}\left(1+\cos\left(kS_{12}\frac{\Delta p}{p}\right)\right) \quad . \tag{0}$$

Taking into account that the damping decrement is proportional to $d\Delta \mathrm{E}/dp$ one obtains that the interference of radiation from two undulators amplifies the damping rate due to their synchrotron radiation by the ratio of beam energy to it's the cooling range, $\Box\, p/n_{\sigma p}\sigma_p$. The same statement is justified for the betatron motion. Note that an average energy loss presented in Eq. (0) is compensated by an RF system and does not effect on the cooling dynamics.

The cooling rates are determined by Eqs. (0) and (0) where parameters k and κ introduced in Eq. (0) are equal to:

$$k = \frac{2\gamma^2\omega_u}{c}, \qquad \kappa = \frac{2e^4 B_0^{\,2}\gamma}{3m^3c^5} L_u \, K_a f_L\left(\gamma\theta_{\mathrm{m}}\right). \tag{0}$$

Here we added an effect of e.-m. wave amplification in an optical amplifier with gain K_a (in amplitude). We also assume that the bandwidth of optical amplifier is large enough so that the spectrum widening due to finite number of undulator periods $2\gamma^2\omega_u / n_w$ and the angular spread of radiation $2\gamma^4\omega_u\theta_{\max}$ would be inside the amplifier bandwidth. Here n_w is the number of undulator periods. Otherwise one needs to average the cooling force within amplifier bandwidth. Note also that for large amplitude oscillations the fudge factors introduced in Eqs. (0) and (0) have to be taken into account.

In the general case of arbitrary undulator parameter the amplitude of electric field in the kicker undulator can be expressed in the following form:

$$E_x = \frac{4e\omega_u^{\,2}\gamma^4\theta_e}{3c^2} F_h\left(\gamma\theta_e, \gamma\theta_m\right), \tag{0}$$

where

$$F_h(\Theta_e,\Theta_m)=\frac{3}{\pi^2}\int_0^{\Theta_m}d\Theta\int_0^{2\pi}d\phi\int_0^{2\pi}d\tau\,\frac{\Theta F_c(\Theta,\Theta_e,\tau,\phi)}{1+\Theta^2+\frac{\Theta_e^{\,2}}{2}}\,\frac{1+\Theta^2\left(1-2\cos^2\phi\right)-2\Theta\Theta_e\cos\phi\sin\tau-\Theta_e^{\,2}\sin^2\tau}{\left(1+\Theta^2+2\Theta\Theta_e\cos\phi\sin\tau+\Theta_e^{\,2}\sin^2\tau\right)^3},$$

$$F_c(\Theta,\Theta_e,\tau,\phi)=\left(1+\frac{4\Theta\Theta_e\cos\phi\sin\tau-\Theta_e^{\,2}\cos(2\tau)}{2\left(1+\Theta^2+\frac{\Theta_e^{\,2}}{2}\right)}\right)\exp\left(-i\tau+i\,\frac{\Theta_e^{\,2}\sin(2\tau)+8\Theta\Theta_e\cos\phi\cos\tau}{4\left(1+\Theta^2+\frac{\Theta_e^{\,2}}{2}\right)}\right)\cos\tau\,. \qquad (0)$$

For the large acceptance lens, $\theta_m \geq \theta_e+3/\gamma$ the function $F_h(\Theta_e,\theta_m)$ computed with numerical integration can be interpolated by the following equation:

$$F_h(K,\infty)\approx\frac{1}{1+1.07K^2+0.11K^2+0.36K^4}\,,\quad 0\leq K\leq 4\,. \qquad (0)$$

Integrating the force along the kicker length one obtains the longitudinal kick amplitude in a flat undulator:

$$\Delta E=\frac{2\pi}{3}\alpha_F n_w\hbar\omega_0 K^2\left(1+\frac{K^2}{2}\right)F_h(K,\gamma\theta_m)F_u(\kappa_u),\quad \begin{matrix}F_u(\kappa_u)=J_0(\kappa_u)-J_1(\kappa_u),\\ \kappa_u=K^2/\left(4\left(1+K^2/2\right)\right).\end{matrix} \qquad (0)$$

Here $\alpha_F=e^2/\hbar c$ is the fine structure constant, and $\omega_0=2\gamma^2\omega_u\left(1+K^2/2\right)$ is the base frequency of the radiation. For small K this equation coincides with Eq.(0). Figure 8 presents a dependence of dimensionless kick, $F_t(K,\gamma\theta_m)=K^2\left(1+K^2/2\right)F_h(K,\gamma\theta_m)F_u(\kappa_u)$, on the undulator parameter for different values of $\gamma\theta_m$. The same as above we imply here that the optical amplifier gain is equal to one and its bandwidth is larger than the bandwidth of the first harmonic radiation coming from the pickup undulator. Otherwise averaging over the bandwidth is additionally required.

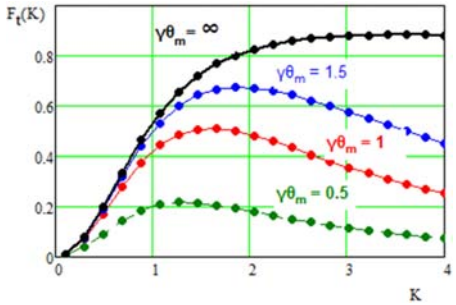

Figure 8: Dependence of dimensionless longitudinal kick on the undulator parameter.

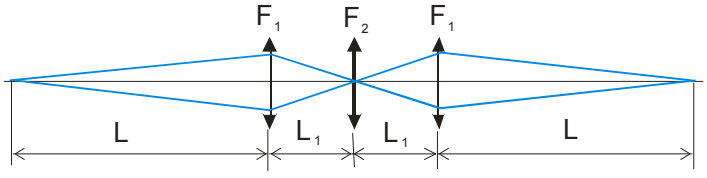

Figure 9: Light optics layout for passive cooling.

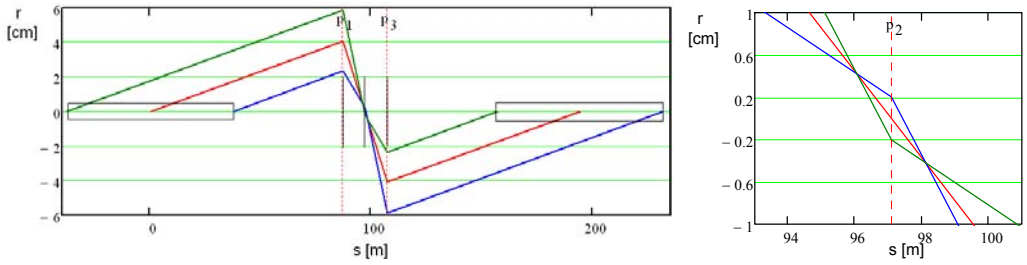

Figure 10: Trajectories of rays radiated at the beginning, in the middle and at the end of pickup undulator. Right pain shows details near the center of the system. Vertical lines show positions of the lenses.

2.9.8 **Light Optics**

In above discussion we assumed that the radiation emitted by a particle in the course of its motion in the pickup is focused to the location of the same particle in the kicker (when the particle arrives to it) in the course of particle entire motion in the kicker. It is automatically achieved for the lens located at the infinity (*i.e.* if the distance to the lens is much larger than the length of undulator) – the condition which is impossible to achieve in practice. A practical solution can be obtained with lens telescope which has the transfer matrix $\mathbf{M}_T$ from the center of pickup to the center of kicker equal to $\pm\mathbf{I}$, where **I** is the identity matrix. In this case the transfer matrix between emitting and receiving points is $\mathbf{O}(l)\mathbf{M}_T\,\mathbf{O}(-l) = \pm\mathbf{I}$, *i.e.* coincides with the matrix for the system where the lens is located at infinity. Here $\mathbf{O}(l)$ is the transfer matrix of a drift with length l. The simplest telescope requires 3 lenses. An example is presented in Figure 9. For symmetrically located lenses their focusing distances are:

$$F_1 = \frac{LL_1}{L+L_1}, \quad F_2 = \frac{L_1^2}{2(L+L_1)} \quad . \tag{0}$$

Here F_1 is the focal distance for two outer lenses, and F_2 is the focal distance for the central lens. Figure 10 presents an example of ray propagation through such focusing system. As one can see the light focus is propagated together with particle displacement in the kicker undulator.

2.9.9 **Conclusions**

The optical stochastic cooling can support the cooling rates orders of magnitude larger than have been achieved with the micro-wave stochastic cooling. Its experimental study is required before it can be used in practical application for high intensity storage rings and hadron colliders. Such applications will require a new generation of optical amplifiers with the following requirements: (1) small signal delay (less than few mm), (2) large gain (more than ~20-30 Db), duration of single pulse amplification sufficient to cover a bunch of cooled particles (0.1-1 ns), and (3) sufficiently large power (10 – 100 W). Fermilab plans to do the OSC tests with 100 MeV electrons in the IOTA ring [12] within next few years. Choice of small energy electrons greatly simplifies the experiment and reduces its cost.

2.9.10 **Acknowledgements**

The author would like to express his sincere gratitude to Dr. Max Zolotorev for initiating this work, for multiyear collaboration and many contributions without which this work would not be possible. I also would like to thank Dr. K. Yonehara for help in editing this paper.

2.9.11 **References**

1. S. Van der Meer, "Stochastic damping of betatron oscillations", internal report CERN/ISR PO/72/31 (1972).
2. R. Billinge and M. C. Crowley-Milling, "The CERN proton-antiproton colliding beam facilities", IEEE Transactions on Nuclear Science, Vol. NS-26, No. 3, June 1979.
3. J. Bisognano and C. Leemann, "Stochastic Cooling" in 1981 Summer School on High Energy Particle Accelerators, AIP Conf. Proceedings 87, Melville, NY, 1982, pp. 584-655.
4. V. Lebedev and V. Shiltsev (Eds.), "Accelerator Physics at the Tevatron Collider", Springer, 2014.
5. M. Blaskiewicz, J. M. Brennan, F. Severino, "Stochastic Cooling of High-Energy Bunched Beams", Proceedings of PAC07, Albuquerque, New Mexico, USA.
6. M. S. Zolotorev and A. A Zholents, "Transit-time method of optical stochastic cooling", Phys. Rev. E, 50, 4, p. 3087 (1994).
7. A. Zholents and M. Zolotorev, "An amplifier for optical stochastic cooling", p. 1804, PAC'97 (1997).
8. V. Lebedev, "Optical Stochastic Cooing in Tevatron", Proceedings of HB2010, Morschach, Switzerland, 2010.
9. M. Babzien, et.al, "Optical stochastic cooling for RHIC using optical parametric amplification", PRST-AB, 7, 012801 (2004).
10. W. Franklin, et. al., "Optical Stochastic Cooling Experiment at the MIT-Bates South Hall Ring", p. 117, COOL-2007 (2007)
11. V. Lebedev, "Test of Optical Stochastic Cooling in Fermilab", Proceedings of HB2012, Beijing, China.
12. V. Lebedev, "Test of Optical Stochastic Cooling in the IOTA Ring", Proceedings of PAC2013, Pasadena, CA USA.
13. A. Burov and V. Lebedev, "Coupling and its Effects on Beam Dynamics", Proceedings of Hadron Beam 2008, Nashville, Tennessee, USA.
14. L. D. Landau, "Classical theory of fields", Nauka (1973).

2.10 Simulating Single-pass Dynamics for Relativistic Electron Cooling

David L. Bruhwiler
RadiaSoft LLC, Boulder, CO 80304, USA
RadiaBeam Technologies LLC, Santa Monica, CA 90404, USA
Mail to: bruhwiler@radiasoft.net

We briefly summarize a decade of work simulating single-pass dynamics for a single relativistic hadron through electron cooling systems relevant to high-luminosity electron-hadron colliders [1,2,3]. We consider both 'conventional' electron cooling [4,5,6] and 'coherent' electron cooling (CeC) [7,8,910]. A proper review article is out of

scope, so this summary is restricted to work in which the author participated, and to closely related work. Physical insights drawn from simulations are emphasized over computational details.

Both types of electron cooling are, in essence, variations of stochastic cooling [11,12]. In stochastic cooling processes, the single-pass diffusive kick on a hadron trajectory can greatly exceed the desired friction-like force. However, the friction-like forces accumulate linearly with each pass (i.e. with turn number in the accelerator ring), while diffusive kicks accumulate with the square root of the turn number. Hence, after a sufficient number of turns, damping due to the friction-like forces greatly exceeds the diffusive aspect of the dynamics. When simulating the dynamical friction force on a hadron that is co-propagating with an electron beam, both numerical artifacts and the intrinsically stronger diffusive dynamics make it difficult to accurately measure the friction force. The solution is to numerically suppress all diffusive effects (both numerical and physical) to the extent possible. Although very different in the algorithmic details, the same strategy is also used for CeC simulations.

Simulations of the single-pass friction-like force on individual ions, which we discuss here, is only one element in the larger problem of electron cooling simulations. Full electron cooling simulations must combine analytic or semi-analytic models of the friction-like force with a variety of competing effects, to study equilibration of the ion beam phase space over many turns in a collider ring. For example, the codes BETACOOL [13] or MOCAC [14] can be used to study cooling rates over many turns for conventional electron cooling. However, first principles simulation of single-pass dynamical friction can improve physical understanding and provide important new insights. Also, detailed single-pass simulations can be used to improve the friction force models in a code like BETACOOL (see e.g. [15]).

The distinction between relativistic electron cooling and the many successful nonrelativistic facilities is important. The CeC concept [10] is only applicable to relativistic energies, because it requires the copropagating, modulated electron beam to excite the free electron laser (FEL) instability in a magnetic undulator. For conventional electron cooling, the ion and electron beams propagate with the same velocity, so even for the relativistic case the dynamical friction can be simulated in the beam frame, where the dynamics is nonrelativistic. However, the cooling time increases as γ^2, with one γ factor due to Lorentz expansion of the beams (i.e. reduction of the electron density) and the other due to Lorentz contraction of the interaction time.

Due to this scaling with γ, the cooling time for 100 GeV/nucleon Au^{+79} ions is ~30 minutes for RHIC parameters [15]. Such a time scale could be acceptable for eRHIC operation, but any further increase of the cooling time (due e.g. to unexpected effects) would have serious negative consequences. Hence, any electron-ion collider (EIC) design [3] that depends on conventional electron cooling requires a thorough understanding of the single-pass dynamics. As an untested concept, CeC is the subject of a proof-of-principle experiment [16], and new ideas are still under development [17], so continuing computational studies are warranted.

2.10.1 **Simulating Dynamical Friction for Relativistic Electron Coolers**

A conventional electron cooling system in a relativistic hadron collider ring consists of an equal-velocity copropagating electron beam in a straight section of significant length (~10s of meters). The electrons may be strongly magnetized in a long solenoid of

exceptionally high field quality, which can greatly reduce the cooling time. A great deal can be learned from nonrelativistic simulations of the dynamical friction force on a single hadron in the beam frame, where the electron beam is approximated as a stationary, thermal (perhaps magnetized) plasma of finite transverse extent. The very short interaction times in a relativistic electron cooler (see discussion below) mean that the dynamical friction is dominated by transient dynamics, in contrast to existing low-energy electron cooling systems; hence, some results described in this section are not important for existing electron coolers. Likewise, some ideas derived from operation and understanding of low-energy coolers cannot be directly applied to the problem of relativistic electron coolers.

The dynamical friction force exerted on a test-particle moving in a collisionless plasma with no external fields was calculated by Chandrasekhar [18] and Trubnikov [19], while Derbenev and Skrinsky [20,21] calculated an asymptotic approximation in the limit of cold, strongly magnetized electrons. Parkhomchuk [22] developed a parametric expression for the magnetized friction force, with a modified Coulomb logarithm, and inclusion of effective velocities to encapsulate physical effects like transverse space charge forces and deviations of the solenoid magnetic field from uniformity. These two approximations to the magnetized friction force showed strong disagreement (as much as an order of magnitude) in relevant parameter regimes.

In 2003, we began developing the ability to simulate dynamical friction via direct treatment of binary collisions. Initially, we used the fast multipole algorithm (FMA) [23] to avoid the N^2 scaling of binary collisions between N particles; however, the problem of artificially close collisions required the use of untenably small time steps, or else an unacceptable softening of near collisions. Considering this attempt a failure, we chose a radically different approach – use of a 4^{th}-order Hermite algorithm with variable time-stepping (over orders of magnitude in the size of the time step) for each particle [24,25]. To avoid the N^2 scaling problem, we only allowed interactions between a few hadrons (typically 8) and the electrons (i.e. no electron-electron or hadron-hadron interactions). This approximation is acceptable when treating the hadrons as test particles, and for a thermal electron distribution that is not significantly altered. To suppress diffusive dynamics and numerical noise, it was necessary to replace half of the electron macroparticles with positrons having the identical position and momentum, but which responded to external magnetic fields as though they were electrons, [26] a technique which also simplifies boundary conditions and removes unphysical bulk electric fields.

The subsequent simulations [15,27] produced a number of important results. We showed that the asymptotic approximations of Derbenev and Skrinsky are only accurate in the limit of zero-temperature electrons, and that the friction force is incorrectly strong by a factor of two or more for electron temperatures comparable to what might be achieved with a low-emittance electron accelerator. In contrast, Parkhomchuk's parametric equations often produce reasonable results, and appear to be more reliable for simple estimates; however, the predicted friction forces could also differ from simulation results by order unity, sometimes even differing in sign. The details are provided in Ref. [27], where the asymptotic equations of Derbenev and Skrinsky are presented as Eq.'s (5) and (6), along with similar analytic calculations due to Parkhomchuk [28] in Eq.'s (7) and (8), as well as Parkhomchuk's parametric form in Eq.'s (9) and (10).

More important than these somewhat negative results, we showed that simulation results agree well with the penultimate equation in the analysis of Derbenev and Skrinsky – equations requiring 1D quadrature to evaluate, prior to any asymptotic expansion. These equations are repeated as Eq. (4) in Ref. [27]. Hence, this is the correct approach to be used for electron cooling simulations, and BETACOOL offers this option. This insight is not only important for the magnetized case. Any simple equation for the friction force assumes a Gaussian distribution function for the electrons. In order to remove this assumption, it is necessary to evaluate the final 1D integral numerically, even for unmagnetized cooling, which is possible in BETACOOL simulations. This will be especially true for the MEIC design [1,3], in which the electron beam distribution will evolve significantly as it interacts many times with the hadron beam.

After the success at Fermilab in cooling moderately relativistic antiproton beams via unmagnetized electron cooling [29,30], it was proposed by the electron cooling team at BNL to seriously consider the unmagnetized approach, replacing the expensive and technically challenging solenoid with a much less expensive magnetic undulator, which would simultaneously focus the electron bunches and reduce electron-ion recombination rates. Physical intuition suggests that the unmagnetized friction force would only be reduced logarithmically, because the minimum radius for binary collisions would be increased to something on the order of the electron wiggle amplitude inside the undulator. In attempting to simulate this scenario, we realized that the Hermite algorithm was unable to correctly model the dynamics of electrons that are strongly oscillating in spatially-varying magnetic fields.

Based on a suggestion from Ilan Ben-Zvi, we developed a completely new algorithm (Sec. 4 of Ref. [25]), in which close electron-hadron encounters are treated analytically, via well-known two-body dynamics, while distant interactions use a 2^{nd}-order predictor-corrector algorithm, and strong external fields are included via operator-splitting methods that preserve the 2^{nd}-order accuracy. We call this the binary coulomb collision (BCC) algorithm. As with the Hermite algorithm, the BCC algorithm neglects electron-electron scattering, in order to avoid the N^2 scaling of a full molecular dynamics approach; however, collective electron dynamics can be included via standard Poisson solves, with these 'external' fields included through operator splitting. The BCC algorithm has important benefits in comparison with the Hermite algorithm – it is significantly faster, more robust, works well with strong external electric and magnetic fields, and completely solves the problem of artificially-strong Coulomb scattering events, which occasionally occurred with the Hermite algorithm, unless some softening of near collisions was applied. Use of the BCC algorithm confirmed the predicted logarithmic reduction in the friction force in the presence of a magnetic undulator (Sec. 8 of Ref. [25]), increasing confidence that this dramatically less expensive option could be used in place of magnetized cooling.

Complete removal of uncertainty regarding artificially-strong scattering events in the BCC algorithm also enabled fundamentally improved understanding of small impact parameter collisions, including an important generalization of the Coulomb logarithm for electron cooling applications. Students of plasma physics learn in their introductory course that small impact parameter collisions are essentially negligible – that it is acceptable to use a weak-interaction approximation that diverges at small impact parameter and then choose an *ad hoc* minimum to avoid the divergence. Simulations of dynamical friction for electron cooling parameters show, in stark contrast, that small-

impact-parameter collisions occur routinely, with significant impact on the dynamics of the affected hadrons. Details are provided in Sec. 1.1 and App. A of Ref. [25], where it is shown that finite interaction time and simple statistical considerations can be used to calculate the appropriate cut-off value for the impact parameter, which differs from the standard ρ_{min} of plasma physics. This ~10% reduction in the corrected Coulomb logarithm (Λ_1 of Eq. (7) in Ref. [25]) is not included in BETACOOL, but it should be considered when designing electron cooling systems for relativistic hadron rings.

Sergei Nagaitsev suggested that we consider the problem of transverse magnetic field perturbations, and quantify how they reduce dynamical friction in the unmagnetized case, including any wavelength dependencies. The magnetic field quality of a solenoid is often quantified by constraining the maximum of a 1D longitudinal integral of the transverse field components – a constraint which provides no information regarding the wavelength spectrum of the unwanted perturbations. Defining our perturbation strength in these terms, we showed for single-wavelength perturbations [31] that the effects can be accurately captured through an intuitive splitting and modification of the dynamical friction integral. For details, see Eq.'s (19) to (22) and associated discussion. The results could be generalized to the case of any wavelength spectrum, by integrating the single-wavelength results appropriately over wavelength. These results may be relevant to the complex beam dynamics of Fermilab's relativistic electron cooler [29,30]; however, there was no effort to directly apply our techniques, and that cooler is no longer operating.

Building on our previous work [25], we present in Sec. 2 of Ref. [31] the 'standard' derivation of unmagnetized dynamical friction, carefully describing all of the implicit assumptions. It is shown that the calculation is not mathematically well posed, and how certain limits must be taken in a specific order to obtain the expected result. Then in Sec. 4 it is shown how to correctly and efficiently calculate the unmagnetized friction force with a numerical algorithm that correctly captures all the finite-time effects of relativistic electron coolers, including asymmetric collisions. This algorithm shows there are no divergences when the calculation is done correctly – the contributions converge to a finite value at zero impact parameter, while they quickly asymptote to zero as the impact parameter increases (see Fig. 6 of Ref. [31]). These results emphasize the incorrectness of the widely taught and accepted physical intuition that small impact parameters can be neglected. By using the importance sampling method (ISM), this new algorithm achieves a speedup factor of 10^4, as compared to the BCC algorithm, with no need for the use of correlated electron-positron pairs to suppress numerical noise and physical diffusion. Of course, the BCC algorithm is much more general.

As described in Sec. 5 of Ref. [31], use of the ISM algorithm enables fundamentally improved understanding of how small impact parameters affect the dynamical friction. The distribution of small impact parameters is a modified Pareto distribution, with the characteristic of rare events that each have a large effect. Hence, the central limit theorem (CLT) does not apply, meaning that it is not correct to find the average friction force by averaging over a number of interactions that exceeds by orders of magnitude the physical number of interactions in a single pass – in fact, this 'average' increases slowly with the number of interactions, ultimately converging only after an inordinate number of events (see Fig. 8 of Ref. [31]), when the CLT does eventually become applicable. Hence, for a physically correct number of electron-hadron interactions during a single pass, there is a large (can be of order unity) uncertainty in the dynamical friction, and this uncertainty is intrinsic to the statistical properties of the physical

system. This result is consistent with over 6 years of simulation experience, where the slow increase of mean value with ensemble size has been observed.

Fig. 8 of Ref. [31] shows that the 50% quintile for the friction force generated by 10^4 electron-hadron scattering events is about 25% lower than the fully converged value obtained with 10^9 events, with order unity variation in the friction force obtained from pass to pass. This result has potentially important physical consequences, and merits consideration when designing future facilities. However, the question of small impact parameters must be reconsidered for magnetized electron coolers or, for example, the unmagnetized case with a magnetic undulator field for focusing – in such cases, there is a physical lower limit on the impact parameter for non-ignorable interactions (i.e. the gyroradius and the wiggle amplitude, respectively), which could significantly lessen any impact from the statistics of very small impact parameters. It would be worthwhile to reconsider previously simulated parameter regimes, using the physically correct number of electron macro-particles, then running many such simulations to determine the range of friction forces obtained in this manner – if the variance is large, then Pareto statistics are likely at play and the simulated (physically correct) forces will likely be smaller than the semi-analytic results obtained via quadrature.

A great deal of work has been conducted on the topic of dynamical friction in plasmas – see e.g. Ref. [32] for a broad discussion of theory and computation, and Ref. [33] for a discussion specifically of binary collision algorithms. Other relevant numerical approaches include Langevin/Fokker-Planck [14], Vlasov/Poisson [34,35] and FMM [36], where these sample references are not comprehensive. Some dynamical friction work considers strongly coupled plasmas and so does not apply to electron cooling, where the lab-frame electron bunch distribution constitutes a weakly-coupled non-neutral plasma. Other dynamical friction work considers nonlinear interactions between a hadron and a weakly-coupled plasma; whereas, in electron cooling the hadron-plasma interaction is predominantly linear; however, nonlinear effects can be relevant to highly-ionized high-Z hadrons like Au^{+79}, if the charge state is comparable to the number of electrons in a Debye sphere. Also, some analyses assume screened potentials, implicitly assuming the interaction time is long compared to any initial transient dynamics, which can be a good approximation for low-energy coolers; however, the relativistic electron cooling system designed for RHIC [37,38,39] has an interaction time less than the beam-frame plasma period, so the dynamics is predominantly transient and steady-state shielding of the potential is an incorrect model.

There have been both experimental [40] and theoretical [41] reports that the Q^2 scaling of the dynamical friction force is weakened for highly-ionized high-Z hadrons; however, this theoretical analysis used a screened Coulomb potential, which is incorrect for the transient dynamics of the RHIC design. Likewise, the experimental work was conducted at a low-energy cooler, where the electron density and the interaction time are large enough that steady-state dynamics and screened potentials are reasonable approximations. The $1/\gamma$ reduction of the beam-frame electron density and interaction time in relativistic electron cooling systems, together with technological constraints, will tend to yield interaction times less than the plasma period, which implies transient dynamics. However, partial electron shielding of the hadron potential will occur on this time scale, so it is important to address this question with the BCC algorithm, including collective electron dynamics through electrostatic particle-in-cell (PIC).

The binary coulomb collision (BCC) algorithm and associated work discussed in this report is unique in that the transient, short-time dynamics of relativistic coolers has

been treated rigorously, including important advances in the theoretical understanding of small-impact-parameter scattering events. To date, BCC simulations have used perfectly-correlated electron/positron macro-particle pairs to suppress noise and diffusive dynamics; however, this quiet start is only valid in the limit of linear dynamics, an assumption which may become invalid for hadrons with charge state comparable to the number of the electrons in a Debye sphere. Also, BCC simulations to date have mostly ignored collective electron dynamics, which means that plasma shielding effects could not have been observed. Hence, more work is required to fully address some important questions, and to better resolve the discrepancies between the work described here and other approaches to computing dynamical friction.

Recently, Bell *et al*. have modeled dynamical friction for parameters of the MEIC electron cooler design [42], using both the BCC algorithm and the δf-PIC [43,44,45,46] algorithm. The δf-PIC algorithm captures dynamical friction through gridded fields generated via tiny deviations of the electron distribution from equilibrium, in stark contrast to the gridless particle-scattering approach of the BCC algorithm – it is a notable achievement to obtain the correct result through two such different methods. Important advantages of δf-PIC are that it simultaneously captures both the ion dynamics (i.e. friction) and the bulk electron response (i.e. Debye shielding) with no need for artificial noise suppression used for BCC (i.e. correlated electron-positron macro-particles). A significant weakness of δf-PIC is that it has no knowledge of small impact parameters – the effective value of the minimum impact parameter is likely a function of the grid resolution. These results suggest that the dynamical friction is not very sensitive to the choice of ρ_{min} for the parameters of this MEIC cooler design, as long as short-interaction-time effects are included by using the modified Coulomb logarithm of Ref. [25], which is shown also as Eq. (5) of Ref. [42]. The δf-PIC algorithm could be useful for addressing the question of nonlinear effects and possible loss of Q^2 scaling at high Q, although the nonlinear version of the algorithm would be required (linear δf is used in [42]), and the relative importance of small impact parameters would have to be addressed independently via the BCC algorithm.

2.10.2 **Coupled Simulations of a Single-pass for Coherent Electron Cooling (CeC)**

A coherent electron cooling system [9,10], analogous with stochastic cooling [11,12], includes three distinct subsystems: the modulator, the amplifier and the kicker. The modulator is very much like a conventional relativistic electron cooler; however, the purpose is entirely different – the goal is to maximize Debye shielding of each hadron, so that the resulting density and energy perturbations in the electron distribution can be subsequently amplified. Dynamical friction does occur in the modulator, but theoretical calculations indicate that this will be negligible compared to the total friction-like force exerted by the CeC system on each hadron. A free electron laser (FEL) operating in the linear regime (i.e. no saturation) has been proposed as the amplifier [10], which can amplify the hadron-generated Debye-scale perturbations of the electron distribution by orders of magnitude, including a modulated train of unwanted secondary perturbations behind the primary. Recently, new ideas for the amplifier have been suggested [17], including use of a microbunching instability [47]. The kicker also looks very much like a conventional relativistic electron cooler; however, the purpose is for the appropriately time-delayed hadrons to experience the electrostatic (in the beam frame) kick of the previously amplified density perturbations,

which originated from Debye shielding of the same hadron. This electric field is, essentially, the friction-like force that will cool the hadron beam, in a manner that is closely analogous to stochastic cooling.

The electron cooling team at BNL has developed extensive theoretical analyses for each of the three CeC subsystems. [48-57] A computational effort was launched in 2008 to simulate single-pass CeC dynamics, guided by these analytical results and with the goal of finding their limits and, perhaps, to develop a parametric representation of the full system. The δf-PIC algorithm (discussed above) was used for initial simulations of the CeC modulator [58], taking parameters from the proposed cooling of RHIC, and close agreement was found between δf-PIC and the theory of Wang and Blaskiewicz [49], if the thermal electrons follow the special 'kappa-2' distribution; whereas, for a more conventional Gaussian electron distribution, the agreement remained qualitative.

Coupling from δf-PIC simulations of the modulator to standard FEL simulations of the amplifier was included in Ref. [58], and this work was extended to subsequent coupling from the FEL amplifier into electrostatic PIC simulations of the kicker. [59] Particle loading in FEL codes (e.g. we used GENESIS [60,61]), especially for self-amplified spontaneous emission (SASE), must be handled in a fundamentally different manner from what is done in PIC codes. Coupling of the very subtle, small-amplitude perturbations in density and energy from the δf-PIC simulations into the FEL simulations used special features of GENESIS that could not fully capture some of the important details. Deciding this situation was unacceptable, we proceeded to develop a more sophisticated algorithm for the modulator-to-amplifier coupling.

To enable accurate coupling of Debye shielding perturbations in an electron distribution directly into a SASE FEL simulation, we decided to implement a completely new approach [62] to particle initialization. The simplest variant of this novel algorithm has been implemented in a fork of the GENESIS code [63], and initial testing indicates reasonable agreement with the standard approach. Further work is required, in order to complete implementation of more sophisticated variants, and to verify that the resulting FEL physics is correct and robust.

In parallel with the novel approach described above, we continued to improve and further develop the ability to use native GENESIS capabilities for coupling subtle electron beam modulations into the SASE FEL simulation, as described in Ref. [64]. Given the importance of this modulator-to-amplifier coupling, it would be worthwhile to complete the initial work of Pogorelov et al. [63] and to benchmark those results with simulations using the approach described in Ref. [64]. In any case, the latter approach has already achieved a notable success – the electric fields simulated in the kicker show reasonable agreement with analytical calculations. However, these kicker simulations were essentially 1D, and so future work will be required to explore the effects of 3D dynamics in the kicker.

In parallel with this work on code coupling, simulations of the modulator were continuing to improve and grow in sophistication. In Ref. [65], it is shown that δf-PIC and Vlasov/Poisson simulations show agreement with Wang & Blaskiewicz [49]. The Vlasov simulations, restricted to 1D, do however show significant deviations from theory in the presence of a plasma density gradient. In Ref. [66], an improved δf-PIC implementation is used to consider anisotropic Debye shielding in a beam-like electron distribution that varies in both time and space, showing that the analysis of Ref. [49] remains valid for time-varying density with weak spatial gradients, if the analytical prediction is integrated in time to track the local density. For significant spatial density

gradients, simulations show slightly enhanced shielding on the high-density side and significantly weaker shielding on the low-density side – effects that cannot be easily quantified from the theory.

The most recent work on modulator simulations [67] considers a likely scenario, where the modulator consists of a quadrupole transport line focusing the electron beam into the amplifier. In this scenario, the transverse electron beam size(s) and thermal velocities are asymmetric and rapidly varying, which results in correspondingly rapid variation of the beam-frame plasma density and Debye length. It is shown that δf-PIC can correctly define the time-varying Vlasov equilibrium in terms of the Twiss parameters, so that the algorithm remains valid, with the caveat that transverse electron velocities in the beam frame appear to become relativistic for the chosen quadrupole lattice, resulting in technical difficulties. In this complex scenario, the comparison of Debye shielding details between theory and simulation is not straightforward. More work will be required in the future to better understand the implications.

2.10.3 **Acknowledgments**

Preparation of this report was supported by RadiaSoft LLC. Much of the work discussed here was supported by the US Department of Energy, Office of Science, Office of Nuclear Physics, in part through the SBIR program. The author gratefully acknowledges the contributions made by all his coauthors, but especially thanks the following scientists for key contributions: George Bell, Ilan Ben-Zvi, Michael Blaskiewicz, Alexey Burov, Yaroslav Derbenev, Alexei Fedotov, Vladimir Litvinenko, Sergei Nagaitsev, Gregg Penn, Ilya Pogorelov, Sven Reiche, Brian Schwartz, Andrey Sobol, Peter Stoltz and Gang Wang. Most of the simulations discussed here were conducted using the parallel VORPAL framework (now known as VSim) [25,68], including the implementation of several algorithms (Hermite, BCC, δf-PIC, Vlasov/Poisson), and we acknowledge the important contributions of John Cary and all members of the VORPAL development team at Tech-X Corp.

2.10.4 **References**

1. S. Abeyratne et al., “Science Requirements and Conceptual Design for a Polarized Medium Energy Electron-Ion Collider at Jefferson Lab,” Eds. Y. Zhang & J. Bisognano (2012), arXiv; http://arxiv.org/abs/1209.0757
2. L. Ahrens et al., “eRHIC – Zeroth-order design report,” Eds. M. Farkhondeh & V. Ptitsyn (2009); bnl.gov/cad/eRhic/eRHIC_ZDR.asp
3. ICFA Beam Dynamics Newsletter 58, Sec. 4, Eds. E. Métral & W. Chou (2012); http://icfa-usa.jlab.org/archive/newsletter/icfa_bd_nl_58.pdf
4. G.I. Budker, “An effective method of damping particle oscillations in proton and antiproton storage rings,” Atomnaya Énergiya 22, 346 (1967).
5. V.V. Parkhomchuk and A.N. Skrinsky, “Electron cooling: physics and prospective applications” Rep. Prog. Phys. 54, 919 (1991).
6. I. Meshkov, “Electron cooling – recent developments and trends,” Nucl. Phys. A 626, 459 (1997).
7. Ya. S. Derbenev, in Proc. 7th All-Union Conf. Charged Particle Accel., 269 (Dubna, USSR, 1980), in Russian.
8. Ya. S. Derbenev, “On possibilities of fast cooling of heavy particle beams,” AIP Conf. Proc. 253, 103 (1992).
9. Ya. S. Derbenev, “Use of an electron beam for stochastic cooling,” in Proc. COOL,

THM2105 (2007).
10. V.N. Litvinenko and Y.S. Derbenev, "Coherent electron cooling," Phys. Rev. Lett. 102, 114801 (2009).
11. S. van der Meer, "Stochastic cooling and the accumulation of antiprotons," Rev. Mod. Phys. 57, 689 (1985).
12. M. Blaskiewicz, J. M. Brennan and F. Severino, "Operational Stochastic Cooling in the Relativistic Heavy-Ion Collider," Phys. Rev. Lett. 100, 174802 (2008).
13. A.O. Sidorin, I.N. Meshkov, I.A. Seleznev, A.V. Smirnov, E.M. Syresin and G.V. Trubnikov, "BETACOOL program for simulation of beam dynamics in storage rings," Nucl. Instrum. Methods Phys. Res. A558, 325 (2006).
14. Zenkevich, A. Bolshakov, I. Hofmann, T. Katayama, I. Meshkov, A. Sydorin, "Modeling of Electron Cooling by Monte-Carlo method," International Symposium on Cooling and Related Topics (Bad Honnef, 2001), http://betacool.jinr.ru/COOL/COOL'01/Paper_contributions/Zenkevich.pdf
15. A.V. Fedotov, I. Ben-Zvi, D.L. Bruhwiler, V.N. Litvinenko and A.O. Sidorin, "High-energy electron cooling in a collider," New J. Phys. 8, 283 (2006).
16. I. Pinayev et al., "Present Status of Coherent Electron Cooling Proof of Principle Experiment," Proc. of COOL, WEPP014 (2013); see also I. Pinayev and V. Litvinenko, Section 2.7 of this newsletter.
17. V.N. Litvinenko, G. Wang, G.I. Bell, D.L. Bruhwiler, A. Elizarov, Y. Hao, Y. Jing, D. Kayran, I.V. Pogorelov, D. Ratner, B.T. Schwartz, O. Shevchenko, A. Sobol and S.D. Webb, "Advances in Coherent Electron Cooling," Proc. IPAC, MOPRO015 (2014).
18. S. Chandrasekhar, Principles of Stellar Dynamics (U. Chicago Press, 1942).
19. B.A. Trubnikov, Rev. Plasma Physics 1, 105 (1965).
20. Ya. Derbenev and A. Skrinsky, "The effect of an accompanying magnetic field on electron cooling," Part. Acc. 8, 235 (1978).
21. Ya.S. Derbenev and A.N. Skrinsky, Fiz. Plazmy 4, 492 (1978) [Sov. J. Plasma Phys. 4, 273 (1978)].
22. V.V. Parkhomchuk, "New insights in the theory of electron cooling," Nucl. Instrum. Methods Phys. Res. A441, 9 (2000).
23. L. Greengard, The rapid evaluation of potential fields in particle systems (MIT Press, 1987).
24. D.L. Bruhwiler, R. Busby, A.V. Fedotov, I. Bev-Zvi, J.R. Cary, P. Stoltz, A. Burov, V.N. Litvinenko, P. Messmer, D. Abell and C. Nieter, "Direct simulation of friction forces for heavy ions interacting with a warm magnetized electron distribution," AIP Conf. Proc. 773, 394 (Bensheim, 2004).
25. G.I. Bell, D.L. Bruhwiler, A. Fedotov, A. Sobol, R.S. Busby, P. Stoltz, D.T. Abell, P. Messmer, I. Ben-Zvi and V. Litvinenko, "Simulating the dynamical friction force on ions due to a briefly co-propagating electron beam," J. Comput. Phys. 227, 8714 (2008).
26. The use of correlated electron/positron pairs to suppress diffusion (without changing the dynamical friction force) was initially suggested by A. Burov and then independently by V. Litvinenko.
27. A.V. Fedotov, D.L. Bruhwiler, A.O. Sidorin, D.T. Abell, I. Ben-Zvi, R. Busby, J.R. Cary, V.N. Litvinenko, "Numerical study of the magnetized friction force," Phys. Rev. ST/AB 9, 074401 (2006).
28. V.V. Parkhomchuk, "Physics of fast electron cooling," Proceedings of the Workshop on Electron Cooling and Related Applications, Ed. H. Poth, 71 (Karlsruhe, 1985).
29. S. Nagaitsev et al., "Experimental Demonstration of Relativistic Electron Cooling," Phys. Rev. Lett. 96, 044801 (2006).
30. L.R. Prost, A. Burov, K. Carlson, A. Shemyakin, M. Sutherland and A. Warner, "Electron Cooling Status and Characterization at Fermilab's Recycler," Proc. of COOL, MOA2I06 (Bad Kreuznach, 2007).
31. A.V. Sobol, D.L. Bruhwiler, G.I. Bell, A. Fedotov and V.N. Litvinenko, "Numerical

calculation of dynamical friction in electron cooling systems, including magnetic field perturbations and finite time effects," New J. Phys. 12, 093038 (2010).
32. H.B. Nersisyan, C. Toepffer and G. Zwicknagel, Interactions Between Charged Particles in a Magnetic Field – A Theoretical Approach to Ion Stopping in Magnetized Plasmas (Springer, 2007).
33. H.B. Nersisyan and G. Zwicknagel, "Binary collisions of charged particles in a magnetic field," Phys. Rev. E 79, 066405 (2009).
34. O. Boine-Frankenheim, "Nonlinear stopping power of ions in plasmas," Phys. Plasmas 3, 1585 (1996).
35. O. Boine-Frankenheim and J. D'Avanzo, "Stopping power of ions in a strongly magnetized plasma," Phys. Plasmas 3, 792 (1996).
36. S. Abeyratne, S. Manikonda and B. Erdelyi, "Optimal Fast Multipole Method Data Structures," Proc. IPAC, MOPPC093 (2012).
37. I. Ben-Zvi et al., "Status of the R&D towards electron cooling of RHIC," Proc. of PAC07, WEOCKI03 (2007).
38. I. Ben-Zvi, "The ERL High-Energy Cooler for RHIC," Proc. of EPAC, TUZBPA01 (2006).
39. A. Fedotov, "Electron Cooling studies for RHIC-II" (2006), unpublished; http://www.c-ad.bnl.gov/ardd/ecooling/docs/PDF/Electron_Cooling.pdf
40. T. Winkler, K. Beckert, F. Bosch, H. Eickhoff, B. Franzke, F. Nolden, H. Reich, B. Schlitt and M. Steck, "Electron cooling forces for highly charged ions in the ESR," Nucl. Instrum. Methods Phys. Res. A391, 12 (1997).
41. G. Zwicknagel, C. Toepffer and P.-G. Reinhard, "Molecular Dynamics Simulation of Electron Cooling," Workshop on Beam Cooling and Related Topics, 245 (Montreaux, 1993); www.iaea.org/inis/collection/NCLCollectionStore/_Public/25/073/25073723.pdf
42. G.I. Bell, I.V. Pogorelov, B.T. Schwartz, Y. Zhang and H. Zhang, "Single Pass Electron Cooling Simulations for MEIC," Proc. NA-PAC, TUPHO02 (2013).
43. S.E. Parker and W.W. Lee, "A fully nonlinear characteristic method for gyrokinetic simulation," Phys. Fluids B 5, 77 (1993).
44. G. Hu and J.A. Krommes, "Generalized weighting scheme for δf particle-simulation method," Phys. Plasmas 1, 863 (1994).
45. Q. Qian, W.W. Lee and R.C. Davidson, "Nonlinear δf simulation studies of intense ion beam propagation through an alternating-gradient quadrupole focusing field", Phys. Plasmas 4, 1915 (1997).
46. N. Xiang, J.R. Cary, D.C. Barnes and J. Carlsson, "Low-noise electromagnetic δf particle-in-cell simulation of electron Bernstein waves," Phys. Plasmas 13, 062111 (2006).
47. D. Ratner, "Microbunched Electron Cooling for High-Energy Hadron Beams," Phys. Rev. Lett. 111, 084802 (2013); see also D. Ratner, Section 2.8 of this newsletter.
48. V.N. Litvinenko, I. Ben Zvi, Y. Hao, D. Kayran, E. Pozdeyev, G. Wang, S. Reiche, O.A. Shevchenko and N.A. Vinokurov, "High Gain FEL Amplification of Charge Modulation caused by a Hadron," Proc. FEL, MOPPH026 (2008).
49. G. Wang and M. Blaskiewicz, "Dynamics of ion shielding in an anisotropic electron plasma," Phys. Rev. E 78, 026413 (2008).
50. G. Wang, M. Blaskiewicz and V.N. Litvinenko, "Analytical Studies of Coherent Electron Cooling," Proc. PAC, TU6PFP074 (2009).
51. G. Wang, V.N. Litvinenko and S.D. Webb, "The physics of FEL in an infinite electron beam," Proc. FEL, MOPB04 (2010).
52. G. Wang, M. Blaskiewicz and V.N. Litvinenko, "Progress on Analytical Modeling of Coherent Electron Cooling," Proc. IPAC, MOPD077 (2010).
53. S.D. Webb, G. Wang and V.N. Litvinenko, "Three-dimensional model of small signal free-electron lasers," Phys. Rev. Special Topics – Accel. & Beams 14, 051003 (2011).

54. S.D. Webb, G. Wang and V.N. Litvinenko, "Effects of e-beam parameters on coherent electron cooling," Proc. PAC, MOP066 (2011).
55. G. Wang, V.N. Litvinenko and S.D. Webb, "Amplification of current density modulation in a FEL with an infinite electron beam," Proc. PAC, THP149 (2011).
56. A. Elizarov, V.N. Litvinenko and G. Wang, "Shielding of a hadron in a finite e-beam," Proc. IPAC, WEPPR099 (2012).
57. Y. Jing, V.N. Litvinenko, Y. Hao and G. Wang, "Model independent description of FEL shot noise, amplification and saturation using Green's function," Proc. IPAC, THPRO039 (2014).
58. B.T. Schwartz, D.L. Bruhwiler, V.N. Litvinenko, S. Reiche, G.I. Bell, A. Sobol, G. Wang and Y. Hao, "Massively parallel simulation of anisotropic Debye shielding in the modulator of a coherent electron cooling system and subsequent amplification in a free electron laser," Proc. SciDAC Conf. (2010).
59. B.T. Schwartz, D.L. Bruhwiler, I. Pogorelov, V.N. Litvinenko, G. Wang, Y. Hao and S. Reiche, "Simulations of a single-pass through a coherent electron cooler for 40 GeV/n Au+79," Proc. PAC, MOP074 (2011).
60. S. Reiche, "GENESIS 1.3: a fully 3D time-dependent FEL simulation code," Nucl. Instrum. and Methods A 429, 243 (1999).
61. The GENESIS website; http://genesis.web.psi.ch
62. V.N. Litvinenko, "Macro-particle FEL model with self-consistent spontaneous radiation," unpublished (2002).
63. I.V. Pogorelov, G.I. Bell, D.L. Bruhwiler, B.T. Schwartz, S.D. Webb, V.N. Litvinenko, G. Wang and Y. Hao, "Coupling modulator simulations into an FEL amplifier for coherent electron cooling," Proc. IPAC, MOPPC090 (2012).
64. B.T. Schwartz, G.I. Bell, D.L. Bruhwiler, I. Pogorelov, S.D. Webb, V.N. Litvinenko, Y. Hao, G. Wang and S. Reiche, "Coherent Electron Cooling: Status of Single-Pass Simulations," Proc. IPAC, MOPWO071 (2013).
65. G.I. Bell, D.L. Bruhwiler, B.T. Schwartz, I. Pogorelov, V.N. Litvinenko, G. Wang and Y. Hao, "Vlasov and PIC simulations of a modulator section for coherent electron cooling," Proc. PAC, MOP067 (2011).
66. G.I. Bell, D.L. Bruhwiler, B.T. Schwartz, I. Pogorelov, V.N. Litvinenko, G. Wang and Y. Hao, "High-fidelity 3D modulator simulations of coherent electron cooling systems," Proc. IPAC, THEPPB002 (2012).
67. G.I. Bell, I. Pogorelov, B.T. Schwartz, D.L. Bruhwiler, V.N. Litvinenko, G. Wang and Y. Hao, "Modulator simulations for coherent electron cooling using a variable density electron beam," Phys. Rev. Special Topics – Accel. & Beams (2014), submitted; http://arxiv.org/abs/1404.2320v1
68. The VSim website; http://www.txcorp.com/home/vsim/vsim-overview

2.11 BETACOOL Code

Anatoly Sidorin and Alexander Smirnov
Joint Institute for Nuclear Research, Dubna, Russia
Mail to: sidorin@jinr.ru, smirnov@jinr.ru

2.11.1 **Introduction**

The program title – BETACOOL - reflects the basic physical model realized in the first version of the program developed on 1995 [1]. Initially the program provided turn by turn simulation of a single particle BETAtron motion in a storage ring under influence of a COOLing force acting on the particle inside a magnetized electron beam.

In difference with similar codes developed in 80-th the cooling (friction) force was calculated in accordance with the formula derived by Ya.Derbenev and A.Skrinsky in asymptotic form proposed by I.Meshkov [2]. Also the model accounted influence on the particle motion a solenoidal magnetic field in the cooling section and self electric field of the cooling electron beam.

In the present time the BETACOOL code simulates a variation of the ion distribution function in 6 dimensional phase space using a few models of the ion beam. The simulations include different models of a few physical processes which can act on the distribution function in storage rings: electron, stochastic and laser cooling, intrabeam scattering, scattering on atoms of the residual gas and different types of internal target, colliding regime, particle losses, etc.

2.11.2 **Base Algorithms**

Further development of the initial BETACOOL model resulted in creation of ***Tracking algorithm*** which simulates turn by turn motion of small array consisting from real particles. The Intrabeam Scattering (IBS) in the ion beam is simulated from the first principles by adding to the ion Hamiltonian in the storage ring the space charge term:

$$H = -\frac{xp_z}{\rho} + \frac{p_z^2}{2\gamma_0^2} + \frac{{p_x}^2 + {p_y}^2}{2} + \frac{x^2}{2\rho^2} + \frac{K_1}{2}\left(x^2 - y^2\right) + \\ + \frac{K_2}{6}\left(x^3 - 3xy^2\right) + \frac{r_{ion}}{\gamma_0^2\beta_0^2}\sum_i \frac{1}{\sqrt{(x-x_i)^2 + (y-y_i)^2 + \gamma_0^2(z-z_i)^2}}, \qquad (1)$$

where as usual ρ is the curvature radius of the reference orbit, p_x, p_y, p_z, x, y, z are normalized momenta and corresponding coordinates, γ_0, β_0– relativistic factors, $K_{1,2}$ - gradients of the focusing structure, i is the number of particle in the array. To speed up the calculations the last term describing the space charge effects can be replaced in accordance with so called Molecular Dynamics (MD) approximation [3]. The MD method assumes that particles have a periodical distribution along the beam orbit. Typical number of particles per the periodical cell is about 10-100 that is sufficient to simulate formation of a crystalline state of the ion beam at very low temperature in the beam rest frame. Investigation of the beam ordering and properties of IBS at small particle number are the general goals of the Tracking algorithm.

The main goal of two other algorithms is to simulate long term processes (in comparison with the ion revolution period) in a storage ring leading to variation of the ion distribution function in 6 dimensional phase space [4]. In both algorithms the betatron motion inside the storage ring is supposed to be stable and it is treated in linear approximation.

The so called ***RMS Dynamics*** algorithm is based on the following general assumptions:

- the ions have Gaussian distribution over all degrees of freedom, and the distribution shape is not changed during the process;
- algorithm for analysis of the problem is considered as a solution of the equations for the second order momenta of the distribution function and the particle number;

- maxima of all the distribution functions coincide with equilibrium orbit (the first order momenta are equal to zero).

The evolution of the ion beam parameters during its circulation inside the storage ring is described by the following system of four differential equations:

$$\begin{cases} \dfrac{\varepsilon_i}{dt} = \varepsilon_i \sum_j \dfrac{1}{\tau_{i,j}} \\ \dfrac{dN}{dt} = N \sum_j \dfrac{1}{\tau_{life,j}} \end{cases}, \tag{2}$$

where N is the particle number, $\varepsilon_i = \{\varepsilon_{hor}, \varepsilon_{ver}, \varepsilon_{lon}\}$ are the r.m.s. (root mean square) values of the beam phase space volumes (emittances) in each of three degrees of freedom. Characteristic times $\tau_i = \{\tau_{hor}, \tau_{ver}, \tau_{lon}\}$ are functions of all three emittances and particle number and have positive sign for a heating process and negative for cooling one. The negative sign of the lifetime (τ_{life}) corresponds to the particle loss and the sign of the lifetime can be positive in the presence of particle injection, when particle number increases.

Index j in Eq.(2) is the number of process (effect) involved into calculations. The program structure is designed in such a way that allows including into calculation each process, which can be described by cooling or heating rate. Characteristic times of the beam parameter evolution for the processes are calculated under assumption of Gaussian shape of the ion distribution function.

Due to simplicity of the model (the beam model does not contain particles) the RMS Dynamics permits to provide very fast calculation of the processes, which real duration can be of the order of a few hours. Additionally for fast estimation of equilibrium beam parameters (that corresponds to zero left-hand sides of the system 2) the original graphic-analytical algorithm can be used.

However the basic assumptions of the RMS Dynamics are not satisfied in a few important cases. For instance a friction force having sufficiently non-linear dependence on the ion momentum leads to distribution very fare from the Gaussian one. Also an interaction with a dense internal target leads to sufficiently non-Gaussian distribution in the longitudinal (and in principle in the transverse) phase space. To simulate the evolution of the distribution function in such cases the Model Beam algorithm was developed.

The ***Model Beam algorithm*** uses the beam model including a few thousands of test particles with arbitrary distribution. Evolution of the ion co-ordinates and momentum components is described in the frames of the Fokker-Plank approach. The algorithm realizes solution of Langevin equation (equivalent to the Fokker-Plank equation for the distribution function) for each test particle in momentum space using Monte Carlo method. In the frame of this algorithm the ion beam is presented as a particle array. Each particle is presented as a 6 co-ordinate vector: $\{x, p_x/p, y, p_y/p, s-s_0, \Delta p/p\}$, where x and y are the horizontal and vertical co-ordinates, p_x and p_y are corresponding momentum components, s-s_0 is the distance from the bunch center (in the case of coasting beam – distance from a reference particle), Δp is the particle momentum deviation from momentum of reference particle p. Action of each effect is simulated as the particle momentum variation in accordance with the following equation:

$$\left(p_{x,y,s}/p\right)_{fin} = \left(p_{x,y,s}/p\right)_{in} + \Lambda_{x,y,s}\Delta T + \sqrt{D_{x,y,s}\Delta T}\,\xi_{x,y,s}\,, \qquad (3)$$

where p_s is the particle longitudinal momentum deviation, subscript *in* correspond to initial momentum value, subscript *fin* relates to final particle momentum after action of the effect, Λ and D are the drift (friction) and diffusion terms for corresponding degree of freedom, ΔT is step of the integration over time, ξ is Gaussian random number at unit dispersion. The friction and diffusion terms in the general case depend on the distribution function. Variation of the particle number is simulated also using Monte Carlo method based on the calculation of a particle loss probability.

Presently the Model Beam is most developed algorithm in the BETACOOL. It permits to simulate different schemes of the beam storage, the beam bunching process, IBS process at arbitrary distribution function. Interaction of the test particles with an internal target is described even accurately than permits the equation 3 (see later).

All the BETACOOL algorithms use the same model of the ion ring and the same models of the processes acting on the ion distribution that permits to provide from one hand a cross-check of the algorithms and from the other hand to solve the task step by step. First ruff estimation can be done using RMS dynamics and thereafter accurate simulation can be performed with Model Beam or Tracking. Additionally the BETACOOL has a set of utilities aimed to a fine tuning of the basic effects.

2.11.3 **Physical Processes**

All physical processes are realized in different presentations in accordance with numerical algorithms involved in the BETACOOL code. This structure permits to investigate beam dynamics under different physical descriptions. For some specific tasks (pellet target, barrier bucket, ordered beams) the combination of numerical algorithms with different time scales were realized. Presently the models of electron, stochastic and laser cooling, intrabeam scattering, scattering on atoms of the residual gas and different types of internal target, colliding regime, particle losses, etc are implemented into the code. Below structure and peculiarity of the model realization are illustrated by a few examples.

Electron Cooling is the first and most developed process in the BETACOOL code. Usually an action of electron cooling on the ion dynamics inside a storage ring is described using a few standard simplifications:

- Angular deviation of the longitudinal magnetic field line is substantially less than the ion beam angular spread.
- Ion transverse displacement inside the cooling section is substantially less than electron beam radius.
- Ion beam temperature is substantially larger than electron one and ion diffusion in the electron beam can be neglected.
- Electron beam has a round shape of cross-section and uniform density distribution in the radial direction.

Under these assumptions and using asymptotic of the analytical friction force presentation the formulae for characteristic times of emittance and momentum spread decrease at electron cooling were obtained. Depending on the ion and electron beam parameters one can use a few analytical models of the friction force. In some cases for

accurate simulation of the cooling process results of numerical calculation of the friction force is necessary.

In the last time modifications of the usual configuration of the electron cooling system were proposed. To avoid instability of the ion beam related with extremely large density of the cooled beam it was proposed to use so called “hollow” electron beam – the beam at small density in the central part. Extension of the electron cooling method in the region of electron energy of a few MeV related with an RF acceleration of the electrons. In this case one can expect Gaussian distribution of the electrons in radial plane and, if the electron bunch is shorter than the ion one, in longitudinal direction also. Calculation of the cooling times in this case requires modification both the electron beam model and the base physical model.

Other expected peculiarity of the medium energy cooling system is a big length of the cooling section – up to about 20 - 50 m. To obtain very high accuracy of the magnetic field is difficult technical task and cost of the cooling system will strongly depend on the required level of the accuracy. Therefore, before design of the cooling section solenoid, one needs to investigate influence of the magnetic field line curvature on the cooling process. All the effects can be taken into account by numerical solution of the ion motion equations in the cooling section.

To solve all the problems related with the cooling process simulation a hierarchy of objects was developed in the frame of the BETACOOL program. Structure of the electron cooler presentation permits to extract procedures of different levels and to include them into calculation of the cooling process in other programs. The cooling simulation is based on a friction force calculation in the particle rest frame. The next layer of the simulation is related with a cooler representation as a map, transforming particle coordinates from entrance to the exit of the cooling section. The map of the cooler can be used directly in the frame of the Molecular Dynamics algorithm, or in other tracking procedures. On the basis of the map one can calculate kick of the ion momentum after crossing the cooling section that is necessary for simulation of the ion distribution evolution in the frame of the Model Beam algorithm. The map of the cooler is used also for the cooling rate calculation that is necessary for RMS dynamics simulation.

Intrabeam scattering (IBS) in the ion beam causes two processes: relaxation of the beam to a thermal equilibrium between degrees of freedom and diffusion growth of 6D phase volume of the beam due to variation of lattice parameters along ring circumference. All usually used numerical algorithms of IBS growth rate calculation are based on the model of the collisions proposed by A. Piwinski.

Four models for IBS calculation – Piwinski, Martini (extended Piwinski), Bjorken-Mtingwa and Jie Wei models are realized in BETACOOL code for Gaussian distribution of ions over velocity. The Martini model does not require additional assumptions for calculation of the beam emittance growth times. Piwinski model can be deduced from Martini model neglecting a variation of dispersion and beta function along the ring orbit (uniform optics). In the model proposed by Jie Wei characteristic times of emittance variation are calculated for real lattice parameters of the ring under a few additional assumptions, which correspond to storage rings at ion energy over the transition energy (for instance RHIC). The new IBS model based on the Bjorken-Mtingwa formalism for the arbitrary particle distribution was elaborated especially for the Model Beam algorithm [5].

To have a possibility to simulate internal target influence in the frame of all three algorithms ***Internal Target*** process is presented in the program at three layers. For multi particle tracking the target is presented as a thin lens associated with some optic element of the storage ring and the target action on the ion is presented in the form of transformation map. On the basis of the map for RMS dynamics simulation a few models for characteristic time of emittance and particle number variation are developed. For investigation of long term processes in the frame of Model Beam algorithm the internal target is presented in the form related to kick of the ion momentum and loss probability calculation.

Map of an effect is used in turn by turn tracking procedure and has to provide variation of the particle coordinates in 6-dimensional phase space and calculate the particle loss probability. Internal target is treated in BETACOOL program as a thin lens, therefore the particle co-ordinates are not changed after crossing the target, but all three components of the particle momentum are changed and the particle can be loosed with some probability. Change of the transverse momentum components is related mainly with a multiple Coulomb scattering from nuclei of the target atoms. Change of the longitudinal momentum component takes a place due to ionization energy loss in interaction with electrons of the target atoms.

Detailed simulation of the ion momentum variation can be provided using Monte-Carlo method based on Urban model for the longitudinal degree of freedom and plural scattering model for the transverse ones. In the frame of the Urban model the total energy losses, calculated using Bethe-Bloch formula, are distributed between ionization and excitation events. The number of events has Poissonian distribution around expectation, the energy loss due to ionization are distributed from mean ionization energy to maximum transferable energy determined by kinematics of the process. The plural scattering model is based on generation of scattering angle in accordance with Rutherford cross-section for a screened Coulomb potential.

At large number of events the Coulomb scattering distribution is well presented by the theory of Moliere. It is roughly Gaussian for small deflection angles, but at large angles (larger than a few r.m.s. value) it behaves like Rutherford scattering, having larger tail than a Gaussian distribution. The core of the distribution can be described by rms value of the scattering angle. The ionization energy loss in the simplest case also can be described by two parameters: mean energy loss and standard deviation of the energy loss fluctuations. RMS parameters of the scattering process is a base of Gaussian model of the target simulation. The Gaussian model of the ion interaction with an internal target permits to provide fast estimations of the heating rates and equilibrium beam parameters in the case of cooling application.

Probability of the particle loss after crossing a target is determined mainly by three processes: single scattering on large angles, charge exchange and nuclear reactions in the target. Cross-section of the single scattering on large angle is calculated in accordance with Rutherford formula. The charge exchange in the target in the present version is taken into account only for fully stripped ions. For such an ion the program calculates cross-section of a capture of an electron in the target. For antiprotons particle losses due to charge exchange are not exist.

2.11.4 **Source Codes**

The software is divided in two independent parts: physical code (BETACOOL) and interface part (BOLIDE) which is an executable program working under Windows environment only. Connection between two parts is provided using three types of the files: input, output and file used for control of the calculation process. Such a structure on the one hand allows to use the program on PC, to control and analyze results during simulations. From the other hand the physical part of the program can be compiled under any operation system and can be used for calculations independently on the interface.

The BETACOOL code is written in the frame of the Object Oriented Programming (OOP) with C++ language and includes a few hundred objects with the complicate hierarchy structure. The total size of the BETACOOL source code is about 1 MB (approximately 10^5 lines) and BOLIDE is about 0.6 MB. All source codes, executable files and documentation are achievable on the BETACOOL home page [6].

A good graphical interface is one of the advantages of the program package which also much helps to distribute the BETACOOL code over the world. BETACOOL was used for beam dynamics simulations in different scientific centers where scientists got an experience with simulations and continued investigations independently. A few Doctoral Theses were presented with simulation results obtained with the BETACOOL program [7,8,9].

2.11.5 **Applications**

The BETACOOL code was elaborated in the collaboration with different scientific centers in the world where was benchmarked on the existing experiments and used for the simulation of new accelerator projects.

The most investigation of beam dynamics with magnetized electron beam was done at CELSIUS [10] and COSY [11]. The comparison of the different variants of the magnetized and non-magnetized electron beams was investigated with BETACOOL for the new electron cooling system at COSY on energy up to 2 MeV/u. The new magnetized electron cooling system was installed at COSY as prototype of the electron cooler for HESR [12].

The benchmarking of the non-magnetized friction force model was produced at Recycler electron cooling system (FNAL). Results of this investigation were used for the simulation of the beam dynamics with new 100 MeV electron cooler for RHIC [13]. Finally simulations show that the non-magnetize electron cooling system is not enough for the effective suppression of the intrabeam scattering and the new stochastic cooling system was installed on RHIC.

Large number investigations were devoted to existing and new experiments with different types of internal targets. Experiments with gas cell target at ESR were simulated with BETACOOL [14] for the optimization of electron cooling process. The new model of the pellet target implemented in BETACOOL was benchmarked with experiments on WASA@COSY [15]. The numerical simulation of the experiments with the pellet target PANDA@HESR permits to formulate the additional requirements on the target and detector parameters [16].

The new algorithm of the RF barrier bucket system was implemented into BETACOOL for the simulation of new accelerator projects [17]. This algorithm was

used for the simulation of the stacking process with the electron cooling at the HESR storage ring [18] and heavy ion collider NICA [19]. For the NICA project the optimization of cooling process (electron and stochastic) in booster and collider rings was also performed [20].

A lot of investigations were devoted to the ordered ion beams. Simulations with BETACOOL were used for reproducing of existing experimental results with ordered ion beam on different storage rings [21]. Experimental and numerical studies of ordered proton beams with the electron cooling were performed on COSY [22] and S-LSR [23] storage rings. Finally the ordered proton beam was achieved on S-LSR at energy 7 MeV and proton number about few thousand [24].

2.11.6 **References**

1. A.Yu.Lavrentev, I.N.Meshkov. The Computation of Electron Cooling Process in a Storage Ring. Preprint JINR E9-95-317, Dubna, Russia (1995).
2. I.Meshkov, Electron cooling: Status and Perspectives, Phys. Part. Nucl., 25 (6), (1994), 631.
3. V.Avilov, Calculation of Electrostatic Energy of Planar Lattices. Solid State Communications, v.44, No.4 p.555-558 (1982).
4. I.N.Meshkov, A.O.Sidorin, A.V.Smirnov, et.al. BETACOOL program for simulation of beam dynamics in storage rings. NIM A, 558, 325-328 (2006).
5. A.V. Fedotov, A. O. Sidorin, A. V. Smirnov. IBS for Non-Gaussian Distributions. Hadron Beams'10, Morschach, Switzerland (2010).
6. http://betacool.jinr.ru
7. T.Shirai. One-dimensional Beam Ordering of Protons at Ion Storage Ring S-LSR. PhD Thesis. Kyoto University, Japan (2007).
8. V.Gostishchev. Internal Target Effects in Ion Storage Rings with Beam Cooling. PhD Thesis. Goethe University Frankfurt am Main, Germany (2008).
9. MAO LI-Jun. Simulation and Experiments of Electron Cooling in HIRFL-CSRm. PhD Thesis. IPM, Lanzhou, China (2008).
10. A. V. Fedotov, B. Gålnander, V. N. Litvinenko, et al. Experimental studies of the magnetized friction force. Phys. Rev. E 73, 066503 (2006).
11. J. Dietrich, I. Meshkov, A.Sidorin, et al. Studies of Beam Dynamics in Cooler Rings. COOL'05, Galena, USA., 154-158, AIP, 821 (2005).
12. V.B. Reva, N. Alinovsky, A.M. Batrakov, et al. The First Commission Results of the High Voltage Magnetized Cooler for COSY. COOL'11, Alushta, Ukraine.
13. A.Fedotov, I.Ben-Zvi, A.Sidorin, et.al. Cooling Dynamics Studies and Scenarios for the RHIC Cooler. PAC'05, Knoxville, USA, 4236 (2005).
14. V.Gostishchev, C.Dimopoulou, A.Dolinskii, et.al. Comparison of measurements and simulations of internal target effects in the ESR storage ring. NIM A 641 (2011) 12–18.
15. A.Smirnov, A.Sidorin, D.Krestnikov, et.al. Simulation of Pellet Target Experiments with BETACOOL Code. RuPAC'08, Zvenigorod, Russia (2008).
16. A. Smirnov, A. Sidorin, D. Krestnikov. Effective Luminosity Simulation for PANDA Experiment at FAIR. COOL'09, IMP, Lanzhou, China, (2009).
17. A.Smirnov, A.Sidorin, D.Krestnikov, et.al. Implementation of Longitudinal Dynamics with Barrier RF in BETACOOL and Comparison to ESME. COOL'09, Lanzhou, China (2009).
18. A.V.Smirnov, D.A.Krestnikov, I.N.Meshkov, et.al. Particle Accumulation with a Barrier Bucket RF System. COOL'09, IMP, Lanzhou, China, 67-70, 2009.
19. A.O.Siodrin, A.V.Smirnov. Long Term Beam Dynamics Simulation with the BETACOOL Code. RuPAC, Zvenigorod, Russia (2008).

20. S.Kostromin, I.Meshkov, A.Sidorin, et.al. Application of Cooling Methods to NICA projects. COOL'11, Alushta, Ukraine, p.25-30 (2011).
21. A.Smirnov, I.Meshkov, A.Sidorin, et.al. Necessary Condition for Beam Ordering. COOL'07. Bad Kreuznach, Germany (2007).
22. I.Meshkov, Yu. Korotaev, A. Smirnov, et.al. Electron Cooling of Proton Beam at COSY and S-LSR. RuPAC'06, Novosibirsk, Russia (2006).
23. A. Noda, T. Shirai, H. Souda, et.al. Experimental Approach to Ultra-Cold Ion Beam at S-LSR. PAC'07, FNAL, Albuquerque, USA, p.2035-2037 (2007).
24. T.Shirai, M.Ikegami, A.Noda, et.al. One-Dimensional Beam Ordering of Protons in a Storage Ring. Phys. Rev. Lett. 98, 204801 (2007).

2.12 Beam Crystallization

Igor Meshkov, Alexander Smirnov, JINR, Dubna, Russia
Mail to: meshkov@jinr.ru.ru, smirnov@jinr.ru.ru

Akira Noda
National Institute of Radiological Sciences, Chiba, Japan
Mail to: a_noda@nirs.go.jp

2.12.1 Introduction

One of the brightest phenomena discovered in particle beam physics and related to cooling method is undoubtedly crystalline beam state. The story began with an experiment at NAP-M in 1979 when V. Parkhomchuk and team have observed a suppression of Schottky noise of proton beam as its momentum spread reduces under *electron cooling* (Figure 1) [1].

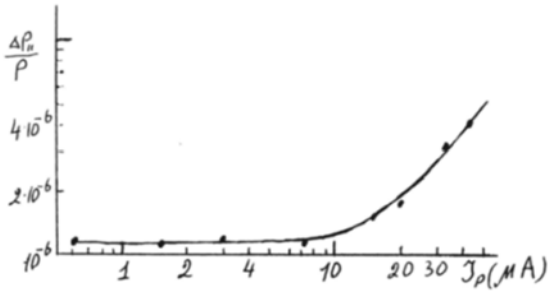

Figure 1: Proton beam momentum spread vs beam current under electron cooling in NAP-M cooler-ring (1 μA = $2{,}64\times10^6$ protons).

In 1984 V. Parkhomchuk has formulated the concept of crystalline beam [2]. Such a beam has a form of three dimensional (3D) crystals which circulates in storage rings as a whole and particles of the beam don't overpass each other kept by the ring focusing system and electrostatic field of neighborhood particles. Interparticle distance averaged by time is constant, although particles oscillate around average position like "normal" solid matter crystal. 1D crystal has a form of line (a "chain") and was called "the ordered beam".

2.12.2 **Development of Crystalline Beam Models**

In succeeding years it was followed by an outburst of theoretical studies (A. Sessler, J. Wei, J. Schiffer, R. Hasse and others [3,4,5]).The common criterion of the "beam crystallization" formulated by R. Hasse [4] is a decrease of the particle temperature T in particle rest frame (PRF) below interparticle potential energy U, so that:

$$\Gamma \equiv \frac{U}{T} = \frac{1}{4\pi\varepsilon_0}\frac{Z^2e^2}{aT} > 1 \ . \tag{1}$$

Here Ze is the ion charge, a – interparticle distance (in PRF).

The second condition is related to the lattice of the storage ring. It must be strong focusing one and operated below its transition energy [6,7,8]:

$$\gamma < \gamma_T \ . \tag{2}$$

The third condition follows from the requirement of absence of a linear resonance between the phonon modes of the crystalline structure and the machine lattice periodicity N_{sp}:

$$N_{sp} \geq 2\sqrt{\nu_x^2 + \nu_y^2} \ , \quad \text{or} \quad \mu_0 < \pi/2 \ , \tag{3}$$

where μ_0 is the betatron phase advance per lattice period. The shape of the crystals depends on the dimensionless linear density of particles:

$$\lambda_{ion} \equiv \left(\frac{3}{8\pi^2} \cdot \frac{Z^2}{A} \cdot \frac{r_p N^2}{\nu^2 C_{ring} \beta_0^2 \gamma^5} \right)^{1/3} , \ r_p = \frac{1}{4\pi\varepsilon_0}\frac{e^2}{m_p c^2}, \tag{4}$$

where N is particle number in the ring, C_{Ring} is the ring circumference, $\beta_0 = v_0/c$ is relativistic factor, ν is betatron tune, r_p is proton classic radius, m_p is proton mass, c is the speed of light. This theory confirmed by numerical simulation [8] predicts formation of different crystalline states of the cooled beam:

$\lambda_{ion} < 0.709$ - string (or "ordered" beam), $\lambda_{ion} < 0.964$ - zigzag, $\lambda_{ion} < 3.10$ - helix, etc.

Numerical simulation of crystalline beam formation and state is usually performed with molecular dynamic (MD) technique [9, 10]. The beam crystalline state formation in cooler rings can be explained from the specific behavior of the IBS heating force at low temperature of stored ions. As MD numerical simulation shows the IBS heating rate has a maximum when the conditions of crystalline state are satisfied. The crystalline state can be achieved when cooling power (electron or laser cooling) can suppress IBS heating one.

The progress of the crystalline beam theory was very significant. It was turn of experiment.

2.12.3 **Phase Transition to Ordered Beam**

The effect obtained on NAP-M was not confirmed during a long time by experiments on other cooler storage rings. In 1996 a qualitative leap happened in experimental studies of electron cooling of particle beams when M. Steck with colleagues observed a sudden and abrupt decrease of ion momentum spread during

gradual reduction of particle number in the beam (Figure 2) [11]. The experiments at ESR were continued and led to conclusion that "very cool" ion beam takes the form of one dimensional string where ions, like beads on a thread, do not pass each other, i.e. state of the *beam ordering* is formed. Later such a beam phase transition into ordered state has been observed at CRYRING as well [12].

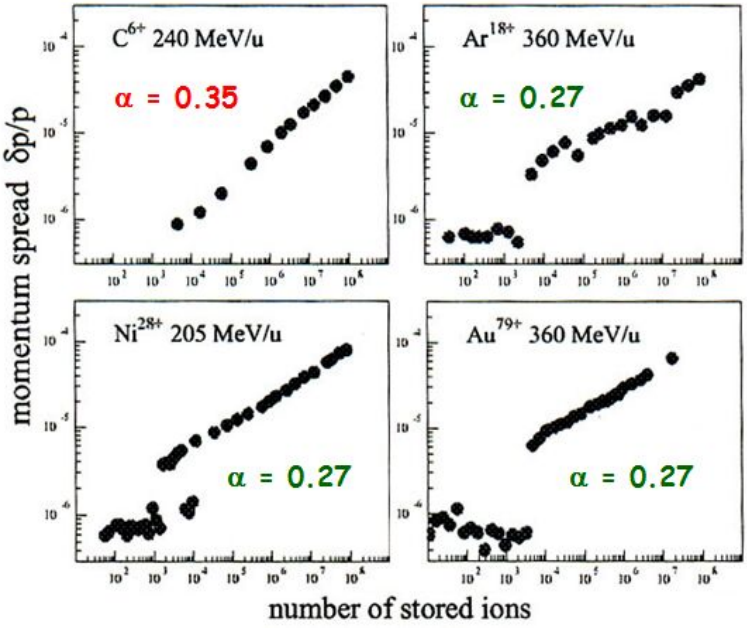

Figure 2: Ion momentum spread vs ion number under electron cooling in ESR [11].

The model employed by R. Hasse [4] predicts the beam temperature at which a one-dimensional ordered state of ion beam will be achieved. In this state the ions are not in PRF, but simply do not pass each other; i.e., remain in the same (ordered) sequence. The model is applicable to an ultra-low-density beam where collective Coulomb interaction is negligible. Later I. Meshkov formulated different criterion based on ion interaction in both longitudinal and transverse dimensions [13, 14]:

$$\Gamma_2 = \frac{Z^2 e^2}{T_{\|}\sigma_{\perp}} > \pi \ . \qquad (5)$$

Here $T_{\|}$ is particle longitudinal temperature (in PRF), $\sigma_{\perp}$ is the beam transverse size. Before ordering criteria of a particle beam were formulated by several authors. None of them fits to experimental data properly. Actually this criterion gives beam parameters which agrees with (4) for ordered beam.

All these experiments have been performed with ion beam. The question remained: why phase transition in proton beam was not observed in NAP-M experiment. An attempt to study this problem was made at COSY [15]. However, the phase transition was not obtained. It was explained by magnetic field ripples level in the ring magnets. One year later similar experiment at S-LSR (Kyoto University) has brought a success (Figure 3a) [16].

It turned out also that a particle beam under electron cooling undergoes the phase transition if particle momentum spread depends on the beam particle number N_p as

$$\frac{\Delta p}{p} \propto (N_p)^{\alpha}. \qquad (6)$$

with $\alpha = 0.3 \pm 0.3$ (Figure 2). In NAP-M experiment (Figure 1) $\alpha = 0.98$, at COSY $\alpha = 0.5$. Such a peculiarity was demonstrated with numerical simulation based on BETACOOL code developed by A.Smirnov (Figure 3b) [13]. This simulation had confirmed also criterion (5). The dependence (6) is defined by equilibrium between cooling power and IBS heating one in the beam (equilibrium trajectory in Figure 3b). Later more universal approach was derived for the description of the achievement of the ordered state [17]. The result agrees in general with criterion (5), as the authors of Ref. 17 noted.

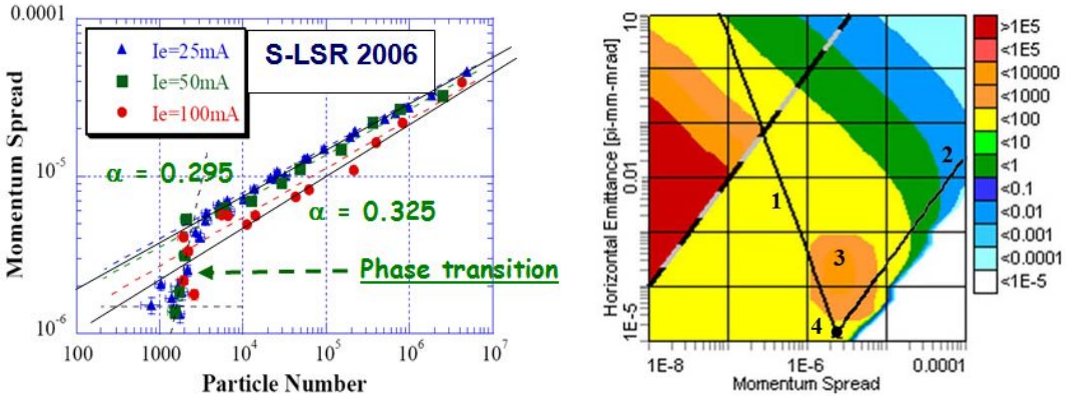

a) b)

Figure 3: 7 MeV protons at SLS-R. a) Experiment: proton momentum spread vs proton number under electron cooling; b) MD simulation with BETACOOL: 3D dependence of IBS longitudinal heating rates (in colours, sec^{-1}) vs horizontal emittance and momentum spread at $N_p = 10^3$; 1 – criterion Γ_2 (5); 2 – equilibrium trajectory ($T_{\|} \sim T_{\perp}$); 3 –anomalous island of longitudinal IBS heating rate; 4- ordering point.

2.12.4 **Experiments on Crystalline Beam Formation**

Only successful experiment on 3D crystalline beam formation has been performed at the radio-frequency quadrupole storage ring PALLAS (PAuL Laser cooling Acceleration System) [18]. It is a small "table-top" device which resembles a linear Paul trap, bent in a circle (Figure 4). Sixteen drift tubes are distributed around the ring and can be powered individually. The tubes enclose the quadrupole rods which provide transport and positioning ions along the orbit. The drift tubes at the two opposite locations are used for laser cooling and laser probing. Stripping injection of $^{24}Mg^{+}$ ions are provided by electron bombardment.

The PALLAS lattice is similar to that one of the stationary crystalline traps and meets the requirements (2), (3). The betatron tune of PALLAS ring is of several hundreds that is very different from conventional ion storage rings.

An attempt to form 3D crystalline beam was undertaken by the S-LSR group that designed and constructed a dedicated ring with lattice having high super-periodicity of 6 (Figure 5). It allows to meet the conditions (2), (3). To provide formation of 3D crystalline beam of 40 keV $^{24}Mg^{+}$ ions by application of 3D laser cooling, much

stronger cooling force based on "Synchro-Betatron Resonance Coupling (SBRC) was developed. This version of laser cooling was successfully demonstrated and extremely low ion temperature of $T_H = 6.4$ and $T_V = 2.1$ eV (in PRF) has been achieved in 2013-2014 [19]. Unfortunately, the studies have been stopped due to reorganization of the Laboratory at Kyoto University.

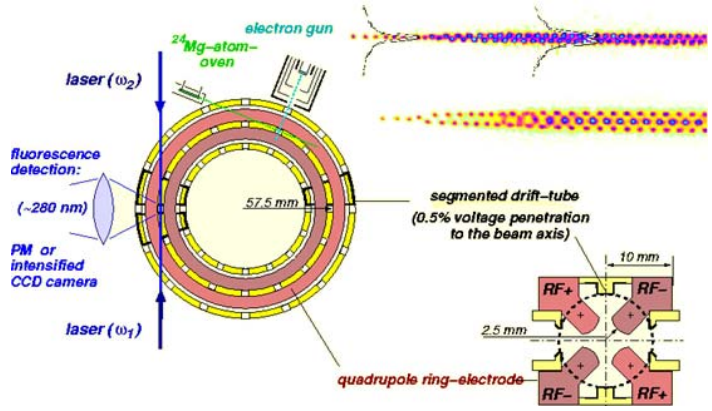

Figure 4: The scheme of PALLAS ring and structure of crystalline bunches.

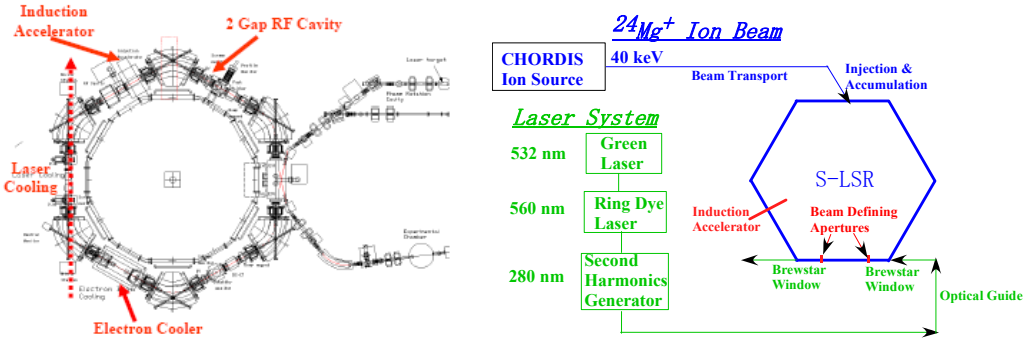

(a) (b)

Figure 5: Layout of S-LSR(a) and its laser cooling system (b).

2.12.5 **Application of Crystalline Beams**

As follows from written above intensity of ordered and crystalline beams is relatively low. Therefore, application of such beams should be addressed to rare and exotic isotopes. The necessary time for electron cooling restricts the application to short-lived isotopes. The first proposal of such application was Schottky Mass Spectroscopy of radioactive nuclei and their life times measurement in ordered ion beams at ESR [20]. The method proved to be very successful and more than 100 mass values of predominantly proton-rich nuclear fragments of stable Bi, Au and U projectiles have been determined experimentally, many of them with relative errors $\Delta M/M \sim 10^{-7}$.

Another proposal relates to ion-ion and electron-ion colliders with radioactive nuclei where ordered beam state can increase collider luminosity by several orders of magnitude. Recently an interest to heavy ion collider in merging beams' mode has been

expressed as well [21]. It allows studying of physical vacuum structure in collision of ions with high electric charge.

And last remark: 3D crystalline beam is very good model for experimental test of different theoretical speculations in solid state physics.

2.12.6 **Conclusion**

Crystalline state of charged particle beam in storage rings promises many fruitful applications. Many of them are not outspoken yet and will appear undoubtedly with the technique of such beams is being developed. The first step – the ordered beam formation – is done and the necessary conditions for this state existence are the following:

- Particle linear density (4) has to correspond the string structure;
- Beam parameters have to meet the ordering criterion (5);
- The power coefficient in dependence (6) has not exceed $\alpha < 0.3$;
- The sudden reduction of the momentum spread and/or transverse emittances has to be observed during decreasing of the circulating particle number.

2.12.7 **References**

1. V.Parkhomchuk et al., Journ. of Tech. Physics (in Russian), 50 (1980) 1001.
2. V.Parkhomchuk, Proc. of the Workshop on Electron Cooling and Related Applications, FZ Karlsruhe (1984) p.71.
3. A.Rahman and J.P.Schiffer, Phys. Rev. Lett. 57 (1986) 1133.
4. R.W.Hasse, Phys. Rev. Lett. 83 (1999) 3430.
5. J.Wei, X-P Li, and A.M.Sessler. Phys. Rev. Lett. 73 (1994) 3089.
6. J.Wei, A.Draeseke, M.Sessler, X.Li. Diverse topics in crystalline beams. Proceedings of the 31st Workshop of the INFN Eloisatron Project. Erice, Italy, November 12-21 (1995) p.229.
7. X.Li, H.Enokizono, H.Okamoto, Y.Yuri, A.Sessler, J.Wei. Phonon spectrum and the maintenance condition of crystalline beams. Physical Review Special Topics - Accelerators and Beams 9, 034201 (2006).
8. J.Wei, X.P.Li, A.M.Sessler, Crystalline Beam Ground State. BNL-52381 (1993).
9. A.Sidorin, A.Smirnov. BETACOOL code. ICFA BD, This issue.
10. J.Wei, H.Okamoto, A.Sessler. Necessary Conditions for attaining a crystalline beam. Phys. Rev. Lett., 80, (1998) 2606.
11. M.Steck et al., PRL. 77 (1996) 3803.
12. H.Danared et al., PRL 88 (2002) 1003.
13. I.Meshkov, D.Moehl, T.Katayama, A.Smirnov, et al., NIM A, 532 (2004), 19.
14. I.Meshkov, A.Sidorin, ibid., p.474.
15. J.Dietrich, I.Meshkov, J.Stein et al., Proc. of COOL'2005 Workshop, p. 154.
16. T.Shirai, A.Noda, I.Meshkov et al., PRL, 98 (2007) 204801.
17. H.Okamoto, K.Okabe, Y.Yuri, et al. Phys. Rev. E69, (2004) 066504.
18. T.Schätz, U.Schramm, D.Habs. Crystalline ion beams, Nature, 412, (2001) 717.
19. A.Noda et al., Proc. IPAC'14 (2014) p.28
20. B. Franzke, H. Geissel, G. Münzenberg, Mass and Lifetime Measurements of Exotic Nuclei in Storage Rings. Mass Spectrometry Reviews, 2008, 27, 428-469.
21. I.Meshkov, Yu.Oganissian, G.Ter-Akopian, G.Trubnikov, Report on Seminar at Frankfurt Institute for Advanced Studies, Frankfurt, 4 November 2013.

2.13 Theory and Simulation on Beam Crystallization

Hiromi Okamoto
Graduate School of Advanced Sciences of Matter, Hiroshima University,
1-3-1 Kagamiyama, Higashi-Hiroshima 739-8530, Japan
Mail to: okamoto@sci.hiroshima-u.ac.jp

2.13.1 Introduction

Beam crystallization is one of the most unique and attractive phenomena in accelerator physics. It is a kind of phase transition of a charged-particle beam spatially confined and guided by external electromagnetic forces. The concept of the beam's phase transition was first discussed by Dikansky, Pestrikov and Parkhomchuk to explain the anomalous Schottky signal from an electron-cooled proton beam in the NAP-M storage ring [1]. Shortly after that, Schiffer and co-workers applied the molecular dynamics (MD) simulation technique to explore the nature of Coulomb crystalline states in detail [2]. Their seminal work was generalized by Wei, Li, and Sessler who explicitly took the alternating-gradient (AG) lattice structure of a modern accelerator into consideration [3]. It is now believed that beam crystallization is, in principle, possible if several necessary conditions given in the next section are satisfied.

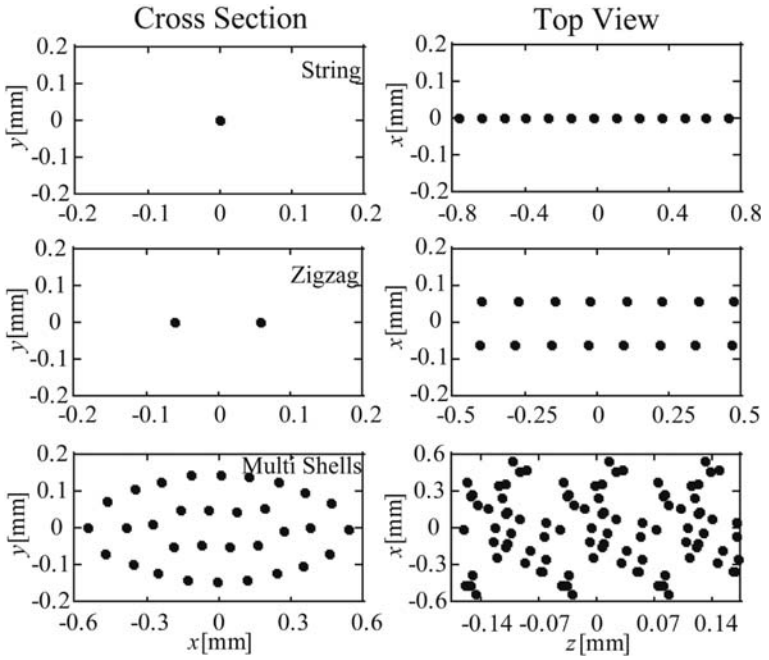

Figure 1: Typical spatial configurations of coasting crystalline beams.

The spatial configuration of a crystalline beam varies depending on the line density. Hasse and Schiffer theoretically derived critical line densities at which the structural transition of a particular crystalline configuration to another takes place [4]. Figure 1 shows three typical configurations of crystalline beams. Each dot represents a single charged particle circulating around a storage ring at relativistic speed. At low density, the crystalline structure is the so-called "string" where all particles are aligned along the

design orbit of the ring at equal intervals. If we increase the line density, the string configuration is suddenly converted into the "zigzag" configuration. By adding more particles, we can eventually construct a three-dimensional (3D) crystalline configuration with one or more "shells". The example in Fig. 1 (bottom) is a double-shell coasting crystalline beam. Crystallizing a bunched beam under the influence of a longitudinal radio-frequency (rf) field is also feasible.

These crystalline states are very different from any regular beams that have relatively low phase-space density and high temperature. Once a crystalline state is reached, everything is frozen out; the ordinary betatron and synchrotron oscillations of particles just disappear owing to the perfect balance between the external artificial focusing and internal Coulomb repulsion. The tune shifts are thus 100% in all three directions. Ideally, the emittance can be zero except for quantum noise. In order to establish such an ultimate high-quality state, we somehow need to compress a beam very strongly in phase space.

2.13.2 **Necessary Conditions for Crystallization**

2.13.2.1 ***Lattice Requirements***

In a uniform focusing channel assumed by Schiffer et al. [2], there should be no serious heating mechanisms that prevent the beam from approaching a crystalline state. Since the system is closed, we could always achieve beam crystallization by constantly removing the thermal energies of stored particles with an ideal cooling force. By contrast, in an AG storage ring a crystalline state can be reached only when the ring satisfies the following conditions [3,5]:

(a) γ(beam energy) < γ_T (transition energy of the ring), and

(b) the transverse *bare* tunes (ν_x, ν_y) < $N_{sp}/4$ with N_{sp} being the number of lattice superperiods around the ring.

The latter condition is associated with the transverse resonant instability of linear collective modes; the stop bands of the lowest-order coherent resonance are known to appear at high density whenever the betatron phase advance per unit lattice period exceeds 90 degrees.

In any crystalline state, the *effective* tunes have been depressed to zero (100% tune shifts) as mentioned above. This means that in the cooling process the actual operating point of the ring moves over a wide tune range crossing all stop bands in-between the initial high-temperature state and the final zero-temperature state. If the condition (b) is broken, the beam inevitably encounters the linear coherent resonance before arriving at a crystalline state, but this instability is generally too strong to be overcome with realistic cooling. Therefore, the cooling process will be interrupted seriously once one of the effective tunes comes close to $N_{sp}/4$ [6].

2.13.2.2 ***Transverse Cooling***

As discussed extensively in this Newsletter, several useful cooling methods have been invented and often employed around the world to improve the qualities (emittance) of stored, circulating beams of charged particles. For beam crystallization, however, the most popular "electron cooling" and "stochastic cooling" do not work because the

lowest beam temperature achievable with these conventional techniques is too high. The phase transition to a crystalline state occurs typically in a mK range, which suggests that "Doppler laser cooling" [7,8] is the only choice for the present purpose. While this advanced technique can only be applied to limited ion species, the reachable temperature is very close to the absolute zero where we can reasonably expect beam crystallization. In early 1990's, two European groups succeeded in cooling low-energy heavy-ion beams with longitudinal lasers [9,10].

An essential issue of Doppler cooling is that the radiation pressure from laser photons operates only in the direction of laser propagation. Since we introduce a cooling laser along a straight section of the ring so that the stored beam interacts with laser photons over a sufficiently long distance, no direct cooling force can be produced in the transverse directions. This is a serious obstacle toward beam crystallization that necessitates rather strong dissipative effects in all three degrees of freedom to cope with various heating sources. In fact, as the beam temperature decreases due to cooling, natural heating from intrabeam scattering (IBS) becomes severer and is maximized in the liquid phase where the *Coulomb coupling constant* $\Gamma \approx 1$ [5,11]. The dimensionless parameter Γ that characterizes the phase of a charged-particle beam is defined as the ratio of the average Coulomb potential energy to the beam temperature [12]. An ordinary gaseous beam before cooling has a Γ-value much less than unity while in the crystalline phase Γ goes beyond 170. Interestingly, if the ring is properly designed in consideration of the above-mentioned lattice requirements, the IBS heating effect starts to be weaker at lower temperature once the beam comes into the range $\Gamma > 1$. The internal heating mechanism eventually disappears in a perfect crystalline state because random Coulomb collisions no longer exist there. In order to enter the solid phase passing through the liquid phase where IBS is most active, we need to develop some 3D cooling force strong enough to surmount the peak IBS heating near $\Gamma \approx 1$.

2.13.2.3 ***Dispersion Compensation***

An ideal crystalline beam is stable even without cooling, maintaining an ordered spatial configuration as shown in Fig. 1 for many turns around the ring. In the string crystalline state, all particles are completely frozen in the beam frame at fixed points. Even in the zigzag and multi-shell crystalline states, the relative positions of individual particles do not change much except for very small coherent periodic oscillations driven by the AG lattice [13]. This indicates that the path length of a particle is exactly the same every turn but depends on which particle we observe; a radially outer particle has to follow a longer closed orbit than inner particles (and those closed orbits never intersect). On the other hand, the revolution frequencies of all particles must be identical to hold the crystalline structure, which implies that the radially outer particle has to travel a bit faster than the inner ones as long as their orbits are closed. This trivial fact originating from the existence of bending magnets causes a big trouble in practice. Any regular cooling forces, including the radiation pressure by an axial laser, simply try to equalize the velocities of all particles. Such conventional cooling does not match the dispersive nature of a crystalline state with finite horizontal extent; the equalization of the *linear* particle velocities rather than the *angular* velocities strongly disturbs the ordered structure and can even destroy it. In order to stabilize a crystalline configuration, we need to develop the *tapered force* that gives slightly larger equilibrium velocities to radially outer particles [5,14]. The tapered cooling for linear dispersion compensation can be expressed as

$$\Delta P_z = -f_z(P_z - C_{xz}x), \tag{1}$$

where ΔP_z stands for the change of the longitudinal momentum P_z in the beam frame before and after the cooling section, x is the horizontal coordinate, f_z is the friction coefficient, and C_{xz} is the *tapering factor* depending on the lattice design. Once a perfect equilibrium is reached, ΔP_z becomes zero leading to $P_z = C_{xz}x$. C_{xz} can be determined by solving the crystal-orbit equations that have a form similar to the root-mean-squared (rms) envelope equations for zero-emittance beams [15].

It is practically very difficult to *taper* the Doppler cooling force. A possible method probably the simplest is to displace an axial cooling laser slightly from the central beam orbit. If there is finite momentum dispersion in the cooling straight section, the horizontally displaced Gaussian laser naturally induces a tapered force as first experimentally demonstrated at the Test Storage Ring (TSR) in Heidelberg [16]. It is, however, impossible to adjust the tapering factor over a sufficient range. The controllability of C_{xz} can be improved to some degree by using two horizontally displaced, counter-propagating lasers with different wavelengths [17], but that is still not enough.

2.13.3 **Possible Approaches toward Ultracold Ion Beams**

All requirements summarized in the previous section have to be met simultaneously to realize beam crystallization. The first condition $\gamma < \gamma_T$ is usually satisfied in cooler storage rings operated at relatively low beam energy. It is also an easy matter to design a ring lattice that fulfills the second condition $\max(\nu_x, \nu_y) < N_{sp}/4$, but strictly speaking, this condition can only approximately be satisfied in reality due to inevitable error fields. It is thus very important to minimize imperfection fields so that the original lattice periodicity can be maintained as precisely as possible. If the symmetry breakdown is too strong, the stop band of linear collective resonance induced by the error fields will hinder the progress of beam cooling toward a crystalline state.

Even if we set another laser light perpendicular to the beam orbit, that is almost useless for transverse cooling because of a very limited spatial overlap between the laser and fast traveling beam. In order to achieve a dramatic enhancement of transverse cooling efficiency, several methods have been proposed theoretically. One of them is the so-called *resonant coupling method* (RCM) that makes use of emittance transfer between the longitudinal and transverse directions via linear dynamic coupling. This scheme is practically easy to implement; all we need is to move the operating point of the ring onto a difference resonance together with a linear synchrobetatron coupling potential on [18,19]. As the coupling source, we can employ either a regular rf cavity placed at a position with finite momentum dispersion [19] or a special coupling cavity excited in a deflective mode [18]. Linear coupling between the two transverse directions can readily be provided by either a skew quadrupole magnet or a solenoid. The effectiveness of RCM has already been confirmed in recent cooling experiments at Kyoto University [20,21]. In theory, RCM can equalize the cooling efficiencies of all three directions, which enables us to overcome the strong IBS heating at low temperature. Another practical solution for indirect transverse laser cooling is the use of a Wien filter [22]. We can extend the longitudinal Doppler cooling force to the transverse directions simply by putting a Wien filter in a cooling straight section.

The dispersion compensation is probably the most troublesome issue from a technical point of view. As briefly described above, no satisfactory method has been invented yet to generate a strong tapered force with a proper size of the tapering coefficient C_{xz}. Past MD simulations have pointed out that without a properly tapered cooling force, it is impossible to form a stable 3D crystalline state. It has also been shown that the longitudinal tapered force as defined in Eq. (1) naturally yields horizontal energy dissipation, which can further be extended to the vertical degree of freedom through a coupling resonance [14]. Cooling with properly tapered axial lasers, if it is available, can thus solve two important issues of beam crystallization (i.e. transverse cooling and dispersion compensation) simultaneously.

A completely different approach to the problem of dispersion compensation has been investigated by Ikegami et al. [23,24] who considered a special bending element rather than the special cooling force. If we can bend particle orbits without causing the dispersive effect, tapered cooling is no longer necessary. Such a unique bending element can be constructed by superimposing a horizontal electric dipole field on an ordinary vertical magnetic dipole field [23,25]. We can eliminate the linear dispersion of the ring, adjusting the strength of the deflective electric field. The required optimum electric field is proportional to the magnetic field strength and the velocity of the reference particle. This idea is, therefore, usable only for low energy beams. To the best of the author's knowledge, the storage ring S-LSR at Kyoto University is the only machine equipped with the dispersion-free bending elements [26].

2.13.4 **Concluding Remarks**

In a crystalline ground state, each individual particle plays an essential role in forming and stabilizing a spatially ordered configuration. The MD simulation technique is thus indispensable to the systematic numerical study of beam crystallization; particle-in-cell simulations and other popular approaches relying on macro-particles and/or meshes are not applicable to this study.

Several necessary conditions for attaining a crystalline beam have been found through past extensive theoretical effort. Since a beam has to be cooled to near the absolute zero for the phase transition to a crystalline ground state, Doppler laser cooling is currently the only means to accomplish our final goal. Other cooling methods technically established now do not suffice. We then need a compact storage ring that has sufficiently long straight sections for laser cooling. The beam energy must be chosen below the transition energy of the ring. A few practical methods have been proposed to extend the powerful longitudinal Doppler cooling force to the transverse dimensions. In principle, we can artificially produce a 3D cooling force strong enough to overcome IBS heating toward ultralow temperature.

High lattice symmetry and dispersion compensation are of crucial importance in beam crystallization. The former requirement is made to avoid the excitation of linear coherent resonance in the process of beam cooling. The betatron phase advance per lattice period has to be less than 90 degrees in both transverse directions. The lattice symmetry is, however, always broken weakly because of error fields, which gives rise to stop bands of non-structure resonances. It is essential to minimize lattice imperfections and carry out careful orbit correction prior to cooling experiments. The latter requirement, i.e. dispersion compensation, is very difficult to meet in regular storage rings. There are two possible ways to this issue, namely, either creating a

special tapered force optimized for the ring lattice or eliminating the momentum dispersion induced by bending magnets.

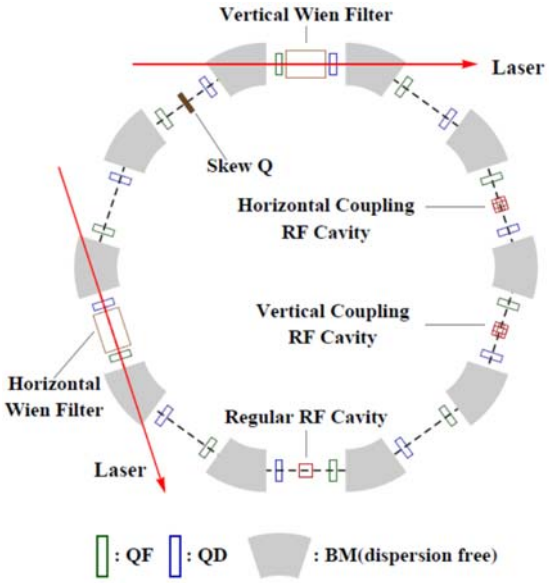

Figure 2: Outline of a cooler storage ring for ultracold beam generation [27]

Figure 2 shows an example of a possible storage-ring configuration aimed at the production of ultimately cold ion beams. QF and QD stand for quadrupole focusing and defocusing magnets while BM for bending elements. The ring consists of 10 lattice periods, each of which includes a simple doublet of quadrupoles. The bare betatron tunes around the ring must then be set below 2.5. Each bending magnet should have a movable electrostatic deflector inside to suppress linear momentum dispersion. Needless to say, the beam is naturally heated due to IBS in the region without the cooling force (80% of the ring circumference in this example). Although we have considered two counter-propagating lasers here, introducing even more lasers would certainly be preferable. In order to transfer the axial laser-induced dissipation to the other two degrees of freedom, we put two coupling rf cavities in separate straight sections, one of which correlates the longitudinal motion with the horizontal and the other with the vertical motion. Both cavities have the same structure but are axially rotated from each other by 90 degrees. A regular rf cavity is also placed in a dispersive position for beam bunching and for developing another linear coupling between the longitudinal and horizontal directions. In addition to these rf coupling sources, it would be convenient to have a skew quadrupole magnet or a solenoid for direct coupling between the two transverse directions. As an alternative tool for indirect transverse cooling, the ring is equipped with Wien filters in cooling sections.

Even in such a dedicated machine as sketched in Fig. 2, it might still be difficult to completely stabilize a large multi-shell crystalline state [24,28]. That is primarily due to the weak symmetry breakdown inevitably caused by coupling elements. As long as we rely on the Doppler laser cooling technique, some coupling sources must be introduced in the ring for indirect transverse cooling. It then becomes almost hopeless to make the structures of all straight sections perfectly identical including various coupling components. The degree of such symmetry breakdown should indeed be weak, but

unfortunately, it is not generally negligible in the ultimate low-temperature state considered here. However, with cooling lasers on, we could at least maintain string, zigzag, and even three-dimensionally ordered configurations in a carefully designed, dedicated cooler ring. The normalized rms emittance is expected to reach the order of 10^{-12} m in all three dimensions, according to previous MD simulations.

2.13.5 **References**

1. N. S. Dikansky and D. V. Pestrikov, in *Proc. Workshop on Electron Cooling and Related Applications*, (Karlsruhe, 1984), edited by H. Poth, KfK 3846 (1984); V. Parkhomchuk, ibid.
2. J. P. Schiffer and P. Kienle, Z. Phys. A**321**, 181 (1985); A. Rahman and J. P. Schiffer, Phys. Rev. Lett. **57**, 1133 (1986); J. P. Schiffer and A. Rahman, Z. Phys. A. **331**, 71 (1988).
3. J. Wei, X.-P. Li and A. M. Sessler, Phys. Rev. Lett. **73**, 3089 (1994); J. Wei, X.-P. Li, and A. M. Sessler, Brookhaven National Laboratory Report No. BNL-52381 (1993).
4. R. Hasse and J. P.Schiffer, Ann. Phys. **203**, 419 (1990).
5. J. Wei, H. Okamoto, and A. M. Sessler, Phys. Rev. Lett. **80**, 2606 (1998).
6. K. Okabe and H. Okamoto, Jpn. J. Appl. Phys. **42**, 4584 (2003).
7. D. J. Wineland and H. Dehmelt, Bull. Am. Phys. Soc. **20** , 637 (1975).
8. T. Hänsch and A. Shawlow, Opt. Commun. **13**, 68 (1975).
9. S. Schröder et al., Phys. Rev. Lett. **64**, 2901 (1990).
10. J. S. Hangst et al., Phys. Rev. Lett. **67**, 1238 (1991).
11. H. Okamoto, H. Sugimoto, and Y. Yuri, J. Plasma Fusion Res. Ser. **8**, 950 (2009).
12. See, e.g., S. Ichimaru, Rev. Mod. Phys. **54**, 1017 (1982).
13. In addition to the periodic breathing oscillation, any crystalline beam executes a sort of head-tail oscillation whenever it is bunched by an rf electric field. The head-tail motion is driven by momentum dispersion and energy modulation from the rf field. See, e.g., H. Okamoto, Y. Yuri, and K. Okabe, Phys. Rev. E **67**, 046501 (2003).
14. H. Okamoto and J. Wei, Phys. Rev. E **58**, 3817 (1998).
15. H. Okamoto, Phys. Plasmas **9**, 322 (2002).
16. I. Lauer et al., Phys. Rev. Lett. **81**, 2052 (1998).
17. N. Kjærgaard and M. Drewsen, Phys. Lett. A **260**, 507 (1999).
18. H. Okamoto, A. M. Sessler and D. Möhl, Phys. Rev. Lett. **72**, 3977 (1994).
19. H. Okamoto, Phys. Rev. E **50**, 4982 (1994).
20. M. Nakao et al., Phys. Rev. ST Accel. Beams **15**, 110102 (2012).
21. H. Souda et al., Jpn. J. Appl. Phys. **52**, 030202 (2013).
22. M. Ikegami, H. Sugimoto, and H. Okamoto, J. Phys. Soc. Jpn. **77**, 074502 (2008).
23. M. Ikegami et al., Phys. Rev. STAB **7**, 120101 (2004).
24. M. Ikegami, H. Okamoto, and Y. Yuri, Phys. Rev. STAB **9**, 124201 (2006).
25. R.E. Pollock, Z. Phys. A, **341**, 95 (1991).
    A. Noda, Nucl. Intsrum. Meth. A **532**, 150 (2004).
26. H. Okamoto, in *Proc. Int. Workshop on Beam Cooling and Related Topics* (Mürren, Switzerland, 2013), 152 – 156 (2013).
27. Y. Yuri and H. Okamoto, Phys. Rev. STAB **8**, 114201 (2005).

3 Workshop and Conference Reports

3.1 Superconducting Undulator Workshop

Jim Clarke, STFC Daresbury Laboratory and
Tom Bradshaw, STFC Rutherford Appleton Laboratory
Mail to: jim.clarke@stfc.ac.uk

3.1.1 The Workshop

The Superconducting Undulator Workshop was held at the STFC Rutherford Appleton Laboratory, Oxfordshire, UK, 28 – 29 April, 2014. Previous workshops have been held on this topic, with the most recent being held at Argonne National Laboratory in September 2010. Highlights from the Superconducting Undulator (SCU) Workshop are reported below. Details of the workshop, including a complete timetable and talks for download are available here: https://eventbooking.stfc.ac.uk/news-events/superconducting-undulator-workshop-203?agenda=1

The workshop attracted 37 delegates: 5 from USA, 4 from Asia and the remainder from Europe. Interestingly, two of the delegates were from industry actively involved in the development of SCUs. The workshop was chaired jointly by Jim Clarke (STFC Daresbury Laboratory) and Tom Bradshaw (STFC Rutherford Appleton Laboratory) who have both worked on the design, construction, and testing of SCUs since 2002.

The first session of the workshop heard status reports from seven laboratories active in the field of SCUs. The later sessions focussed on particular technical areas, these included: magnet modelling, field quality and magnet measurement, cryogenics and

heat loads, materials, and quench protection. In addition, there were dedicated close-out sessions at the end of each day to allow time to discuss and summarise common issues or areas where alternative solutions were being pursued.

3.1.2 **Recent Results**

The workshop opened with a report from Advanced Photon Source (APS) of Argonne National Laboratory who installed their first short prototype SCU in December 2012, this is the first SCU in user operation on a 3rd generation light source. It was commissioned in January 2013 and has been in continuous operational use since then. The device is only 33 cm long and has a period of 16 mm. The design peak magnetic field is 0.66 T but in fact 0.8 T has been achieved in operation with a vacuum gap of 7 mm. Although the device is relatively short it still outperforms the standard Undulator A 33 mm period, that is common at APS, in terms of brightness at specific high photon energies and can reach 100 keV using only the 5th harmonic. The magnet did not require any shimming to achieve the impressive ~2° rms phase error. The undulator is a standalone cryosystem through the use of four cryocoolers and no helium has needed to be added since it was first commissioned. It has been noted that if the undulator quenches it does not cause the APS beam to be lost but the reverse has been found to be true – beam loss in the APS can cause the undulator to quench. Fortunately recovery from a quench is very straightforward and only takes a few minutes.

The group at the APS are now working on a second prototype with an 18 mm period but this time 1.2 m long. It is due for installation at the end of 2014 and, if successful, this device will give an order of magnitude increase in brightness compared with the Undulator A over all photon energies above about 30 keV. The group is also collaborating with SLAC and LBNL on an SCU solution for the proposed X-ray FEL, LCLS-II, at SLAC.

Karlsruhe Institute of Technology reported on the performance of SCU15DEMO developed in collaboration with the industrial partner Babcock Noell GmbH, which has a period of 15 mm and is just over 1.5 m long. The device has achieved extremely good mechanical tolerances at room temperature (< 50 μm over 1.5 m) and magnetic measurements show a peak field on axis of 0.69 T with a magnetic gap of 8 mm. A challenge is seen in keeping the mechanical tolerances reached at room temperature in cold conditions. The beam vacuum chamber of the SCU15DEMO is movable to open from 7 mm vacuum gap to 15 mm, needed during electron beam injection and energy ramping in the ANKA storage ring. Even if all other projects concentrate on fixed gap devices, this feature might be appealing for other light sources during commissioning and/or operation. Lessons learnt from this device are now being applied to the latest prototype, SCU20. Detailed changes include the wire cross-section, the particular steel grade to be used, the winding scheme, and the mechanical arrangement of the winding formers. The KIT-BNG group has changed the winding scheme to avoid a possible unwanted increase in the first and second field integrals.

The SSRF in Shanghai has a project to develop a 0.88 T, 16 mm period SCU at a magnetic gap of 8 mm. A short test piece has been wound and potted already and tests carried out to measure the critical current of the device. Plans are now being developed to build a short undulator using a pair of these test pieces. The group is also looking at a more challenging device for use in an FEL which only has a period of 7 mm and a gap of 2 mm. This uses a novel winding scheme that avoids tight bending radii in the wire.

In the UK, STFC and Diamond Light Source are working together to develop a 15.5 mm period undulator with a 2 m long magnetic length and physical aperture of 5.4 mm. Several trial windings have been fabricated and a 30 cm long test piece has been tested up to 287 A, a little way off the 400 A required to reach 1.25 T. The engineering tolerances are very challenging, as for all the devices discussed, and almost every aspect of the SCU requires specific R&D. Good progress was reported however on how these aspects are being tackled one by one.

The report from NSRRC highlighted particular issues with field quality, the beam vessel, and the coil performance. The beam vessel is only 0.3 mm thick and unusually the magnet coil windings are glued to the vessel itself. Field shimming is also possible in their design via additional coils on the back side of the windings. These coils enable field adjustments of a few percent.

The BINP group from Novosibirsk has considerable experience with the design and fabrication of superconducting wigglers for light sources and they are now starting to apply their expertise to SCUs. They plan to build up the SCU using individually wound coils which is a different approach to the other teams. This approach requires very many low temperature electrical connections but they are confident that they can reliably make joints with very low resistance and don't see this as an issue.

The group from LBNL focus on the use of Nb3Sn, rather than the more common NbTi used in all other projects reported above. Nb3Sn gives a better temperature margin, although it is more difficult to work with. They are developing a novel shimming method based upon the use of thin high temperature superconducting tapes which are fixed to the vacuum chamber. The tape is configured using lithography or dedicated heaters to force the current to flow around small loops which then shim the field in that region.

3.1.3 **Technology Reports**

Although all of the SCU designs are magnetically quite simple there is still significant effort put into more and more detailed magnet models to answer questions about engineering tolerances, quench protection, and exact wire configurations, for example. A surprising feature that has been measured at ANL is that the exact winding geometry on the back side of the coils, away from the electron beam, can cause unwanted dipole and quadrupole terms to be generated.

Magnet measurements remain a major challenge for SCUs with all groups carrying out vertical tests in a cryostat with a Hall probe, prior to full magnet assembly. The workshop consensus was that this was necessary but not sufficient and that horizontal tests are also required. These are more challenging because of the need for the electron beam vessel to be under vacuum (the vessels are always operated at low temperature). Nevertheless, several groups are developing magnet measurement systems for the horizontal tests, some rely on Hall probes and other use stretched wire or pulsed wire systems. The APS team has implemented a system where the magnet is cold and under vacuum but the Hall probe is in a separate vessel at room temperature, this appears to be a very cost effective method with promising results for short magnets. The KIT group have developed an in vacuum conduction cooled test stand to measure undulator coils up to 2 m. They have presented preliminary results of the local magnetic field measured with Hall probes mounted on an in vacuum cooled sledge, which allows to accurately

determine the Hall probe position. First and second field integrals measured using the stretched wire method have been presented as well.

The LBNL group presented pulsed wire measurements performed on a short undulator. After correcting for dispersion effects it is possible to reconstruct the magnetic field. This method is very promising for applications in the final cryostat for small gap devices.

A major theme at the workshop was the estimation of the beam heating on the beam vessel caused by resistive wall wakefields and other effects. The KIT group have developed a dedicated experiment, COLDDIAG, to measure this heating directly and this was installed on the Diamond Light Source during 2012 and 2013. The measurements show a significantly higher power deposition per metre than is predicted by theory and this is backed up by analysis of the operating performance of two superconducting wigglers installed on Diamond as well. The Shanghai team have also built and installed a dedicated device for measuring deposited power. The results from this device are still being analysed. The workshop agreed that estimating the thermal loads due to wakefields was one of the largest areas of uncertainty for the SCU in general and the solution adopted is generally to install extra cooling capacity to ensure the SCUs meet their specification. There is no consensus on the optimum material to use for the beam vacuum vessel with aluminium, copper, and steel coated with copper or gold all being used or proposed.

3.1.4 **Future Prospects**

All of the various SCU project teams are very focussed on designing and building SCUs which can be installed in storage rings or FELs in the near future. Nevertheless, there is an eye on the next generation of SCUs which would make use of the novel high temperature superconductors which continue to develop rapidly. Several speakers described their initial test results on small prototypes using these materials and whilst there are still several major challenges that have to be addressed the long term benefits would be very considerable. Research and development in this area will continue and it will be interesting to see how quickly the SCUs reach the same level of maturity as their low temperature cousins.

3.1.5 **Conclusion**

The progress that has been achieved across several different institutes, since the last workshop, was very striking. There are more teams than ever working on these challenging undulators because the potential benefits to storage rings and FELs remain very significant compared with other technologies, despite the impressive progress made on competing technologies such as cryogenic permanent magnet undulators (CPMUs).

The successful and reliable operation of the first short SCU on a 3rd generation light source is a major milestone for this technology. As a next important goal to be demonstrated by the community is the higher spectral performance of SCUs with respect to the newest generation of CMPUs in operation in a light source. The community of physicists and engineers working on this technology are very enthusiastic and are systematically ticking off all of the issues one by one. The remaining challenges appear to all have feasible solutions but they do rely upon state of the art engineering.

The progress was so clear and so impressive that it was proposed to hold another workshop in 2015.

4 Forthcoming Beam Dynamics Events

4.1 EUCard2/XBeams Workshop: SPACE CHARGE 2015

Chris Prior
Rutherford Appleton Laboratory, Harwell Oxford OX11 0QX, U.K
Mail to: chris.prior@stfc.ac.uk or chris.prior@trinity.ox.ac.uk

The next EuCARD2/XBeams workshop devoted to issues involving space-charge will be held in Oxford, England, from March 23rd to 27th, 2015. This follows the remarkable success of SPACE CHARGE 2013 at CERN, which attracted people from many laboratories world-wide and revealed a pressing need for further study in the subject. The talks in Oxford will be aimed at stimulating discussion of topics such as space-charge effects and beam loss mitigation in high intensity machines, developments in the theoretical treatment of space-charge, simulation methods and codes, as well as addressing some of the issues thrown up in the designs of future high current proton and ion facilities. There will be a dinner in Trinity College and there may be an opportunity to tour the accelerators at the ISIS spallation neutron source at the Rutherford Appleton Laboratory.

Registration will open in December 2014. A block of rooms has been reserved at Trinity, and the workshop is likely to be shared between the College and the nearby John Adams Institute (JAI). Further details will be available on the workshop web-site http://www.cockcroft.ac.uk/events/SpaceCharge15/

4.2 The 56th ICFA Advanced Beam Dynamics Workshop on Energy Recovery Linacs, ERL 2015

Sergey Belomestnykh
Brookhaven National Laboratory, Upton, NY 11973, USA
Mail to: sbelomestnykh@bnl.gov

We are pleased to announce that the 56th ICFA Advanced Beam Dynamics Workshop on Energy Recovery Linacs (ERL 2015) will be held at Stony Brook University, Stony Brook, NY, USA from June 7 to 12, 2015. This will be the sixth workshop in the series of of international workshops covering accelerator physics and technology of Energy Recovery Linacs. The workshop will serve as a forum for scientists and engineers from around the world to review the latest developments in ERL physics, technology and applications, to exchange ideas and discuss “hot topics” of this field of research. Among the issues to be addressed are: beam stability in multi-pass ERLs, design of photoemission electron injectors, superconducting RF systems, beam optics, instrumentation, alignment, emittance requirements. The talks will cover commissioning and operations experience, ERL applications, status presentations from

different projects. There will be opening and closing plenary sessions, working group sessions, and a poster session. The proceedings will be published at JACoW.

Workshop organizers: Sergey Belomestnykh (sbelomestnykh@bnl.gov), IOC Chair
Dmitry Kayran (dkayran@bnl.gov), IPC Chair
Vadim Ptitsyn (vadimp@bnl.gov), LOC Chair

4.3 ICFA Mini-Workshop: Advanced Optics Control

The Advanced Optics Control workshop will take place 5-6 February, 2015 and be hosted by CERN. It aims at reviewing recent advancements in optics measurement, correction, and understanding from colliders and synchrotrons around the world. This workshop may be regarded as the third of a saga:

1) The 2011 Optics Measurements, Corrections and Modeling for High-Performance Storage Rings: http://indico.cern.ch/event/132526/.
2) The 2013 LHC Optics Measurement and Corrections Review: http://indico.cern.ch/event/246159/.

Organizers:

Mei Bai
Giuliano Franchetti
Massimo Giovannozzi
Mike Lamont
Rogelio Tomas Garcia
Frank Zimmermann

Web site: http://indico.cern.ch/e/AOC.

4.4 The Second Announcement on "ICFA Mini-Workshop on Beam Commissioning for High Intensity Accelerators"

As announced in the Beam Dynamics Newsletter No. 64, a mini-workshop devoted to commissioning of high intensity accelerators will be held at the CSNS site, Dongguan, Guangdong, China, from June 8-10, 2015. The website has been set up:

http://indico.ihep.ac.cn/categoryDisplay.py?categId=208.

A preliminary workshop agenda will be published on the website. The accommodation, transport and registration information are available online. The registration will be open soon. We hope you will be able to attend the workshop and contribute.

Workshop Co-chair:	Weiren Chou and Sheng Wang
Scientific Program Committee Co-chair:	Alex Chao, Shinian Fu

For administrative information, please contact:

Weiling Huang, workshop secretary,
Dongguan branch, IHEP,
huangwei@ihep.ac.cn ,
Tel: 86-0769-89156408

5 Announcements of the Beam Dynamics Panel

5.1 ICFA Beam Dynamics Newsletter

5.1.1 Aim of the Newsletter

The ICFA Beam Dynamics Newsletter is intended as a channel for describing unsolved problems and highlighting important ongoing works, and not as a substitute for journal articles and conference proceedings that usually describe completed work. It is published by the ICFA Beam Dynamics Panel, one of whose missions is to encourage international collaboration in beam dynamics.

Normally it is published every April, August and December. The deadlines are 15 March, 15 July and 15 November, respectively.

5.1.2 Categories of Articles

The categories of articles in the newsletter are the following:

1. Announcements from the panel.
2. Reports of beam dynamics activity of a group.
3. Reports on workshops, meetings and other events related to beam dynamics.
4. Announcements of future beam dynamics-related international workshops and meetings.
5. Those who want to use newsletter to announce their workshops are welcome to do so. Articles should typically fit within half a page and include descriptions of the subject, date, place, Web site and other contact information.
6. Review of beam dynamics problems: This is a place to bring attention to unsolved problems and should not be used to report completed work. Clear and short highlights on the problem are encouraged.
7. Letters to the editor: a forum open to everyone. Anybody can express his/her opinion on the beam dynamics and related activities, by sending it to one of the editors. The editors reserve the right to reject contributions they judge to be inappropriate, although they have rarely had cause to do so.

The editors may request an article following a recommendation by panel members. However anyone who wishes to submit an article is strongly encouraged to contact any Beam Dynamics Panel member before starting to write.

5.1.3 How to Prepare a Manuscript

Before starting to write, authors should download the template in Microsoft Word format from the Beam Dynamics Panel web site:

http://www-bd.fnal.gov/icfabd/news.html

It will be much easier to guarantee acceptance of the article if the template is used and the instructions included in it are respected. The template and instructions are expected to evolve with time so please make sure always to use the latest versions.

The final Microsoft Word file should be sent to one of the editors, preferably the issue editor, by email.

The editors regret that LaTeX files can no longer be accepted: a majority of contributors now prefer Word and we simply do not have the resources to make the conversions that would be needed. Contributions received in LaTeX will now be returned to the authors for re-formatting.

In cases where an article is composed entirely of straightforward prose (no equations, figures, tables, special symbols, etc.) contributions received in the form of plain text files may be accepted at the discretion of the issue editor.

Each article should include the title, authors' names, affiliations and e-mail addresses.

5.1.4 **Distribution**

A complete archive of issues of this newsletter from 1995 to the latest issue is available at

http://icfa-usa.jlab.org/archive/newsletter.shtml.

This is now intended as the primary method of distribution of the newsletter.

Readers are encouraged to sign-up for electronic mailing list to ensure that they will hear immediately when a new issue is published.

The Panel's Web site provides access to the Newsletters, information about future and past workshops, and other information useful to accelerator physicists. There are links to pages of information of local interest for each of the three ICFA areas.

Printed copies of the ICFA Beam Dynamics Newsletters are also distributed (generally some time after the Web edition appears) through the following distributors:

Weiren Chou	chou@fnal.gov	North and South Americas
Rainer Wanzenberg	rainer.wanzenberg@desy.de	Europe[++] and Africa
Toshiyuki Okugi	toshiyuki.okugi@kek.jp	Asia[**]and Pacific

++ Including former Soviet Union.

** For Mainland China, Jiu-Qing Wang (wangjq@mail.ihep.ac.cn) takes care of the distribution with Ms. Su Ping, Secretariat of PASC, P.O. Box 918, Beijing 100039, China.

To keep costs down (remember that the Panel has no budget of its own) readers are encouraged to use the Web as much as possible. In particular, if you receive a paper copy that you no longer require, please inform the appropriate distributor.

5.1.5 **Regular Correspondents**

The Beam Dynamics Newsletter particularly encourages contributions from smaller institutions and countries where the accelerator physics community is small. Since it is impossible for the editors and panel members to survey all beam dynamics activity worldwide, we have some Regular Correspondents. They are expected to find interesting activities and appropriate persons to report them and/or report them by themselves. We hope that we will have a "compact and complete" list covering all over the world eventually. The present Regular Correspondents are as follows:

Liu Lin	Liu@ns.lnls.br	LNLS Brazil
Sameen Ahmed Khan	Rohelakan@yahoo.com	SCOT, Oman
Jacob Rodnizki	Jacob.Rodnizki@gmail.com	Soreq NRC, Israel
Rohan Dowd	Rohan.Dowd@synchrotron.org.au	Australian Synchrotron

We are calling for more volunteers as Regular Correspondents.

5.2 ICFA Beam Dynamics Panel Members

Name	eMail	Institution
Rick Baartman	baartman@lin12.triumf.ca	TRIUMF, 4004 Wesbrook Mall, Vancouver, BC, V6T 2A3, Canada
Marica Biagini	marica.biagini@lnf.infn.it	INFN-LNF, Via E. Fermi 40, C.P. 13, Frascati, Italy
John Byrd	jmbyrd@lbl.gov	Center for Beam Physics, LBL, 1 Cyclotron Road, Berkeley, CA 94720-8211, U.S.A.
Yunhai Cai	yunhai@slac.stanford.edu	SLAC, 2575 Sand Hill Road, MS 26 Menlo Park, CA 94025, U.S.A.
Swapan Chattopadhyay	swapan@cockcroft.ac.uk	The Cockcroft Institute, Daresbury, Warrington WA4 4AD, U.K.
Weiren Chou (Chair)	chou@fnal.gov	Fermilab, MS 220, P.O. Box 500, Batavia, IL 60510, U.S.A.
Wolfram Fischer	wfischer@bnl.gov	Brookhaven National Laboratory, Bldg. 911B, Upton, NY 11973, U.S.A.
Yoshihiro Funakoshi	yoshihiro.funakoshi@kek.jp	KEK, 1-1 Oho, Tsukuba-shi, Ibaraki-ken, 305-0801, Japan
Jie Gao	gaoj@ihep.ac.cn	Institute for High Energy Physics, P.O. Box 918, Beijing 100039, China
Ajay Ghodke	ghodke@cat.ernet.in	RRCAT, ADL Bldg. Indore, Madhya Pradesh, 452 013, India
Ingo Hofmann	i.hofmann@gsi.de	High Current Beam Physics, GSI Darmstadt, Planckstr. 1, 64291 Darmstadt, Germany
Sergei Ivanov	sergey.ivanov@ihep.ru	Institute for High Energy Physics, Protvino, Moscow Region, 142281 Russia
In Soo Ko	isko@postech.ac.kr	Pohang Accelerator Lab, San 31, Hyoja-Dong, Pohang 790-784, South Korea
Elias Metral	elias.metral@cern.ch	CERN, CH-1211, Geneva 23, Switzerland
Yoshiharu Mori	mori@rri.kyoto-u.ac.jp	Research Reactor Inst., Kyoto Univ. Kumatori, Osaka, 590-0494, Japan
George Neil	neil@jlab.org	TJNAF, 12000 Jefferson Ave., Suite 21, Newport News, VA 23606, U.S.A.
Toshiyuki Okugi	toshiyuki.okugi@kek.jp	KEK, 1-1 Oho, Tsukuba-shi, Ibaraki-ken, 305-0801, Japan
Mark Palmer	mapalmer@fnal.gov	Fermilab, MS 221, P.O. Box 500, Batavia, IL 60510, U.S.A.
Chris Prior	chris.prior@stfc.ac.uk	ASTeC Intense Beams Group, STFC RAL, Chilton, Didcot, Oxon OX11 0QX, U.K.
Yuri Shatunov	Yu.M.Shatunov@inp.nsk.su	Acad. Lavrentiev, Prospect 11, 630090 Novosibirsk, Russia
Jiu-Qing Wang	wangjq@ihep.ac.cn	Institute for High Energy Physics, P.O. Box 918, 9-1, Beijing 100039, China
Rainer Wanzenberg	rainer.wanzenberg@desy.de	DESY, Notkestrasse 85, 22603 Hamburg, Germany